



HAL
open science

Physics of superconducting nickel oxides from first principles calculations

Alvaro Adrian Carrasco Alvarez

► **To cite this version:**

Alvaro Adrian Carrasco Alvarez. Physics of superconducting nickel oxides from first principles calculations. Physics [physics]. Normandie Université, 2023. English. NNT : 2023NORMC272 . tel-04504289

HAL Id: tel-04504289

<https://theses.hal.science/tel-04504289>

Submitted on 14 Mar 2024

HAL is a multi-disciplinary open access archive for the deposit and dissemination of scientific research documents, whether they are published or not. The documents may come from teaching and research institutions in France or abroad, or from public or private research centers.

L'archive ouverte pluridisciplinaire **HAL**, est destinée au dépôt et à la diffusion de documents scientifiques de niveau recherche, publiés ou non, émanant des établissements d'enseignement et de recherche français ou étrangers, des laboratoires publics ou privés.

THÈSE

Pour obtenir le diplôme de doctorat

Spécialité **PHYSIQUE**

Préparée au sein de l'**Université de Caen Normandie**

Physics of superconducting nickel oxides from first principles calculations

Présentée et soutenue par

ALVARO ADRIAN CARRASCO ALVAREZ

Thèse soutenue le 18/12/2023

devant le jury composé de :

M. PHILIPPE GHOSEZ	Professeur - Université de Liège	Rapporteur du jury
M. JAVIER JUNQUERA	Professeur - Universidad de Cantabria	Rapporteur du jury
MME EVA BENCKISER	Directeur de recherche - Université de Stuttgart	Membre du jury
M. JULIEN VARIGNON	Maître de conférences - Université de Caen Normandie	Membre du jury
M. ETIENNE JANOD	Directeur de recherche - Institut des matériaux Jean Rouxel	Président du jury
M. WILFRID PRELLIER	Directeur de recherche au CNRS - ENSICAEN	Directeur de thèse
M. MANUEL BIBES	Directeur de recherche au CNRS - Université Paris-Saclay	Co-directeur de thèse

Thèse dirigée par **WILFRID PRELLIER** (Laboratoire de cristallographie et sciences des matériaux (Caen)) et **MANUEL BIBES** (Université Paris-Saclay)

Este manuscrito se lo dedico a mis padres que siempre han estado a mi lado durante este largo viaje, a aquellas personas que desafortunadamente no me podrán acompañar más, y finalmente pero no por ello menos importante, a Nishu quien ha cuidado de mi durante todo este tiempo.

Acknowledgements

First of all, I thank the CNRS for the founding, as well as the University of Caen, the ENSICAEN, and the doctoral school for allowing this thesis to take place.

I would like to acknowledge and thank my thesis director and Director of the CRISMAT Lab, Dr. Wilfrid Prellier, for making this work possible, being helpful, and trying to keep a good work environment for the whole lab. I would also like to thank my thesis co-director, Dr. Manuel Bibes, for his scientific guidance and support in spite of the distance, as well as his welcoming attitude and kindness. I would like to express a special thanks to my supervisor, Dr. Julien Varignon, for his guidance in both scientific and human aspects and his kindness throughout these three years. Despite some bureaucratic technicalities, Dr. Julien Varignon should be considered the third director of this thesis by all means. I feel very lucky and proud to have you as a supervisor, and definitely, this thesis would not have been possible without you. I also have a special mention for Dr. Sébastien Petit for his help in so many ways over these three years.

I would also like to thank the administrative people from CRISMAT Lab, both the IT department, Mr. Gratien Cherrier, and Mr. Eric Lecourt, with special thanks to Gratien for being so helpful and kind. I would also like to mention the HR department, Marie, Benoit, Sandrine, and Soizic, for being so helpful and easy to reach. I would also like to acknowledge the help of Veronique, especially at the beginning of my Ph.D.

Thank you as well to the jury members for coming to Caen to judge this work. I would like to say thank you to Prof. Javier Junquera and Prof. Philippe Ghosez for taking all the time to read and write the report of this manuscript, as well as the other jury members, Dr. Eva Benckiser and Dr. Etienne Janod, for reading my manuscript and giving suggestions of improvement.

I would like to say many thanks to my friends and coworkers. From Thales lab, Fernando Gallego, Srijani Mallik, Luis Moreno, Dongxin Zhang, Hugo Witt and Lucia Iglesias for their kindness and being so welcoming. I hold very good memories with all of you in spite of not sharing a big amount of time together. From the CRISMAT lab, I would like to give a special thanks to my friends Oualyd Elkhoulfi and Abhishek Yadav for being the best buddies I could ask for. I would also like to thank my good friends Krishnendu, Mufeed, Jefry, Hari, Paribesh, Abdelhaq, Mudit, Sara, Christoph, and Erica. I feel very lucky to have you guys by my side in one way or another. Muchas gracias a Cintli y Miguel por ser papa and mama for the whole

group. I would also like to mention some of my coworkers, Serge, Marie, Loïc, and Moussa. I also want to mention my friends from outside the lab: Mukul, Moizine, Alejandro, Luis Miguel, Ignacio, and Anjali, and all those whose names have not been mentioned; thank you all.

Finally, I would like to thank Nishu, my parents, and my family for all being very supportive. This manuscript belongs to all of you.

Abstract

The understanding of high temperature superconductors based on Cu oxides could be improved by finding possible oxide analogues with different transition metals. In that regard Ni oxide superconductors were proposed to be promising candidates to better understand the origin of the high temperature superconductivity in the cuprates. In the following manuscript, we present a first-principles study of the physics of the superconducting nickel oxides discovered in 2019 based on Density Functional Theory. From our study we reveal that the undoped infinite layer RNiO_2 compounds present an antiferromagnetic metallic phase at low temperature. A strong Hund's coupling that dominates over the crystal field explains the coexistence between antiferromagnetism and metallic behavior. Regarding the doping phase diagram, we propose understanding the normal state of these superconducting compounds, starting from an insulating nickel oxide phase R_2NiO_4 instead of the metallic RNiO_2 phase. This allows us to find a charge-ordering instability in the doping phase diagram when the Ni cations present a 1.5+ oxidation state. We explore this charge ordering and show that it is a consequence of an electronic instability that produces a double local environment of Ni^+ and Ni^{2+} cations, which is accompanied by a breathing distortion of the NiO_4 complexes B_{oc} . From this point, we further study this charge ordering instability revealing that decreasing the Ni oxidation state quenches the instability and it disappears in the vicinity of the reported superconducting region. We then build a superconducting model based on the B_{oc} phonon modes which can reproduce quantitatively well the superconducting critical temperature dome accounting for the metallic but non-superconducting region in the doping phase diagram. Furthermore, we discuss the importance of the crystal structure when designing new superconducting compounds and how these nickel-based superconductors relate to other superconducting compounds. Finally, we extend the model to other compounds such as the ruthenates, explaining their superconducting properties as bulk and nanofilm materials.

La compréhension de l'origine de la supraconductivité haute température est entravée par l'absence de matériaux analogues aux cuprates. Bien que proposée depuis longtemps dans les oxydes de nickel de formule générale $\text{R}_{n+1}\text{Ni}_n\text{O}_{2n+2}$, matériaux isoélectronique aux cuprates, la supraconductivité n'a été observée qu'en 2019 mais les mécanismes mis en jeu reste à déterminer. Dans cette thèse, nous présentons une étude des oxydes de nickel supraconducteurs à partir de simulations de premiers principes basées sur la théorie fonctionnelle de la densité. Nous révélons que les composés RNiO_2 à couche infinie non dopés présentent une phase métallique antiferromagnétique à basse température. Un fort couplage de Hund qui domine le champ cristallin explique la coexistence entre l'antiferromagnétisme et le comportement métallique. En

étudiant le diagramme de phase en fonction de n , nous identifions un ordre de charge entre des Ni^{1+} et Ni^{2+} pour $n = 2$. Il est la conséquence d'une instabilité électronique du degré d'oxydation 1.5+ des Ni qui préfère dismuter vers les degrés 1+ et 2+ qui sont plus stables, produisant une distorsion B_{oc} des complexes NiO_4 pour accommoder les différentes charges. À partir de ce point, le dopage en électron supprime progressivement l'ordre de charge et il disparaît à proximité de la région supraconductrice observée expérimentalement. Nous construisons alors un modèle supraconducteur basé sur les modes de phonons B_{oc} reproduisant quantitativement le dôme de température critique supraconductrice en fonction du dopage. Nous discutons en outre de l'importance de la structure cristalline lors de la conception de nouveaux composés supraconducteurs et de la relation entre ces supraconducteurs à base de nickel et d'autres composés supraconducteurs. Enfin, nous étendons le modèle à d'autres composés tels que les ruthénates, expliquant leurs propriétés supraconductrices en tant que matériaux massifs et nanofilms.

Table of contents

1	Introduction	1
1.1	Superconductivity	1
1.1.1	London phenomenological theory	2
1.1.2	Ginzburg-Landau Theory	3
1.1.3	The BCS theory of Superconductivity	5
1.1.4	Alternatives to the BCS theory	14
1.2	Oxide compounds	15
1.2.1	Perovskite oxides	16
1.2.2	Perovskite-based nickel oxides	19
1.2.3	Layered nickel oxides	23
1.2.4	Superconducting Nickel oxides	25
1.3	Scope of the thesis	30
2	Methods	33
2.1	The electronic many body problem	33
2.2	Density Functional Theory	34
2.2.1	Kohn-Sham DFT	36
2.2.2	Density functionals	38
2.2.3	Spin polarized DFT	41
2.2.4	Basis set	43
2.2.5	Wannier Functions	44
2.2.6	Paramagnetism with DFT	46
2.2.7	Models of magnetism and DFT	48
2.3	Landau Theory of Phase Transitions	48
2.4	Superconductivity	51
3	The self-interaction problem in RBO_3 perovskites and related compounds	55
3.1	Self interaction errors	55
3.2	Rare earth perovskite oxides RBO_3	56
3.2.1	Structural relaxation	56
3.2.2	Compounds with a half-filled $4f$ shell	58
3.2.3	Compounds with a degenerate $4f$ shell	60
3.3	Related compounds: Infinitely layered Nickelates RNiO_2	61
3.4	Conclusion	63

4	Properties of bulk RNiO₂ compounds	65
4.1	Structural Properties	65
4.1.1	Relaxation results	66
4.1.2	Role of the size of the A-site cation	70
4.1.3	Role of the epitaxial strain	71
4.1.4	Hydrogen intercalation	72
4.2	Magnetic properties	74
4.2.1	Intrinsic magnetism	74
4.2.2	Magnetic ground state	75
4.3	Electronic Structure	78
4.3.1	Role of local spin formation	78
4.3.2	Trends on the electronic structure with magnetism	80
4.3.3	Orbital character of the electronic structure	81
4.3.4	Electronic structure and lattice distortions	85
4.3.5	Effects of H intercalation	86
4.4	Conclusion	87
5	Superconductivity in doped RNiO₂ nickel oxides	89
5.1	Technical parameters of the calculations	89
5.2	Understanding the phase diagram	90
5.3	Nickelates at half-doping	91
5.3.1	Origin of the disproportionation mode	95
5.4	Evolution of the charge ordering with the doping	96
5.4.1	Evidence of an electronic phase transition	97
5.5	Superconducting model	100
5.6	Discussion	105
5.6.1	Doping phase diagram and the spin degree of freedom	106
5.6.2	Pairing symmetry	110
5.6.3	Similarities with other superconductors	111
5.7	Conclusion	111
6	Strengths and limitations of the superconducting model	113
6.1	General phase diagram of layered nickel oxides	113
6.2	Importance of spin polarization	115
6.3	Properties of La based RRP compounds	116
6.3.1	Band dispersion of La ₆ Ni ₅ O ₁₂	122
6.4	Origin of the charge orderings on nickelates	122
6.5	Superconducting properties	125
6.6	Superconductivity and crystal structure	127
6.6.1	Structure and physical properties of Nd _{0.8} Sr _{1.2} NiO ₃	128
6.6.2	Electronic structure calculations	129
6.6.3	Prediction of charge ordering	132

6.6.4	Understanding the magnetic properties of $\text{Nd}_{0.8}\text{Sr}_{1.2}\text{NiO}_3$	134
6.7	Conclusion	135
7	Extension of the model to other systems: Ruthenates	137
7.1	Gap openings in perovskite-related compounds	137
7.2	Ruthenate perovskite-based oxides	138
7.3	Ground state properties of A_2RuO_4 compounds	139
7.3.1	Structural relaxation results	139
7.3.2	Electronic and structural parameters	140
7.4	Superconductivity in ruthenate compounds	147
7.4.1	Band structure of Sr_2RuO_4 ground state	148
7.4.2	Evaluating the electron-phonon coupling	148
7.5	Confirmation of the model in Ca_2RuO_4 nanofilm	151
7.6	Conclusion	155
	Conclusion and perspectives	157
	List of figures	159
	List of tables	169
	References	171

Chapter 1

Introduction

The results and works covered in this thesis were carried mainly in the theoretical team of the thin films group of the Laboratoire de Crystallographie et Sciences Matériaux (CRISMAT) in Caen, as a joint collaboration with the experimental team of Unité Mixte de Physique CNRS/Thales (UMPhy) in Paris. This thesis aims to understand the superconductivity in the nickel-based superconductors recently discovered in 2019. The main interest in these particular compounds is due to the possible similarity with the Cu-based superconductors, which are arguably up-to-date, the most important family of high-temperature superconductors. Nonetheless, the superconductivity of Cu-based compounds is not fully understood. Thus, finding possible analogs and comprehending their nature could unlock the design of high-temperature superconductors.

This chapter contains the main concepts and state-of-the-art of the thesis topic, namely superconductivity and nickel-based superconductors. The first section involves a general introduction to superconductivity and the main theories to explain it. The second section introduces the main results regarding the family of compounds that we are interested in. Introducing the oxides and ABO_3 perovskite compounds, then the $RNiO_3$ perovskite nickelates, and finally explain the main experimental results on superconducting nickelates.

1.1 Superconductivity

Superconductivity is one of the most interesting properties of matter exhibited by several materials. This property is characterized by zero electrical resistance and the expulsion of the magnetic field flux from the material's interior. In other words, a superconducting compound is a perfect conductor and diamagnet simultaneously. It was discovered in 1911 by Dutch physicist Heike Kamerlingh Onnes, who studied the conducting properties of pure metals, finding that at $T_c = 4.2$ K, the mercury resistance drops to zero. These works were later acknowledged by the Swedish Academy of Science with the Nobel Prize in 1913, and in the coming decades, several compounds were also found to be superconductors. More than twenty years after its discovery, Walther Meissner and Robert Ochsenfeld found that superconductors were perfect diamagnets

since they expelled applied magnetic fields. This phenomenon was later called the Meissner effect.

Although this property of matter was discovered more than a century ago, the origin is still much debated and not completely unified for all compounds. In particular, the biggest challenge comes when understanding its origin in high-temperature superconductors, with a record temperature at ambient conditions of $T_c = 133$ K in $\text{HgBa}_2\text{Ca}_2\text{Cu}_3\text{O}_{1+x}$ [1]. The fact that it is possible to obtain a superconductor above the boiling point of liquid nitrogen has very important implications. First, the superconductors allow to obtain very strong magnetic fields, and they are widely used in nuclear magnetic resonance machines in hospitals for diagnosis purposes. Second, these superconducting magnets are also used for levitation purposes in transport such as high-speed trains where the friction of the vehicle is minimized improving considerably the energy consumption. Lastly and perhaps the most important reason why high-temperature superconductors are so interesting is the fact that they allow to transport electrical energy with negligible losses. Thus, obtaining a room-temperature superconductor would potentially solve many of the energy consumption problems that we face nowadays. In the coming sections, the main theories to explain superconductivity are described in detail.

1.1.1 London phenomenological theory

Soon after the discovery of superconductivity, the first phenomenological theory for the superconducting state appeared. It was developed by the two brothers Fritz and Heinz London, introducing the constitutive equation of the superconducting state

$$\frac{\partial \mathbf{J}_s}{\partial t} = \frac{n_s e^2}{m} \mathbf{E}. \quad (1.1)$$

where \mathbf{J}_s is the superconducting current density, t represents the time variable, \mathbf{E} is the electric field, n_s is a phenomenological constant usually associated with the density of superconducting carriers known as superfluid density and m the mass of these carriers (all vector quantities in this thesis are in bold). By taking the curl on equation (1.1) and recalling the Faraday law of Maxwell's equations

$$\nabla \times \mathbf{E} = -\frac{\partial \mathbf{B}}{\partial t} \quad (1.2)$$

we can obtain the second London equation

$$\frac{\partial}{\partial t} (\nabla \times \mathbf{J}_s) = -\frac{n_s e^2}{m} \frac{\partial \mathbf{B}}{\partial t} \quad (1.3)$$

We now integrate over time on both sides and we arrive to

$$\nabla \times \mathbf{J}_s = -\frac{n_s e^2}{m} \mathbf{B}. \quad (1.4)$$

Here we must note that the integration constant is set to zero to account for the absence of a magnetic field inside the superconductor (note that this is not true if we would be dealing just with a perfect conductor). We can then take the curl of the expression (1.4) and make use of

Ampere's law

$$\nabla \times \mathbf{B} = \mu_0 \mathbf{J} \quad (1.5)$$

and Gauss's law for magnetism

$$\nabla \cdot \mathbf{B} = 0 \quad (1.6)$$

to obtain an equation for the magnetic field in the superconductor

$$\nabla^2 \mathbf{B} = \frac{1}{\lambda_L^2} \mathbf{B} \quad (1.7)$$

where $\lambda_L^2 = \frac{m}{\mu_0 n_s e^2}$, is called the London penetration depth. This equation produces solutions of the form

$$\mathbf{B} \sim \frac{1}{4\pi r} \exp\left(-\frac{r}{\lambda_L}\right) \quad (1.8)$$

where r is the radial spherical coordinate. These types of solutions are able to account for the extinction of the magnetic field inside a superconductor since we have a strongly decaying function with the distance (see Figure 1.1).

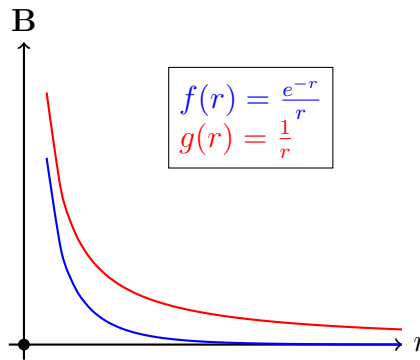


Fig. 1.1 Representation of two functions for the magnetic field \mathbf{B} as a function of the radial coordinate r . The first $f(r) = \frac{e^{-r}}{r}$ (in blue) and the second $g(r) = \frac{1}{r}$ (in red).

In spite of the success of the theory in describing certain aspects of the superconductors, we note that it is constructed *ad hoc* to match the experimental observations and it does not explain where the superconducting current density \mathbf{J}_s originates from or how does the superconducting transition occur.

1.1.2 Ginzburg-Landau Theory

The next step in understanding superconductors was made in 1950, by Lev Landau and Vitaly Ginzburg when they applied the Landau theory of phase transitions to the superconducting state, postulating that the order parameter in the superconducting state could be a complex order parameter $\Psi = |\Psi|e^{i\theta}$ such that $|\Psi|^2$ is the local density, in a similar fashion as in the Schrödinger equation. In that regard, the free energy of the system can be expressed as

$$\mathcal{F} = \mathcal{F}_n + \alpha |\Psi|^2 + \frac{\beta}{4} |\Psi|^4 + \frac{1}{2m^*} |(-i\hbar \nabla - e^* \mathbf{A}) \Psi|^2 + \frac{|\mathbf{B}|^2}{2\mu_0} \quad (1.9)$$

where α and β are parameters, m^* and e^* are the effective mass and charge of the superconducting carriers respectively that can be taken as phenomenological parameters, \mathcal{F}_n is the free energy in the normal state, and \mathbf{A} is the magnetic vector potential, such that $\nabla \times \mathbf{A} = \mathbf{B}$. We obtain the Ginzburg-Landau equations by minimizing the free energy with respect to the order parameter.

$$\alpha\Psi + \beta|\Psi|^2\Psi + \frac{1}{2m^*}(-i\hbar\nabla - e^*\mathbf{A})^2\Psi = 0 \quad (1.10)$$

This first equation depicted in (1.10) is a condition for the stability of the system. If we consider that the system does not present currents or fluctuations, we are left with the usual polynomial expansion of the Landau theory.

$$\alpha\Psi + \beta|\Psi|^2\Psi = 0 \implies |\Psi|^2 = -\frac{\alpha}{\beta} \quad (1.11)$$

The solution to this can be viewed as the behavior of order parameter $|\Psi|^2$ deep inside the bulk of the superconductor. We will then rename it $|\Psi_\infty|^2$ for clarity reasons. To get further insight into the behavior of (1.10) we can consider the case in one dimension in the absence of fields obtaining

$$\alpha\Psi + \beta|\Psi|^2\Psi - \frac{\hbar^2}{2m^*}\partial_x^2\Psi = 0 \quad (1.12)$$

considering real solutions of Ψ , we obtain

$$\Psi = \sqrt{\frac{|\alpha|}{\beta}} \tanh\left(\frac{x}{\sqrt{2}\xi}\right) = |\Psi_\infty| \tanh\left(\frac{x}{\sqrt{2}\xi}\right) \quad (1.13)$$

where $\xi = \sqrt{\frac{\hbar^2}{2m^*|\alpha|}}$ is called the Ginzburg-Landau coherence length, which shows that the perturbations from the bulk state $|\Psi_\infty|$, would decay with a characteristic length ξ . The second equation that we obtain by minimizing the free energy is

$$\mathbf{J}_s = \frac{1}{\mu_0}\nabla \times \mathbf{B} = -\frac{i\hbar e^*}{2m^*}(\Psi^*\nabla\Psi - \Psi\nabla\Psi^*) - \frac{e^{*2}}{2m^*}|\Psi|^2\mathbf{A} \quad (1.14)$$

where we have used the gauge condition $\nabla \cdot \mathbf{A} = 0$. We can effectively see that by taking the curl of the equation we arrive at a familiar equation of the London theory

$$\nabla \times \mathbf{J}_s = -\frac{e^{*2}}{m^*}|\Psi|^2\nabla \times \mathbf{A} = -\frac{e^{*2}n_s^*}{m^*}\mathbf{B}. \quad (1.15)$$

Thus it becomes evident that from the Ginzburg-Landau theory, we can effectively recover the London equations for the magnetic field. From both (1.10) and (1.15) equations, we can see that we obtain two characteristic lengths, the London penetration depth λ_L and the coherence length ξ , and we can define a new quantity $\kappa = \frac{\lambda_L}{\xi}$ which has no dimensions and it helps to distinguish two types of superconductors. Those superconductors with $\kappa < \frac{1}{\sqrt{2}}$ are called type-I superconductors, where it is easy to see that in this case the bulk of the superconductor $|\Psi_\infty|$ would not be affected by the magnetic field. In contrast, those superconductors where $\kappa > \frac{1}{\sqrt{2}}$ are called type-II superconductors, where the magnetic field can penetrate enough to perturb

the bulk $|\Psi_\infty|$ of the superconductor. In this second case, the magnetic flux can be trapped leading to pinning centers of flux depending on the applied magnetic field. We will not elaborate more on this topic and for further explanations, we refer to Ref. [2]. Hence it becomes clear that the Ginzburg-Landau theory can account for the different phenomena that occur in the superconducting phase rather accurately. However, the theory does not give a microscopic explanation for the phenomena.

1.1.3 The BCS theory of Superconductivity

Despite the success of the Ginzburg-Landau theory in describing the superconducting state and accounting for the London equations, the microscopic origin of the superconductivity remained elusive. It was finally in 1957 that a microscopic theory was developed by John Bardeen, Leon N. Cooper, and Robert Schrieffer named BCS theory for its developers, who obtained the physics Nobel Prize for it.

Cooper pairs

The modern interpretation of the superfluid density is that electronic quasiparticles are formed in the material, and they are responsible for the superconducting properties. In particular, the most widely accepted interpretation is that these quasiparticles are formed by pairs of electrons called Cooper pairs. A Cooper pair is formed by two electrons attracting each other through an effective interaction which produces a bound state (see Figure 1.2). This interaction

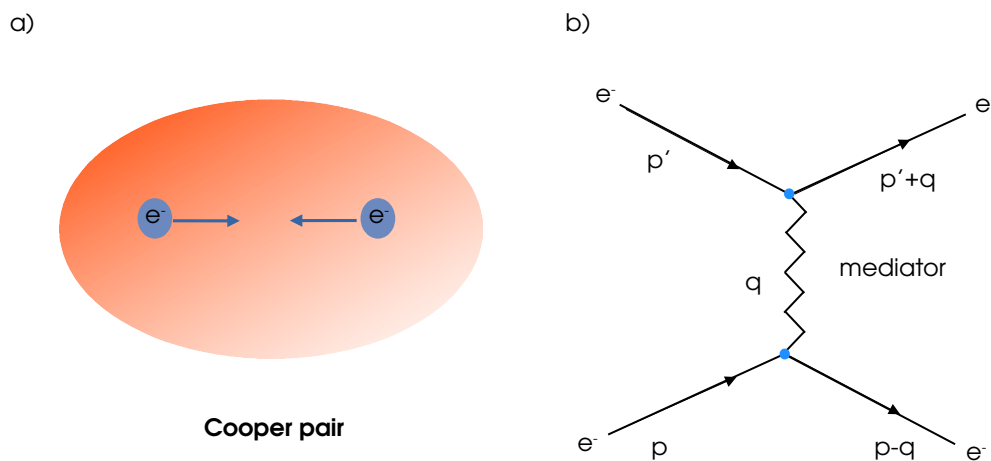


Fig. 1.2 Picture of (a) one Cooper pair formed by two electrons, and (b) Feynman diagram of the effective electron-electron interaction.

is generally mediated by other particles or quasiparticles depending on the specific theory and in particular, in the Bardeen-Cooper-Schrieffer (BCS) theory the interaction is mediated by phonons (in the original work it involves only acoustic phonons) producing an effective attractive interaction between the electrons.

The effective interacting Hamiltonian

In order to understand the origin of the attractive interaction, we consider the Hamiltonian of a free electron system

$$\mathcal{H}_{free} = \sum_{\mathbf{k}} \frac{\hbar^2 k^2}{2m_e} c_{\mathbf{k}}^\dagger c_{\mathbf{k}} = \sum_{\mathbf{k}} \varepsilon_{\mathbf{k}} c_{\mathbf{k}}^\dagger c_{\mathbf{k}} \quad (1.16)$$

where $k = |\mathbf{k}|$ is the modulus of the electron wave vector, m_e is the mass of the electron, $\varepsilon_{\mathbf{k}}$ is the electron energy and $c_{\mathbf{k}}^\dagger$ ($c_{\mathbf{k}}$) are the creation (annihilation) spinorial electronic operators. Then we introduce different terms of interaction. The first interaction that we can have is the Coulomb interaction. The Hamiltonian \mathcal{H}_{el-el} of the Coulomb interaction $V_C(\mathbf{r})$ can be expressed as

$$\mathcal{H}_{el-el} = \sum_{\mathbf{k}, \mathbf{k}'} \sum_{\mathbf{q}} V_C(\mathbf{q}) c_{\mathbf{k}+\mathbf{q}}^\dagger c_{\mathbf{k}'-\mathbf{q}}^\dagger c_{\mathbf{k}} c_{\mathbf{k}'} \quad (1.17)$$

where $V_C(\mathbf{q})$ is the Fourier transform of the Coulomb interaction characterized by the carried momentum $\hbar\mathbf{q}$ defined as:

$$V_C(\mathbf{q}) = \int V_C(\mathbf{r}) e^{-i\mathbf{q}\mathbf{r}} d\mathbf{r} \quad (1.18)$$

If we consider a point-like source, it can be shown that $V_C(\mathbf{q})$ takes the form of

$$V_C(\mathbf{q}) = \frac{1}{4\pi\epsilon_0} \frac{e^2}{q^2} \quad (1.19)$$

with $q = |\mathbf{q}|$. This would represent the bare Coulomb interaction. However, there is a finite screening of the repulsive interaction in a metallic system. Thus, the effective Coulomb interaction would be

$$V_C(\mathbf{q}) = \frac{1}{4\pi\epsilon_0} \frac{e^2}{q^2 + \kappa_s^2} \quad (1.20)$$

where κ_s^{-1} is the screening length, and it would take the following form in real space:

$$V_C(\mathbf{r}) = \frac{1}{4\pi\epsilon_0} \frac{e^2}{r} \exp(-\kappa_s r) \quad (1.21)$$

which is a potential with a shorter repulsive range. Nonetheless, we still need an attractive interaction between the electrons. For that reason, the next ingredient that we consider is the ions. More in particular, we are interested in the oscillations of the ions around the equilibrium position in the harmonic regime which are represented by the phonons. The phonon Hamiltonian can be modeled with two terms in the harmonic approximation. The first one accounts for the free phonon field with $b_{\mathbf{q},\nu}^\dagger$ ($b_{\mathbf{q},\nu}$) creation (annihilation) operators for a given vibration mode of branch ν , wave vector \mathbf{q} and dispersion relation $\Omega_{\mathbf{q},\nu}$

$$\mathcal{H}_{ph} = \sum_{\mathbf{q},\nu} \hbar\Omega_{\mathbf{q},\nu} \left(b_{\mathbf{q},\nu}^\dagger b_{\mathbf{q},\nu} + \frac{1}{2} \right) \quad (1.22)$$

The second term models the interaction of phonons with the electrons

$$\mathcal{H}_{el-ph} = \sum_{\mathbf{k}} \sum_{\mathbf{q},\nu} g_{\mathbf{q},\nu} c_{\mathbf{k}+\mathbf{q}}^\dagger c_{\mathbf{k}} \left(b_{\mathbf{q},\nu}^\dagger + b_{\mathbf{q},\nu} \right) \quad (1.23)$$

with an interaction strength $g_{\mathbf{q},\nu}$. Now it can be shown that by applying the appropriate unitary transformation we can eliminate the second Hamiltonian with phonons coupled to electrons. The result is that the phonon Hamiltonian \mathcal{H}_{ph} is completely separable from the electronic Hamiltonian, allowing to deal only with the electronic part of a new effective electronic Hamiltonian \mathcal{H}_{eff} defined as:

$$\mathcal{H}_{eff} = \mathcal{H}_{free} + \mathcal{H}_{el-el} + \mathcal{H}_1 + \mathcal{H}_2 \quad (1.24)$$

where we have a renormalization of the onsite energy $\varepsilon_{\mathbf{k}}$

$$\mathcal{H}_1 = \sum_{\mathbf{k}} \sum_{\mathbf{q},\nu} |g_{\mathbf{q},\nu}|^2 \frac{\hbar\Omega_{\mathbf{q},\nu}}{(\varepsilon_{\mathbf{k}} - \varepsilon_{\mathbf{k}-\mathbf{q}})^2 - (\hbar\Omega_{\mathbf{q},\nu})^2} c_{\mathbf{k}}^\dagger c_{\mathbf{k}} \quad (1.25)$$

and an effective electron-electron interaction

$$\mathcal{H}_2 = \sum_{\mathbf{k},\mathbf{k}'} \sum_{\mathbf{q},\nu} |g_{\mathbf{q},\nu}|^2 \frac{\hbar\Omega_{\mathbf{q},\nu}}{(\varepsilon_{\mathbf{k}'} - \varepsilon_{\mathbf{k}'-\mathbf{q}})^2 - (\hbar\Omega_{\mathbf{q},\nu})^2} c_{\mathbf{k}+\mathbf{q}}^\dagger c_{\mathbf{k}'-\mathbf{q}}^\dagger c_{\mathbf{k}'} c_{\mathbf{k}} \quad (1.26)$$

From the second term, we can see that if $|\varepsilon_{\mathbf{k}'} - \varepsilon_{\mathbf{k}'-\mathbf{q}}| < \hbar\Omega_{\mathbf{q},\nu}$ the effective electron-electron interaction would become attractive instead of repulsive. This is a good starting point, but it is not enough. We must show that this attractive interaction dominates over the repulsive Coulomb interaction. The great success of the theory was to show that effectively, the ground state of a free electron gas is unstable toward the superconducting state no matter how weak the attractive interaction is. This implies that pairs of electrons can form a bound state called Cooper pair and the binding energy would increase when the electron-phonon interaction becomes stronger. We will not elaborate more on this topic; we refer to Refs. [2–4] for further clarifications.

If we now gather all the terms involving the electronic operators after this transformation, we can arrive at an effective electronic Hamiltonian of the form

$$\mathcal{H}_{eff} = \mathcal{H}_{free} + \mathcal{H}_{el-el} + \mathcal{H}_1 + \mathcal{H}_2 = \sum_{\mathbf{k}} \xi_{\mathbf{k}} c_{\mathbf{k}}^\dagger c_{\mathbf{k}} + \sum_{\mathbf{k},\mathbf{k}'} \sum_{\mathbf{q}} \tilde{V}_{\mathbf{k},\mathbf{k}'} c_{\mathbf{k}+\mathbf{q}}^\dagger c_{\mathbf{k}'-\mathbf{q}}^\dagger c_{\mathbf{k}'} c_{\mathbf{k}} \quad (1.27)$$

here $\xi_{\mathbf{k}}$ is the renormalized onsite energy including terms from \mathcal{H}_{free} and \mathcal{H}_1 , and $\tilde{V}_{\mathbf{k},\mathbf{k}'}$ is the effective electron electron interaction that includes terms from \mathcal{H}_{el-el} and \mathcal{H}_2 . However, from this effective Hamiltonian, we still face challenges in diagonalizing it and resolving the spectra.

The mean-field approximation

The usual procedure to solve the Hamiltonian in equation (1.27) is what is called the mean-field approximation in which we expand the product of two operators O and O' as follows

$$OO' \simeq O\langle O' \rangle + O'\langle O \rangle - \langle O \rangle \langle O' \rangle \quad (1.28)$$

In addition, we must point out that in the BCS theory, the dominant interaction would be between electrons of opposite momentum ($\hbar\mathbf{k} = -\hbar\mathbf{k}'$) since all electrons in the Fermi surface

are able to contribute to this process. Additionally, the center of mass of the interacting pair has zero momentum meaning that there is no extra kinetic energy required. Thus the effective Hamiltonian becomes

$$\mathcal{H}_{eff} = \sum_{\mathbf{k}} \xi_{\mathbf{k}} c_{\mathbf{k}}^{\dagger} c_{\mathbf{k}} + \sum_{\mathbf{k}, \mathbf{k}'} \tilde{V}_{\mathbf{k}, \mathbf{k}'} c_{\mathbf{k}}^{\dagger} c_{-\mathbf{k}}^{\dagger} c_{-\mathbf{k}'} c_{\mathbf{k}'} \quad (1.29)$$

By applying the mean-field approximation, we can rewrite the Hamiltonian as follows

$$\mathcal{H}_{BCS} = \sum_{\mathbf{k}} \xi_{\mathbf{k}} c_{\mathbf{k}}^{\dagger} c_{\mathbf{k}} - \sum_{\mathbf{k}} \Delta_{\mathbf{k}}^* c_{-\mathbf{k}} c_{\mathbf{k}} - \sum_{\mathbf{k}} \Delta_{\mathbf{k}} c_{\mathbf{k}}^{\dagger} c_{-\mathbf{k}}^{\dagger} + U_0 \quad (1.30)$$

where U_0 is a constant term and $\Delta_{\mathbf{k}}$ is commonly known as the gap function defined as

$$\Delta_{\mathbf{k}} = - \sum_{\mathbf{k}'} \tilde{V}_{\mathbf{k}, \mathbf{k}'} \langle c_{-\mathbf{k}'} c_{\mathbf{k}'} \rangle \quad (1.31)$$

and it follows that $\Delta_{\mathbf{k}}^*$ is

$$\Delta_{\mathbf{k}}^* = - \sum_{\mathbf{k}'} \tilde{V}_{\mathbf{k}, \mathbf{k}'} \langle c_{\mathbf{k}'}^{\dagger} c_{-\mathbf{k}'}^{\dagger} \rangle. \quad (1.32)$$

From here the usual and most simple procedure is to use a unitary transformation to obtain a diagonalized Hamiltonian by changing the basis of our creation and annihilation operators as follows

$$\begin{pmatrix} \gamma_{\mathbf{k}} \\ \gamma_{\mathbf{k}}^{\dagger} \end{pmatrix} = \begin{pmatrix} u_{\mathbf{k}}^* & -v_{\mathbf{k}} \\ v_{\mathbf{k}}^* & u_{\mathbf{k}} \end{pmatrix} \begin{pmatrix} c_{\mathbf{k}} \\ c_{\mathbf{k}}^{\dagger} \end{pmatrix} \quad (1.33)$$

and unitarity enforces that

$$|u_{\mathbf{k}}|^2 + |v_{\mathbf{k}}|^2 = 1. \quad (1.34)$$

This is commonly known as the Bogoliubov transformation and $\gamma_{\mathbf{k}}$ are Fermionic operators. Rewriting the Hamiltonian in terms of these operators is a lengthy process, and we refer the reader to Refs. [4–6] for a complete development of the equations. Nonetheless, it leads to the following condition if we want the Hamiltonian to be diagonal in the basis of $\gamma_{\mathbf{k}}$ operators

$$\frac{v_{\mathbf{k}}}{u_{\mathbf{k}}} = \frac{\sqrt{\xi_{\mathbf{k}}^2 + |\Delta_{\mathbf{k}}|^2}}{\Delta_{\mathbf{k}}^*} \quad (1.35)$$

By making use of the unitarity condition, we obtain finally

$$|u_{\mathbf{k}}|^2 = \frac{1}{2} \left(1 + \frac{\xi_{\mathbf{k}}}{\sqrt{\xi_{\mathbf{k}}^2 + |\Delta_{\mathbf{k}}|^2}} \right) \quad (1.36)$$

and

$$|v_{\mathbf{k}}|^2 = \frac{1}{2} \left(1 - \frac{\xi_{\mathbf{k}}}{\sqrt{\xi_{\mathbf{k}}^2 + |\Delta_{\mathbf{k}}|^2}} \right). \quad (1.37)$$

This enables us to obtain the diagonalized Hamiltonian

$$\mathcal{H} = \sum_{\mathbf{k}} E_{\mathbf{k}} \gamma_{\mathbf{k}}^{\dagger} \gamma_{\mathbf{k}} + E_0 \quad (1.38)$$

where $E_{\mathbf{k}}$ is defined as

$$E_{\mathbf{k}} = \sqrt{\xi_{\mathbf{k}}^2 + |\Delta_{\mathbf{k}}|^2} \quad (1.39)$$

and E_0 is a constant energy term defined as

$$E_0 = \sum_{\mathbf{k}} \left(\xi_{\mathbf{k}} - E_{\mathbf{k}} + \Delta_{\mathbf{k}} \langle c_{\mathbf{k}}^{\dagger} c_{-\mathbf{k}}^{\dagger} \rangle \right). \quad (1.40)$$

Here we have made the assumption of time-reversal symmetry to be conserved which implies that $\xi_{\mathbf{k}} = \xi_{-\mathbf{k}}$ and $|\Delta_{\mathbf{k}}| = |\Delta_{-\mathbf{k}}|$. From the definition of $E_{\mathbf{k}}$ it is easy to understand why $\Delta_{\mathbf{k}}$ is called the gap function, since even at the Fermi level where $\xi_{\mathbf{k}} = 0$, the superconducting excitations would require a minimum energy of $|\Delta_{\mathbf{k}}|$, or in other words, the energy spectrum is gapped. Thus, in order to obtain these quasi-particles, we need to give an energy of at least $2|\Delta_{\mathbf{k}}|$ to the system. As we can note the fermionic quasi-particles $\gamma_{\mathbf{k}}^{\dagger}$ are a linear combination of electrons $c_{\mathbf{k}}^{\dagger}$ and holes $c_{\mathbf{k}}$ and are commonly known as Bogoliubons.

Although we have successfully obtained a basis that diagonalizes the Hamiltonian, the energy spectra is not completely resolved since we still need to determine the gap $\Delta_{\mathbf{k}}$. In that regard, we rewrite in the new basis and obtain

$$\Delta_{\mathbf{k}} = - \sum_{\mathbf{k}'} V_{\mathbf{k},\mathbf{k}'} u_{\mathbf{k}'}^* v_{\mathbf{k}'} \left(\langle \gamma_{-\mathbf{k}'} \gamma_{-\mathbf{k}'}^{\dagger} \rangle - \langle \gamma_{\mathbf{k}'}^{\dagger} \gamma_{\mathbf{k}'} \rangle \right) = - \sum_{\mathbf{k}'} V_{\mathbf{k},\mathbf{k}'} u_{\mathbf{k}'}^* v_{\mathbf{k}'} (1 - 2n_{\mathbf{k}'}) \quad (1.41)$$

where $n_{\mathbf{k}'}$ is the number operator and we have used the fact that $\langle \gamma_{-\mathbf{k}'} \gamma_{\mathbf{k}'} \rangle = \langle \gamma_{\mathbf{k}'}^{\dagger} \gamma_{-\mathbf{k}'}^{\dagger} \rangle = 0$. Since $\gamma_{\mathbf{k}'}^{\dagger}$ are fermionic particles, the number operator will be given by the Fermi-Dirac distribution

$$n_{\mathbf{k}'} = \frac{1}{e^{\beta E_{\mathbf{k}'}} + 1} \quad (1.42)$$

With help of the definition of $u_{\mathbf{k}'}$ and $v_{\mathbf{k}'}$, we can obtain that

$$u_{\mathbf{k}'}^* v_{\mathbf{k}'} = \frac{\Delta_{\mathbf{k}'}}{2\sqrt{\xi_{\mathbf{k}'}^2 + |\Delta_{\mathbf{k}'}|^2}} = \frac{\Delta_{\mathbf{k}'}}{2E_{\mathbf{k}'}} \quad (1.43)$$

By substituting this result in the gap equation, we obtain:

$$\Delta_{\mathbf{k}} = - \sum_{\mathbf{k}'} \frac{V_{\mathbf{k},\mathbf{k}'} \Delta_{\mathbf{k}'}}{2E_{\mathbf{k}'}} \tanh\left(\frac{\beta E_{\mathbf{k}'}}{2}\right) \quad (1.44)$$

The weak coupling isotropic approximation

Now at this point, the classical BCS derivation assumes an isotropic potential V_0 within a small shell of energy $\hbar\omega_c$ with characteristic phonon frequency ω_c (the original work takes the

Debye frequency for the cut-off energy) around the Fermi energy so that

$$V_{\mathbf{k},\mathbf{k}'} = \begin{cases} -V_0 & \text{if } |\xi_{\mathbf{k}'}| \leq \hbar\omega_c \\ 0 & \text{if } |\xi_{\mathbf{k}'}| > \hbar\omega_c \end{cases} \quad (1.45)$$

and consequently $\Delta_{\mathbf{k}} = \Delta$ is also momentum independent. Substituting these terms in equation (1.44) we are left with the well-known result

$$1 = V_0 \sum_{k' \leq k_F} \frac{1}{2E_{\mathbf{k}'}} \tanh\left(\frac{\beta E_{\mathbf{k}'}}{2}\right). \quad (1.46)$$

This is called the *s*-wave solution of the gap equation since the superconducting gap is proportional to the Y_{00} spherical harmonic. From this point, we can then pass to the continuum by changing the sum with an integral

$$1 = V_0 \int_{-\hbar\omega_c}^{\hbar\omega_c} N(\varepsilon) \frac{1}{2E} \tanh\left(\frac{\beta E}{2}\right) d\varepsilon. \quad (1.47)$$

where ε is the energy of the electrons, and $N(\varepsilon)$ is the density of states. Now since $\varepsilon_F \gg \hbar\omega_c$ with ε_F being the Fermi energy, we can take the value of the density of state at the Fermi level $N(\varepsilon_F)$ out of the integral obtaining

$$\frac{1}{V_0 N(\varepsilon_F)} = \int_0^{\hbar\omega_c} \frac{d\varepsilon}{\sqrt{\varepsilon^2 + \Delta^2}} \tanh\left(\frac{\sqrt{\varepsilon^2 + \Delta^2}}{2k_B T}\right). \quad (1.48)$$

At this point, we can consider two interesting cases. The first one is when $T \rightarrow 0$ for which the hyperbolic tangent in the previous expression would tend to the unity and we would have

$$\frac{1}{V_0 N(\varepsilon_F)} = \int_0^{\hbar\omega_c} \frac{d\varepsilon}{\sqrt{\varepsilon^2 + \Delta_0^2}} = \sinh^{-1}\left(\frac{\hbar\omega_c}{\Delta_0}\right) \quad (1.49)$$

We can note that typically the superconducting gap Δ_0 at 0 K is much larger than the cutoff energy and as a result, we can take approximately

$$\frac{1}{V_0 N(\varepsilon_F)} = \log\left(\frac{2\hbar\omega_c}{\Delta_0}\right) \quad (1.50)$$

from which we obtain

$$\Delta_0 = 2\hbar\omega_c \exp\left(\frac{-1}{N(\varepsilon_F)V_0}\right). \quad (1.51)$$

This result, reveals that the system will be a superconductor regardless of how small the interaction strength is at 0 K, further showing that the free electron gas is unstable with respect to an attractive interaction.

The other interesting limit to consider is the temperature T_c for which the superconducting gap vanishes $\Delta(T_c) = 0$, or in other words the transition temperature. In this case, the integral

becomes

$$\frac{1}{V_0 N(\varepsilon_F)} = \int_0^{\hbar\omega_c} \frac{d\varepsilon}{\varepsilon} \tanh\left(\frac{\varepsilon}{2k_B T_c}\right) = \int_0^{\frac{\hbar\omega_c}{2k_B T_c}} \frac{\tanh(x)}{x} dx. \quad (1.52)$$

This integral in general has no primitive, but we can use the fact that $\frac{\hbar\omega_c}{2k_B T_c} \gg 1$ and integrate by parts obtaining

$$\int_0^{\frac{\hbar\omega_c}{2k_B T_c}} \frac{\tanh(x)}{x} dx \approx (\tanh(x) \log(x))_0^{\frac{\hbar\omega_c}{2k_B T_c}} - \int_0^\infty \frac{\log(x)}{\cosh^2(x)} \approx \log\left(\frac{2e^{\gamma_E} \hbar\omega_c}{\pi k_B T_c}\right) \quad (1.53)$$

where $\gamma_E \approx 0.577$ is the Euler-Mascheroni constant. From this result, we can obtain that the critical temperature T_c is given by

$$T_c = \frac{2e^{\gamma_E} \hbar\omega_c}{\pi k_B} \exp\left(\frac{-1}{N(\varepsilon_F) V_0}\right) \approx 1.14 \frac{\hbar\omega_c}{k_B} \exp\left(\frac{-1}{\lambda}\right) \quad (1.54)$$

where here we denote by $\lambda = V_0 N(\varepsilon_F)$ the electron-phonon coupling, although it is also known as the mass renormalization parameter. We can combine the results for the gap Δ_0 and the critical temperature T_c and obtain the famous relation

$$\frac{\Delta_0}{T_c} \approx 1.76. \quad (1.55)$$

This is what is called the weak coupling limit of the BCS theory.

Beyond the isotropic pairing

One could ask however what is the validity of these results regarding the pairing symmetry, since we have assumed an isotropic pairing. However, the general electron-phonon interaction would depend on both momenta of the electron $\hbar\mathbf{k}$ and the mediating phonon $\hbar\mathbf{q}$. Thus we can decompose the interacting potential $V_{\mathbf{k},\mathbf{k}'}$ as follows:

$$V_{\mathbf{k},\mathbf{k}'} = \sum_{l=0}^{\infty} (2l+1) V_{\mathbf{k},\mathbf{k}'}^l P_l^m(\mathbf{k} \cdot \mathbf{k}') \quad (1.56)$$

where $V_{\mathbf{k},\mathbf{k}'}^l$ is the interaction strength for the pairing channel with angular momentum l and $P_l^m(\mathbf{k} \cdot \mathbf{k}')$ are Legendre polynomials defined in terms of the spherical harmonics $Y_l^m(\mathbf{k})$ as follows:

$$P_l^m(\mathbf{k} \cdot \mathbf{k}') = \frac{4\pi}{2l+1} \sum_{m=-l}^l Y_l^m(\mathbf{k}) Y_l^m(\mathbf{k}')^*. \quad (1.57)$$

The physical meaning of such complex pairing interaction is the fact that the Cooper pairs can carry some angular momentum l even if they are in a spin singlet state $S=0$. Consequently, the gap function can be expanded as well in terms of different contributions with angular momentum l . By substituting the expansion of $V_{\mathbf{k},\mathbf{k}'}$ into our previous definition of $\Delta_{\mathbf{k}}$ we can obtain

$$\Delta_{\mathbf{k}} = - \sum_{l=0}^{\infty} \sum_{\mathbf{k}'} (2l+1) V_{\mathbf{k},\mathbf{k}'}^l P_l^m(\mathbf{k} \cdot \mathbf{k}') \langle c_{-\mathbf{k}'} c_{\mathbf{k}'} \rangle \quad (1.58)$$

which can be expressed as

$$\Delta_{\mathbf{k}} = \sum_{l=0}^{\infty} \Delta_{\mathbf{k}}^l \quad (1.59)$$

where each $\Delta_{\mathbf{k}}^l$ is the gap function for a given angular momentum l . In this way, we already allow to have any possible combinations of pairing symmetries without the loss of generality. The existence of several pairing symmetries in our gap function implies that there will be several critical temperatures T_c^l , which, except in very rare cases will not be equivalent. Thus in order to get the transition temperature from metallic to superconducting, we can consider only one of the pairing symmetries of the channel l . In that regard, we can note that for a given gap with angular momentum l , we can express it as follows

$$\Delta_{\mathbf{k}}^l = \Delta(T) \sum_{m=-l}^l \eta_m Y_l^m(\mathbf{k}). \quad (1.60)$$

Where $\Delta(T)$ is the gap dependence of the temperature and η_m are constants. In that regard, we can recover the previous gap equation but now for angular momentum l

$$\Delta_{\mathbf{k}}^l = - \sum_{\mathbf{k}'} (2l+1) V_{\mathbf{k},\mathbf{k}'}^l P_l^m(\mathbf{k} \cdot \mathbf{k}') \Delta_{\mathbf{k}'}^l \frac{\tanh\left(\frac{\beta E_{\mathbf{k}'}}{2}\right)}{2E_{\mathbf{k}'}} \quad (1.61)$$

which we can expand in terms of the spherical harmonics

$$\Delta_{\mathbf{k}}^l = - \sum_{\mathbf{k}'} \sum_{m=-l}^l 4\pi V_{\mathbf{k},\mathbf{k}'}^l Y_l^m(\mathbf{k}) Y_l^m(\mathbf{k}')^* \Delta(T) \sum_{m'=-l}^l \eta_{m'} Y_l^{m'}(\mathbf{k}') \frac{\tanh\left(\frac{\beta E_{\mathbf{k}'}}{2}\right)}{2E_{\mathbf{k}'}} \quad (1.62)$$

Here, we must note that when summing over all the \mathbf{k}' only terms with $m = m'$ will give a non-zero value since the spherical harmonics are orthogonal to each other upon integrating the \mathbf{k}' variable. Thus, the important terms are

$$\Delta_{\mathbf{k}}^l = -4\pi \Delta(T) \sum_{m=-l}^l \eta_m Y_l^m(\mathbf{k}) \sum_{\mathbf{k}'} V_{\mathbf{k},\mathbf{k}'}^l |Y_l^m(\mathbf{k}')|^2 \frac{\tanh\left(\frac{\beta E_{\mathbf{k}'}}{2}\right)}{2E_{\mathbf{k}'}} \quad (1.63)$$

At this point, we can proceed as before where we will take $V_{\mathbf{k},\mathbf{k}'}^l$ to be a constant for a characteristic energy range $\hbar\omega_c^l$

$$V_{\mathbf{k},\mathbf{k}'}^l = \begin{cases} -V_0^l & \text{if } |\xi_{\mathbf{k}'}| \leq \hbar\omega_c^l \\ 0 & \text{if } |\xi_{\mathbf{k}'}| > \hbar\omega_c^l \end{cases} \quad (1.64)$$

and by substituting we obtain

$$\Delta_{\mathbf{k}}^l = 4\pi \Delta(T) V_0^l \sum_{m=-l}^l \eta_m Y_l^m(\mathbf{k}) \sum_{\mathbf{k}'} |Y_l^m(\mathbf{k}')|^2 \frac{\tanh\left(\frac{\beta E_{\mathbf{k}'}}{2}\right)}{2E_{\mathbf{k}'}} \quad (1.65)$$

Now at $T = T_c$, we compare the expressions for $\Delta_{\mathbf{k}}^l$ in (1.60) and (1.65) and obtain the following condition

$$1 = 4\pi V_0^l \sum_{\mathbf{k}'} |Y_l^m(\mathbf{k}')|^2 \frac{\tanh\left(\frac{\beta \varepsilon_{\mathbf{k}'}}{2}\right)}{2\varepsilon_{\mathbf{k}'}} \quad (1.66)$$

for which we can recover the BCS-type solution for the critical temperature with a characteristic energy scale $\hbar\omega_c^l$

$$k_B T_c \approx 1.14 \hbar\omega_c^l \exp\left(\frac{-1}{V_0^l N(\varepsilon_F)}\right) \quad (1.67)$$

This result indicates that as a first approximation, we can disregard the symmetry of the superconducting gap as long as we can account well for the energy scale $\hbar\omega_c^l$ and the interacting potential V_0^l . This however does not hold true in the case of calculating the gap at $T = 0$, and as a consequence, the gap relation is not the same as in the simple s -wave case. We will not elaborate more on this topic; for a more detailed discussion, we refer to Refs. [7–9].

The effective electron-electron interaction

As we mentioned before, apart from the attractive electron-phonon interaction, the Coulomb repulsion is still present in spite of being screened in a metal. Thus the effective electron-electron interaction would present both a repulsive and attractive part. We can consider then that for a given band characterized by a bandwidth $W > \xi_{\mathbf{k}}$ centered at $\xi_{\mathbf{k}} = 0$ and nearly constant density of states $N(\varepsilon_F)$, we can have the effective electron-electron interaction $\tilde{V}_{\mathbf{k},\mathbf{k}'}$ as repulsive and attractive part $V_{\mathbf{k},\mathbf{k}'}^{el-el}$ and $V_{\mathbf{k},\mathbf{k}'}^{el-ph}$ and define the interaction potential

$$N(\varepsilon_F) \tilde{V}_{\mathbf{k},\mathbf{k}'} = N(\varepsilon_F) V_{\mathbf{k},\mathbf{k}'}^{e-e} + N(\varepsilon_F) V_{\mathbf{k},\mathbf{k}'}^{el-ph} = \begin{cases} N(\varepsilon_F) V^{el-el} & = \begin{cases} \mu^* > 0 & \text{if } |\xi_{\mathbf{k}}| \leq W \\ 0 & \text{if } |\xi_{\mathbf{k}}| > W \end{cases} \\ N(\varepsilon_F) V^{el-ph} & = \begin{cases} -\lambda < 0 & \text{if } |\xi_{\mathbf{k}}| \leq \hbar\omega_c \\ 0 & \text{if } |\xi_{\mathbf{k}}| > \hbar\omega_c \end{cases} \end{cases} \quad (1.68)$$

with μ^* being the effective Coulomb repulsion coupling constant

$$\mu^* = \frac{\mu_c}{1 + \mu_c \log\left(\frac{W}{\hbar\omega_c}\right)}. \quad (1.69)$$

where μ_c is the bare Coulomb repulsion coupling constant. If we use this potential to solve the gap equation for the critical temperature, we can obtain

$$k_B T_c = 1.14 \hbar\omega_c \exp\left(-\frac{1}{\lambda - \mu^*}\right) \quad (1.70)$$

Thus, we can see that a transition to the superconducting phase exists as long as $\lambda > \mu^*$. The importance of this effect is to account for the renormalized Coulomb interaction μ^* that produces a retardation effect of the electron-phonon interaction which is much expected since

the polarization of the lattice due to interaction with an electron will persist for bigger time scales than the characteristic time scales of the electron ($\hbar/\varepsilon_F \ll \omega_c^{-1}$).

The critical temperature equation at strong coupling

The equation for the critical temperature can be improved by including the full retardation effects in the equations of the superconducting instability by means of the Eliashberg-formulation in the strong coupling limit

$$k_B T_c = \frac{\hbar\omega_c}{1.2} \exp\left(-\frac{1.04(1+\lambda)}{\lambda - \mu^*(1+0.62\lambda)}\right). \quad (1.71)$$

This more advanced formula is called the Mc. Millan-Allens equation and takes also into account a renormalization of the quasi-particle spectra given by the $(1+\lambda)$ term in the numerator. Apart from these simple effects, there are several other details that can affect the critical transition temperature, like for example (i) the existence of magnetic and non-magnetic impurities, (ii) considering a density of states $N(\varepsilon_F)$ with a finite bandwidth W , and (iii) anharmonicities of the phonon spectra among others.

1.1.4 Alternatives to the BCS theory

Nonetheless, there are other theories beyond the phonon BCS approach that deal with other types of interactions, such as magnetic excitations like magnons, paramagnons, or spin density waves to name some. These types of theories would follow a similar procedure as the phonon-mediated scheme but with a different type of bosonic quasiparticle which would lead to different types of symmetries for the superconducting mechanism. In particular, in the Cu based superconductors, a quite popular theory where antiferromagnetic excitations with in-plane wave vectors $\mathbf{Q}_{\text{AFM}} = (\pm\frac{\pi}{a}, \pm\frac{\pi}{a})$ producing a nesting on the Fermi surface (see Figure 1.3.a). This interaction is a quantum effect where the exchange and superexchange interaction between the electrons would be responsible for the pairing. Thus, the gap equation would become

$$\Delta_{\mathbf{k}} = - \sum_{\mathbf{k}'} \frac{V_{\mathbf{k},\mathbf{k}'}^{\text{AFM}} \Delta_{\mathbf{k}'}}{2E_{\mathbf{k}'}} \tanh\left(\frac{\beta E_{\mathbf{k}'}}{2}\right) \quad (1.72)$$

where $V_{\mathbf{k},\mathbf{k}'}^{\text{AFM}}$ is the interacting potential from antiferromagnetic exchange. Unlike in the BCS theory, the interacting potential could be strictly positive $V_{\mathbf{k},\mathbf{k}'}^{\text{AFM}} > 0$ and still produce pairing. The key idea is in the nesting vectors \mathbf{Q}_{AFM} and the sign of the gap function $\Delta_{\mathbf{k}}$. In order to illustrate this we can consider a gap function that presents the following wave vector \mathbf{k} dependence:

$$\Delta_{\mathbf{k}} = \Delta(T)(\cos k_x a - \cos k_y a) \quad (1.73)$$

where k_x and k_y are the x and y components of the wave vector \mathbf{k} . This particular pairing symmetry is known as the d -wave pairing and more concisely the $d_{x^2-y^2}$ pairing symmetry. As one can notice in Figure 1.3.b, the gap function would take positive and negative values in the Fermi surface. Thus, if the nesting vector \mathbf{Q}_{AFM} connects two regions with different signs in the

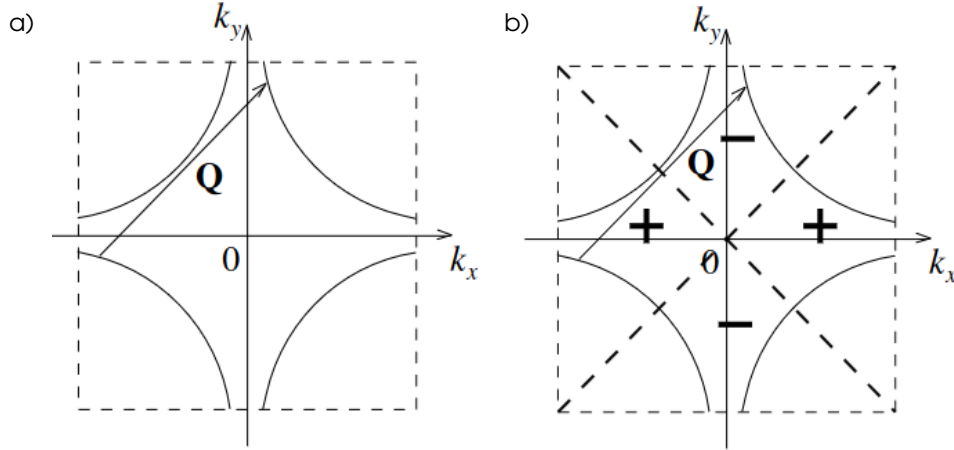


Fig. 1.3 Typical Fermi surface of the Cu-based superconductors (a) the nesting vector $\mathbf{Q}_{\text{AFM}} = (\pm\frac{\pi}{a}, \pm\frac{\pi}{a})$ connecting two regions of the Fermi surface, and (b) the positive and negative regions of the superconducting gap $\Delta_{\mathbf{k}}$ with a sign + and - respectively and the dashed lines represent the nodal lines of the gap function.

Fermi surface, then we would have an attractive interaction. This would imply that although the interacting potential $V_{\mathbf{k},\mathbf{k}'}^{\text{AFM}}$ is positive, if $\mathbf{k}' = \mathbf{k} + \mathbf{Q}_{\text{AFM}}$ the interaction produces attraction between the electrons. One particular feature of this interaction is that it produces nodal lines in the gap when $|k_x| = |k_y|$ since the gap function would be exactly zero $\Delta_{\mathbf{k}} = 0$ at these points. We would not elaborate more on this topic since it would only add extra complexity to some aspects of the interaction and would not add much insight into the overall superconducting mechanism. In that regard, we now proceed to give a general introduction to the compounds that we are particularly interested in this thesis.

1.2 Oxide compounds

The oxide family of compounds is one of the biggest and most interesting family of materials found in nature. In particular, the abundance of oxides on Earth's crust is so big that the first ten most abundant compounds on it are all oxides, making up to 99.72% of the total crust material. This is mainly caused by the high reactivity of O with other elements and the high abundance of O in the atmosphere since it is its second most abundant component. Interestingly, the oxide family of compounds presents almost all phenomena in solid-state physics, making it a very versatile family to study. In addition, one of the greatest interests in oxides nowadays is the fact that they are at the core of modern electronic devices due to their multi-functional properties. In this thesis, we are more interested in the perovskite oxide family and related compounds, which by themselves host almost all the properties exhibited by the oxide compounds including their multi-functionality.

1.2.1 Perovskite oxides

The perovskites are ternary compounds formed generally by two metal species A and B cations, and one anion X which is often oxygen O, although other anions such as fluorine F are also common. These compounds are named after the mineralogist Lev Perovski who found and described the crystal structure of CaTiO_3 . In the ideal case, the perovskites adopt a cubic $Pm\bar{3}m$ structure, where the A cations sit on the corners of the cube, the X anions are placed at the center of the faces of the cube producing an octahedron, and the B cation sits at the center of the octahedron, with a general composition formula ABX_3 (see Figure.1.4). The most common

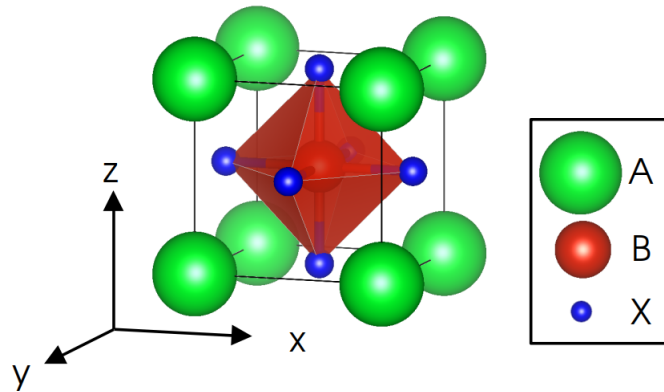


Fig. 1.4 Cubic perovskite crystal structure ABX_3 .

and widely studied type of perovskite materials are the perovskite oxides that in their simplest structure present a composition formula ABO_3 . These compounds belong to a wider class of materials called Ruddlesden-Popper phases characterized by the following chemical formula $\text{A}_{n+1}\text{B}_n\text{O}_{3n+1}$ and an integer number n . The structure of the Ruddlesden-Popper compounds involves groups of n ABO_3 layers stacked along the z axis separated by a AO slab, where the ABO_3 perovskites are the limiting phase $n = \infty$ of these compounds (see Figure 1.5). The

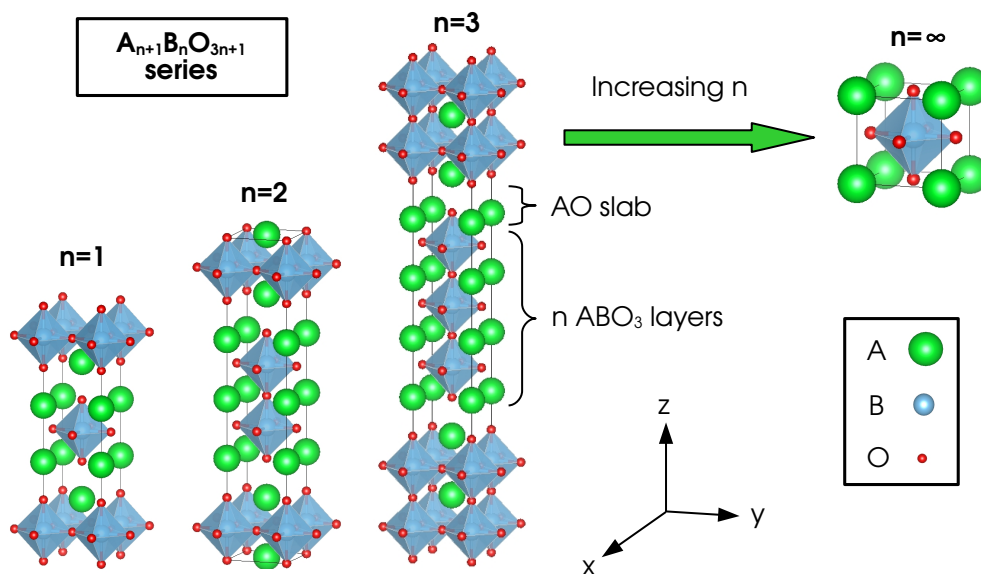


Fig. 1.5 Structure of the Ruddlesden-Popper compounds $\text{A}_{n+1}\text{B}_n\text{O}_{3n+1}$.

perovskite oxide materials are very versatile in terms of composition, allowing them to host

almost any cation in both the B and A sites of the structure. Depending on the orbital filling and the cation size mismatch, the perovskites can show several features and properties such as octahedral rotations, ferroelectricity, magnetism, charge and orbital orderings, or superconductivity to name a few. Furthermore, these compounds are characterized by strong couplings between their structural, electronic, and magnetic degrees of freedom. Hence, these materials are multifunctional since acting on one parameter may tune another one. One of the most famous examples of such couplings are the multiferroic materials that present a magnetoelectric coupling in which, an electric field \mathbf{E} can tune the magnetization \mathbf{M} , and vice versa with a magnetic field \mathbf{H} and the electric polarization \mathbf{P} . A paradigmatic example of such compounds is the case of BiFeO_3 hosting a rich phase diagram that depends on the different lattice mismatch [10].

Although we mention that the ideal ABO_3 case presents a cubic structure, there are not as many cases that present this highly symmetric configuration, since several lattice distortions are prone to appear and move the atoms from their original positions. This was widely studied by Victor Goldschmidt [11], who developed a classification based on one parameter t called tolerance factor, considering the atoms as hard spheres defined as

$$t = \frac{r_A + r_O}{\sqrt{2}(r_B + r_O)} \quad (1.74)$$

where r_j represents the atomic radius of the A, B, and O ions. When this parameter is bigger or smaller than 1, the cation A would be too large or small to have a highly symmetric cubic structure, and as a consequence, several lattice distortions will appear. The usual tilt patterns are the oxygen cage octahedral rotations such as $a^-a^-c^0$, $a^0a^0c^+$, $a^0a^0c^-$, $a^-a^-a^-$, and $a^-a^-c^+$ in Glazer's notation [12] giving rise to different crystalline structures. The most common tilt pattern is the $a^-a^-c^+$ that produces a structure with $Pbnm$ symmetry.

One of the most interesting features of the ABO_3 perovskites is evidenced when we place a transition metal on the B site cation. This produces different d shell configurations on the transition metal and depending on the orbital filling of the d shell one may find very different properties as we mentioned before. In general, these compounds with non-empty d shells show a metallic paramagnetic (PM) phase at high temperatures, and then they present a magnetically ordered phase at low temperatures. One may naively expect that for all temperatures, the conducting properties would generally show a metallic character. However, many of the transition metal perovskite oxides present a metal-insulator transition (MIT) when the temperature is lowered. This metal-insulator transition is generally caused by four main mechanisms [13].

The first mechanism is to consider the octahedral crystal field Δ_{CF} that is induced on the d manifold, which produces a lifting of the degeneracy of the orbitals into groups of $3t_{2g} := \{d_{xy}, d_{xz}, d_{yz}\}$ and $2e_g := \{d_{x^2-y^2}, d_{z^2}\}$ degenerate orbitals (see Figure 1.6). It follows that in materials where the t_{2g} energy levels are half filled, while the e_g levels are completely empty, one can expect an insulator instead of a metal. This would correspond to compounds

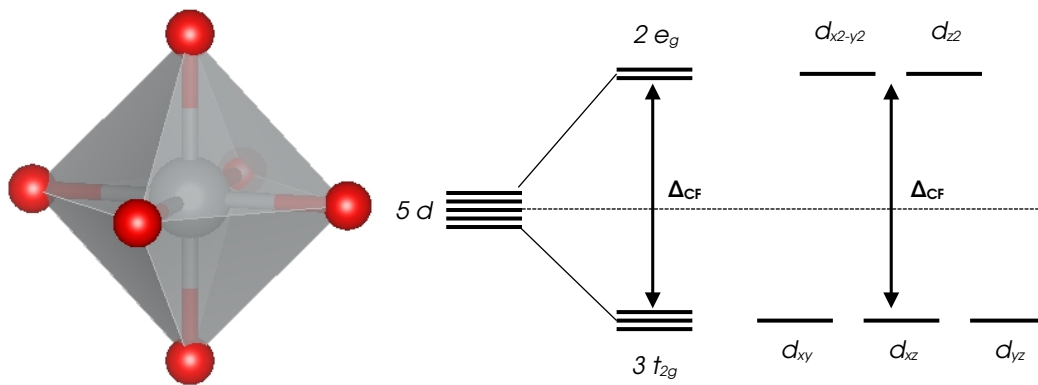


Fig. 1.6 Crystal field splitting Δ_{CF} of the d orbital in a O_6 octahedral environment.

with for example a d^3 configuration such as CaMnO_3 . The other ingredient that one may consider is Hund's coupling J_H since in the case of being bigger than the crystal field $J_H > \Delta_{\text{CF}}$ it produces a splitting between the two spin channels on each cation (see Figure 1.7). Similarly

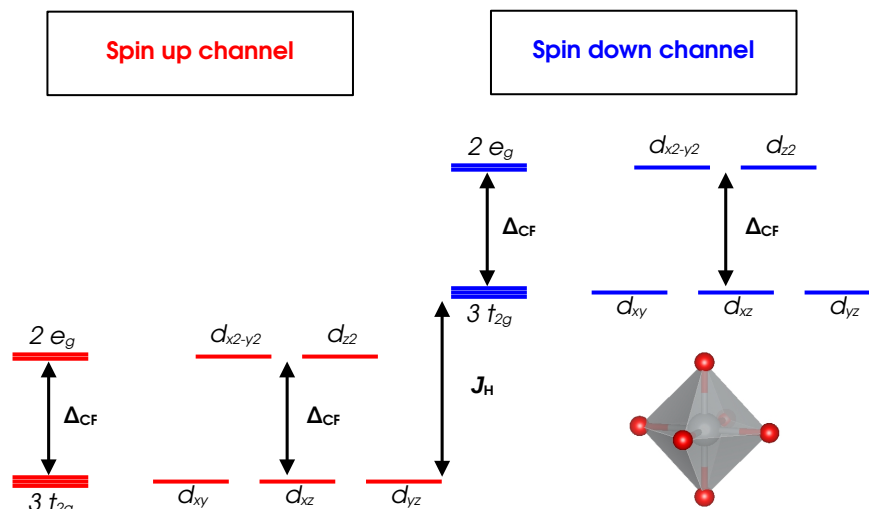


Fig. 1.7 Crystal field splitting Δ_{CF} of the d orbital in a O_6 octahedral environment with a strong Hund's coupling J_H splitting the two spin channels completely.

to the previous case, it follows that if both t_{2g} and e_g levels are filled only in one spin channel, a gap would open. This situation would correspond to cases with a d^5 configuration such as LaFeO_3 .

The second mechanism involves compounds with for instance a d^1 or d^4 electronic configuration. In such cases, the octahedral crystal field mechanism is not sufficient to explain the MIT since for a perfect cubic environment, the e_g or t_{2g} levels will be partly filled. However, the existence of octahedral rotations and tilt patterns can further change the crystal field, induce

certain orbital orderings and level splitting, and effectively recover the previous situation where the energy levels are filled without degeneracies on each spin channel. This would be the case of YTiO_3 or LaMnO_3 . We can note that this mechanism is strongly dependent on the amplitude of the tilt pattern and the hybridization with the O environment. Examples of compounds where there is no gap opening are SrVO_3 or CaVO_3 where there is either no tilt pattern or weak octahedral rotations, respectively. The two last mechanisms essentially involve electronic instabilities.

The third mechanism involves compounds where the energy levels are not completely filled in one spin channel for instance with a d^2 shell for the $3t_{2g}$ orbitals. Under these circumstances, the system would be Jahn-Teller active, and the Jahn-Teller effect (JTE) would be responsible for lifting the degeneracy of the t_{2g} orbitals through the Jahn-Teller distortion (JTD). Then the JTD can produce an orbital ordering and a double local environment on the transition metal cations. Examples of compounds showing such behavior are LaVO_3 or KCrF_3 . We must note that the JTE is purely electronic in origin and the distortion pattern as well as the orbital ordering (OO) is a consequence of it.

The fourth and last gapping mechanism in perovskite oxides is related to the formal oxidation state (FOS) on the transition metal. It is well known that elements such as Ti, V, Fe, or Ni present several oxidation states and can accommodate different orbital fillings of their $3d$ shells. However, in some cases such as in CaFeO_3 [14], BaBiO_3 [15], or the nickelates, the system presents a breathing oxygen complex distortion B_{oc} that produces a double local environment on the B cations in the ABO_3 perovskites. This is a consequence of unstable FOS on the B cation such as Fe^{4+} in CaFeO_3 or Ni^{3+} in the nickelates, that prefers to produce two different FOS on the B cation. In the case of CaFeO_3 it produces a charge ordering (CO) of Fe^{5+} and Fe^{3+} cations producing a net energy gain. This mechanism as in the case of the JTD is purely electronic in its origin and the B_{oc} distortion is a consequence of it. In the case of the nickelates, we can find it in the rare earth nickel oxides RNiO_3 that we discuss in greater detail in the next section.

1.2.2 Perovskite-based nickel oxides

The interest in this series of compounds is due to the proximity of Ni to Cu in the periodic table, and a similar formal oxidation state (FOS) as the famous Cu-based oxide superconductors. In fact, the analogy between the two systems was proposed for the first time in 1999 by Anisimov and coauthors, suggesting that nickel oxides could host superconductivity [16], and lately similar claims were made for superlattice structures [17]. The main family of perovskite-based nickel oxides is usually described in terms of a broader chemical formula $\text{R}_{n+1}\text{Ni}_n\text{O}_{3n+1}$ characterized by an integer number n . This family of compounds is the already mentioned RP phase in the previous section (see Figure 1.11), with the A cation being a rare-earth R and the B cation being Ni. Unfortunately, most of the possible chemical compositions are in general not easy to synthesize, and most of the efforts and studies focus either on a few of the first members of the series or on the limiting member $n = \infty$ corresponding to a simple perovskite RNiO_3 . This last member

phase is the most studied type of compound of the series since it is relatively simple to obtain and grow with precision. We now mainly focus on the perovskite RNiO_3 phase diagram for illustration purposes, although broadly speaking, similar features are found in the other RP members.

These nickelates present an effective $\text{Ni}^{3+}(3d^7)$ open shell configuration which would suggest at least an unpaired electron on each Ni cation. Thus paramagnetism (PM), antiferromagnetism (AFM), or ferromagnetism (FM) is much expected. In particular, these nickelates are PM metals in the high-temperature phase, and then at low temperature, they present a phase transition to an AFM order as it is depicted in Figure 1.8, with the exception of LaNiO_3 that remains a PM metal for all temperatures. From the point of view of the tolerance ratio, all of these

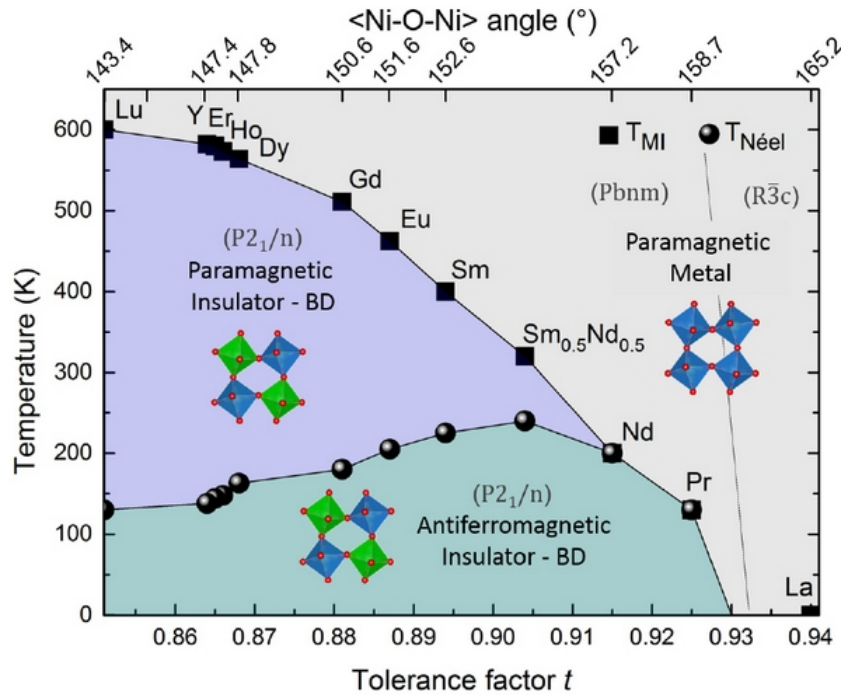


Fig. 1.8 Experimental phase diagram of RNiO_3 compounds as a function of the tolerance factor t and the Ni-O-Ni angle for different rare-earth species. Squares and circles represent the MIT temperature (T_{MIT}) and the Neel temperature (T_{N}). Adapted from Refs. [18–22].

compounds present $t < 1$ being the biggest LaNiO_3 with $t_{\text{LaNiO}_3} = 0.94$. As we mentioned before, a tolerance ratio $t < 1$ implies that the perfect ABO_3 cubic structure would present some distortions and tilt patterns. In particular, all RNiO_3 compounds except LaNiO_3 present an orthorhombic $Pbnm$ crystal symmetry at high temperatures (see Figure 1.8), characterized by a $a^-a^-c^+$ distortion pattern in Glazer's notation [12]. The tilt pattern involves two different distortions: the $a^-a^-c^0$ which corresponds to out-of-plane anti-phase rotations of the octahedra (see Figure 1.9.a), and the $a^0a^0c^+$ rotation which involves in-phase in-plane rotations of the octahedra (see Figure 1.9.b). However, at low temperatures, all the RNiO_3 compounds except LaNiO_3 present a monoclinic $P2_1/n$ symmetry, characterized by the appearance of the breathing distortion of the octahedral complexes B_{oc} (see Figures 1.9.c and 1.8 for the distortion and the structure phase diagram, respectively). In the case of LaNiO_3 the crystal structure presents

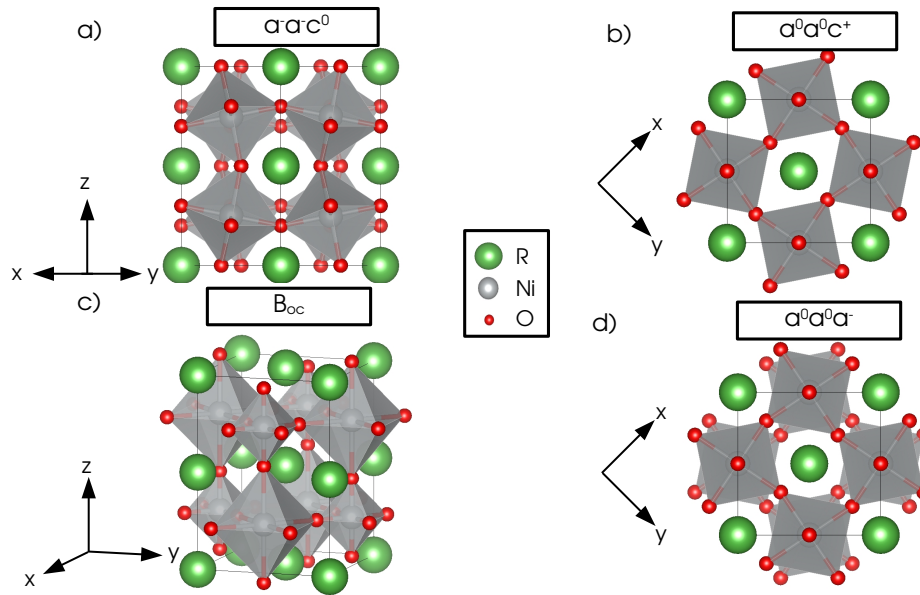


Fig. 1.9 The different tilt patterns found in RNiO_3 compounds, (a) the out-of-plane anti-phase rotations $a^- a^- c^0$, (b) the in-plane in-phase rotations $a^0 a^0 c^+$, (c) the breathing distortion B_{oc} , and (d) the in-plane anti-phase rotations $a^0 a^0 a^-$.

a $R\bar{3}c$ symmetry at all temperatures with a $a^- a^- a^-$ distortion pattern. The tilt pattern is characterized by a combination of the already mentioned $a^- a^- c^0$ rotations, and in addition, there are in-plane anti-phase rotations $a^0 a^0 a^-$ (see Figure 1.9.d).

The most interesting feature of these nickelates is that all of them except LaNiO_3 present a MIT at low temperatures accompanied by the structural transition from the orthorhombic $Pbnm$ structure to the monoclinic $P2_1/n$ structure. In the case of LaNiO_3 the system remains metallic at all temperatures with the $Pbnm$ structure. This is quite interesting since the appearance of the B_{oc} mode is what triggers the MIT and the structural transition. Interestingly, for most of the series, the MIT occurs at a higher temperature than the PM to AFM transition (this is $T_N < T_{MIT}$) [23]. Only for the case of PrNiO_3 and NdNiO_3 the Neel temperature correspond with the MIT temperature ($T_N = T_{MIT}$). This shows that effectively the MIT is not strictly related to the AFM order in these materials since there is a PM insulating phase for most of the phase diagram (see Figure.1.8). As we mentioned in the previous section, the B_{oc} mode is associated with an unstable FOS, in this case, Ni^{3+} cations, prefer to dismutate into a Ni^{2+} and a Ni^{4+} FOS ultimately resulting in a charge ordering (CO) producing a rock salt pattern of the octahedra [24].

Additionally, the appearance of the B_{oc} mode is assisted by lattice mode couplings between the octahedral rotations. As discussed in Ref. [25] the $a^- a^- c^+$ distortion is coupled to the B_{oc} mode and produces a renormalization of the effective frequency ω_{eff} since the energy depends on the amplitude of the modes as follows:

$$E \approx (\alpha + \delta_1 Q_M^2 + \delta_2 Q_R^2) Q_{B_{oc}}^2 + \dots \approx \frac{1}{2} M_O \omega_{\text{eff}}^2 Q_{B_{oc}}^2 + \dots \quad (1.75)$$

where α , δ_1 and δ_2 are constants, Q_R , Q_M and $Q_{B_{oc}}$ are the distortion amplitudes for the $a^-a^-c^0$, $a^0a^0c^+$ and B_{oc} modes, respectively, and M_O is the mass of the oxygen atom. Thus, at a finite amplitude of the octahedral rotations, the effective frequency becomes negative and produces a double well potential assisting the transition (see Figure 1.10). As we mentioned, the origin of

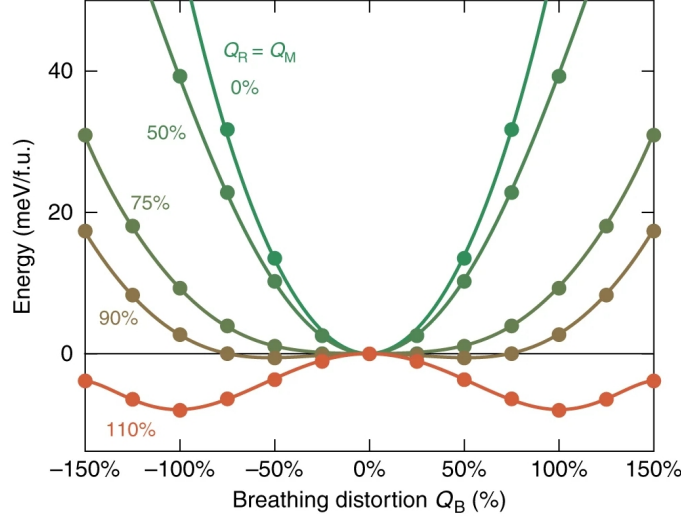


Fig. 1.10 Potential energy surface of $YNiO_3$ associated with the B_{oc} mode in the presence of a finite percentage amplitude of the $a^-a^-c^+$ distortion. Adapted from Ref. [25].

the MIT is the B_{oc} mode, and although it is assisted by the octahedral rotations for most of the compounds, for the end members $PrNiO_3$ and $NdNiO_3$ the tilting pattern would not have a big enough amplitude to induce a MIT in the PM phase. Nonetheless, this does not prevent the MIT from occurring since at low enough temperatures the transition occurs at the same time as the PM to AFM transition. This significant difference between the PM phase of $PrNiO_3$ and $NdNiO_3$, and the rest of the insulating members of the $RNiO_3$ compounds can be understood as a matter of band capacities. As discussed in Ref. [26] the magnetic order directly affects the band capacities of the bands involved in the conduction, which has a direct effect on the localization of the electrons on Ni cations since AFM interactions induce a more localized electronic structure. Hence, without an important tilt pattern on $PrNiO_3$ and $NdNiO_3$, the AFM order assists the electronic instability and the B_{oc} mode appears.

Nonetheless, several theoretical and experimental studies have shown that the MIT transition temperature T_{MIT} can be tuned either by controlling the amplitude of the tilt pattern [27], or by doping the $RNiO_3$ compounds [28, 29]. Moreover, at sufficient doping concentrations of a given cation A with different FOS than the rare-earth, the $R_{1-x}A_xNiO_3$ compounds can become metallic at all temperatures by hole or electron doping [30]. These features are also shared by the RP compounds, where compounds on the first member of the series ($n = 1$) with chemical formula R_2NiO_4 are found insulating in general. Then increasing the number of $RNiO_3$ layers n would induce an effective hole doping of the system since the Ni valency would increase, and at a high enough number n , the $R_{n+1}Ni_nO_{3n+1}$ compounds show metallic behavior instead of insulating. This highlights that the conducting properties of the RP series are similar and the

effective Ni valence would be more important than the precise geometry. Additionally, the rare earth RP compounds are highly sensitive to external stimuli such as strain, and as a consequence, the behavior of bulk and thin films can be qualitatively different showing metallicity instead of a CO insulating phase [31].

1.2.3 Layered nickel oxides

Tightly related to the perovskite nickelates, we have another family of compounds: the layered nickelates. This set of compounds presents a similar structure as the perovskite case, but the two oxygens at the apex of the octahedra have been removed, producing a fundamental building block of NiO_2 planes sandwiched in between rare-earth planes. Most of these compounds are obtained through a topotactic reduction with either CaH_2 , NaH , or some other reducing agent that can remove the O from the RO planes of a perovskite parent structure [32–37]. After chemical reduction, most of these materials can be represented with the following chemical formula $\text{R}_{2n+2}\text{Ni}_n\text{O}_{2n}$, where the limiting member RNiO_2 ($n = \infty$) is called infinite layer phase (see Figure 1.11) In practice, the synthesis process of these compounds is quite challenging; only

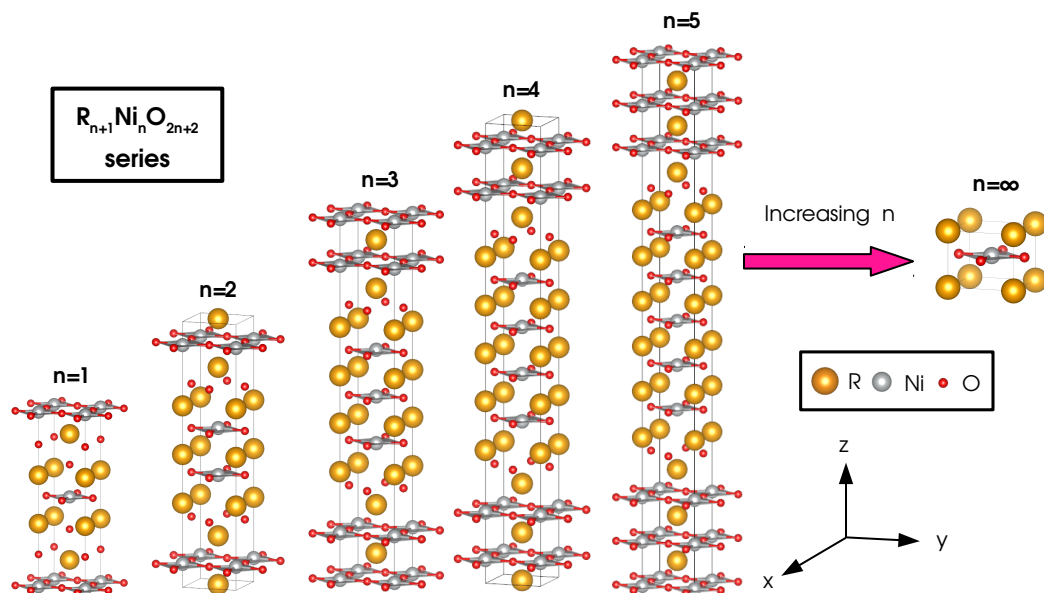


Fig. 1.11 Crystal structure of the reduced Ruddlesden-Popper series (RRP) with chemical formula $\text{R}_{n+1}\text{Ni}_n\text{O}_{2n+2}$, for different members of the series.

a few have been synthesized.

The first member of the series ($n = 1$) with chemical formula R_2NiO_4 has been synthesized with several cations ($\text{R} = \text{La}, \text{Pr}, \text{and Nd}$) presenting insulating behavior [38–41]. This insulating behavior is accompanied by a tendency to form an antiferromagnetic spin stripe-ordered phase of Ni^{2+} cations in a high spin state $S = 1$ [38]. In addition, hole doping the system either by Sr substitution on the rare-earth site has been shown to produce a charge-stripe ordered phase with a breathing distortion of the in-plane oxygen square [40, 41]. From the electronic structure point of view, this compound has been discussed theoretically to present a $d - d$ gap with a finite contribution of O p states suggesting more Mott-like character [42] in contrast with the

clear charge-transfer regime in the cuprate case [43–46].

The next member of the series ($n = 2$) has also been synthesized for some cases ($R = \text{La}$ and Nd) with a chemical formula $\text{R}_3\text{Ni}_2\text{O}_6$. These compounds also present a highly insulating phase with Mott-like character [47–50]. Some studies suggest that the insulating phase can potentially be suppressed and obtain a metallic compound once the lattice parameters are changed by either mechanical or chemical pressure [48, 50]. Regarding the magnetic structure, these compounds present antiferromagnetic behavior [51] and a stripe-ordered phase but with a double local environment of Ni^+ and Ni^{2+} stripes as depicted in Figure 1.12.a [47, 49]. This means that apart from the spin stripe ordering there is a charge stripe order. Additionally, we can note that the Ni^{2+} cations, in this case, are in an $S = 0$ low spin configuration, suggesting an enhancement of the crystal field Δ_{CF} with respect to Hund's coupling J_H when compared to the $n = 1$ case.

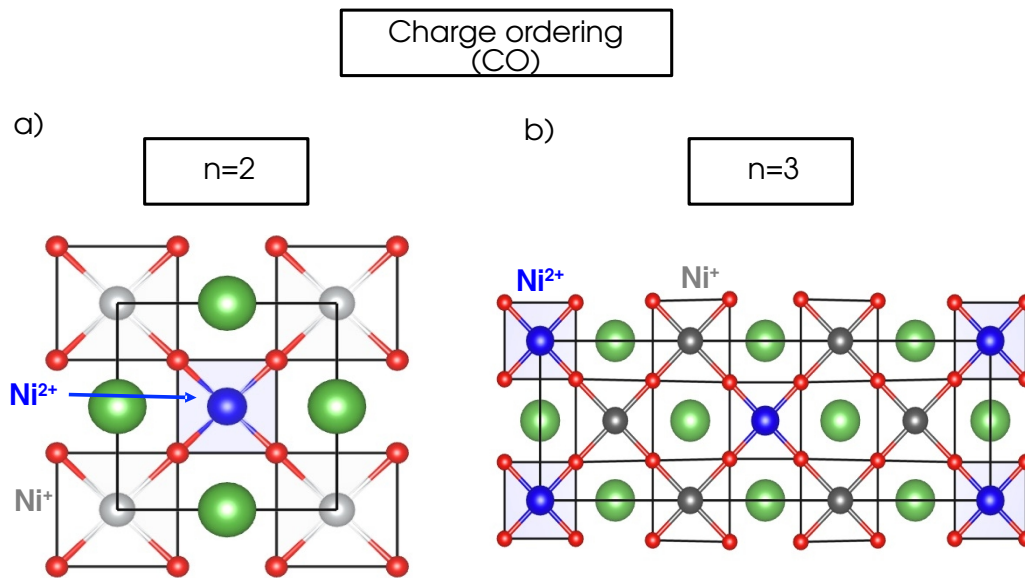


Fig. 1.12 Charge ordering patterns of Ni^+ and Ni^{2+} cations for (a) the case of $\text{R}_3\text{Ni}_2\text{O}_6$ ($n = 2$) compounds, and (b) $\text{R}_4\text{Ni}_3\text{O}_8$ ($n = 3$).

Higher members of the reduced RP series (RRP) have also been synthesized although they do not present such a strong insulating behavior. We can see that in the $n = 3$ case with chemical formula $\text{R}_4\text{Ni}_3\text{O}_8$, the compounds remain metallic for most of the temperatures and only at low temperatures below 150 K a MIT can be observed in the case of the La cation [52–54] while in the case of Pr, the compound is metallic [55, 56]. This difference may originate from a pressure effect since the Pr cation is smaller than La and can change the lattice parameter suppressing the insulating phase [57]. The origin of this MIT is also the presence of a spin and charge-ordered phase of Ni^+ and low spin Ni^{2+} cations (see Figure 1.12.b). The nature of this ordering has been evidenced in the case of La as a phase transition at $T_c = 105$ K [52, 54, 58] which can be suppressed by Pr substitution at the La site for higher contents than $x = 0.4$ [57]. This insulating behavior is also present in the case of Nd although there are no signatures of phase transition in the heat capacity [59–61]. Nonetheless, there are experimental signatures of a

charge-ordered phase although it might be dynamical [61]. From the point of view of magnetism, there are reports pointing to a strong AFM in-plane exchange from Ni sites [52, 62] but with a short-range character, since the AFM magnetic ordering is only confirmed in the La case while in the case of Pr and Nd a PM, behavior is reported [56, 61]. The electronic character of these compounds seems to indicate a mixture between Mott and charge transfer behavior [63, 64] with Ni d states being dominant at the Fermi level but hybridization with O p is present.

Apart from the $n = 3$ case, only two other higher-order members have been synthesized up to date: the $n = 5$ and $n = \infty$ cases. However, these members present a phase transition to the superconducting state, and as a consequence, they will be discussed in greater detail in the next section.

1.2.4 Superconducting Nickel oxides

As we have mentioned before, superconductivity in these layered nickelates has been proposed long ago [65], but the experimental realization was only achieved recently in 2019 in the infinite layer phase $\text{Nd}_{1-x}\text{Sr}_x\text{NiO}_2$ with $x = 0.2$ as thin-films grown on a SrTiO_3 substrate [66]. The synthesis of these compounds involves a topotactic reduction of the parent perovskite RNiO_3 phase which originally was with CaH_2 . The resistivity measurements on the original samples

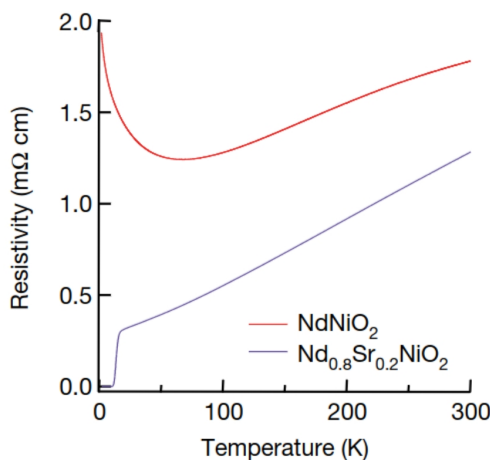


Fig. 1.13 Resistivity curves of NdNiO_2 (in red) and $\text{Nd}_{0.8}\text{Sr}_{0.2}\text{NiO}_2$ (in blue). Adapted from [66].

depicted in Figure 1.13 showed clearly that the undoped NdNiO_2 nickelate was not superconducting with a small resistivity upturn at low temperatures. This behavior is in contrast with the hole-doped $\text{Nd}_{0.8}\text{Sr}_{0.2}\text{NiO}_2$ sample showing a superconducting transition at around $T_c = 15$ K. This important difference highlights the crucial need to dope the material when obtaining a superconducting compound.

Soon after, several investigations led to the discovery of superconductivity in IL compounds with different rare earths such as La or Pr instead of Nd [67, 68], different doping concentration x [68–71], and different doping cations such as Ca instead of Sr [72]. Gathering the available data of the critical temperature as a function of the $3d$ electron count on Ni sites, a narrow

region of doping centered at a $3d^{8.8}$ electron count ($x = 0.2$) is identified for the emergence of SC (see Figure 1.14). Finally but not less important a recent study has revealed the existence

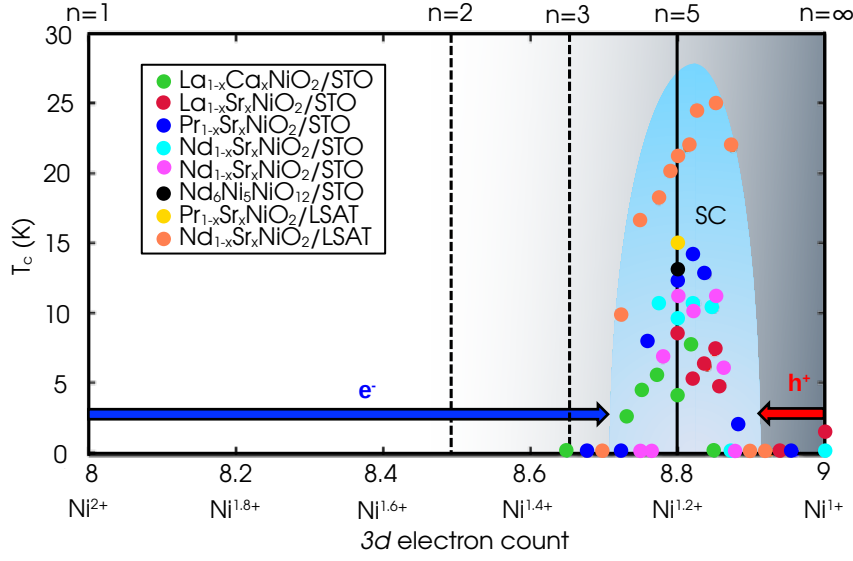


Fig. 1.14 Critical temperature T_c of the different superconducting nickelates as a function of the electron count. Experimental critical temperatures T_c are taken from Ref. [68–74]. Blue and red arrows indicate electron and hole doping the extremes of the phase diagrams respectively.

of superconductivity in $\text{Nd}_6\text{Ni}_5\text{O}_{12}$ [73] in thin films with a SrTiO_3 substrate. This compound is the $n = 5$ case of the RRP series and presents a $\text{Ni}^{1.2+}$ effective valence, in a similar way as the original compound $\text{Nd}_{0.8}\text{Sr}_{0.2}\text{NiO}_2$ for the infinite layer case $n = \infty$. The superconducting transition also seems similar to the infinite layer phase, opening the question of whether it is possible to dope other members of the series and obtain a superconductor.

Bulk or thin films and role of the substrate

All the synthesized superconducting nickelates share the similarity that they are obtained in thin films grown on a substrate. In that regard, investigations on bulk materials were carried out, but they did not obtain a superconducting transition [75, 76], suggesting that the origin of superconductivity in this compound might be a finite size effect, or even coming from the interface between the substrate and the thin film. In the early days of the discovery of the SC on these nickelates, the substrate was only SrTiO_3 which led to different studies on the interface of these compounds. In that regard, early propositions of a polar discontinuity between the two materials were made [77], but recent studies on the interface of these nickelates have shown that such polar discontinuity is absent since a small diffusion of the Nd cations into the substrate prevents such scenario [78]. Additionally, several studies have recently reported superconducting samples using $(\text{La}_{0.18}\text{Sr}_{0.82})(\text{Al}_{0.59}\text{Ta}_{0.41})\text{O}_3$ (LSAT) as a substrate [74, 79], which is not an incipient ferroelectric like SrTiO_3 . Thus, these results indicate that the origin of the superconductivity is not in the substrate but in the nickelates, being an intrinsic property.

Although the specific substrate does not seem to be crucial to obtain superconducting samples, only thin film samples show superconductivity. Nonetheless, the thickness of the superconducting samples has been pushed up to 40 nm [80]. It is true that this is not direct evidence of bulk superconductivity. However, it strongly suggest it since 40 nm would correspond to more than 100 unit cells along the z-axis of these nickelates. The absence of superconductivity in bulk samples could be understood as a result of the difficult reduction process and the lack of control of H intercalation [81], O stoichiometry [82], homogeneous reduction of the samples, and crystallinity of the parent perovskite structure although this point will be later discussed in chapter 4.

From the point of view of the nature of the superconducting phase transition, several studies have investigated this issue by applying an external stimulus and observing the different changes in the superconducting state. In that regard, some studies have reported an enhancement of the critical temperature using LSAT instead of SrTiO_3 as a substrate, suggesting that compressive strain can enhance the critical temperature [79, 74]. This is also supported by pressure experiments with a SrTiO_3 substrate showing a monotonic enhancement of the critical temperature by applying pressure [83]. Nonetheless, all the synthesized IL nickelates present a perfectly layered P_4/mmm structure in both SC and non SC regime. Thus the role of the lattice distortions, strain or whether other cations can produce a SC transition is not clarified and it will be subject of study in chapter 4 of this thesis from a theoretical point of view.

Role of the $4f$ electrons

From a chronological point of view, the SC samples that were synthesized at the beginning involved only Pr and Nd cations. These early results lead to the hypothesis that the $4f$ electrons may play an important role in the SC samples [84] and several authors incorporate them in their effective theoretical models to describe the normal state electronic properties [85, 86]. In that regard, we explore in chapter 4 how important are these $4f$ states in the conducting properties. Nonetheless, this hypothesis has nowadays been abandoned due to the experimental realization of La-based samples [68] which strongly suggest that the $4f$ electrons play a marginal role if any in the superconducting nickelates.

Normal state electronic properties and magnetism

Besides these results, many questions remain unanswered and the connection or equivalence with the Cu-based superconductors is still not clear. One important difference is the fact that the undoped samples in the case of the cuprates are strong antiferromagnetic charge-transfer insulators, that become superconductors upon hole doping [44, 45], while undoped nickelates (RNiO_2 case) present a metallic or semimetallic behavior and they seem to be closer to the Mott regime than the charge transfer of the cuprates. Several spectroscopic studies have shown that the O p states seem to be 2 eV below the Fermi level besides some hybridization with the Ni and the conduction is given by Ni and rare-earth d states [64, 87–90] (see Figure 1.15).

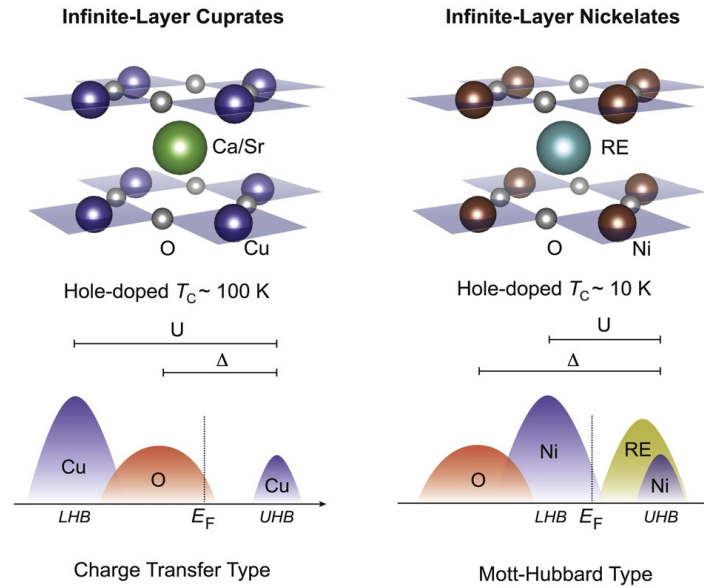


Fig. 1.15 Comparison of the electronic structure of IL cuprates and nickelates. Adapted from [87].

The magnetism, however, seems close to the cuprate case since the in-plane magnetic exchange is antiferromagnetic for nearest neighbors $J \sim 60$ meV which is one-half of the cuprate case [91, 92]. From the theoretical point of view, several reports point to an antiferromagnetic ground state [93–95] but experimentally no long-range magnetic order has been found [33, 37]. There is however evidence of antiferromagnetic interactions with some authors pointing to an antiferromagnetic glassy behavior [96, 97]. In addition, studies of the excitation spectra have revealed the existence of magnons and spin-density waves supporting an AFM ground state [91]. This short-range AFM ground state seems to be also present in the doped case where several studies have also revealed antiferromagnetic excitations [98, 99]. Additionally, studies on the exchange bias and magnetic circular dichroism of the SC nickelate film with a ferromagnetic film suggest an antiferromagnetic order even in the superconducting region [80]. This coexistence is also supported by other authors using muon spectroscopy [100]. However other studies using ^{139}La substitution have revealed through nuclear magnetic resonance experiments that bulk samples do not present a magnetic phase transition, suggesting a paramagnetic behavior [101]. Thus up to date the ground state magnetic structure is still not experimentally resolved with the existing literature pointing to a PM or short-ranged AFM ordering.

Superconducting state and pairing symmetry

When studying superconductors, a typical measurement is to apply a magnetic field which can give information about the pairing symmetry and the nature of the Cooper pairs. In that regard, recent studies on the susceptibility have revealed that effectively the superconducting samples present perfect diamagnetism regardless of the thickness [102]. This result confirms that there is a superconducting transition in the system and also suggests that the superconductivity on these nickelates is a bulk property. However, measuring the susceptibility is not the only

important parameter to measure when a magnetic field is applied, for instance, measuring the critical field upon which the superconducting transition is suppressed is also insightful. Although early reports showed an isotropic critical field on Nd samples suggesting that it is Pauli limited [103], other experiments seem to contradict these results, pointing to an anisotropic critical field although agreeing on the Pauli limited upper critical field [104, 105]. However recent studies have also suggested the existence of a Pauli limit violation in the coercive field [106, 107]. Unfortunately, its origin is still much debated but several studies suggest an unconventional pairing mechanism.

In what concerns the pairing symmetry, early studies on single particle tunneling spectrum found evidence of two different superconducting gaps suggesting a $d + s$ pairing symmetry with a major contribution from the d channel [108]. However, a recent study has put the tunneling results into question since they show that the measured gap does not vanish once the critical temperature is surpassed. In that regard, they suggest a Coulomb blockade originating from nanodomains in the surface of the film as the source of these gaps [109]. Despite these contradicting results, there are other methods to prove the pairing symmetry of the superconductor. Among them, we can clearly point to studies of the London penetration depth λ_L and superfluid density as important probes to reveal the superconducting pairing symmetry. In that regard, some studies have revealed an anisotropic pairing suggesting a nodal pairing [110], although lately it was shown to be node-less [111]. The results of these studies point to several candidates from s -wave pairing, which can be isotropic or anisotropic depending on the rare earth, node-less $d + s$ pairing, or multigap $s + s'$ symmetry. Other early studies based on the original raw data of Ref. [66] have suggested that a simple s -wave pairing is actually compatible and the easiest explanation [112]. In addition, a recent global analysis of all the existing data on the superfluid density and the London penetration depth has shown that a simple s -wave phonon-mediated mechanism can properly explain these experiments [113]. Nonetheless, the author also points to a lack of homogeneity of the samples which ultimately can lead to different interpretations on the pairing symmetry [113]. These results are also supported by optical studies of the superconducting samples, revealing that both d -wave and s -wave pairing symmetry are possible, and suggesting that these superconductors would be type-II superconductors in the dirty limit, where the Drude scattering rate is bigger than the superconducting gap $\frac{\hbar}{\tau} > 2\Delta$ [114].

Superconducting pairing mediators

Nonetheless, the pairing mediator is still not well established where some theoretical DFT studies seem to discard a phonon-mediated mechanism [115, 116], and propositions of spin wave mediated mechanism have been made in a similar fashion to the cuprates [117–119]. In what concerns the excitation spectra of the infinite layer phase, the existence of spin waves has been shown in these compounds [91, 92], although they do not seem to be able to account for the T_c enhancement [92]. Other excitations have been reported such as charge density waves (CDW) even in the undoped case with a $(1/3, 0)$ in-plane propagation vector although by doping the

CDW peak is not clear anymore [120, 121, 98]. This type of modulation has been also proposed to be able to account for the C_4 and C_2 rotational symmetry breaking in the superconducting state [122], although up to date there is no clear picture of it since other studies suggest that a contribution of the $4f$ states of the rare earth can also produce these anisotropies [106].

In that regard, several authors try to understand the physics of the undoped RNiO_2 phase and explore how hole doping (h^+ in Figure 1.14) affects the electronic structure. Although this is a valid approach, theoretical calculations show that these compounds are metallic, and experimentally they are generally found metallic or semi-metallic with a small upturn of the resistivity at low temperatures [66, 67, 123]. The mentioned upturn does not resemble however a metal-insulator transition since the resistivity does not increase at least one order of magnitude (see Figure 1.13 for NdNiO_2), but rather an impurity scattering scenario such as the Kondo effect or weak localization [86]. In addition, some magnetic fluctuations are found [92, 91] with some theoretical studies suggesting non-collinear magnetism [94, 124]. These results suggest that the metallic phase of the RNiO_2 compounds is complex, albeit without clarifying how hole doping these unusual metallic systems would improve the conducting properties and produce a superconducting transition.

1.3 Scope of the thesis

As it is evident from the previous section, there are many questions about these nickelates that are not completely resolved. Thus, in this thesis we aim to explore these compounds from a theoretical point of view from first principles.

In particular we will address the following questions: What is the role of the lattice distortions? How does the cation size and the substrate affect the electronic properties? How strong are the magnetic interactions? Who is responsible for the main magnetic interactions Ni cations or the rare earths? What are the normal state electronic properties? How should we understand the role of the doping in the superconductivity? What are the main instabilities and how do they relate to the superconducting transition? What are the mediators of the superconducting pairing? Is the electron count the only important factor to consider when designing new superconductors? Are these compounds a real analogue to the Cu-based superconductors?

We proceed in chapter 2 to explain the main theoretical tools that we use to answer these questions, most notably Density Functional Theory, and in chapter 3 we assess the reliability and limitations of some of the first principles methods that we employ in this study. Once we are aware of the reliability of the methods, we proceed to study the layered nickelates. Guided by the absence of different synthesized rare-earth cations, we explore in general the rest of the undoped rare earth compounds in chapter 4. In particular, we explore in greater detail the structure depending on the R cation, the substrate and epitaxial strain induced, and H intercalation on these compounds. Additionally we prove the magnetic ground state and how

strongly the $4f$ electrons may interact with the environment. Then we further investigate the electronic properties of the undoped compounds and how they are affected by the magnetism and the lattice. Once we understand the general properties of the undoped RNiO_2 compounds, we proceed to study the doping phase diagram in chapter 5 where we aim to explain the main experimental results and the origin of the superconductivity developing a model. In chapter 6 we further explore the applicability of the model and what other aspects are worth considering when designing new superconducting compounds, concluding with a comparison with other superconducting compounds. Finally in chapter 7 we aim to extend the identified superconducting model and apply it to related compounds, further discussing the applicability and other details that may affect the superconducting transition in general.

Chapter 2

Methods

In this chapter we present the theoretical background and methods that are used in this thesis. The main tool of this thesis is Density Functional Theory (DFT), a technique awarded with a Nobel prize in 1998, which is used to solve the electronic problem in a solid. In this chapter, the basics behind the technique are introduced without covering all details of DFT and its practical implementation since it can cover an entire book. We also present the theoretical aspects behind Landau's theory of phase transitions and its applications in studying structural transitions. Finally, the practical implementation of phonon-mediated superconductivity is presented as well as its particular implementation with DFT.

2.1 The electronic many body problem

In general, if we are interested in the steady state of an electronic system where the energy does not change in time, the many-body atomic Hamiltonian containing N electrons and N_a ions can be expressed as

$$\mathcal{H} = -\sum_j^N \frac{\hbar^2}{2m_e} \nabla_j^2 - \sum_J^{N_a} \frac{\hbar^2}{2M_J} \nabla_J^2 - \sum_{J,j}^{N_a, N} \frac{Z_J e^2}{4\pi\epsilon_0 |\mathbf{R}_J - \mathbf{r}_j|} + \sum_{\substack{i,j \\ i>j}} \frac{e^2}{4\pi\epsilon_0 |\mathbf{r}_i - \mathbf{r}_j|} + \sum_{\substack{I,J \\ I>J}} \frac{Z_I Z_J e^2}{4\pi\epsilon_0 |\mathbf{R}_I - \mathbf{R}_J|} \quad (2.1)$$

where m_e is the mass of the j -th electrons with position vector \mathbf{r}_j , and M_J are the masses of the J -th nuclei with Z_J atomic number and position vector \mathbf{R}_J . Within the Born-Oppenheimer approximation, we can disentangle the movement of the cores from the electrons and we can separate the Hamiltonian in two terms, the electronic part \mathcal{H}_{elec} and the nuclear part \mathcal{H}_{core}

$$\mathcal{H} = \mathcal{H}_{elec} + \mathcal{H}_{cores} \quad (2.2)$$

where the nuclear part is:

$$\mathcal{H}_{cores} = -\sum_J^{N_a} \frac{\hbar^2}{2M_J} \nabla_J^2 + \sum_{\substack{I,J \\ I>J}} \frac{Z_I Z_J e^2}{4\pi\epsilon_0 |\mathbf{R}_I - \mathbf{R}_J|} \quad (2.3)$$

and the electronic part is:

$$\mathcal{H}_{elec} = - \sum_i \frac{\hbar^2}{2m_e} \nabla_i^2 - \sum_{I,i} \frac{Z_I e^2}{4\pi\epsilon_0 |\mathbf{R}_I - \mathbf{r}_i|} + \sum_{\substack{i,j \\ i>j}} \frac{e^2}{4\pi\epsilon_0 |\mathbf{r}_i - \mathbf{r}_j|} = T + V_{ext} + U \quad (2.4)$$

in which we can identify three main terms: the kinetic energy T , the electron-electron repulsion U , and the attraction to the cores V_{ext} commonly known as the external potential. This is also known as the adiabatic approximation which is usually good when dealing with solids and low-density liquids, gases, or molecules where the movements of the cores are supposed to be much slower than the movement of the electrons. Thus, one may consider to solve equation (2.5) considering only the electronic Hamiltonian

$$\mathcal{H}_{elec} |\Psi\rangle = E |\Psi\rangle \quad (2.5)$$

where E is the energy of the system and $|\Psi\rangle = |\Psi(\mathbf{r}_1, \dots, \mathbf{r}_N, \sigma_1, \dots, \sigma_N)\rangle$ is the many-body wave function of N electrons with spin σ in the Hilbert space of $\mathbb{R}^{3N} \otimes \mathcal{S}^N$, where \mathcal{S} is the spin Hilbert space. The most general solution to the many-body Schrodinger equation can be obtained with the many-body Green's function G .

$$\Psi = \int_{\mathbb{R}^{3N} \otimes \mathcal{S}^N} G V d\mu \quad (2.6)$$

where V represents all the terms that contribute to the potential energy in the Hamiltonian (In this specific case $V = U + V_{ext}$) and μ is the Lebesgue measure. In fact, obtaining the solution of equation (2.5) is always possible for any Hamiltonian \mathcal{H} that is a linear differential operator.

2.2 Density Functional Theory

In order to solve the many-body electronic problem, we consider using Density Functional Theory (DFT), which is one of the main tools in condensed matter physics to study solids and molecules. The main advantage of the technique is to avoid the computation of the many-body wave function Ψ , which presents $3N$ degrees of freedom plus the spin. Instead, the framework relies on calculating the electronic density, which presents only 3 spatial degrees of freedom plus the spin, making it immensely cheaper to use than solving the Schrodinger equation directly.

In that regard, instead of solving the electronic part of equation (2.5) directly using the wave function. One can use the electronic density which can be defined as

$$\rho(\mathbf{r}, \sigma) = N \int_{\mathbb{R}^{3N-3} \otimes \mathcal{S}^{N-1}} \Psi^*(\mathbf{r}_1, \dots, \mathbf{r}_N, \sigma_1, \dots, \sigma_N) \Psi(\mathbf{r}_1, \dots, \mathbf{r}_N, \sigma_1, \dots, \sigma_N) d\mu \quad (2.7)$$

It is quite straightforward to see that a given ρ determines the number of electrons in the system N . The interesting part of DFT is that for a given Hamiltonian with interacting potential V , the electron density ρ uniquely defines the potential V , which is known as the first Hohenberg-Kohn theorem [125]. The proof of this is quite simple. One considers two different Hamiltonians \mathcal{H}

and \mathcal{H}' with the same ground state densities ρ but different wave functions Ψ and Ψ' . The ground state energy E_0 of \mathcal{H} then verifies

$$E_0 = \langle \Psi | \mathcal{H} | \Psi \rangle \leq \langle \Psi' | \mathcal{H} | \Psi' \rangle \quad (2.8)$$

Then if the ground state of the two Hamiltonians is different we can state that

$$E_0 < \langle \Psi' | \mathcal{H} | \Psi' \rangle = \langle \Psi' | \mathcal{H}' | \Psi' \rangle + \langle \Psi' | \mathcal{H} - \mathcal{H}' | \Psi' \rangle \quad (2.9)$$

which can be simplified as

$$E_0 < E'_0 - \int_{\mathbb{R}^3 \otimes \mathcal{S}} \rho(\mathbf{r}, \sigma) (V - V') d\mu \quad (2.10)$$

where E_0 and E'_0 are the ground state energies of \mathcal{H} and \mathcal{H}' , respectively, and V and V' are the potentials that uniquely defines each Hamiltonian. It is also straightforward to identify that

$$E'_0 < E_0 - \int_{\mathbb{R}^3 \otimes \mathcal{S}} \rho(\mathbf{r}, \sigma) (V' - V) d\mu \quad (2.11)$$

If we add both (2.10) and (2.11) equations, we reach a contradiction since we obtain that $E_0 + E'_0 < E'_0 + E_0$. This means that V and V' are the same as long as they have the same ground state density ρ . This is quite convenient since we know that for an interacting system, a Hamiltonian \mathcal{H} is uniquely defined by its potential V , and for a given Hamiltonian \mathcal{H} we can obtain a unique solution Ψ as long as the Hamiltonian is a linear differential operator from equation (2.6). Now since ρ determines V as it is given by combining the two inequalities (2.10) and (2.11), and V determines Ψ as it is expressed in (2.6), then it follows that Ψ is determined by ρ , or in other words, the many-body wave function is a functional of the density $\Psi = \Psi[\rho]$. As a consequence, one is also able to express the energy as a functional of the density

$$E[\rho] = \frac{\langle \Psi[\rho] | \mathcal{H}_{elec} | \Psi[\rho] \rangle}{\langle \Psi[\rho] | \Psi[\rho] \rangle} \quad (2.12)$$

and assuming a normalized Ψ we get

$$E[\rho] = \langle \Psi[\rho] | \mathcal{H}_{elec} | \Psi[\rho] \rangle. \quad (2.13)$$

the different contributions to the total energy can be separated as follows

$$E[\rho] = T[\rho] + U[\rho] + V_{ext}[\rho] = F[\rho] + V_{ext}[\rho] \quad (2.14)$$

where $F[\rho]$ is called the universal functional since it is not material specific. The functional of the external potential can be expressed as

$$V_{ext}[\rho] = \int_{\mathbb{R}^3 \otimes \mathcal{S}} \rho(\mathbf{r}, \sigma) V_{ext} d\mu. \quad (2.15)$$

From this point, one can obtain the ground state energy by minimizing the energy functional with respect to the density using variational calculus. This is known as the second Hohenberg-Kohn theorem. The proof is also quite simple to state. One consider again a Hamiltonian \mathcal{H} with a density ρ and an energy functional $E[\rho]$ such that

$$\langle \Psi[\rho] | \mathcal{H} | \Psi[\rho] \rangle = E[\rho] < \langle \Psi'[\rho'] | \mathcal{H} | \Psi'[\rho'] \rangle = E[\rho'] \quad (2.16)$$

since ρ' is a different density then it follows that $E[\rho]$ is lower in energy than $E[\rho']$ and so by minimizing E we can obtain the ground state energy. The corollary of this theorem is that by means of variational calculus, we can obtain the true ground state just by minimizing the energy functional $E[\rho]$. These two theorems show that we get the same information concerning the ground state energy and properties related to the energy from Ψ , which is a $3N$ dimensional object plus the spin, than from ρ that has only 3 dimensions plus the spin. This means that it is much more appealing to work with ρ than with Ψ in terms of computational resources.

2.2.1 Kohn-Sham DFT

Although the two Hohenberg-Kohn theorems allow to reformulate the many-body problem in terms of the electronic density, DFT would have remained dormant since obtaining the density is not an easy task and in general the $F[\rho]$ energy functional is unknown. Here is where the Kohn-Sham scheme comes into place and what in practice gave DFT real predictive power [126]. In order to alleviate the notation and avoid extra technical details, we drop the spin degree of freedom to illustrate the ideas behind the Kohn-Sham scheme. Nonetheless, the same ideas apply when the spin degree of freedom is introduced. One considers that the many-body wave function can be expressed as the antisymmetrized product of single-particle wave functions ϕ_i (the Slater determinant of single-particle wave functions)

$$\Psi = \sqrt{N!} \mathcal{A}[\phi_1 \phi_2 \dots \phi_N] \quad (2.17)$$

where \mathcal{A} is the antisymmetrizing operator. This is known as the Kohn-Sham ansatz. One can then express the density as follows

$$\rho(\mathbf{r}) = \sum_{i=1}^N |\phi_i(\mathbf{r})|^2 \quad (2.18)$$

Under this assumption, we make use of an auxiliary problem of single independent particles and we can express the energy functional in the following manner

$$E[\rho] = T_s[\rho] + E_H[\rho] + E_{xc}[\rho] + \int V_{ext}(\mathbf{r})\rho(\mathbf{r})d\mathbf{r} \quad (2.19)$$

where T_s is the non-interacting kinetic energy that can be expressed as

$$T_s[\rho] = -\frac{\hbar^2}{2m_e} \sum_{i=1}^N \langle \phi_i | \nabla_i^2 | \phi_i \rangle = -\frac{\hbar^2}{2m_e} \sum_{i=1}^N |\nabla \phi_i|^2 \quad (2.20)$$

then we define the classical Coulomb interaction as the Hartree energy term E_H

$$E_H[\rho] = \frac{1}{2} \frac{e^2}{4\pi\epsilon_0} \iint \frac{\rho(\mathbf{r})\rho(\mathbf{r}')}{|\mathbf{r} - \mathbf{r}'|} d\mathbf{r}d\mathbf{r}' \quad (2.21)$$

and now the next term will take into account all extra effects that the two previous terms are not accounting. This term is commonly known as the exchange and correlation energy functional E_{xc} and is defined as

$$E_{xc}[\rho] = T[\rho] + U[\rho] - T_s[\rho] - E_H[\rho] = (T[\rho] - T_s[\rho]) + (U[\rho] - E_H[\rho]) \quad (2.22)$$

it is easy to see that the exchange and correlation functional would account for corrections in both the kinetic and potential energy. From this point we can now minimize the energy with respect to the density obtaining the following Euler-Lagrange equation

$$\tilde{\mu} = V_{eff}(r) + \frac{\delta T_s[\rho]}{\delta \rho(\mathbf{r})} \quad (2.23)$$

where $\tilde{\mu}$ is a Lagrange multiplier (also known as the chemical potential) that ensures the constraint

$$\int \rho(\mathbf{r})d\mathbf{r} = N \quad (2.24)$$

and $V_{eff}(\mathbf{r})$ is the Kohn-Sham effective potential defined by

$$V_{eff}(\mathbf{r}) = V_{ext}(\mathbf{r}) + V_H(\mathbf{r}) + V_{xc}(\mathbf{r}) \quad (2.25)$$

Here V_H is the Hartree potential defined as

$$V_H(\mathbf{r}) = \frac{\delta E_H[\rho]}{\delta \rho(\mathbf{r})} = \frac{e^2}{4\pi\epsilon_0} \int \frac{\rho(\mathbf{r}')}{|\mathbf{r} - \mathbf{r}'|} d\mathbf{r}' \quad (2.26)$$

and V_{xc} is the exchange-correlation potential defined as

$$V_{xc}(\mathbf{r}) = \frac{\delta E_{xc}[\rho]}{\delta \rho(\mathbf{r})} \quad (2.27)$$

We must note that we do not have an explicit formula for most of the terms in the exchange and correlation functional. However, we can use an indirect approach to obtain the real density using the chain rule so that

$$\tilde{\mu} - V_{eff}(\mathbf{r}) = \frac{\delta T_s[\rho]}{\delta \phi_i} \frac{\delta \phi_i}{\delta \rho(\mathbf{r})} \quad (2.28)$$

which defines a set of N one-electron equations

$$\left[-\frac{\hbar^2}{2m_e} \nabla^2 + V_{eff}(\mathbf{r}) \right] \phi_i = \varepsilon_i \phi_i \quad (2.29)$$

where ε_i are the Lagrange multiplier identified as the Kohn-Sham energies. We can realize that this is the same as solving N Schrodinger equations for non-interacting electrons. From this

point, we can obtain a self-consistent equation by first introducing a guess density ρ in (2.25), then the density defines the effective potential V_{eff} , and then from the potential we obtain the single particle wave function ϕ_i by solving (2.29), which defines the new density ρ as it is stated in (2.18).

2.2.2 Density functionals

Now we have mentioned that we have a term in the effective potential called exchange-correlation potential, that depends only on the exchange-correlation energy functional (2.27). One can express this energy term as two separate contributions

$$E_{xc}[\rho] = E_c[\rho] + E_x[\rho]. \quad (2.30)$$

The first term is the correlation energy E_c and the second is the exchange energy E_x . The correlation energy accounts for the collective behavior of the electrons in the material screening and decreasing the Coulomb repulsion, while the exchange energy often called Pauli energy accounts for the fermionic behavior of the electrons producing that the electrons with similar spin stay far from each other respecting the Pauli principle. As we can note the correlation energy becomes more important for electrons with opposite spins since the exchange energy do not push them away from each other. The exact expression of these two terms is completely unknown and must be approximated.

Local Density Approximation

The first and most famous approximation is the Local Density Approximation (LDA) which assumes that the interaction between electrons will be weak and short-ranged so that only the local electrons will play an important role. Under these assumptions, the kinetic energy is evaluated in the so-called Thomas-Fermi approximation as the expectation value of the kinetic energy of a homogeneous electron gas

$$T_s[\rho] = C_F \int \rho(\mathbf{r})^{\frac{5}{3}} d\mathbf{r} \quad (2.31)$$

where $C_F = \frac{3}{10}(3\pi^2)^{\frac{2}{3}}$. In LDA, the exchange energy can be computed as

$$E_x[\rho] = \int \rho(\mathbf{r})\varepsilon_x[\rho]d\mathbf{r} = C_x \int \rho(\mathbf{r})^{\frac{4}{3}}d\mathbf{r} \quad (2.32)$$

with $C_x = \frac{3}{4}(\frac{3}{\pi})^{\frac{1}{3}}$ and $\varepsilon_x[\rho] = C_x\rho^{\frac{1}{3}}$ the exchange energy density. The last term would be the correlation energy which can be expressed in terms of the correlation energy density ε_c as

$$E_c[\rho] = \int \rho(\mathbf{r})\varepsilon_c[\rho]d\mathbf{r} \quad (2.33)$$

Unfortunately, there is no closed analytical expression for this terms. Only two expressions are known for the homogeneous electron gas (HEG) at high and low-density limits. In the case of high density, we have that the correlation energy density for the unpolarized case can be

computed by

$$\varepsilon_c = A \log(r_s) + B + r_s (C \log(r_s) + D) + \dots \quad (2.34)$$

and in the low-density limit, we have

$$\varepsilon_c = \frac{1}{2} \left(\frac{a_0}{r_s} + \frac{a_1}{r_s^{3/2}} + \frac{a_2}{r_s^2} + \dots \right) \quad (2.35)$$

where $A, B, C, D, a_0, a_1, a_2$ are constant terms and r_s is a dimensionless parameter that is related to the electron density as follows

$$\frac{4}{3} \pi r_s^3 = \frac{1}{\rho} \quad (2.36)$$

In practice, the correlation energy is interpolated from Quantum Monte-Carlo methods, where the most used parametrization of the correlation energy is given by Vosko et al, [127] and Perdew and Zunger [128].

Generalized Gradient Approximation and beyond

Despite its success, the local density has the propensity to over bind the system. Nonetheless, the exchange and correlation energy functionals can be better improved by means of the gradient expansion, in what is known as the Generalized Gradient Approximation (GGA) [129, 130], in which the energy functionals will now depend on the gradient of the electron density $|\nabla\rho|$.

$$E_{xc}^{\text{GGA}}[\rho] = \int \rho(\mathbf{r}) \varepsilon_{xc}[\rho, |\nabla\rho|] d\mathbf{r} \quad (2.37)$$

This approach improves the exchange and correlation description of the system with respect to LDA, although it is well known that not every aspect is improved since in general it produces underbinding as opposed to the overbinding of LDA. Popular examples of these types of exchange-correlation functionals are the Perdew Burke Ernzerhof (PBE) [131], Perdew Wang (PW91) [132] and Becke Lee Yang Perdew (BLYP) [133–135]. From this point, there are other improvements, such as meta-GGA functionals that include the Laplacian of the density $\nabla^2\rho$.

$$E_{xc}^{\text{meta-GGA}}[\rho] = \int \rho(\mathbf{r}) \varepsilon_{xc}[\rho, |\nabla\rho|, \nabla^2\rho] d\mathbf{r} \quad (2.38)$$

In some cases, they are also semi-local functionals since they introduce a dependence on the kinetic energy density τ of the occupied Kohn-Sham eigenstates that is computed as

$$\tau = \frac{\hbar^2}{2m} \sum_i^{\text{occ}} |\nabla\phi_i(\mathbf{r})|^2 \quad (2.39)$$

The nonlocality comes from the dependence on the occupied Kohn-Sham eigenfunctions ϕ_i since they are nonlocal objects of the density. These types of corrections would account mainly for a correction in the kinetic energy, or in other words, would improve the description of the correlation term of the energy. In this case, the exchange and correlation energy is expressed as

$$E_{xc}^{\text{meta-GGA}}[\rho] = \int \rho(\mathbf{r}) \varepsilon_{xc}[\rho, |\nabla\rho|, \tau] d\mathbf{r} \quad (2.40)$$

Examples of these types of functionals are the Tao Perdew Staroverov Scuseria (TPSS) [136] and the Strongly Constrained and Appropriately Normed (SCAN) [137].

So far, most of these functionals are still not able to properly account for the exchange and correlation phenomena delocalizing the electronic density too much. This produces delocalization errors that lead to underestimating the band gap in insulators and, in some cases, predicting metallic systems instead of insulating. This is especially the case of highly localized states like $3d$ or $4f$ electrons. The main origin of this is the fact that the E_H energy includes the electron density of all the electrons, and as a result when the V_H potential is acting on each electron, each electron would interact partly with its own potential, producing a self-interaction. This is not a flaw of the theory since, in principle, the self-interaction part of the V_H potential should be canceled by the V_{xc} potential. It is actually a problem of implementation since the E_{xc} energy term has to be approximated.

Hybrid functionals

However, a different approach can be used. One can recall that in Hartree Fock (HF) theory, the energy of the systems includes both Coulomb and Exchange energy terms and they present closed analytical forms. The main drawback is the absence of correlations. Nonetheless, this means that we can design a functional that includes elements from both pure DFT and HF theory, obtaining a DFT+HF functional so that is able to better cancel the V_H potential, and reduce the self interaction errors. This is the essence of the so-called hybrid functionals that include a fraction of HF exact exchange expressed as

$$E_x^{\text{HF}} = -\frac{e^2}{2} \sum_{i,j} \iint \frac{\phi_i^*(\mathbf{r})\phi_j^*(\mathbf{r}')\phi_j(\mathbf{r})\phi_i(\mathbf{r}')}{4\pi\epsilon_0|\mathbf{r}-\mathbf{r}'|} d\mathbf{r}d\mathbf{r}' \quad (2.41)$$

Then, we can construct the energy functional as a combination of DFT and HF contributions as follows

$$E_{xc}^{\text{hyb}} = aE_x^{\text{LDA}} + bE_x^{\text{GGA}} + cE_x^{\text{HF}} + dE_c^{\text{LDA}} + (1-d)E_c^{\text{GGA}} \quad (2.42)$$

where a, b, c, d are constants ranging between 0 and 1. The actual parametrization usually is fitted to match experiments or theoretical results of higher methods. Famous examples of such functionals are the Becke (1 parameter) Wu Cohen (B1WC) [138] with the particular choice of $a = d = 0, b = 1 - c$ and $c = 0.16$ using the PW91 GGA functional, and the Becke (3 parameter) Lee Yang Perdew (B3LYP) [139] with the particular choice of $a = 1 - c - b, c = 0.2, b = 0.72$ and $d = 0.81$ using the BLYP GGA functional. These types of functionals are called global hybrids since the correction on the exchange energy is made for all ranges. In contrast with these functionals, we can mention the range-separated hybrid functionals where the exact exchange is only introduced as a correction in the short-range regime, while leaving the long-range exchange DFT energy uncorrected. In practice, this implies partitioning the electron-electron interaction kernel as follows

$$\frac{1}{|\mathbf{r}-\mathbf{r}'|} = \frac{\xi_{\mu}^{\text{SR}}(|\mathbf{r}-\mathbf{r}'|)}{|\mathbf{r}-\mathbf{r}'|} + \frac{1-\xi_{\mu}^{\text{SR}}(|\mathbf{r}-\mathbf{r}'|)}{|\mathbf{r}-\mathbf{r}'|} = \frac{\xi_{\mu}^{\text{SR}}(|\mathbf{r}-\mathbf{r}'|)}{|\mathbf{r}-\mathbf{r}'|} + \frac{\xi_{\mu}^{\text{LR}}(|\mathbf{r}-\mathbf{r}'|)}{|\mathbf{r}-\mathbf{r}'|} \quad (2.43)$$

here ξ_μ^{SR} is a smooth range separation function which is commonly chosen to be an error function $\xi_\mu^{\text{SR}} = \text{erf}(\mu|\mathbf{r} - \mathbf{r}'|)$, or an exponential $\xi_\mu^{\text{SR}} = e^{-\mu|\mathbf{r} - \mathbf{r}'|}$, where μ is the range separation parameter that determine the considered short and long range length scales. In this way, the functional is constructed by considering the HF exact exchange with the short-range kernel while the long-range part is left untouched. A popular way to construct the functional is given by

$$E_{xc}^{\text{hyb}} = \alpha E_x^{\text{HF,SR}}(\mu) + (1 - \alpha) E_x^{\text{GGA,SR}}(\mu) + E_x^{\text{GGA,LR}}(\mu) + E_c^{\text{GGA}} \quad (2.44)$$

with $0 \leq \alpha \leq 1$. As we can note, the range separation is only applied to the exchange part and the correlation energy term is left untouched. The success of these hybrid functionals is the fact that they start to predict rather accurate results, while not being as expensive as usual quantum chemistry methods such as the coupled cluster expansion, or the configuration interaction methods. In particular, in this thesis, we will be using in some cases the range-separated hybrid functional of Heyd Scuseira Ernzerhof of 2006, known as HSE06 [140] with $\alpha = \frac{1}{4}$ and $\mu = 0.2$. The choice of this functional is made by the fact that is in general well suited for solids and in particular rare earth oxides.

DFT+U scheme

Apart from introducing some exact Hartree Fock exchange to our DFT functional, there is another way to improve the exchange-correlation description, which is to introduce an onsite potential U acting on a subset of orbitals, in order to improve the electron localization reducing the self interaction errors. This approach is known as the DFT+U approach [141], in which in its simplest formulation, the energy can be computed as

$$E_{\text{DFT+U}} = E_{\text{DFT}} + \frac{U}{2} \sum_{\sigma i, I} n_{i,\sigma}^I (n_{i,\sigma}^I - 1) \quad (2.45)$$

where, $n_{i,\sigma}^I$ is the occupation number of an electron i with a given angular momentum, with spin σ at the ion I . The inclusion of this term ensures that the minimum energy is achieved at integer electron occupation numbers $n_{i,\sigma}^I$ preventing delocalization. This type of corrections accounts for the electronic correlations that can be important for transition metal elements and rare-earths, where the electronic structure is more localized. This type of approach is very popular since we may achieve a similar accuracy as employing a hybrid functional but with a more modest computational cost using a functional within LDA or GGA approximation. The drawback is that the U potential is a free parameter and it has to be carefully selected for each specific case.

2.2.3 Spin polarized DFT

The discussion that we made in the previous sections did not involve explicitly the spin degree of freedom. In that regard, we elaborate a bit on the difference in the previous results

when the spin degree of freedom is introduced without giving too many details.

In what concerns to the Hohenberg and Kohn theorems essentially they remain the same with a small difference. Instead of using the density ρ , it can be decomposed into spin up and spin down densities

$$\rho(\mathbf{r}) = N \int_{\mathbb{R}^{3N-3} \otimes \mathcal{S}^N} \Psi^*(\mathbf{r}_1, \dots, \mathbf{r}_N, \sigma_1, \dots, \sigma_N) \Psi(\mathbf{r}_1, \dots, \mathbf{r}_N, \sigma_1, \dots, \sigma_N) d\mu = \rho_\alpha(\mathbf{r}) + \rho_\beta(\mathbf{r}) \quad (2.46)$$

where $\rho_\alpha(\mathbf{r}) = \rho(\mathbf{r}, \uparrow)$ and $\rho_\beta(\mathbf{r}) = \rho(\mathbf{r}, \downarrow)$ are the spin up and down densities, respectively. Then the energy minimization can be made with respect to ρ_α and ρ_β in the same spirit as previously discussed.

Regarding the practical implementation in the Kohn-Sham scheme, the main difference is that the many body wave function is constructed with single particle spin wave functions $\phi_{i,\sigma}$, and since we minimize with respect to ρ_α and ρ_β we will have two sets of equations to solve. In practice, this procedure involves selecting a total scalar magnetization M defined by

$$M = \int_{\mathbb{R}^3} (\rho_\alpha(\mathbf{r}) - \rho_\beta(\mathbf{r})) d\mu \quad (2.47)$$

and then minimizing the energy keeping that total magnetization state. In what concerns to the DFT functionals, most of them follow the approach proposed by the Local Spin Density approximation (LSDA) [127], which consists on separating the density into two different terms for up and down spin electrons

$$E_{xc}[\rho] = \int \varepsilon_{xc}[\rho_\alpha, \rho_\beta, \nabla\rho_\alpha, \nabla\rho_\beta, \dots] d\mu \quad (2.48)$$

and then express the energy functional as in (2.48) with a separate dependence on the up or down density, where ε_{xc} is the exchange and correlation energy density. Finally one may wonder what happens if the spin texture of our material would not be colinear but actually present different spin orientations. In such cases, instead of dealing with the density ρ or the two densities ρ_α and ρ_β or alternatively the total density ρ and scalar the magnetization M , we would need to use the density matrix $\rho_{\alpha\beta}$ defined as

$$\rho_{\kappa\nu} = \langle \kappa | \Psi \rangle \langle \Psi | \nu \rangle \quad (2.49)$$

where $\langle \Psi |$ is now a spinor $\langle \Psi | = (\langle \Psi_\alpha |, \langle \Psi_\beta |)$ and $\langle \nu |, \langle \kappa |$ can be $\langle \alpha |$ or $\langle \beta |$ the spin up and down eigenstates, respectively. This can be formulated alternatively as

$$\rho_{\alpha\beta} = \rho \mathbb{I} + \mathbf{m} \cdot \boldsymbol{\sigma} \quad (2.50)$$

where $\sigma = (\sigma_x, \sigma_y, \sigma_z)$ is a vector with the Pauli spin matrices σ_μ , and $\mathbf{m} = (m_x, m_y, m_z)$ is the magnetization density vector whose components are defined as

$$\begin{aligned} m_x &= \langle \alpha | \Psi \rangle \langle \Psi | \beta \rangle + \langle \alpha | \Psi \rangle \langle \Psi | \beta \rangle \\ m_y &= i(\langle \beta | \Psi \rangle \langle \Psi | \alpha \rangle - \langle \alpha | \Psi \rangle \langle \Psi | \beta \rangle) \\ m_z &= \langle \alpha | \Psi \rangle \langle \Psi | \alpha \rangle - \langle \beta | \Psi \rangle \langle \Psi | \beta \rangle \end{aligned} \quad (2.51)$$

However the non-colinear DFT is much more costly in terms of computational resources than the colinear case and in many cases the colinear approach is sufficient to capture the trends in the structure, magnetism and electronic properties of compounds.

2.2.4 Basis set

As we mentioned, the Kohn-Sham approach requires obtaining N single-particle wave functions for which we do not have a closed analytical form. For that reason, we can recall that each of the single-particle wave functions can be expanded in any orthonormal basis $\{|\chi_\alpha\rangle\}$ this is

$$|\phi_i\rangle = \sum_{\alpha} \langle \chi_\alpha | \phi_i \rangle |\chi_\alpha\rangle = \sum_{\alpha} f_{\alpha i} |\chi_\alpha\rangle \quad (2.52)$$

where $f_{\alpha i}$ are the expansion coefficients.

Plane wave basis set

One of the possible choices of basis set especially well suited for solids is the plane wave basis set. This choice exploits the fact that any periodic function can be expressed as a Fourier series, where each of the single-particle wave functions can be computed in the following manner

$$|\phi_i\rangle = \sum_{\mathbf{q}} c_{i,\mathbf{q}} \frac{1}{\sqrt{\Omega}} e^{i\mathbf{q}\mathbf{r}} = \sum_{\mathbf{q}} c_{i,\mathbf{q}} |\mathbf{q}\rangle \quad (2.53)$$

Here $c_{i,\mathbf{q}}$ are the expansion coefficients, Ω is the volume of the system and $|\mathbf{q}\rangle$ are the plane waves basis functions characterized by the wave vector \mathbf{q} . One can easily notice that this basis has the particularity that each of the basis functions is an eigenstate of the momentum operator \hat{q} . Thus allowing us to work directly on the reciprocal space and compute the energy spectra in the first Brillouin zone. In this way, we can express the basis functions as

$$\chi_{\mathbf{k}}^{\mathbf{G}} = \frac{1}{\sqrt{\Omega}} e^{i(\mathbf{k}+\mathbf{G})\mathbf{r}} \quad (2.54)$$

with \mathbf{k} being the electron momentum in the first Brillouin zone and \mathbf{G} is a reciprocal lattice vector. One must note however that making this choice of basis implies an infinite number of basis functions, and in practice, we must define a cut-off of these expansions by $|\mathbf{k} + \mathbf{G}| < \mathbf{G}_{\max}$ which defines as well the maximum kinetic energy, since $T_{\mathbf{k}+\mathbf{G}} \sim |\mathbf{k} + \mathbf{G}|^2$. The strong point of the choice of this basis is that we can increase the accuracy of our description by just increasing a single parameter \mathbf{G}_{\max} , and it is easy to obtain the matrix elements of the different observables. The weakness of this is that upon increasing the energy cut-off, the basis set increases rapidly,

and the number of plane waves required to describe the density fluctuations accurately can be beyond the available computational resources. For that reason, it is usually required to consider the core electrons as an effective potential and explicitly treat only a small amount of the outer electrons. This is known as the pseudopotential approach and is quite successful in reducing the computational resources required for the calculations.

Gaussian basis set

However, we can make a different choice of basis so that it is finite and consequently the computation time can be greatly improved. A classical choice is to use localized orbitals such as Gaussian-type orbitals (GTO) which can be described by

$$\chi_{GTO} = \mathcal{N} r^{2l} e^{-\alpha r^2} Y_l^m(\theta, \varphi) \quad (2.55)$$

where \mathcal{N} is a normalization constant, $Y_l^m(\theta, \phi)$ are the spherical harmonics and α is a fitting parameter to account for the width of the Gaussian. The choice of this basis presents several advantages, especially since the basis increases almost linearly with the size of the system and as a consequence is not as computationally expensive. The main weakness is that it is not a complete basis set and as a consequence, the basis functions are introduced *ad hoc* and there is no guarantee of improvement upon increasing the basis set.

The two options of basis sets present its strengths and weaknesses where the GTO approach would be better for insulators since one could expect a localized electronic structure, while for metals the plane wave approach would be more suitable since a more delocalized structure is expected. In this thesis, we will mainly use the Vienna ab initio simulation package (VASP) [142–144] which is a plane wave code with projector augmented wave (PAW) pseudopotential basis set [145] and so if not stated otherwise we will be dealing with this approach. One must note however that we have used in some cases the code CRYSTAL which uses the method of linear combination of atomic orbitals (LCAO) in particular using GTO. The reason behind using a different type of code and basis set is the fact that when a hybrid functional is needed to obtain accurate results, using plane waves as a basis set is very expensive in terms of computational resources since the explicit evaluation of the exchange integrals requires to calculate the single-particle wave functions at each step and even with pseudopotentials it is still too demanding in some cases. This however is not the case for Gaussian-type orbitals since the exchange integral does not increase especially the computational cost.

2.2.5 Wannier Functions

One of the well-known theorems in solid-state physics is Bloch's theorem which states that the eigenstates of the Schrodinger equation in a periodic potential $V(\mathbf{r} + \mathbf{R}) = V(\mathbf{r})$, where \mathbf{R}

is a lattice vector, can be expressed as

$$|\Psi_{n,\mathbf{k}}(\mathbf{r})\rangle = |u_{n,\mathbf{k}}(\mathbf{r})\rangle e^{i\mathbf{k}\mathbf{r}} \quad (2.56)$$

where $u_{n,\mathbf{k}}$ is a periodic function with the periodicity of the lattice, and \mathbf{k} is the wave vector. Now as we said before, any of these eigenstates can be expanded in a complete basis set, and one of particular interest is the one given by the Fourier transform of these eigenstates, where the basis functions are known as wannier functions w_n .

$$|w_n\rangle = \frac{1}{\Omega_{\text{BZ}}} \int_{\text{BZ}} |\Psi_{n,\mathbf{k}}(\mathbf{r})\rangle e^{-i\mathbf{k}\mathbf{R}} d\mathbf{k} \quad (2.57)$$

where Ω_{BZ} is the volume of the first Brillouin Zone. One could in fact consider several bands n and obtain a wannier function as follows

$$|w_m\rangle = \frac{1}{\Omega_{\text{BZ}}} \int_{\text{BZ}} \sum_n U_{m,n}(k) |\Psi_{n,\mathbf{k}}(\mathbf{r})\rangle e^{-i\mathbf{k}\mathbf{R}} d\mathbf{k} \quad (2.58)$$

where $U_{m,n}$ is an arbitrary unitary matrix. However, this introduces a degree of arbitrariness since there is no unique unitary transformation. A common choice for these types of functions is to be localized and as a result, a strategy is to take the unitary transformation that minimizes a spread function Ω . One of the most popular definitions of this is to minimize the spatial variance defined as follows

$$\Omega = \sum_m \left(\langle w_m | r^2 | w_m \rangle - \langle w_m | r | w_m \rangle^2 \right) = \sum_m \left(\langle r^2 \rangle_m - \langle r \rangle_m^2 \right) \quad (2.59)$$

This particular choice of wannier functions are called maximally localized wannier functions (MLWF)[146, 147]. One of the advantages of the wannier functions is that it can be used to calculate properties related to the electronic structure on coarser \mathbf{k} grids than those obtained by our DFT simulations. For instance, obtaining the density of states in a metal which is defined as

$$\rho(\varepsilon) = \frac{1}{\Omega} \sum_{\mathbf{k}} \delta(\varepsilon - \varepsilon_{\mathbf{k}}) \quad (2.60)$$

can be a very difficult task to obtain directly from our DFT calculations since it requires to evaluate the energy for a very coarse grid of \mathbf{k} points, and hence an immense amount of computational resources. In contrast, we could obtain the projected density of states by means of the Wannier functions (WF) since

$$\rho(\varepsilon_m) = \sum_{n,\mathbf{k}} |\langle w_m | \psi_n, k \rangle|^2 \delta(\varepsilon - \varepsilon_{n,\mathbf{k}}) = \sum_{n,\mathbf{k}} |U_{m,n}(k)|^2 \delta(\varepsilon - \varepsilon_{n,\mathbf{k}}) \quad (2.61)$$

From this point it might seem as if we would not have gained much, but the power behind the scheme is to use interpolation techniques over the band structure so that we can calculate the energy on much more \mathbf{k} -points. This is known as Wannier interpolation and it allows to increase the grid by several orders of magnitude with a modest computational cost. In the

present work, we have employed the WANNIER90 package [148] mainly for constructing MLWF and obtaining accurate values for the density of states.

2.2.6 Paramagnetism with DFT

In many cases, the system that we study does not present a long-range magnetic order, while it can develop a finite magnetization \mathbf{M} without hysteresis when a magnetic field \mathbf{H} is applied. In these particular cases, the system is called paramagnetic (PM). Modeling PM in solids with DFT is quite challenging since for bulk solids DFT uses periodic boundary conditions while a PM compound does not present periodicity on the local magnetic moments μ_i . Nonetheless, we can aim to model a PM with an antiferromagnetic arrangement in a finite supercell but with a random distribution of the local magnetic moments μ_i . This representation converges to the real PM phase in the limit of an infinitely large supercell. Thus increasing the supercell size will always improve the results.

However, this method is not widely used in the literature, and instead of a random spin PM, several authors directly use a non-spin polarized solution (NM) to model PM. This is nothing but a good practice since it neglects the spin degree of freedom in the simulations even though the system presents local magnetic moments. In order to illustrate the limitations of this approach, we can compare the formulation of LDA and LSDA approximation to DFT. As we discussed previously, in LDA, the exchange energy density has the following dependence on the density

$$\varepsilon_x^{\text{LDA}}[\rho] = C_x \rho^{1/3} \quad (2.62)$$

while in the LSDA, there are two quantities that the exchange energy depends on, the total density $\rho(\mathbf{r}) = \rho_\alpha(\mathbf{r}) + \rho_\beta(\mathbf{r})$ and the spin polarization ζ defined as

$$\zeta = \frac{\rho_\alpha(\mathbf{r}) - \rho_\beta(\mathbf{r})}{\rho_\alpha(\mathbf{r}) + \rho_\beta(\mathbf{r})} \quad (2.63)$$

Now the exchange energy density in the LSDA can be written as

$$\varepsilon_x^{\text{LSDA}}[\rho, \zeta] = -\frac{1}{2} C_x \rho^{1/3} [(1 + \zeta)^{1/3} + (1 - \zeta)^{1/3}] \quad (2.64)$$

It is easy to see that if the system has closed shells with all electrons paired, both formulations are equivalent, since

$$\rho_\alpha(\mathbf{r}) = \rho_\beta(\mathbf{r}), \quad \forall \mathbf{r} \in \mathbb{R}^3 \quad (2.65)$$

and we have that LDA and LSDA produce the same exchange functional. This situation would correspond to diamagnetic systems (DM). However, this is the only point in common since if there are unpaired electrons, the equivalence in Eq.(2.65) does not hold, since it requires local symmetry in the spin densities and if there are unpaired electrons in the atoms, by definition the spin densities cannot be equivalent locally in the atoms. In fact, for a PM arrangement, the

condition that the system must obey is a global symmetry that can be expressed as

$$\int (\rho_\alpha(\mathbf{r}) - \rho_\beta(\mathbf{r})) d\mathbf{r} = 0 \quad (2.66)$$

This means LSDA and LDA would not have the same exchange energy. One can also note in Eq.(2.67) that the correlation energy is different between LDA and LSDA, since by construction, the correlation energy in LSDA introduces a correction to the case of $\zeta = 0$ (which is the correlation energy on LDA $\varepsilon_c[\rho, 0] = \varepsilon_c^{\text{LDA}}[\rho]$).

$$\varepsilon_c^{\text{LSDA}}[\rho, \zeta] = \varepsilon_c[\rho, 0] + \Delta\varepsilon_c[\rho, \zeta] \quad (2.67)$$

Both results show that the exchange and correlation phenomena of a DM system is not equivalent in general to a PM system. Thus it becomes quite evident that using the NM approximation is not appropriate to model PM systems and should be used only in DM system or in non-magnetic compounds. In contrast when modeling PM system the spin degree of freedom is crucial to include at any level of description of the exchange and correlation phenomena. One approach to model the PM phase is to increase the size of the supercell used in the calculations and produce a random distribution of spins with equal population on each spin channel (see Figure 2.1).

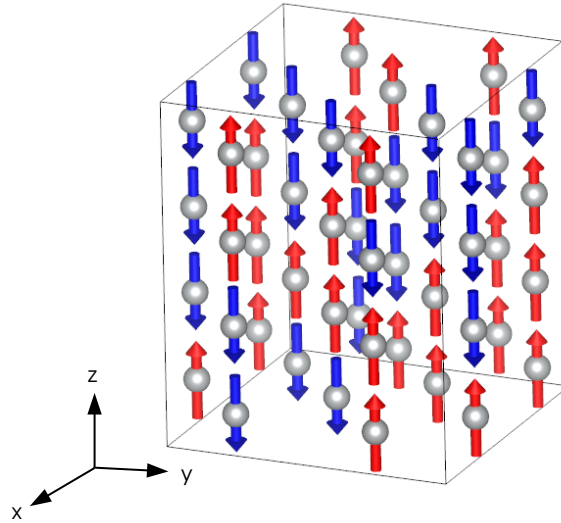


Fig. 2.1 Sketch of the distribution of the magnetic moments in a PM arrangement.

In order to do so, we use the Alloy Theoretic Automatic Toolkit (ATAT) [149] which allows to create a random distribution of two different cations through the Special Quasirandom Structure method (SQS) [150]. Here, the two types of cations would not belong to two different atomic species but to the up and down spin configurations. Thus, by asking for a distribution of two types of atoms on the same sites with equal populations, one is able to obtain a finite-size approximation to the PM state that asymptotically converges to the real PM phase. This approach was successfully applied to oxide compounds [13, 151], allowing us to capture the trends in metallic and insulating behavior in the PM state.

2.2.7 Models of magnetism and DFT

Although the structure of the system is one of the most important features to study in a given material, magnetic interactions usually play a very important role in understanding the low-energy physics of different materials. One of the most simple and widely used models of magnetism is the Heisenberg model which presents the following Hamiltonian

$$\mathcal{H}_{\text{Heis}} = \sum_{i,j} J_{i,j} S_i S_j \quad (2.68)$$

where $J_{i,j}$ is the exchange constant and S_i, S_j are the spins involved in the interaction. Now we can note that this simple Hamiltonian expresses the contribution of the magnetic texture of the system to the total energy. This is quite interesting since from DFT we can evaluate rather easily the total energy of the system in a given magnetic configuration. This means that we could in principle evaluate the exchange constants from DFT by calculating different magnetic textures in different supercells. For instance, for a system with two atoms with the same spin $|S_i| = |S_j|$, the Hamiltonian would be

$$\mathcal{H} = J_{i,j} S_i S_j \quad (2.69)$$

If both spins are parallel to each other in the same direction, then we have that the total energy of the system would be

$$E_{\text{DFT}}^{\text{FM}} = E_0 + JS^2 \quad (2.70)$$

where E_0 is the energy independent of the magnetic arrangement. However, if the spins present opposite directions, then the total energy is

$$E_{\text{DFT}}^{\text{AFM}} = E_0 - JS^2 \quad (2.71)$$

we can now subtract (2.71) from (2.70) and obtain

$$\Delta E = E_{\text{DFT}}^{\text{FM}} - E_{\text{DFT}}^{\text{AFM}} = 2JS^2 \quad (2.72)$$

which allows us to determine both the magnitude and the sign of the exchange constant, with $J > 0$ ($J < 0$) being antiferromagnetic (ferromagnetic) coupling. This Hamiltonian can be further improved by adding different terms that would add complexity to the interactions of the system but in essence, the method to obtain the coupling constants would be equivalent. For further insights about magnetic Hamiltonians and how to model magnetic systems, we refer to Ref. [152].

2.3 Landau Theory of Phase Transitions

The Landau Theory of phase transitions is a phenomenological theory that can be applied in general to any physical system that presents a change in the number of symmetries between the two phases involved in the phase transition. Although there are other theories like the

Renormalization Group (RG) or the finite size scaling theory, that can capture better the physical phenomena than the Landau theory, it remains a rather powerful tool to use when studying second and first-order phase transitions, being able to capture the essential characteristics of them. The key ingredients are that the free energy of a system \mathcal{F} is an analytic function and obeys the symmetries of the Hamiltonian. If this holds true, then it is possible to expand the Free energy in a Taylor series of the order parameter η

$$\mathcal{F}[\eta] = \mathcal{F}_0 + a_1\eta + a_2\eta^2 + a_3\eta^3 + a_4\eta^4 + \dots \quad (2.73)$$

Depending on the symmetries of the system there could be cases where the Hamiltonian is invariant under a sign change of the order parameter η . This means that the free energy would be an even function $\mathcal{F}[\eta] = \mathcal{F}[-\eta]$ and only even powers in the expansion will be considered

$$\mathcal{F}[\eta] = \mathcal{F}_0 + a_2\eta^2 + a_4\eta^4 + \dots \quad (2.74)$$

An example of this could be a magnetic system where the order parameter is the magnetization \mathbf{M} , or a Ferroelectric system where the order parameter would be the polarization \mathbf{P} . In general, this would depend on the specific conditions of the system whether there are odd or only even terms in the expansion. The key to describing these transitions is the fact the expectation value of the order parameter is equal to zero in one of the phases, while it develops a non-zero value in the other phase (see Figure 2.2). This is completely general but we will be particularly

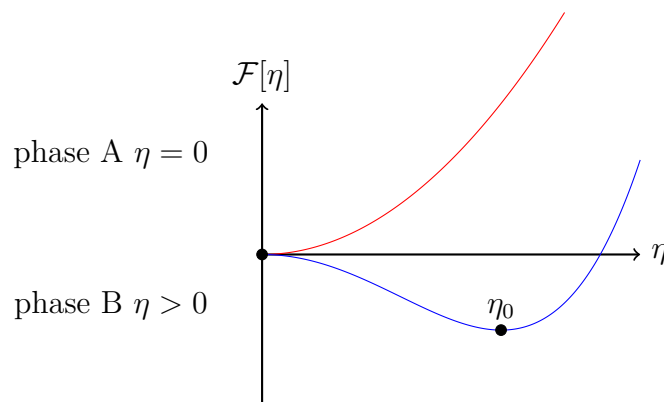


Fig. 2.2 Picture of the free energy \mathcal{F} for two phases A and B (red and blue line, respectively) with an order parameter η .

interested in describing the structural transitions of materials. One can study the structural phase transitions of the materials realizing that when there is a structural transition due to the appearance of certain lattice distortions, some of the spatial symmetries of the previous phase have been broken. In that regard, we can see a change in the symmetry of the system between the two phases. The question here is how do we establish the order parameter and what is the Hamiltonian that can account for it?

Since we are dealing with structural phase transitions, the main parameter to study will be the position of the atoms \mathbf{R} , which of course at finite temperature will oscillate around the equilibrium position \mathbf{R}_0 . Thus the hamiltonian that is suitable to study these transitions is the

vibrational hamiltonian which can be expressed as

$$\mathcal{H}_{vib} = \sum_J \frac{P_J^2}{2M_J} + V_N(\mathbf{R}_J) \quad (2.75)$$

where P_J is the momentum of the atom J , M_J its mass, \mathbf{R}_J the position and $V_N(\mathbf{R}_J)$ is the potential which can be expressed as

$$V_N(\mathbf{R}_J) = \frac{1}{2} \sum_{\mu,\nu=1}^3 k_{\mu\nu}(\mathbf{R}_J)_\mu(\mathbf{R}_J)_\nu + \frac{1}{6} \sum_{\mu,\nu,\sigma=1}^3 k_{\mu\nu\sigma}(\mathbf{R}_J)_\mu(\mathbf{R}_J)_\nu(\mathbf{R}_J)_\sigma + \dots \quad (2.76)$$

where $(\mathbf{R}_J)_\mu$ is the μ component of the position \mathbf{R}_J , and $k_{\mu\nu}$ or $k_{\mu\nu\sigma}$ are the parameters of the expansion. Thus the free energy should have an order parameter η that depends on the positions of the atoms \mathbf{R}_J and is able to incorporate the symmetries involved in the transition. One of the most natural ways to incorporate this is to use group theory and the group-subgroup relations between the two phases.

Lets us consider then that the crystals of the high and low symmetry phases are characterized by the space groups H and L respectively. If there is a group-subgroup relation $L \subset H$ where L is a subgroup of H , we can then express the total displacement of the atoms $\Delta(\mathbf{R})$ as the linear combination of the basis functions $f_\mu(\mathbf{R})$ of an n -dimensional representation Γ of the parent group H .

$$\Delta(\mathbf{R}) = \sum_{\mu=1}^n \eta_\mu f_\mu(\mathbf{R}) \quad (2.77)$$

Then the coefficients η_μ are the components of an n -dimensional vector η which will be called the order parameter [153]. The representation Γ will be a reducible representation containing all the irreducible representations of the symmetry operations $h \in H$ and we can express it as the direct sum of all the irreducible representations of the symmetry operations $D(h)$

$$\Gamma = D(h_1) \oplus D(h_2) \oplus \dots \oplus D(h_N) \quad (2.78)$$

Now the basis functions $f_\mu(\mathbf{R})$ will be the basis functions of an irreducible representation $D(h)$, allowing us to associate the different lattice distortions with a given symmetry $h \in H$. Then the components of the order parameter η_μ , can be identified as the amplitude of these lattice distortions with that given symmetry. To obtain these amplitudes, we will use the software AMPLIMODES implemented in the Bilbao Crystallographic Server which automatically implements an algorithm to obtain the different components of the order parameter η . The details about the implementation can be obtained from the following references [154, 155].

Once we know the order parameter η we are only left with the task of obtaining the free energy expansion. The most general expansion of the free energy would be

$$\mathcal{F} = \mathcal{F}_0 + \sum_{\mu} a_{\mu} \eta_{\mu} + \sum_{\mu,\nu} a_{\mu\nu} \eta_{\mu} \eta_{\nu} + \sum_{\mu\nu\sigma} a_{\mu\nu\sigma} \eta_{\mu} \eta_{\nu} \eta_{\sigma} + \dots \quad (2.79)$$

with a_μ , $a_{\mu\nu}$ and $a_{\mu\nu\sigma}$ are the expansion parameters, and we include all possible couplings between the different components of the order parameter η . As we mentioned before, depending on the symmetries of the system, some of the coefficients in the free energy expansion would be zero since the free energy will respect those symmetries. Thus in our case, the symmetries h associated with the components η_μ of the order parameter must be respected by all the terms in the Taylor expansion of the free energy. Applying a symmetry operation over η , this is $h\eta$ corresponds to the application of the irreducible representation $D(h)$ over the vector η resulting in a vector $\eta' = D\eta$

$$\eta'_\mu = \sum_{\nu=1}^n D_{\mu\nu} \eta_\nu \quad (2.80)$$

Then to get the Taylor polynomial T_p of degree p of our free energy \mathcal{F} that respects a given symmetry operation, we must satisfy the condition $T_p(D\eta) = T_p(\eta)$ since our free energy will also respect $\mathcal{F}[D\eta] = \mathcal{F}[\eta]$. In order to generate the different terms that respect all the symmetries, we use the software INVARIANTS [156] implemented in the package ISOTROPY [157]. In this way, we can study the origin of the phase transitions and associate them to a given term in the free energy expansion as well as studying the possible couplings between different lattice distortions.

2.4 Superconductivity

As mentioned before in the first sections of chapter 1, the superconducting state is characterized by the appearance of an attractive interaction between the electrons that overcomes the Coulomb repulsion. Usually, the simplest mediators that come into place are phonons. As a consequence, the key quantity to calculate is the electron-phonon coupling constant λ . We have presented in the previous chapter the BCS theory which accounts for only acoustic phonons as mediators. However, this can be generalized and we can evaluate the electron-phonon interactions for all types of phonons and for all phonon wave vectors \mathbf{q} where the total interaction will be

$$\lambda = \sum_{\mathbf{q}} \lambda_{\mathbf{q}} \quad (2.81)$$

where $\lambda_{\mathbf{q}}$ is the electron-phonon coupling for a given wave vector \mathbf{q} . Within the Migdal approximation, this quantity can be evaluated as

$$\lambda = \frac{2}{N(\varepsilon_F)N_{\mathbf{q}}} \sum_{\mathbf{k}, \mathbf{q}, \nu} \frac{|M_{\mathbf{k}, \mathbf{k}+\mathbf{q}}^\nu|^2}{\omega_{\mathbf{q}, \nu}} \delta(\varepsilon_{\mathbf{k}} - \varepsilon_{\mathbf{k}+\mathbf{q}} - \omega_{\mathbf{q}, \nu}) \frac{f(\varepsilon_{\mathbf{k}}) - f(\varepsilon_{\mathbf{k}-\mathbf{q}})}{\varepsilon_{\mathbf{k}} - \varepsilon_{\mathbf{k}-\mathbf{q}}} \quad (2.82)$$

where $N(\varepsilon_F)$ is the density of states at the Fermi level per spin, $N_{\mathbf{q}}$ is the number of \mathbf{q} points, $\omega_{\mathbf{q}, \nu}$ is the phonon energy for a given \mathbf{q} point of branch ν , $M_{\mathbf{k}, \mathbf{k}+\mathbf{q}}^\nu$ is the electron-phonon matrix element, and $f(\varepsilon_{\mathbf{k}})$ is the Fermi-Dirac occupation function. One now may assume that the energy range where the pairing occurs is close to the Fermi level so that we can take the last

term as the derivative of the occupation number around the Fermi level ε_F

$$\lambda = \frac{2}{N(\varepsilon_F)N_{\mathbf{q}}} \sum_{\mathbf{k}, \mathbf{q}, \nu} \frac{|M_{\mathbf{k}, \mathbf{k}+\mathbf{q}}^\nu|^2}{\omega_{\mathbf{q}, \nu}} \delta(\varepsilon_{\mathbf{k}} - \varepsilon_{\mathbf{k}+\mathbf{q}} - \omega_{\mathbf{q}, \nu}) \delta(\varepsilon_{\mathbf{k}} - \varepsilon_F) \quad (2.83)$$

This is known as the double delta approximation. Now we can assume that the density of states does not change much above and below the Fermi energy and we can then substitute the $\delta(\varepsilon_F - \varepsilon_{\mathbf{k}})$ by the total density of states at the Fermi level $N(\varepsilon_F)$ obtaining

$$\lambda = \frac{2N(\varepsilon_F)}{N_{\mathbf{q}}} \sum_{\mathbf{k}, \mathbf{q}, \nu} \frac{|M_{\mathbf{k}, \mathbf{k}+\mathbf{q}}^\nu|^2}{\omega_{\mathbf{q}, \nu}} \quad (2.84)$$

The electron-phonon matrix element can be evaluated with

$$M_{\mathbf{k}, \mathbf{k}+\mathbf{q}}^\nu = \sum_j \left(\frac{\hbar^2}{2M_j \omega_{\mathbf{q}, \nu}} \right)^{\frac{1}{2}} \left\langle \Psi_{n, \mathbf{k}} \left| \epsilon_{\mathbf{q}, j}^\nu \cdot \frac{\partial V^{\text{KS}}}{\partial u_{\mathbf{q}, j}^\nu} \right| \Psi_{m, \mathbf{k}'} \right\rangle \quad (2.85)$$

where M_j is the mass of the moving atom, $\epsilon_{\mathbf{q}, j}^\nu$ is the j -th component of the polarization vector, and V^{KS} is the Kohn-Sham potential. If we substitute (2.85) into (2.84)

$$\lambda = \frac{2N(\varepsilon_F)}{N_{\mathbf{q}}} \sum_{\mathbf{k}, \mathbf{q}, \nu} \frac{\hbar^2}{2\omega_{\mathbf{q}, \nu}^2} \left| \sum_j \frac{1}{\sqrt{M_j}} \left\langle \Psi_{n, \mathbf{k}} \left| \epsilon_{\mathbf{q}, j}^\nu \cdot \frac{\partial V^{\text{KS}}}{\partial u_{\mathbf{q}, j}^\nu} \right| \Psi_{m, \mathbf{k}'} \right\rangle \right|^2 \quad (2.86)$$

At this point, we can try to evaluate the expectation value inside (2.86) with a frozen phonon approach. The idea is the following. If we consider the Kohn-Sham potential with a given distortion of the j -th atom $u_{\mathbf{q}, j}^\nu$, we can Taylor expand the Kohn-Sham potential

$$V^{\text{KS}}(u_j) \approx V^{\text{KS}}(0) + \frac{\partial V^{\text{KS}}}{\partial u_{\mathbf{q}, j}^\nu} \cdot u_{\mathbf{q}, j}^\nu \quad (2.87)$$

rearranging terms, we obtain that

$$V^{\text{KS}}(u_j) - V^{\text{KS}}(0) \approx \frac{\partial V^{\text{KS}}}{\partial u_{\mathbf{q}, j}^\nu} \cdot u_{\mathbf{q}, j}^\nu \quad (2.88)$$

and normalizing by the amplitude of the distortion

$$\frac{V^{\text{KS}}(u_j) - V^{\text{KS}}(0)}{|u_{\mathbf{q}, j}^\nu|} \approx \frac{\partial V^{\text{KS}}}{\partial u_{\mathbf{q}, j}^\nu} \cdot \epsilon_{\mathbf{q}, j}^\nu \quad (2.89)$$

where $\epsilon_{\mathbf{q}, j}^\nu$ is the j -th component of the polarization vector $\epsilon_{\mathbf{q}}^\nu$ of the given phonon mode. Now if we recall from the introduction to DFT, a given Hamiltonian is uniquely defined by the potential and so we can write (2.89) as

$$\frac{\partial V^{\text{KS}}}{\partial u_{\mathbf{q}, j}^\nu} \cdot \epsilon_{\mathbf{q}, j}^\nu = \frac{1}{|u_{\mathbf{q}, j}^\nu|} (\mathcal{H} - \mathcal{H}^0) \quad (2.90)$$

where \mathcal{H}^0 is the Hamiltonian with the undistorted Kohn-Sham potential. If we take the expectation value

$$\left\langle \Psi_{n,\mathbf{k}} \left| \epsilon_{\mathbf{q},j}^\nu \cdot \frac{\partial V^{\text{KS}}}{\partial u_{\mathbf{q},j}^\nu} \right| \Psi_{m,\mathbf{k}'} \right\rangle = \frac{1}{|u_{\mathbf{q},j}^\nu|} \left\langle \Psi_{n,\mathbf{k}} \left| (\mathcal{H} - \mathcal{H}^0) \right| \Psi_{m,\mathbf{k}'} \right\rangle = \frac{\epsilon_{\mathbf{k}+\mathbf{q}} - \epsilon_{\mathbf{k}}}{|u_{\mathbf{q},j}^\nu|} = D_{j,\mathbf{k}+\mathbf{q},\mathbf{k}}^\nu \quad (2.91)$$

we can obtain an expression in terms of the Kohn-Sham eigenvalues which is known as the reduced electron-phonon matrix element (REPME) denoted by $D_{j,\mathbf{k}+\mathbf{q},\mathbf{k}}^\nu$. The change in the eigenvalues can be evaluated directly from the band structure close to the Fermi level with and without a given lattice distortion of phonon mode (\mathbf{q}, ν) . Figure 2.3 shows a practical example

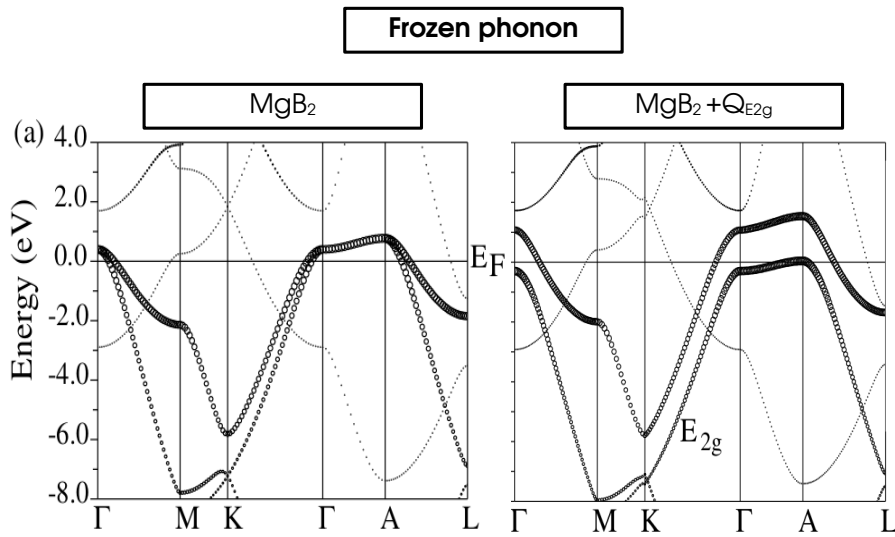


Fig. 2.3 Electronic band structure of MgB_2 . (a) bare band structure, and (b) band structure with the E_{2g} phonon mode frozen in the compound adapted from [158].

of such implementation on MgB_2 with the E_{2g} phonon mode, which is the main phonon mode contributing to the superconductivity in this compound. As we notice in Figure 2.3 the energy shifts are in the whole band dispersion. This allows evaluating directly how each phonon mode affects the electron depending on its momentum \mathbf{k} . After introducing this result back into (2.86), one obtains

$$\lambda = \frac{2N(\epsilon_F)}{N_{\mathbf{q}}} \sum_{\mathbf{k}, \mathbf{q}, \nu} \frac{\hbar^2}{2\omega_{\mathbf{q},\nu}^2} \left| \sum_j \frac{1}{\sqrt{M_j}} \frac{\epsilon_{\mathbf{k}+\mathbf{q}} - \epsilon_{\mathbf{k}}}{|u_{\mathbf{q},j}^\nu|} \right|^2 \quad (2.92)$$

This equation then allows us to obtain the electron-phonon coupling as a function of the energy shifts in the band dispersion once a given distortion is introduced. Once we have obtained the electron-phonon coupling constant, we can aim to calculate the critical temperature. One of the most reliable formulas to estimate the critical temperature is the one derived by Mc. Millan, Allens, and Dynes which we presented in the introduction

$$k_B T_c = \frac{\hbar\omega_c}{1.2} \exp\left(-\frac{1.04(1+\lambda)}{\lambda - \mu^*(1+0.62\lambda)}\right). \quad (2.93)$$

In particular, in this approximation, the characteristic energy scale ω_c is called ω_{\log} which can be approximated by the following formula for a finite number of phonon frequencies

$$\omega_{\log} = \left(\prod_i^n \omega_i \right)^{\frac{1}{n}} \quad (2.94)$$

which can be seen as the geometric average of the frequencies ω_i . Once we evaluate this quantity, we can then estimate the critical temperature, where we can take typical values for the screened Coulomb interaction $\mu^* = 0.1 - 0.2$ [159–161] and give a rough estimate. We note however that it is possible to evaluate this quantity *ab initio*. However, this is a complex calculation and it was not used in this thesis.

Chapter 3

The self-interaction problem in RBO_3 perovskites and related compounds

Although DFT is an exact theory of the ground state, the exact energy functional is yet unknown. As a result, the reliability of the theoretical predictions on the properties of different systems is strongly dependent on the functional that is used to model them. Thus, it becomes quite important to test the reliability of the different density functionals on several systems.

3.1 Self interaction errors

One of the possible inaccuracies of DFT emerges when we map the many body problem into a free electron system that is subject to an effective potential V_{eff} . In this effective potential, there is the Hartree potential V_H that is analogous to the Coulomb potential as we can see on Eq.(3.1)

$$V_H(\vec{r}) = \frac{e^2}{4\pi\epsilon_0} \int \frac{\rho(\vec{r}')}{|\vec{r} - \vec{r}'|} d\vec{r}' \quad (3.1)$$

It is straightforward to see that the expression diverges when r tends to r' . In principle, this term has to be appropriately counterbalanced by the exchange-correlation potential V_{xc} , which unfortunately has an unknown functional dependence on the electronic density. As a result, we have a situation where an electron interacts with its potential, yielding undesired delocalization effects. These types of errors are called Self Interaction Errors (SIE) and are especially important in systems such as transition metal elements or rare earth, where the extremely localized d and f orbitals are the main actors in the low energy physics. In that regard, it is important to assess the capabilities of the different density functionals and be aware of their limits. In this thesis, we have mainly used the newly developed density functional Strongly Constrained and Appropriately Normed (SCAN) [137] which is parameter-free and is able to capture at least qualitatively the metal-insulator transition of $3d$ perovskite oxides [151], cuprates [162, 163], binary oxides [164], and doping effects in SmNiO_3 [30] and bismuth oxide superconductors [165]. However, there are no reports regarding the performance of SCAN on rare earth compounds. Since we are particularly interested in nickelates with rare earth, we study the strengths and limitations of this functional with compounds including rare-earth elements.

3.2 Rare earth perovskite oxides RBO_3

The behavior of SCAN is studied on a set of perovskite compounds (ABO_3) with the rare earth on the A site cation position. We relax the structure of the different materials, keeping the $4f$ electrons as core states in the pseudopotential and also including them as valence electrons. Then we assess the reliability of the electronic structure results with the hybrid functional HSE06 [140] which is generally well suited for solids [166] and in particular has been tested on rare-earth compounds giving a rather good agreement on the band gap and lattice parameters with the experiments [167–170]. In that regard, we perform a single self-consistent calculation using as an input the obtained wavefunction from the relaxed SCAN calculation.

The studied compounds are $\text{Eu}^{2+}\text{TiO}_3$, $\text{Gd}^{3+}\text{TiO}_3$, $\text{Pr}^{3+}\text{CrO}_3$ and $\text{Dy}^{3+}\text{FeO}_3$, which are well-studied lanthanide perovskite oxides with a transition metal cation that present an insulating behavior and complex long-range magnetic order at low temperatures. The choice of compounds is guided by the fact that one can access (i) the role of the different formal oxidation states (FOS) in half-filled compounds with EuTiO_3 and GdTiO_3 , and (ii) the role of greater correlation effects by studying compounds with partly filled degenerated orbitals with PrCrO_3 (less than half filled $4f$ shell) and DyFeO_3 (more than half filled $4f$ shell).

3.2.1 Structural relaxation

The cut-off energy is set to $E_{\text{max}} = 650$ eV for the plane wave expansion and a $8 \times 8 \times 6$ k -mesh for evaluating the electronic structure in the Brillouin zone. The structural relaxations (atomic positions and lattice parameters) are performed until the forces acting on each atom are lower than $1 \text{ meV}/\text{\AA}$, with an energy convergence criteria of $\Delta E < 10^{-7}$ eV. The initial crystal structures are taken from the literature results summarized in Table 3.1. In the single shot HSE06 functional, we reduce the k -mesh to $6 \times 6 \times 4$ while maintaining the same cut-off energy due to computational reasons. Core electrons are treated with the projector augmented wave method [145], with the following PBE PAW datasets: O, Ni, Fe, Ti, Cr, Eu, Eu_3, Gd, Gd_3, Dy, Dy_3, Pr, Pr_3 and La.

The results of the structural relaxation with the SCAN functional are summarized in Table 3.1. We find that the SCAN functional yields an excellent agreement with the experimental lattice parameters with an error of less than 1%, and keeps the structural distortions that characterize the different space group geometry obtained experimentally. Regarding the values of the magnetic moments, we obtain values either with SCAN or HSE06 that are compatible with the electron count on each element, but also with experimental values in the cases where they are available.

Comp. (4f Conf.)	Magnetic Order	Space Group	Method	a(Å) b(Å) c(Å)	E _g (eV)	BEOC	μ _R (μB)	Dist. Pattern
EuTiO ₃ (4f ⁷)	Eu:G-AFM [171]	I ₄ /mcm [172]	SCAN, no 4f	5.47 5.47 7.89	2.10	(O p, Ti d)	-	a ⁰ a ⁰ c ⁻
			SCAN, with 4f	5.47 5.47 7.89	0.00	-	6.68	a ⁰ a ⁰ c ⁻
			HSE06, with 4f exp.	5.52 5.52 7.82 [172]	0.73 0.93 [173]	(Eu f, Ti d) (Eu f, Ti d)	6.79 6.93 [171]	a ⁰ a ⁰ c ⁻
GdTiO ₃ (4f ⁷)	Gd:FM, Ti:FM AFM between Gd and Ti [174, 175]	Pbnm [174]	SCAN, no 4f	5.36 5.72 7.65	0.06	(Ti d, Ti d)	-	a ⁻ a ⁻ c ⁺
			SCAN, with 4f	5.36 5.72 7.65	0.06	(Ti d, Ti d)	6.90	a ⁻ a ⁻ c ⁺
			HSE06, with 4f exp.	5.40 5.70 7.68 [174]	1.60 0.7-1.8 [176, 177]	(Ti d, Ti d) (Ti d, Ti d)	6.90 -	a ⁻ a ⁻ c ⁺
PrCrO ₃ (4f ²)	Pr:C-AFM Cr:G-AFM [178-180]	Pbnm [178]	SCAN, no 4f	5.42 5.48 7.71	2.19	(Cr d, Cr d)	-	a ⁻ a ⁻ c ⁺
			SCAN, with 4f	5.42 5.48 7.71	0.74	(Pr f, Pr f)	1.96	a ⁻ a ⁻ c ⁺
			HSE06, with 4f exp.	5.44 5.47 7.71 [178]	3.34 3.2-3.26 [178, 181]	(Pr f, Cr d) (Pr f, Cr d)	1.96 -	a ⁻ a ⁻ c ⁺
DyFeO ₃ (4f ⁹)	Dy:G-AFM Fe:G-AFM [182, 183]	Pbnm [182]	SCAN, no 4f	5.27 5.58 7.59	1.27	(O p, Fe d)	-	a ⁻ a ⁻ c ⁺
			SCAN, with 4f	5.27 5.58 7.59	1.12	(O p, Fe d)	4.92	a ⁻ a ⁻ c ⁺
			HSE06, with 4f exp.	5.30 5.59 7.61 [182]	2.91 2.10-2.60 [184, 185]	(O p, Fe d) (O p, Fe d)	4.94 -	a ⁻ a ⁻ c ⁺

Table 3.1 Summary of the key quantities characterizing the selected compounds that are computed and experimentally obtained from literature, including the different methods used for each compound, magnetic order on the rare earth and transition metal element, Space group of the computed geometry supported by experiments, DFT functional and inclusion or not of 4f electrons in the pseudopotential, values of the lattice parameters in Å, band edge orbital character (BEOC) on the conduction band minimum (CVM) and valence band maximum (VBM) depicted as (VBM, CVM), effective magnetic moment on the rare earth cation μ_R in μ_B and amplitude of the band gap E_g in eV. Structural relaxation is only performed with SCAN+4f.

3.2.2 Compounds with a half-filled 4*f* shell

Once we can trust the relaxed geometry, we proceed to analyze the electronic structure of these materials one by one. We begin with the simplest compound EuTiO₃ which has a similar structure to SrTiO₃ with a magnetic A site cation, presenting an I_4/mcm structure [172] characterized by a $a^0a^0c^-$ octahedral rotation in Glazer's notation [12]. Unlike SrTiO₃ which is a band insulator with a band gap of 3.2 eV between filled O *p* and empty Ti *d* states, EuTiO₃ is a Mott insulator with a gap of 0.93 eV formed between Eu 4*f* states and empty Ti 3*d* states [173]. If one neglects the 4*f* electrons of Eu, EuTiO₃ is a band insulator akin to SrTiO₃ (see Table.3.1 and Figure.3.1.a). As one can see in Figure 3.1.b including the 4*f* electrons in the

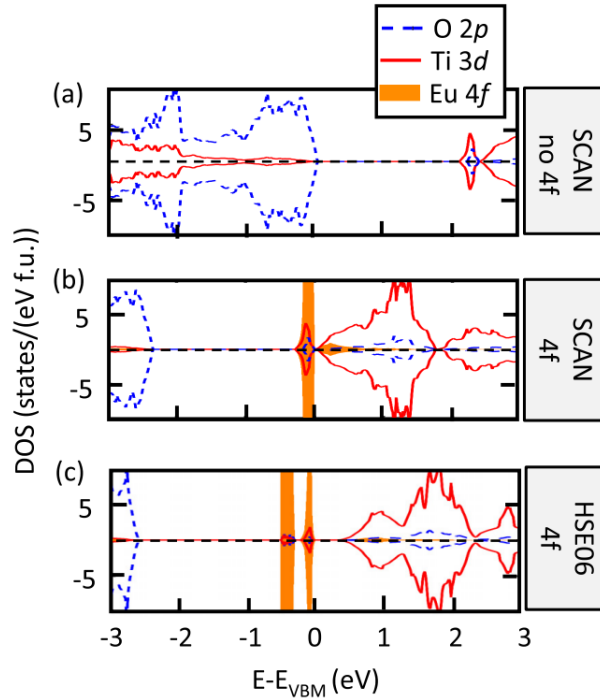


Fig. 3.1 Projected density of states on Ti *d* (red line), O *p* (dashed blue line), and Eu 4*f* (orange area) in EuTiO₃ using the meta-GGA SCAN and hybrid HSE06 functionals and involving or not the 4*f* states in the simulations.

calculation produces the following changes in the electronic structure: (i) although the gap between O *p* and Ti *d* states remains similar, Eu 4*f* states lie at the Fermi level and (ii) it produces a metallic compound, in contrast with the experiments. This also contradicts the one-shot calculation using the HSE06 functional (see Figure 3.1.c) that yields a band gap of 0.73 eV between the occupied Eu 4*f* states and the empty Ti 3*d* states. Further inspecting the projected density of states (DOS) of EuTiO₃ on Figures 3.1.b and 3.1.c, we can see that there is a weaker hybridization of Eu 4*f* with Ti 3*d* and O 2*p* states when the HSE06 functional is used, suggesting that HSE06 produces better localization and a larger Hund's splitting of the 4*f* electrons than SCAN. This ultimately suggests that at least in the case of 4*f* electrons, delocalization errors in the SCAN functional are still important.

We can estimate the strength of the Hund's rule by calculating the energy difference between the occupied and the unoccupied Eu 4*f* states, obtaining values of 5.4 eV and 8.4 eV with SCAN and HSE06 functionals respectively. Thus we see that in the case of the HSE06 functional, the occupied (unoccupied) 4*f* states are pushed down (up) with respect to the O *p* in energy, producing an insulating character in contrast to the SCAN functional that locates the 4*f* states at the bottom of the conduction band. In sight of these results, we can say that the SCAN functional cannot reproduce the insulating character of EuTiO₃. This is due to an underestimation of Hund's splitting despite being a rather simple compound with no orbital degeneracies.

We further investigate the capabilities and the origin of the failure of SCAN by studying the electronic structure of GdTiO₃, which presents a 4*f*⁷ shell for the A site cation similarly to EuTiO₃, but with a 3+ formal oxidation state (FOS) instead of the 2+ FOS of Eu. GdTiO₃ is experimentally a Mott insulator with a band gap formed between occupied and unoccupied Ti *d* states, and an estimated amplitude between 0.7-1.8 eV in the RTiO₃ family (R=La-Lu, Y) [176, 177]. From the crystallographic point of view, GdTiO₃ adopts a *Pbnm* structure characterized by the common *a*⁻*a*⁻*c*⁺ octahedral rotation pattern [174]. Inspecting the electronic structure of Figure 3.2.a and 3.2.b, we obtain that SCAN with or without the 4*f* states

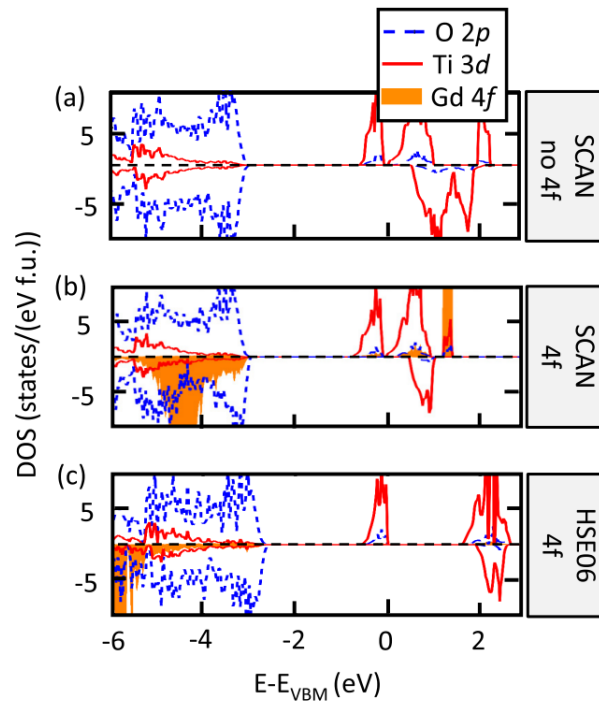


Fig. 3.2 Projected density of states on Ti *d* (red line), O *p* (dashed blue line), and Gd 4*f* (orange area) in GdTiO₃ using the meta-GGA SCAN and hybrid HSE06 functionals and involving or not the 4*f* states in the simulations.

produces a Mott insulator with the band gap between Ti *d* states. The value of the gap is 0.06 eV which is small as compared with the experiment, but compatible with previous studies of SCAN in YTiO₃ reporting a gap amplitude of 0.08 eV [151]. This underestimated band gap value is well-known for semi-local exchange-correlation functionals in DFT (see Table.3.1). We can notice that in this case, the occupied (unoccupied) 4*f* states, are well localized below

(above) the Fermi level, correctly predicting its absence in the band edge orbital character (BEOC). The success of SCAN to predict qualitatively well the insulating character of GdTiO₃ is in contrast with the previous results in EuTiO₃. These differences can be understood in terms of weaker delocalization errors in Gd³⁺TiO₃ than in Eu²⁺TiO₃, since a cation with a 3+ FOS would interact more with the O²⁻ anions p states, producing a more delocalized electronic structure due to stronger hybridization than in the case of a cation with a 2+ FOS. This is further confirmed in the partial density of states (see Figure.3.2.b) as we can see a higher hybridization between Gd $4f$ and O $2p$ states than with Eu $4f$ in EuTiO₃. Performing the one-shot calculation with HSE06 produces a larger band gap in agreement with previous results from HSE06 and DFT+U reporting a gap around 2 eV [177], and also creates a larger Hund's splitting between occupied and unoccupied $4f$ states suggesting better cancellation of SIE.

3.2.3 Compounds with a degenerate $4f$ shell

Once the capabilities of SCAN to model half-filled $4f$ shell materials are established, we proceed to study other rare-earth compounds but with partly filled degenerate $4f$ shells aiming to study possible delocalization errors in these cases. We select two perovskite oxides PrCrO₃ and DyFeO₃ that adopt at low temperatures a $Pbnm$ crystal structure with the usual $a^-a^-c^+$ octahedral rotation pattern [178, 182], showing a $4f^2$ (Pr³⁺) and $4f^9$ (Dy³⁺) electronic configuration respectively. Both compounds are insulators with the gap formed between Pr $4f$ and Cr $3d$ in the case of PrCrO₃ [178, 181], while in the case of DyFeO₃, we are not able to find experimental studies discussing the band gap character. We can however take the example of YFeO₃ and LaFeO₃ whose gap is formed between Fe $3d$ and O $2p$ [184, 185].

Inspecting the projected DOS of Figures 3.3.a and 3.3.d, we can see that neglecting the $4f$ states in DyFeO₃ produces a similar BEOC as found in YFeO₃ and LaFeO₃ (see Table 3.1) but in PrCrO₃ the valence band maximum (VBM) and conduction band minimum (CBM), expressed as (VBM, CBM) is given by (Cr d , Cr d) is the predicted BEOC in contrast the existing literature of (Pr f , Cr d) [184, 185]. By including the $4f$ states, we obtain the correct Pr $4f$ character at the top of the valence band in PrCrO₃ but also the $4f$ character is observed at the bottom of the conduction band in contrast with experiments (see Figure 3.3.b). It is also worth mentioning that as a consequence the band gap amplitude is significantly reduced as compared to the calculations with the $4f$ states treated as core states (i.e included in the PAW potential). Regarding DyFeO₃, we can notice that including the $4f$ electrons in the calculations produces a worse situation since the BEOC is wrongly predicted to be between the f states (see Figure 3.3.e), while experimentally it is observed to be (O p , Fe d) for YFeO₃ and LaFeO₃ respectively [184, 185]. Running the HSE06 functional on top of the SCAN+ $4f$ calculation yields the correct BEOC and gap amplitude for both compounds as depicted in Figures 3.3.c and 3.3.f. Inspecting the DOS with HSE06 functional, we can see that as in previous cases, the splitting between occupied and unoccupied $4f$ states is greatly increased, mainly caused by an insufficient crystal field splitting Δ_{CF} on the $4f$ produced by SCAN ($\Delta_{CF} = 0.74$ eV and

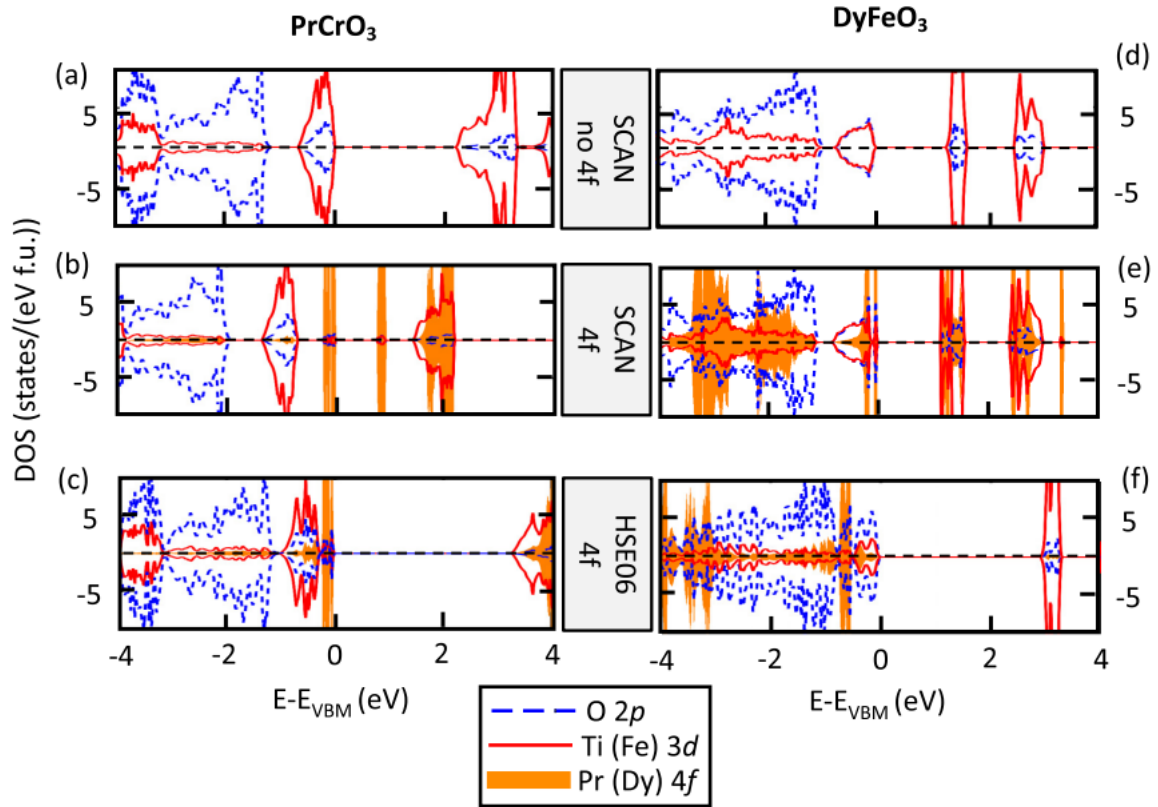


Fig. 3.3 Projected density of states on Cr and Fe d (red line), O p (dashed blue line), and Pr and Dy $4f$ (orange area) in PrCrO₃ (left panels) and DyFeO₃ (right panels) using the meta-GGA SCAN and hybrid HSE06 functionals and involving or not the $4f$ states in the simulations.

$\Delta_{\text{CF}} = 1.12$ eV in PrCrO₃ and DyFeO₃, respectively) with respect to HSE06 ($\Delta_{\text{CF}} = 3.4$ eV and $\Delta_{\text{CF}} = 4.8$ eV in PrCrO₃ and DyFeO₃, respectively).

3.3 Related compounds: Infinitely layered Nickelates RNiO₂

We conclude this chapter by inspecting the ability of SCAN to model properties of other compounds involving $4f$ states. In particular, we are interested in the infinitely layered nickelates which are the main topic of this thesis. In that regard, we explore PrNiO₂ and LaNiO₂ which present a completely layered structure of NiO₂ planes with rare-earth planes in between (see Figure 1.11 in chapter 1). The electronic structure of these compounds is not very well known experimentally but some early theoretical works [65], as well as experiments [67, 68], suggest that in both cases the system presents a completely undistorted tetragonal P_4/mmm cell [186–188]. The detailed analysis regarding the structure, the magnetism, and the electronic properties is the topic of the next chapter. We restrict ourselves to the electronic band structure with an in-plane AFM order.

Using the band structure projected on the different atomic orbital contributions, it is easy to notice a similar trend as in the case of the RBO₃ compounds, obtaining an incorrect splitting

of the $4f$ states with the SCAN functional yielding a strong contribution of the $4f$ electrons at the Fermi level in the case of PrNiO_2 while it is absent in LaNiO_2 (see Figure.3.4). The band dispersion is quite different when the HSE06 functional is used on top of SCAN, where the $4f$ electrons are pushed down or up around 3 eV away from the Fermi level. The failure of SCAN to correctly place the $4f$ electrons is further confirmed in LaNiO_2 in which there are mostly no occupied $4f$ states in the bands close to the Fermi level. Running the HSE06 functional on top of SCAN produces that the small contributions of La $4f$ states identified 0.5 eV above the Fermi level along the A-R-Z path are completely removed with the hybrid functional. One may also notice that the HSE06 functional increases the bandwidth of the bands crossing the Fermi level although the topology remains rather similar to the SCAN results in LaNiO_2 , where the main actors in the conduction are Ni $3d$ and La $5d$ states. Thus, band structure properties of these nickelates may be highly sensitive to the choice of the exchange-correlation functional.

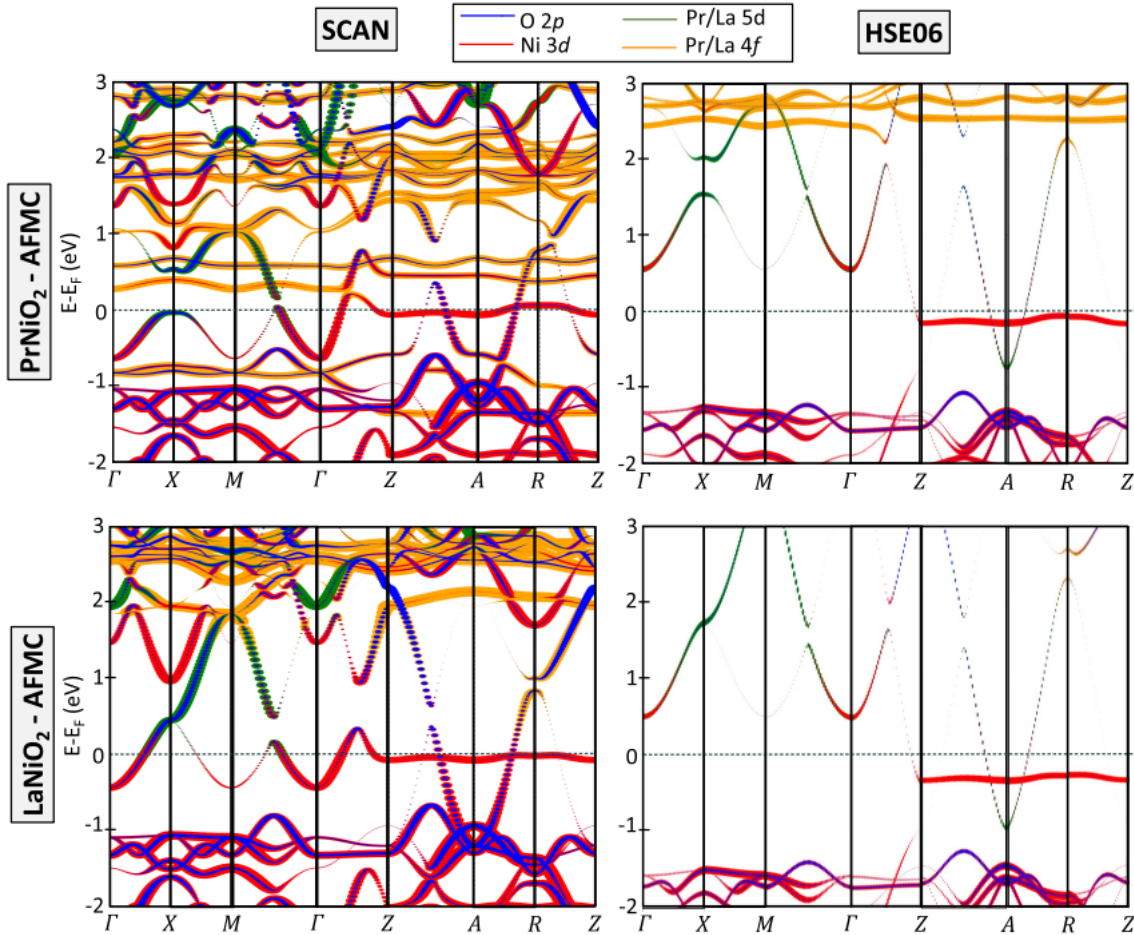


Fig. 3.4 Unfolded band structure to the high-symmetry primitive P_4/mmm cell of PrNiO_2 (top panels) and LaNiO_2 (lower panels) using the meta-GGA SCAN functional (left panels) and hybrid HSE06 (right panels) functionals. Calculations are performed with in plane antiferromagnetic interactions (AFMC) order. Coordinates of the high-symmetry points are $\Gamma(0,0,0)$, $X(\frac{1}{2},0,0)$, $M(\frac{1}{2},\frac{1}{2},0)$, $Z(0,0,\frac{1}{2})$, $A(\frac{1}{2},\frac{1}{2},\frac{1}{2})$, and $R(\frac{1}{2},0,\frac{1}{2})$.

3.4 Conclusion

This collection of results on RBO_3 perovskites and infinite-layer nickelates RNiO_2 , shows that although the meta-GGA SCAN functional constitutes a good improvement in the description of the exchange-correlation phenomena over standard GGA and LDA functionals, predicting better geometries, energies, and formation enthalpies as discussed in the literature [137, 189–191], it insufficiently amends self-interaction errors in systems involving the $4f$ electrons or in transition metals with low FOS. This translates into a general underestimation of Hund’s exchange coupling and produces a bad BEOC in insulators and places the $4f$ states at the Fermi level in metals. We can propose two strategies to deal with these problems (i) benchmark the results with a method or functional that accurately deals with the $4f$ states, and (ii) use a DFT+U approach to increase the localization and amend the self-interaction errors on highly localized states.

Chapter 4

Properties of bulk RNiO_2 compounds

In this chapter, we study several aspects of the RNiO_2 compounds using DFT simulations, since at the beginning of the thesis the lack of experimental evidence related to these compounds blurred the understanding of the different properties of these nickelates. Thus we intend to shed some light on this matter by exploring the RNiO_2 phase diagram as a function of the R cation from a theoretical point of view, focusing mainly on the low-temperature crystal structure, magnetic interactions, and electronic dispersion.

4.1 Structural Properties

So far, all observed infinite layered nickelates RNiO_2 ($\text{R} = \text{La}, \text{Pr}$ and Nd) crystallize within the highly symmetric undistorted, P_4/mmm cell consisting of NiO_2 layers with rare-earth planes in between [33, 96, 123, 192] (see Figure.4.1.a). Nevertheless, experimental reports of the infinite-layer nickelates with other R cations are lacking. This leaves the open question of whether the P_4/mmm structure is present across the whole family, or in contrast the A-to-B cation size mismatch appearing in ABO_3 perovskites, leading to octahedral rotations and potential gap openings [193–196], may also appear in infinite-layered nickelates with small R cations as it has been reported by some authors [186–188, 197]. In that regard, we study the evolution of the crystal structure as a function of the A site cation.

We perform the structural relaxation using the Vienna Ab Initio Simulation Package (VASP) [142–144] for several RNiO_2 compound with R being, La, Pr, Nd, Gd and Y. We set an energy cut-off in the plane wave expansion of 650 eV, a Γ point centered k -mesh of $8 \times 8 \times 6$, with an energy convergence criteria of $\Delta E < 10^{-7}$ eV and force acting on each atom is $\Delta F < 10^{-3}$ eV/Å. We use the PAW method [145] to treat the core electrons using the following PBE PAW pseudopotentials Y_sv, La, Gd, Pr, Nd, Ni, and O. The $4f$ electrons are explicitly treated in all calculations. As we evidenced in chapter 3, the SCAN functional is only problematic when discussing the band position of the $4f$ electrons, while the crystal structure and the magnetism of the studied compounds are well reproduced. Thus all our calculations in this chapter will involve the SCAN functional.

4.1.1 Relaxation results

We relax the crystal structure of YNiO₂ and the output is analyzed with the software FINDSYM [198, 199] obtaining an orthorhombic system with a *Pbcn* crystal symmetry and with lattice parameters $a = 5.29 \text{ \AA}$, $b = 5.70 \text{ \AA}$, and $c = 6.44 \text{ \AA}$, (see Figure.4.1.b). The crystal symmetry and the lattice parameters, agree well with recent theoretical studies on this compound, showing that the *Pbcn* symmetry is dynamically stable [197]. Comparing Figures 4.1.a and 4.1.b we notice that the orthorhombic *Pbcn* phase of YNiO₂, is distorted with respect to the tetragonal *P₄/mmm* infinitely layered phase. In order to identify the different lattice distortions,

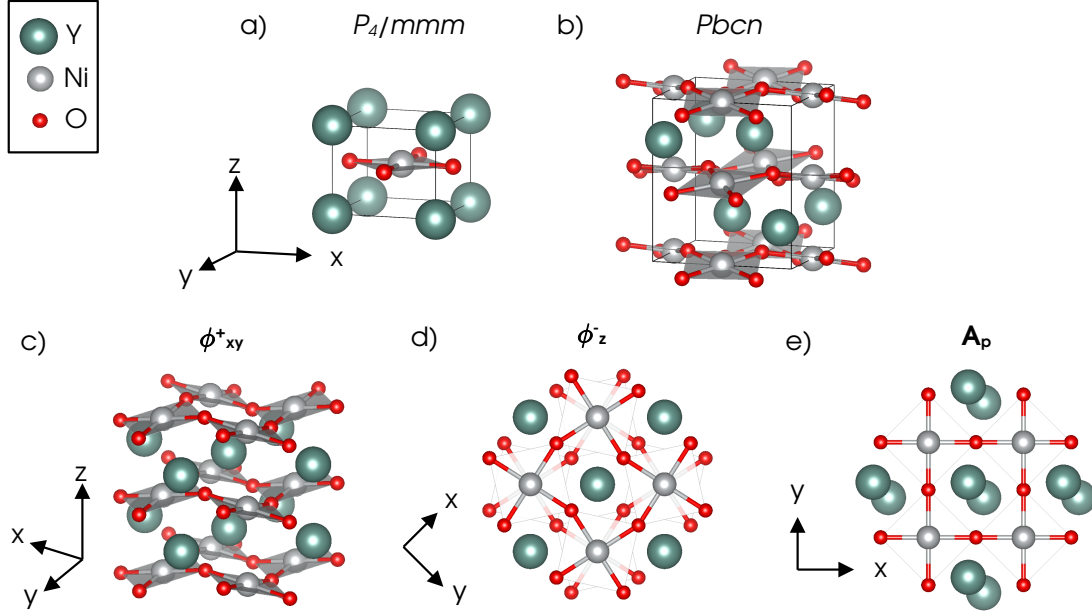


Fig. 4.1 Crystal structure of YNiO₂ for a) undistorted *P₄/mmm* symmetry, b) ground state geometry with *Pbcn* symmetry, c) out of plane in-phase rotations ϕ_{xy}^+ , d) in-plane anti-phase rotations ϕ_z^- , and e) antipolar motion of the A site cation A_p .

we perform the symmetry mode analysis, with the help of the software AMPLIMODES of the Bilbao Crystallographic Server [154, 155]. This allows us to identify three main lattice distortions: (i) out-of-plane in-phase rotations of the NiO₄ squares ϕ_{xy}^+ depicted in Figure.4.1.c with a mode amplitude of $Q_{\phi_{xy}^+} = 0.461 \text{ \AA/f.u.}$, (ii) in-plane anti-phase rotations of the NiO₄ squares depicted in Figure.4.1.d with a mode amplitude of $Q_{\phi_z^-} = 0.610 \text{ \AA/f.u.}$, and (iii) an antipolar motion of the Y cations A_p depicted in Figure.4.1.e with a mode amplitude of $Q_{A_p} = 0.442 \text{ \AA/f.u.}$

We try to understand the origin of these lattice distortions by calculating the potential energy surface associated with each of the modes. Results are depicted in Figure.4.2, finding that among the three of them, only the anti-phase rotations ϕ_z^- is dynamically unstable in the high symmetry undistorted cell, with a double well potential of the form

$$\Delta E[Q_{\phi_z^-}] = \alpha Q_{\phi_z^-}^2 + \beta Q_{\phi_z^-}^4 \quad (4.1)$$

where $\alpha < 0$ and $\beta > 0$ are constants, $Q_{\phi_z^-}$ is the amplitude of the distortion and ΔE is the energy difference with respect to the undistorted P_4/mmm cell. However, the two other lattice

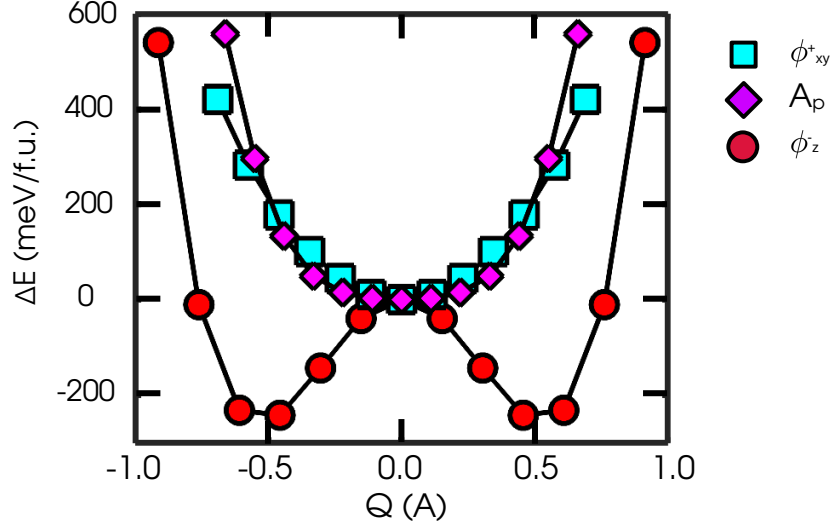


Fig. 4.2 Total energy difference starting from the undistorted P_4/mmm cell in meV/f.u. as a function of the normalized mode amplitude Q in \AA , for the anti-phase rotations ϕ_z^- (red circles), the in-phase rotations ϕ_{xy}^+ (cyan squares) and the antipolar motion A_p (magenta diamonds) in YNiO_2 .

distortions appearing in the ground state $Pbcn$ structure ϕ_{xy}^+ and A_p are dynamically stable presenting a single well potential, which means that they are not willing to spontaneously appear in the material. Nonetheless, their presence in the ground state structure may originate from couplings between two or more lattice distortions, as it is common in ABO_3 perovskite compounds [13].

In order to analyze and explore these couplings, we use the Landau Theory of phase transitions and expand the free energy in terms of the amplitude of the three lattice distortions. The most general expansion in terms of the mode amplitudes $Q_{\phi_z^-}$, $Q_{\phi_{xy}^+}$ and Q_{A_p} can be expressed as

$$\begin{aligned} \mathcal{F}[Q_{\phi_z^-}, Q_{\phi_{xy}^+}, Q_{A_p}] = & \mathcal{F}_0 + \alpha_1 Q_{\phi_z^-}^2 + \beta_1 Q_{\phi_z^-}^4 + \alpha_2 Q_{\phi_{xy}^+}^2 + \beta_2 Q_{\phi_{xy}^+}^4 + \alpha_3 Q_{A_p}^2 + \beta_3 Q_{A_p}^4 + \\ & + \zeta Q_{A_p} Q_{\phi_{xy}^+} Q_{\phi_z^-} + \delta_1 Q_{\phi_z^-}^2 Q_{\phi_{xy}^+}^2 + \delta_2 Q_{\phi_{xy}^+}^2 Q_{A_p}^2 + \delta_3 Q_{A_p}^2 Q_{\phi_z^-}^2 + \dots \end{aligned} \quad (4.2)$$

We notice that several terms in the expansion depend on two or more lattice distortions. Then, the appearance of the ϕ_{xy}^+ and A_p modes in the relaxed ground state of YNiO_2 could be a consequence of lattice mode couplings between the ϕ_z^- and these two modes, resulting in a net energy gain when they develop a non-zero amplitude. The first term in the free energy expansion that couples two of the given lattice distortions, is a biquadratic term that would renormalize the potential energy surface of one of the modes as follows:

$$\mathcal{F}[Q_{\phi_z^-}, Q_{\phi_{xy}^+}, Q_{A_p} = 0] \simeq \mathcal{F}'_0 + [\alpha_2 + \delta_1 Q_{\phi_z^-}^2] Q_{\phi_{xy}^+}^2 + \beta_2 Q_{\phi_{xy}^+}^4 = \mathcal{F}'_0 + \alpha'_{eff} Q_{\phi_{xy}^+}^2 + \beta_2 Q_{\phi_{xy}^+}^4 \quad (4.3)$$

It follows that if $\alpha'_{eff} < 0$ then the energy would be lowered for a non-zero amplitude of the ϕ_{xy}^+ mode obtaining a double well as in the case of the anti-phase rotations. This mechanism is also possible in the case of the antipolar motion A_p , where the free energy in such case can be evaluated as

$$\mathcal{F}[Q_{\phi_z^-}, Q_{\phi_{xy}^+} = 0, Q_{A_p}] \simeq \mathcal{F}''_0 + [\alpha_3 + \delta_3 Q_{\phi_z^-}^2] Q_{A_p}^2 + \beta_3 Q_{A_p}^4 = \mathcal{F}''_0 + \alpha''_{eff} Q_{A_p}^2 + \beta_3 Q_{A_p}^4 \quad (4.4)$$

To verify this mechanism, we calculate the potential energy surface (PES) of each of the modes but with a fixed amplitude of the anti-phase rotation $Q_{\phi_z^-}$. The curves are plotted in Figures 4.3.a and 4.3.b. Upon increasing the amplitude of the anti-phase rotations, both potentials

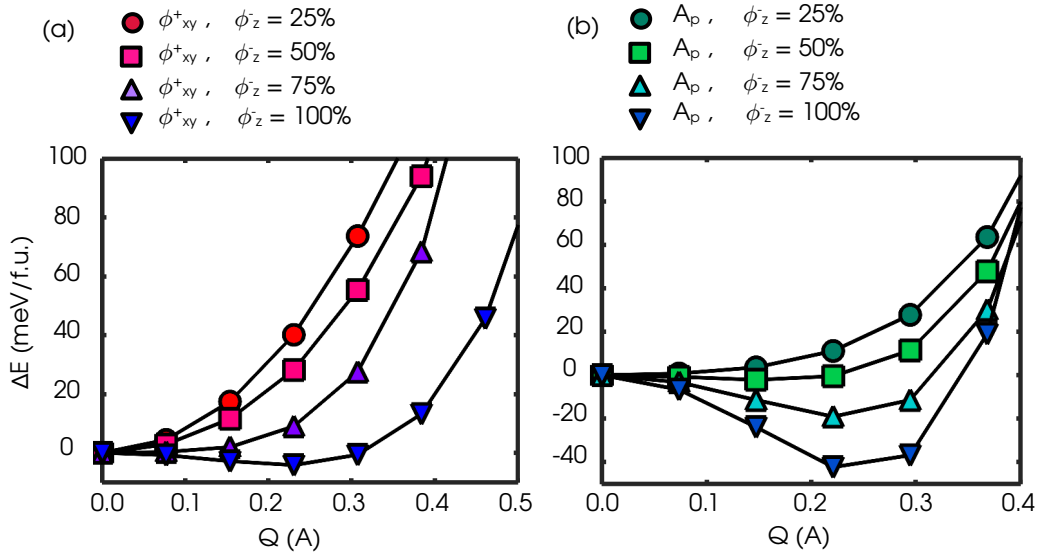


Fig. 4.3 Potential energy surface of (a) the ϕ_{xy}^+ mode in the presence of a fraction of the ground state amplitude of the ϕ_z^- mode, and (b) A_p mode in presence of a fraction of the ground state amplitude of the ϕ_z^- mode.

become softer until they develop a double well potential shape. This produces an energy gain of $\Delta\mathcal{F}[Q_{\phi_z^-}, Q_{\phi_{xy}^+}, Q_{A_p} = 0] = -4$ meV/f.u. and $\Delta\mathcal{F}[Q_{\phi_z^-}, Q_{\phi_{xy}^+} = 0, Q_{A_p}] = -42$ meV/f.u. at a non-zero amplitude of the ϕ_{xy}^+ or A_p modes, respectively, signaling their possible appearance in the material. However, we can notice that the energy gain is achieved at an amplitude of $Q_{\phi_{xy}^+} = 0.231$ Å/f.u. and $Q_{A_p} = 0.221$ Å/f.u. which is around 50% of the ground state amplitude. This means that there could be other couplings favoring the stabilization of these two modes. Other possibilities could be that the ϕ_{xy}^+ mode and the A_p mode are also coupled and produce an energy gain once both are present regardless of the ϕ_z^- mode, where the free energy would be

$$\mathcal{F}[Q_{A_p}, Q_{\phi_{xy}^+}] \simeq \mathcal{F}'''_0 + [\alpha_2 + \delta_2 Q_{A_p}^2] Q_{\phi_{xy}^+}^2 + \beta_2 Q_{\phi_{xy}^+}^4 = \mathcal{F}'''_0 + \alpha'''_{eff} Q_{\phi_{xy}^+}^2 + \beta_2 Q_{\phi_{xy}^+}^4 \quad (4.5)$$

However, as it is depicted in Figure 4.4.a, the PES becomes stiffer upon increasing the amplitude of the A_p mode. This means that $\alpha'''_{eff} > 0$ and its value becomes larger when the amplitude of the A_p mode increases, suggesting that both ϕ_{xy}^+ and A_p modes are competing since they appear in the ground state structure. In addition, we notice that the biquadratic couplings with

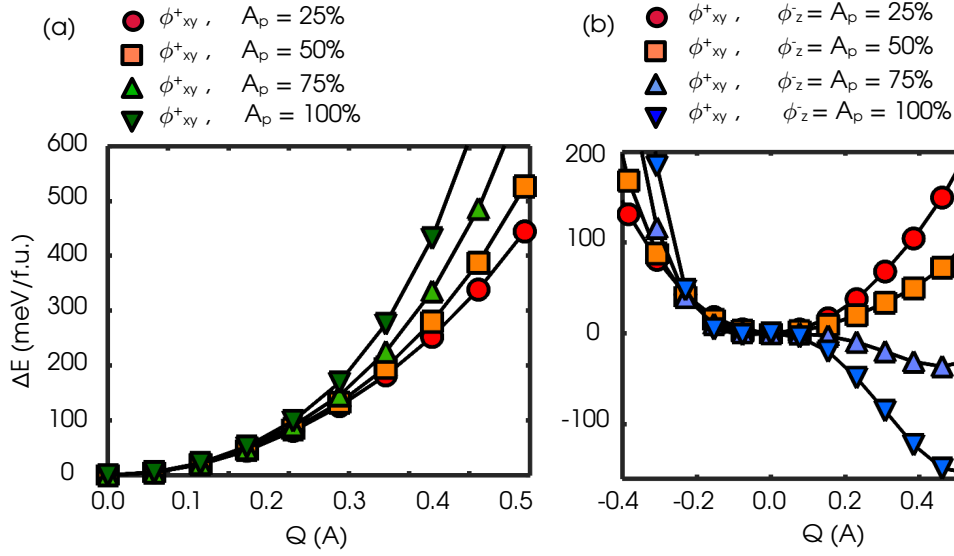


Fig. 4.4 Potential energy surface of the ϕ_{xy}^+ mode in the presence of (a) a fraction of the ground state amplitude of the ϕ_z^- mode, and (b) a fraction of the ground state amplitude of both A_p and ϕ_z^- modes.

the ϕ_z^- mode produce at best a joint energy gain of $\Delta\mathcal{F} = -46$ meV/f.u. at mode amplitudes close to 0.22 Å/f.u. as it is depicted in Figure 4.3. However, the biquadratic coupling between the ϕ_{xy}^+ and the A_p modes, produces an energy penalty of at least $\Delta\mathcal{F} = 100$ meV/f.u. at mode amplitudes of 0.22 Å/f.u. Thus the biquadratic couplings not only are unable to explain the appearance of the ϕ_{xy}^+/A_p modes at the same time but actually lead to a net energy penalty of at least $\Delta\mathcal{F} = 50$ meV/f.u. In that regard, the other allowed term by symmetry in the Free energy expansion, is a trilinear term that couples the three modes together at the same time

$$\begin{aligned} \mathcal{F}[Q_{\phi_z^-}, Q_{\phi_{xy}^+}, Q_{A_p}] &\simeq \mathcal{F}_0 + \zeta Q_{A_p} Q_{\phi_z^-} Q_{\phi_{xy}^+} + [\alpha_2 + \delta_1 Q_{\phi_z^-}^2 + \delta_2 Q_{A_p}^2] Q_{\phi_{xy}^+}^2 + \beta_2 Q_{\phi_{xy}^+}^4 \\ &= \mathcal{F}_0 + \zeta_{eff} Q_{\phi_{xy}^+} + \alpha_{eff} Q_{\phi_{xy}^+}^2 + \beta_2 Q_{\phi_{xy}^+}^4 \end{aligned} \quad (4.6)$$

In this case, if $\zeta_{eff} \neq 0$, we would have a PES that is not symmetric under a sign change of the $Q_{\phi_{xy}^+}$ mode and the sign of the coefficient would determine if the largest energy gain is with a positive or negative amplitude. We then proceed to calculate the potential energy surface of the ϕ_{xy}^+ mode but this time we fix some amplitude of the ϕ_z^- and A_p modes at the same time. The results are depicted in Figure 4.4.b. We clearly see that upon increasing the amplitude of the ϕ_z^- and A_p modes, there is a progressive softening of the ϕ_{xy}^+ potential well until it becomes a double well potential when both modes are sufficiently large. However, we observe that the PES is not symmetric meaning that the sign (direction) of the ϕ_{xy}^+ mode is pinned by that of the A_p and ϕ_z^- modes. We can note however, that the $Q_{\phi_{xy}^+}$ amplitude at the global minimum is slightly bigger than the ground state amplitude of $Q_{\phi_{xy}^+} = 0.461$ Å. The origin of this discrepancy is the fact that we have not taken into account the strain since we have kept a tetragonal symmetry, while the ground state is orthorhombic. In any case, it becomes evident that the existence of this triple coupling is crucial to the stabilization of the ϕ_{xy}^+ and A_p lattice distortions that alone are not dynamically unstable like the ϕ_z^- anti-phase rotations in YNiO_2 . Thus the lattice

mode couplings are the main actors in producing a *Pbcn* structure with three different lattice distortions.

4.1.2 Role of the size of the A-site cation

Once we have understood how the different lattice distortions appear in one of the earliest members of the nickelate series (YNiO₂), we repeat the analysis for other nickelate members in the RNiO₂ series. In that regard, we present in Table.4.1, the different crystal structure information depending on the A site cation (with A = Y, Gd, Nd, Pr, and La).

Compound	Crystallographic System	Space group	R _{ion} /Å	Q _{φ_z⁻/Å}	Q _{φ_{xy}⁺/Å}	Q _{A_p} /Å
YNiO ₂	Orthorhombic	<i>Pbcn</i>	1.015	0.610	0.461	0.442
GdNiO ₂	Tetragonal	<i>I</i> ₄ / <i>mcm</i>	1.060	0.200	0	0
NdNiO ₂	Tetragonal	<i>P</i> ₄ / <i>mmm</i>	1.140	0	0	0
PrNiO ₂	Tetragonal	<i>P</i> ₄ / <i>mmm</i>	1.120	0	0	0
LaNiO ₂	Tetragonal	<i>P</i> ₄ / <i>mmm</i>	1.180	0	0	0

Table 4.1 Summary of important quantities extracted from first-principles calculations and a symmetry mode analysis on selected infinitely layered nickelates. Ionic radius is taken from Ref. [200] for an eight-coordinated complex.

We observe that the members with the smaller cation like YNiO₂ present three lattice distortions (ϕ_z^- , ϕ_{xy}^+ and A_p). Then intermediate members like GdNiO₂, are characterized by only the in-plane anti-phase rotations ϕ_z^- with an amplitude of $Q_{\phi_z^-} = 0.2$ Å/f.u. This amplitude is around 33% of the amplitude in YNiO₂, and as we can see in Figure 4.4.b, GdNiO₂ would be in between the red and orange curves, and although the trilinear coupling is present, is not able to produce a net energy gain as in the case of YNiO₂. This signals that since the A site cation is bigger, the structure presents smaller in-plane anti-phase rotations leaving a structure with only this type of lattice distortion and an *I*₄/*mcm* symmetry instead. Finally, the end members like LaNiO₂ or NdNiO₂ present a perfectly undistorted crystal structure with *P*₄/*mmm* symmetry with no sign of rotations or any other lattice distortions. This further confirms our claim that the size of the A-site cation reduces the amplitude of the ϕ_z^- mode until it disappears, resulting in all the undoped phases of the SC compounds presenting a layered structure without any rotations or lattice distortions.

Some authors however report that the NdNiO₂ ground state should present an *I*₄/*mcm* symmetry with ϕ_z^- rotations [186]. We double check using the SCAN functional finding that indeed the ϕ_z^- rotation pattern and the *I*₄/*mcm* structure is more stable if (i) the pseudopotential employed in the calculation places the 4*f* electrons as an effective core instead of the valence, which (ii) *de-facto* neglects the spin degree of freedom on Nd sites. In that regard, if we follow the experimental literature, NdNiO₂, PrNiO₂ and LaNiO₂ are all found with *P*₄/*mmm* symmetry [33–37, 75, 96, 201], with no signature of a rotation pattern. Thus the overall behavior across

the series correlates with the radius of the A-site cation, where a bigger radius produces a more symmetric crystal structure, and smaller cations present a less symmetric and hence more distorted crystal. This feature is reminiscent of the behavior with the perovskite parent compounds.

4.1.3 Role of the epitaxial strain

The nickelates that show SC have been obtained so far as thin films that are grown on a substrate. Up to date, these thin films have been deposited successfully on SrTiO₃ (STO) and (LaAlO₃)_{0.3}(Sr₂TaAlO₆)_{0.7} (LSAT) [66, 79], which are cubic perovskite materials at ambient conditions. The fact that these nickelates are grown on a substrate implies that the in-plane lattice parameters will not be those obtained in the bulk material, but rather the substrate in-plane lattice parameters. This would induce tensile or compressive strain on the structure depending on the A site cation, which may affect the stability of the different lattice distortions that are prone to appear. We can illustrate this by calculating the PES associated with the in-plane anti-phase rotations ϕ_z^- of YNiO₂ in two situations: (i) under tensile strain and (ii) under compressive strain. In order to model the strain, we change the lattice parameters $a = b = 3.886$ Å, and $c = 3.221$ Å, of the pseudocubic P_4/mmm ground state structure that we use. We impose the in-plane lattice parameters to $a = b = 3.905$ Å, which are STO lattice parameters to simulate a -0.49% of tensile strain, and we fix them to $a = b = 3.868$ Å, which are LSAT lattice parameters to simulate a 0.46% of compressive strain. Results are reported on Figure 4.5.

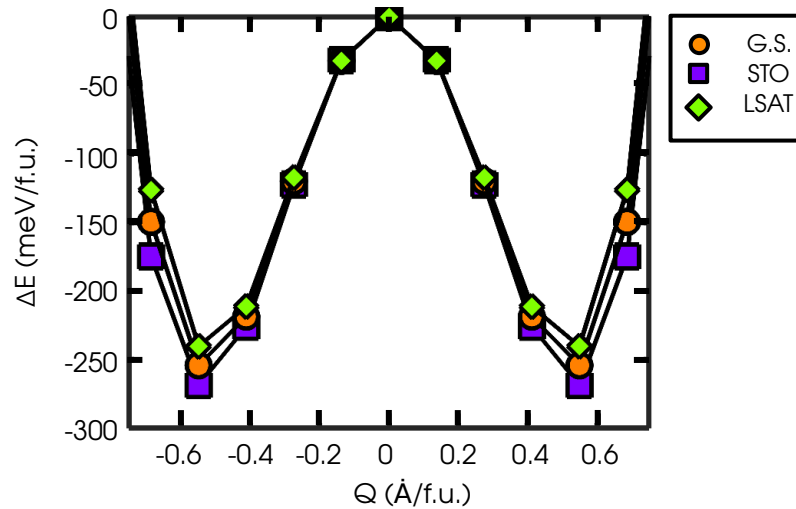


Fig. 4.5 Potential energy surface for the ground state geometry of the ϕ_z^- on YNiO₂ with the ground state geometry (GS), the in-plane lattice parameters of SrTiO₃ (STO), and the in-plane lattice parameters of (LSAT) .

The PES of the ϕ_z^- mode is a double well in both situations with compressive and tensile strain. Nonetheless, comparing the PES in the ground state with the situations under tensile

and compressive strain, we observe that both the energy gain of the ϕ_z^- and the distortion amplitude $Q_{\phi_z^-}$ at the minimum are changed. In particular, we notice that under -0.49% of tensile strain with the STO lattice parameters both the amplitude at the minimum and the energy gain increase when compared to the ground state, while we obtain the opposite situation when the structure is under 0.46% of compressive strain with the LSAT lattice parameters. This is quite revealing since it indicates that the lattice distortions can be tuned by the strain and that depending on the substrate, certain lattice distortions can be favored or disfavoured as it is the case of the ϕ_z^- with tensile or compressive strain, respectively. In particular, we notice that at the amplitude of the ground state minimum, there is an energy gain (penalty) of $\Delta E = -14$ (14) meV/f.u. under -0.49% (0.46%) of tensile (compressive) strain. This would suggest that under a compressive strain of 2% we would induce an energy penalty of $\Delta E = 60$ meV/f.u. which is comparable to the energy gain produced by the trilinear coupling of $\Delta E = -150$ meV/f.u. without strain at the minimum amplitude in YNiO₂ (see Figure 4.4.b). Thus if the amplitude of the ϕ_z^- distortion would be smaller as in the case of RNiO₂ compounds with bigger cations than Y, applying a 2% of strain can disfavor the appearance of the A_p and ϕ_{xy}^+ distortions or even the ϕ_z^- distortion itself. Thus we can confirm the stability of the different phases and lattice distortions can be substantially sensitive to external stimuli such as strain in a similar fashion as in the parent perovskite case [202, 27, 203–207].

4.1.4 Hydrogen intercalation

The synthesis process of these compounds requires growing the parent perovskite phase first on the substrate and then reducing it with a topotactic reduction that in many cases uses CaH₂ as a reducing agent. This would in principle remove the apical oxygen in the octahedron of the perovskite parent phase, leaving a completely layered sample. Nonetheless, this reduction can induce some H intercalation on the sample which may affect the properties of the material. We

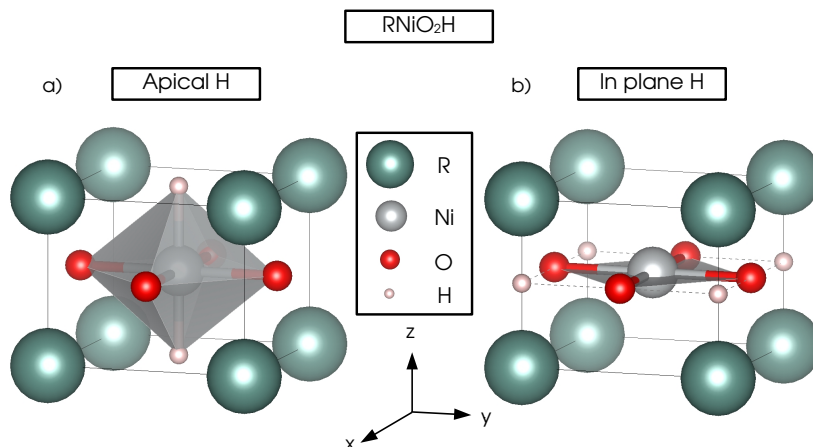


Fig. 4.6 Crystal structure of the two relaxed geometries for the H intercalation in RNiO₂H compounds, with (a) H at the apex of Ni cations, and (b) H in the NiO₂ plane.

investigate this situation by calculating the H binding energy E_B defined in Eq.(4.7)

$$E_B = E(\text{RNiO}_2\text{H}) - E(\text{RNiO}_2) - \frac{1}{2}E(\text{H}_2) \quad (4.7)$$

where $E(\text{RNiO}_2\text{H})$, $E(\text{RNiO}_2)$ and $E(\text{H}_2)$, are the total energies of RNiO_2H (the hydrogen rich limit), RNiO_2 and H_2 respectively. We take as a reference the perfectly symmetric phase with P_4/mmm symmetry for the pristine material. Concerning the location of the H in the material, we compute the energy for two different cases of YNiO_2H , one with H intercalated at the apical site and in the other case the H sits on top of the rare earth in the NiO_2 plane (see Figure 4.6). We find that the most stable configuration is with the H at the apex with an energy difference of $\Delta E = 2.3$ eV/f.u. between the two configurations. This has been explored by several authors arriving at the same conclusion [188, 208–210]. Now regarding the binding energy, the existing literature suggests that H intercalation is energetically favorable, where some authors claim that only LaNiO_2 is willing to capture H cations in the structure [188], while others have shown that NdNiO_2 would also favor H intercalation [209, 208]. In that regard, we explore the phase diagram and we report in Figure.4.7 the binding energy as a function of the rare earth.

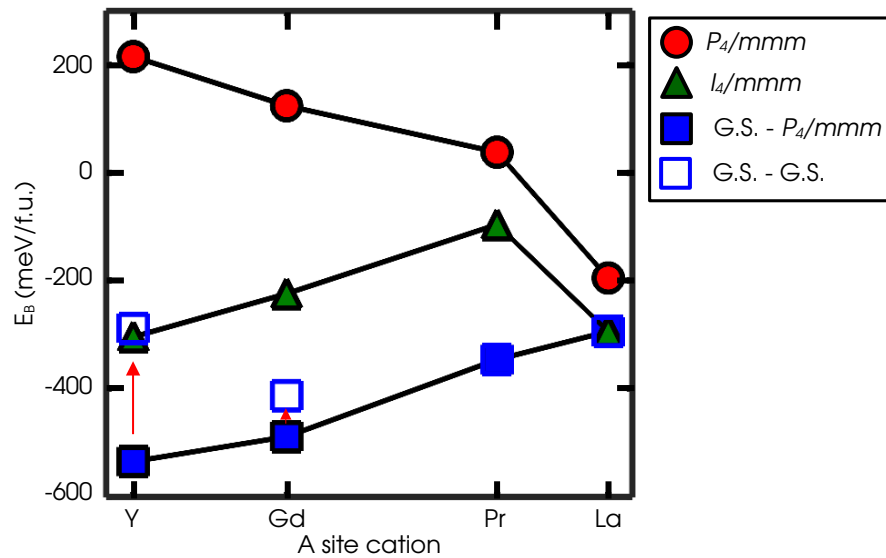


Fig. 4.7 Binding energy in (meV/f.u.) for hydrogen intercalation in different two-dimensional (2D) nickelates. The reference energy is set to pristine materials with a P_4/mmm space group. The RNiO_2H compound is taken to have P_4/mmm symmetry (red circles), I_4/mcm symmetry (green triangles) and global ground state geometry (blue squares), corresponding to I_4/mcm for La, and Pr, $Pbcn$ for GdNiO_2 , and $Pbnm$ for YNiO_2 . Arrows correspond to the binding energy for the hydrogenated ground state with respect to the pristine material ground state structure (blue open squares) P_4/mmm for LaNiO_2 and PrNiO_2 , I_4/mcm for GdNiO_2 and $Pbcn$ for YNiO_2 .

We obtain that the only compound with a negative binding energy is with La, but only if the H-rich compound possesses a P_4/mmm symmetry (see red dots in Figure.4.7). However, if the symmetry of the compound is allowed to be lowered during the relaxation of the H-rich material, the binding energy is negative for all compounds. In fact the H-rich compounds, are prone to

develop some lattice distortions like in-plane and out-of-plane rotations. This result remains valid even if we use the real ground state of the different pristine materials ($Pbcn$ in the case of YNiO₂ or I_4mcm in the case of GdNiO₂), suggesting that H intercalation is in fact favorable in all RNiO₂ compounds. Nonetheless, this also suggests that it can be possible to avoid H intercalation in the material when it is grown on a substrate, since as we saw in the previous section, the strain from the substrate disfavors the appearance of any rotation pattern. This would force the system to keep a P_4/mmm symmetry where the H intercalation is disfavored for almost all members of the RNiO₂ compounds. This could be a possible explanation, for why the SC samples, are only found on thin films instead of bulk when a reducing agent with H such as CaH₂ or NaH is used. In the bulk, the system would not be under strain, allowing rotations and other lattice distortions to appear in the compound, and H intercalation would be favorable. Thus future experiments on bulk may consider to use other reducing agents in order to obtain bulk SC samples.

4.2 Magnetic properties

As we mentioned, these layered nickelates were proposed to be a possible analog to Cu-based high T_c superconductors [16], where in the latter compounds, it is proposed that the magnetic interactions play an important role in the pairing mechanism. In that regard, it becomes mandatory to explore the magnetic properties of these compounds. This IL phase presents a Ni⁺ cation which is an unusual formal oxidation state (FOS) for Ni since most of the chemical compounds present a 2+, 3+, or 4+ FOS instead. This FOS produces a $3d^9$ open shell configuration, resulting in a finite magnetic moment at Ni sites [100]. Some authors report a lack of long-range magnetic order [101], although several experimental studies with different techniques that probe the excitation spectra point to nontrivial antiferromagnetism [91, 92, 96, 97]. From the theoretical point of view, several studies point as well to an antiferromagnetic phase at low temperatures [93–95, 124, 186], and other authors suggest a $3d^8\bar{L}$ on Ni cations where \bar{L} is a ligand hole with a possible mixed $S = 1$ and $S = 0$ state [211, 212].

4.2.1 Intrinsic magnetism

As we have discuss, the intrinsic magnetism and the spin state of Ni cations is not completely well established since some authors claim a possible ligand hole picture on Ni sites similarly to the cuprate case. In that regard, we have probed the stability of the system to develop a finite magnetic moment on YNiO₂ and LaNiO₂, by relaxing the structure structure with the ground state geometry previously identified (this is $Pbcn$ and P_4/mmm for YNiO₂ and LaNiO₂, respectively), with two types of calculations, (i) using the non-spin-polarized (NM) solution, and (ii) the paramagnetic (PM) solution. In the literature, in many cases, the NM solution is taken to be a representation of the paramagnetic state since the total magnetization M is zero. However, strictly speaking, the NM approximation implies that $\mu_i = 0 \forall i$, where μ_i is the magnetic moment of the ion i , whereas a paramagnetic compound has to fulfill only the

following condition

$$M = \sum_i^N \mu_i = 0 \quad (4.8)$$

for N magnetic ions. In fact, in the case where all magnetic moments are zero, the compound would be commonly known as diamagnets. As a result, we will not make use of such equivalence and we will use a different representation of the paramagnetic state where we randomize the spins in a supercell (we use 32 f.u.) using the special quasirandom structure method (SQS) for alloys [150] as implemented in the ATAT package for a finite supercell size [149]. We however enforce the condition that the total magnetization is zero. We report in Table 4.2 the results of the calculations.

Compound	$\Delta E_{\text{NM-PM}}$ (meV/f.u.)	μ_{Ni} (μ_{B})
YNiO ₂	495	0.962
LaNiO ₂	365	0.954

Table 4.2 Calculated total energy difference between the NM and the random PM solution $\Delta E_{\text{NM-PM}}$ in meV/f.u., and average magnetic moment μ_{Ni} on Ni cations extracted from the PM phase in μ_{B} , for both YNiO₂ and LaNiO₂ compounds.

From our calculations, we obtain on the PM solution, an average magnetic moment on Ni sites of $\mu_{\text{Ni}} = 0.965 \mu_{\text{B}}$ and $\mu_{\text{Ni}} = 0.954 \mu_{\text{B}}$ for YNiO₂ and LaNiO₂ respectively (see Table 4.2). These values are consistent with a Ni⁺ cation with a $3d^9$ configuration in contrast with the $3d^8\bar{L}$ configuration that is proposed by some authors [211, 212]. However the most remarkable feature of our calculations is to obtain an important energy gain between the Non-spin-polarized solution NM, and the paramagnetic PM solution of $\Delta E_{\text{NM-PM}} = 495$ meV/f.u. and $\Delta E_{\text{NM-PM}} = 365$ meV/f.u. for YNiO₂ and LaNiO₂, respectively. This establishes that the magnetism in these compounds is intrinsic and should not be overlooked. These concerns are also raised in other theoretical works [93], and evidenced experimentally in Ref. [100] where the intrinsic magnetism of Ni is revealed.

4.2.2 Magnetic ground state

Focusing now on the spin-polarized solutions, we explore the magnetic ground state by relaxing the structure of the two previous compounds, using several long-range magnetic orders at the collinear level that include, ferromagnetic (FM), ferromagnetic planes antiferromagnetically coupled (type-A AFM or AFMA), in-plane antiferromagnetism with AFM interactions on nearest neighbors (type-C AFM or AFMC), full antiferromagnetism with AFM interactions on the three axes (type-G AFM or AFMG). We report on Table.4.3 the total energy difference in meV/f.u. taking as a reference the FM case.

As one can see, the PM solution is 30 meV/f.u. higher in energy than the C-type antiferromagnetic (AFMC) order which in the colinear approximation to magnetism is very likely to be

	YNiO ₂	LaNiO ₂
Mag. order	ΔE (meV/f.u.)	
FM	0	0
PM	-27	-26
AFMA	5	-3
AFMC	-47	-73
AFMG	-45	-51

Table 4.3 Calculated total energy difference ΔE (meV/f.u.) of the different magnetic ground states with respect to the FM order in YNiO₂ and LaNiO₂.

the ground state configuration according to several theoretical and experimental studies [93, 94]. Thus in what concerns to the magnetic ground state of the undoped compounds, our results point to in-plane antiferromagnetism which would be similar to the Cu-based superconductors.

We can further explore the magnetism in these nickelates by employing an effective model of magnetism such as the Heisenberg model, where we consider two different exchange constants J between nearest-neighbor interactions:

$$\mathcal{H} = J_{ab}^{\text{Ni}} \sum_{\langle i,j \rangle} S_i S_j + J_c^{\text{Ni}} \sum_{\langle i,j \rangle} S_i S_j \quad (4.9)$$

where J_{ab}^{Ni} (J_c^{Ni}) are the in-plane (out of plane) exchange couplings between nickel sites (see Figure.4.8) with $J > 0$ ($J < 0$) favoring antiferromagnetic (ferromagnetic) interactions between the cation sites.

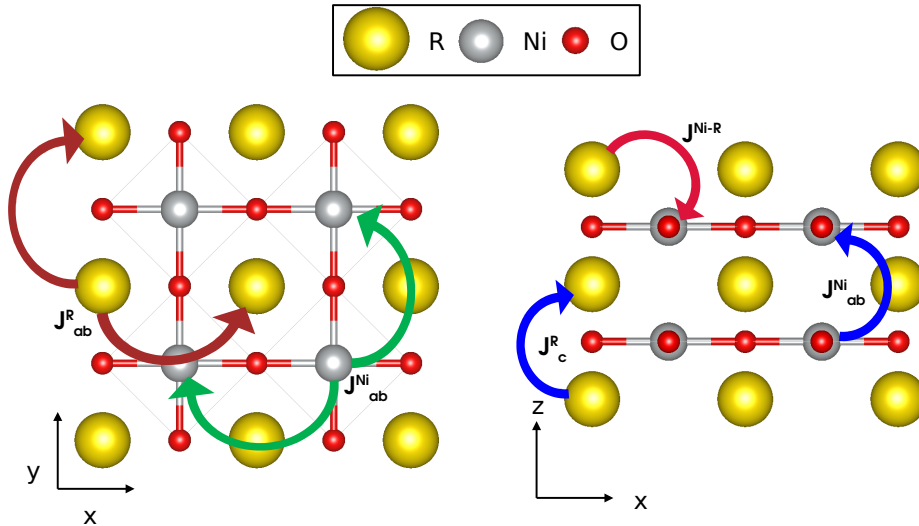


Fig. 4.8 Sketch of the exchange coupling constants considered in a generic RNiO₂ compound.

We calculate the energy of the system for different spin configurations at a fixed crystal structure to avoid magnetostriction effects. We then map the energy difference into our effective model, allowing us to obtain the two exchange constants. We calculate the exchange constants

for YNiO₂, GdNiO₂, and LaNiO₂ and results are reported in Table 4.4.

We find nearly constant values for the exchange couplings across the series, predicting strong

Compound	J_{ab}^{Ni} (meV)	J_c^{Ni} (meV)	J_{ab}^{R} (meV)	J_c^{R} (meV)	$J^{\text{Ni-R}}$ (meV)
YNiO ₂	58	-20	-	-	-
GdNiO ₂	63	-25	0.04	-0.03	0.7
Theo. SmNiO ₂ [186]	82	-6	-	-	-
exp. PrNiO ₂ /SrTiO ₃ [92]	67	-	-	-	-
exp. PrNiO ₂ /LSAT[92]	64	-	-	-	-
Theo. NdNiO ₂ [93]	118	-4	-	-	-
Theo. NdNiO ₂ [124]	77	-3	-	-	-
Theo. NdNiO ₂ [186]	87	-6	-	-	-
exp. NdNiO ₂ /SrTiO ₃ [91]	64	-	-	-	-
LaNiO ₂	66	-19	-	-	-
Theo. LaNiO ₂ [93]	52	-24	-	-	-
Theo. LaNiO ₂ [94]	58	-	-	-	-
Theo. LaNiO ₂ [186]	86	-	-	-	-

Table 4.4 Summary of the exchange constants obtained for different RNiO₂ compounds expressed in meV from our calculations and other theoretical works. Experimental values available for different films are also reported. Positive values for the exchange constants $J > 0$ favor antiferromagnetic interactions, while negative values $J < 0$ favor ferromagnetic interactions.

in-plane antiferromagnetic exchange with an average value for all compounds of $J_{ab}^{\text{Ni}} = 62$ meV. This value is in good quantitative agreement with several experimental studies obtaining a value of $J_{ab}^{\text{Ni}} = 67 - 64$ meV depending on the composition [92, 91] as well as other theoretical studies [93, 94, 124, 186]. We also predict a weaker ferromagnetic exchange with an average value of $J_c^{\text{Ni}} = -21$ meV agreeing with other theoretical values computed with the SCAN functional on LaNiO₂ [93], although they are quantitatively bigger than in Refs. [94, 124, 186]. This discrepancy may come from the exact choice of exchange and correlation functional, since we employ a meta-GGA and in Refs. [94, 124, 186] a GGA+U method is chosen to describe the exchange and correlation phenomena. Additionally, some reports have already shown an overestimation of the magnetization in metallic Fe when using SCAN [213]. Thus experimental studies are needed to assess which of the two methods is more reliable for this particular quantity. Nonetheless, these discrepancies are not dramatic since the technique is able to give a good qualitative picture of the magnetism of these compounds.

In addition to the magnetic interactions produced by nickel sites, we can consider a secondary source of magnetism originating from rare earth cations $\text{R}^{3+} 4f^n$ open shells. We proceed in a similar manner as with the nickel sites but including one extra interaction between nickel sites and the rare-earth as it is shown in the Hamiltonian of Eq.(4.10), where $J_{ab}^{\text{R}}(J_c^{\text{R}})$ are the in-plane (out of plane) exchange couplings between the rare-earth sites and $J^{\text{Ni-R}}$ is the exchange coupling between the rare-earth cation and nickel.

$$\mathcal{H} = J_{ab}^{\text{R}} \sum_{\langle i,j \rangle} S_i S_j + J_c^{\text{R}} \sum_{\langle i,j \rangle} S_i S_j + J^{\text{Ni-R}} \sum_{\langle i,j \rangle} S_i S_j \quad (4.10)$$

We consider the case of GdNiO₂ which has a $4f^7$ half-filled configuration from which we expect to have a good estimate of the rare-earth contribution to magnetic interactions. However as we can see in Table.4.4, the exchange constants on the rare earth cations are actually rather small, where the biggest exchange is between rare-earth and nickel cations although is two orders of magnitude less than the Ni-Ni exchange constants. Thus we can assume that the magnetic ordering of the rare-earth will be imposed by the nickel local environment and very likely the $4f$ states do not play any important role in the superconducting mechanism since (i) the $4f$ states do not contribute to the conduction as we can see from the band structures in chapter 3 for PrNiO₂ and LaNiO₂ (see Figure 3.4), (ii) experiments show highly localized $4f$ states that are completely unaffected by the Sr doping [89], and (iii) the exchange couplings on the rare-earth cation are in the best case scenario an order of magnitude smaller than in between Ni sites.

Finally, as a concluding remark, we have explored the magnetism on the H-rich compounds finding a different magnetic ground state, in this case, the Ni cations present an antiferromagnetic coupling along the three cartesian axes (type-G AFM) with a high spin configuration $S = 1$ on the Ni cations, suggesting that the H acts as an anion H^- and produces a Ni^{2+} cation.

4.3 Electronic Structure

We conclude this chapter by exploring the electronic structure of these nickelates, and how it is coupled with the structural and magnetic degrees of freedom. We take mainly LaNiO₂ as a model system

4.3.1 Role of local spin formation

Before exploring how different long-range magnetic orders can affect the band dispersion, we explore the importance of including the spin degree of freedom when calculating the electronic structure of these nickelates. We have mentioned however that experimentally these nickelates present no long-range magnetic order [33, 37]. In that regard, we calculate the band structure in the paramagnetic case. Band structures are unfolded to the primitive high symmetry P_4/mmm cell, in order to facilitate the comparison of the results between different magnetic orders and supercell sizes. We use the VaspBandUnfold software to unfold and plot the band structures [214].

As we mentioned in chapter 2 and earlier in this chapter, it is quite common to find in the literature that the PM phase in DFT is modeled with the NM approximation instead of the random spin arrangement that we use. In order to reveal the importance of treating spins, we have calculated the band structure of the NM and the random spin PM solution. The band dispersions are reported in Figure 4.9. As one can appreciate by comparing Figure 4.9.a with Figure 4.9.b, the NM and PM solutions yield qualitatively different results. While in the PM case, there are small electron pockets at Γ , a big electron pocket centered at the A point and vanishingly small hole pockets at M point (see Figure 4.9.b), the NM solution in Figure 4.9.a, presents in addition to these features another highly dispersive band centered at Γ with a clear

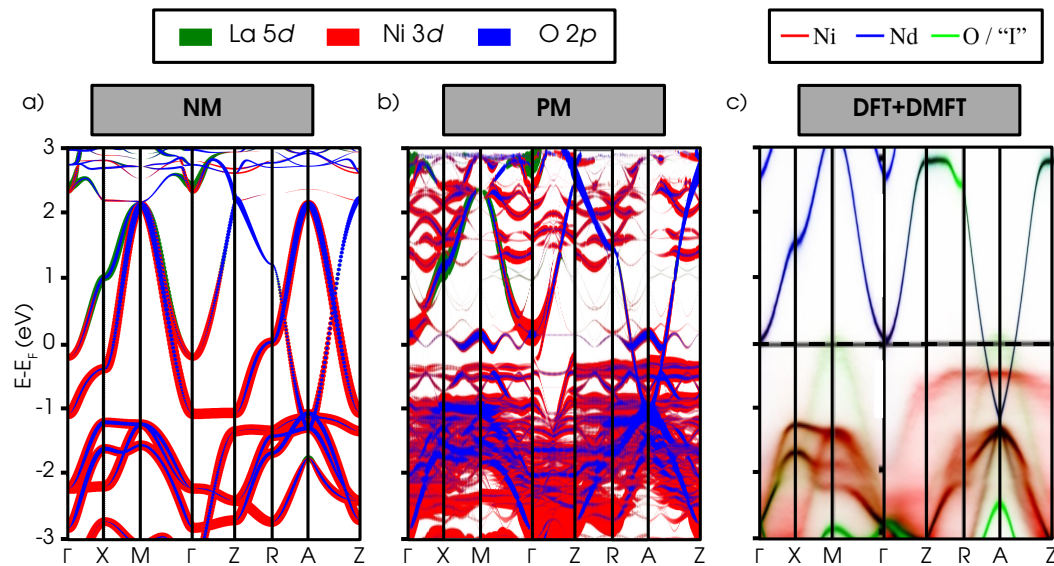


Fig. 4.9 Electronic band structure of (a) DFT in the NM approximation for LaNiO_2 , (b) DFT in the random spin PM magnetic solution for LaNiO_2 , and (c) DFT+DMFT self-consistent PM solution adapted from [215] for NdNiO_2 . For panels (a) and (b) the bands include projections on O $2p$ states (in blue), Ni $3d$ states (in red) and La $5d$ states (in green). For panel (c) the bands present projections on Ni (red) Nd (blue) and O with an interstitial orbital (green). High symmetry points of the first Brillouin Zone are Γ (0,0,0), X (0,0,0), M (1/2,1/2,0), Z (0,0,1/2), R (1/2,0,1/2) and A (1/2,1/2,1/2).

2D nature corresponding to the $d_{x^2-y^2}$ orbital as discussed by other authors [216–223]. This would suggest that the $d_{x^2-y^2}$ band would be highly relevant to the conduction as in the cuprate case. Thus it is tempting to think that perhaps in terms of the electronic structure, the NM approximation is a better approximation than the random PM since the $d_{x^2-y^2}$ band is in the best case centered at the M point as small hole pocket (see Figure 4.9.b). This is nonetheless a bold assumption that can be easily discarded by comparing the random PM dispersion with other methods that treat correlation effects better than DFT such as Density Functional Theory plus Dynamic Mean Field Theory (DFT+DMFT) as depicted in Figure 4.9.c [224, 225, 215]. In fact, it is remarkable that the random PM with DFT reproduces rather accurately the results derived by DFT+DMFT showing a small electron pocket at Γ , an important electron pocket at the A point, and a vanishingly small hole pocket at M point. We can notice that the random PM yields a much blurred dispersion when compared to the DFT+DMFT approach, which is caused by the overlap of the different periodic replica.

We must note however that in the DFT+DMFT approach, the bands from DFT are projected on a localized manifold of typically MLWF that are introduced in the DMFT loop. Hence in order to reproduce the band structure accurately, an interstitial orbital centered at the apex position of a Ni cation is introduced. This is a consequence of using a localized basis to describe a metallic system where a more delocalized electronic structure is expected. Nonetheless, we should not forget that the physical observable is the spectra or the band dispersion, and not the basis that is used to represent it. In that regard, besides the possible basis or orbital

decomposition, which we will discuss later, the band topology should remain the same.

Thus our random PM approach is further validated over the NM, since it is able to produce a band topology much closer to DMFT or DFT+DMFT methods, which are expected to produce better results than DFT, due to better treatment of correlations. These results, in turn, highlight the importance of including the spin degree of freedom even if a PM compound is modeled, since the basic Hund's rule would not be respected and all spin-spin correlations would be neglected.

4.3.2 Trends on the electronic structure with magnetism

The electronic band structure is now calculated for the FM, AFMA, AFMC, and AFMG magnetic orders. Results are depicted in Figure 4.10 with spectral weight projections on the bands for La 5*d*, Ni 3*d*, and O 2*p* states.

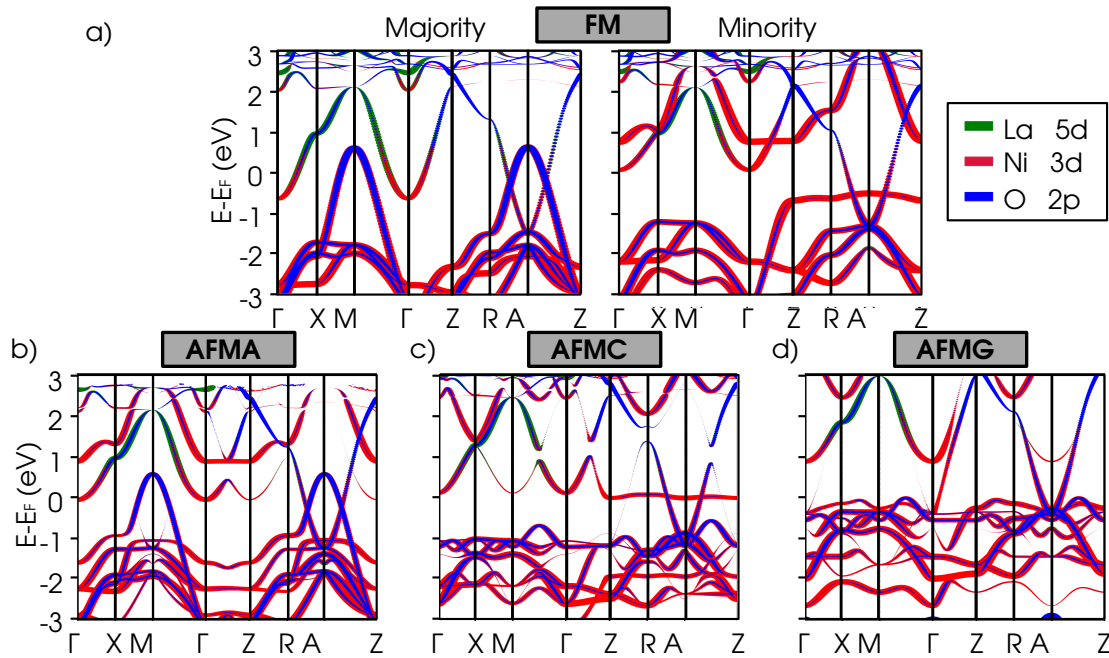


Fig. 4.10 Unfolded band structures for LaNiO₂ in the ground state geometry for (a) FM, (b) type-A AFM, (c) type-C AFM, and (d) type-G AFM. Projected spectral weights are presented for La 5*d* (green), O 2*p* (blue) and Ni 3*d* (red) states. High symmetry points correspond are Γ (0,0,0), X (0,0,0), M (1/2,1/2,0), Z (0,0,1/2), R (1/2,0,1/2) and A (1/2,1/2,1/2).

Comparing the bands of Figure 4.9.b and 4.10, all magnetic orders produce metallic solutions with in general two electron pockets centered at the Γ and A points. This is rather surprising since (i) in the cuprate case the undoped compounds are AFM insulators, and (ii) the magnetic ground state of these nickelates would be an AFM metal which is rather uncommon. In addition, LaNiO₂ is mainly in the Mott regime with Ni *d* states dominating the low energy physics around the Fermi level. Concerning the O *p* states, we compute the band center finding it at 4 eV below the Fermi level. These results are in the same line as other theoretical studies on the undoped nickelates [93, 226–230]. From the experimental point of view, several spectroscopic experiments show that the O *p* states are at least 2 eV below the Fermi level, while only Ni

d states are affected by the doping, suggesting a Mott-Hubbard scenario [87–90]. Thus the electronic structure of these nickelates is significantly different when compared with the cuprates since the undoped phase of the Cu-based superconductors is in the CT regime and they are insulators.

We focus now on specific magnetic orders that we discuss one by one. The FM case presents two different panels: (i) the majority spin on the left, and (ii) the minority spin on the right. The PM and all AFM orders present only one panel since the bands are an average over all Ni cations and both spin channels would present the same band dispersion. The band structure of the FM order is characterized by two electron pockets centered at Γ and A points on both spin channels consisting of Ni $3d$ with contributions from La $5d$ states. In addition to these electron pockets, in the FM case, the majority spin channel presents two hole pockets centered at the M and A points consisting of Ni $3d$ states highly hybridized with the O $2p$ states that would correspond to the $d_x^2 - y^2$ orbital as in the NM approximation although much less dispersive and with the band center lower in energy. These features are also common to the type-A AFM (AFMA). We however notice that along the $\Gamma - Z$ path, there is a gap opening which can be explained by the antiferromagnetic interactions along the z-axis that characterize the type-A AFM. The band topology is slightly different in the case of the type-C AFM (AFMC) since there are some vanishingly small electron pockets at Γ and the only relevant region in terms of conducting properties is the $Z - A - R - Z$ path. The latter presents an electron pocket at A and a flat band mainly dominated by Ni $3d$ states with non-negligible contributions from La $5d$ states. We also notice two gap openings along the $\Gamma - M$ and $\Gamma - Z$ paths, as a consequence of in-plane nearest neighbors interactions, and possibly out-of-plane second nearest neighbors interactions, respectively. The type-G AFM (AFMG) band dispersion does not present any electron pocket along the $\Gamma - X - M - \Gamma$. The bands have been pushed upwards and only electron pockets are found along the $\Gamma - Z$ path and along the $R - A - Z$ path as for other magnetic orders. In addition, we also find a flat band along the $R - A - Z$ as in the type-C AFM. Thus we can see that except for the FM order that presents two different spin channels and the M point hole pockets of the AFMA, the overall character of the bands on the PM and the AFM orders is rather similar.

4.3.3 Orbital character of the electronic structure

We further inspect the orbital character of the electronic dispersion in these nickelates by projecting the spectral weight on specific orbitals of Ni $3d$ and La $5d$ cations. We consider the AFMC magnetic order to illustrate the overall behavior since (i) all PM and AFM orders present similar features (see Figures 4.9.b and 4.10), and (ii) it is the lowest energy state found in our calculations (see Table 4.3). Results are presented on Figure 4.11.

By inspecting the decomposed band structure, we notice four important features, (1) the $d_{x^2-y^2}$ orbital presents one occupied band 1 eV below the Fermi level that does not contribute to the conduction, and one unoccupied band 2 eV above the Fermi level, (2) the d_{z^2} orbital

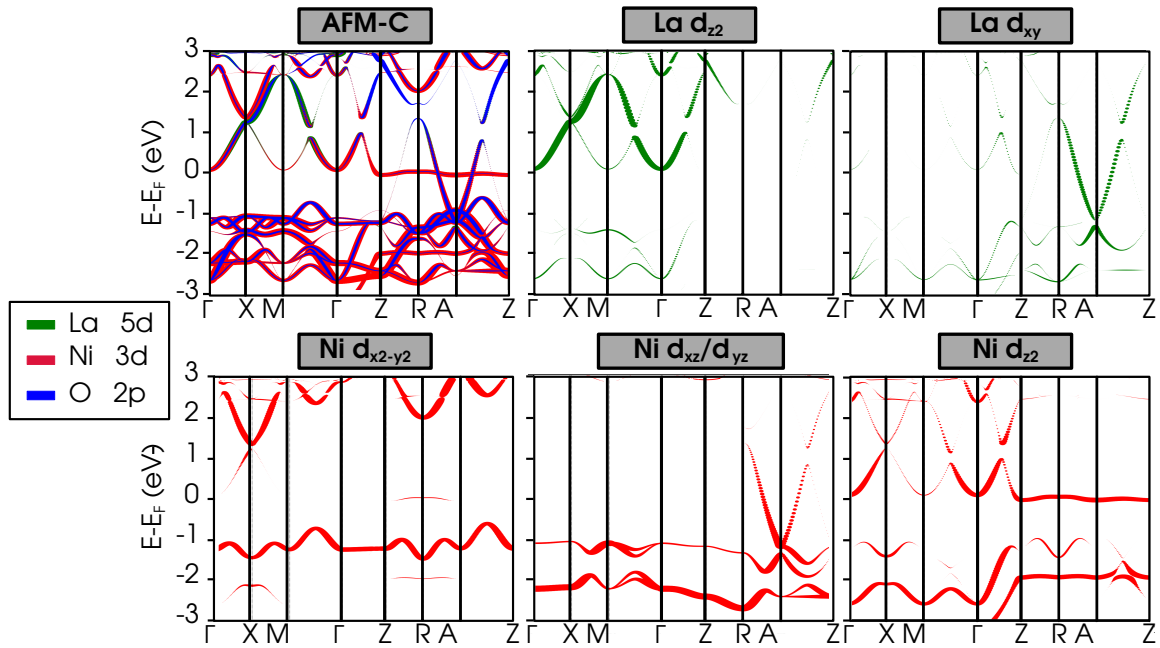


Fig. 4.11 Orbital decomposed band structure on selected Ni d (in red) and La d (in green) orbitals for type-C AFM order with the full band structure including O p states in (blue) on the top left panel. High symmetry points correspond to the P_4/mmm symmetry denoted as Γ (0,0,0), X (0,0,0), M (1/2,1/2,0), Z (0,0,1/2), R (1/2,0,1/2) and A (1/2,1/2,1/2).

shows one occupied band 2 eV below the Fermi level that does not contribute to the conduction, and several occupied bands at the Fermi level, the flat band across the $Z - R - A - Z$ path and the small electron pockets centered at Γ . Nonetheless, these bands are not completely filled, (3) the La 5d states present an important contribution to the electron pockets centered at Γ and the A points coming from the d_{z^2} and d_{xy} orbitals respectively. This behavior is consistent with the existing literature, where the finite population of the La d states at the Fermi level has been called a self-doping effect [86], and (4) the d_{xz}/d_{yz} doublet presents two occupied bands 1 and 2 eV below the Fermi level, although in addition, it presents a finite contribution to the A centered electron pocket at the Fermi level. This is quite unexpected since the d_{xz}/d_{yz} orbitals are expected to be at lower energies than the d_{z^2} and $d_{x^2-y^2}$ orbitals in a square planar environment as it is reported by several authors [231–233].

We aim to understand this apparent contradiction with the expectations, by computing the partial charge density on the AFMC in an energy window where we only have contributions from the A centered parabola. This allows us to visualize the shape of the charge density, a physical observable, disregarding the decomposition on localized atomic-like orbitals, since in the case of a metallic system, such a picture might not be suitable as we discussed previously. The energy window and the partial charge density are depicted in Figure 4.12.

It is remarkable to see that the charge density is mainly centered on the Ni cations presenting a d_{z^2} -like shape with some minor contribution from a $d_{x^2-y^2}$. This suggests that the orbital might be a mixture of several d electrons from Ni producing a d_{z^2} -like orbital and with a finite hybridization with La d_{xy} . Nonetheless, we can infer that the symmetry is not cylindrical and

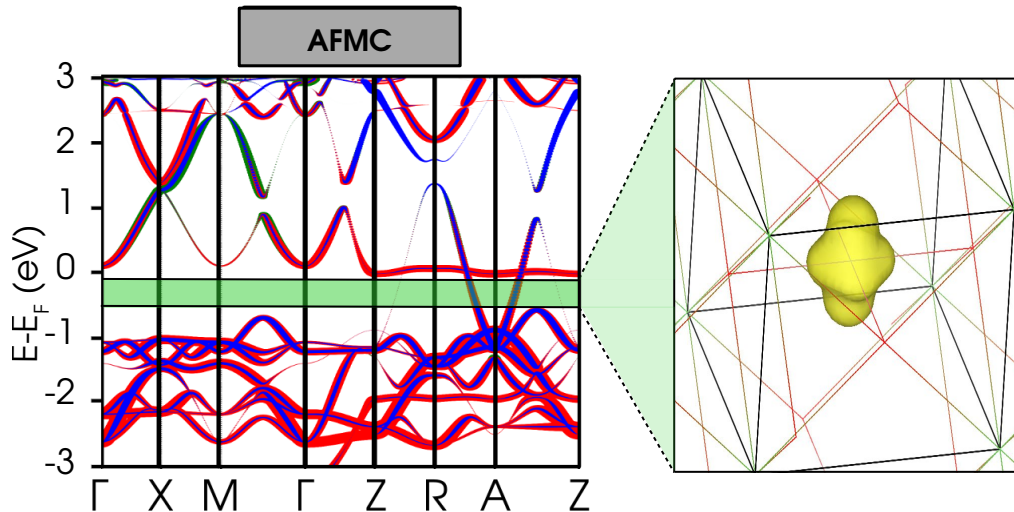


Fig. 4.12 Band structure of the AFMC order on the left panel. Partial charge density on a given energy window (green region on the left panel) centered at the Ni sites as a 3D model isosurface on the right.

there is a squared shape when inspected from the top which explains why we do not have a d_{z^2} character when the orbital decomposition is performed.

Understanding the conduction on RNiO_2 compounds

Gathering the results that we can infer from the orbital decomposed bands presented in Figure 4.11 and summarized in points (1)-(4) in the previous section, we construct a scheme of the energy levels on each Ni cation in Figure 4.13 that will help us to visualize the conduction on these compounds. As one can realize from the sketch of Figure 4.13, the crystal field between the Ni $d_{x^2-y^2}$ and d_{z^2} orbitals Δ_{CF} , turns out to be smaller than J_H the Hund's coupling $\Delta_{\text{CF}} < J_H$. This situation produces that the last occupied orbital is in the minority spin channel on each individual Ni cation with a d_{z^2} orbital character. Although in the literature many theoretical studies assumed that the conduction is given by the $d_{x^2-y^2}$ orbitals with some finite hybridization of the O p states [216–223, 234, 211, 235]. These results show that such an assumption is not well justified by the electronic structure calculations performed in this thesis, and other theoretical studies [93, 226–230], where the $d_{x^2-y^2}$ orbital would at best present a weak hole like conduction for the PM solution.

With this picture of the energy levels in mind, we recall the following experimental results: (i) these nickelates present important AFM interactions [91, 92, 96, 97] and likely an AFM ground state [93, 94, 124, 186], (ii) the undoped nickelates show a metallic character [66, 67, 123] and (iii) there is a non-negligible hybridization between the La d and Ni d states [86]. Then we see that our calculations are in good agreement with points (i) and (ii) since the lowest energy state with collinear level magnetism is a metallic AFM order (type-C AFM). In order to

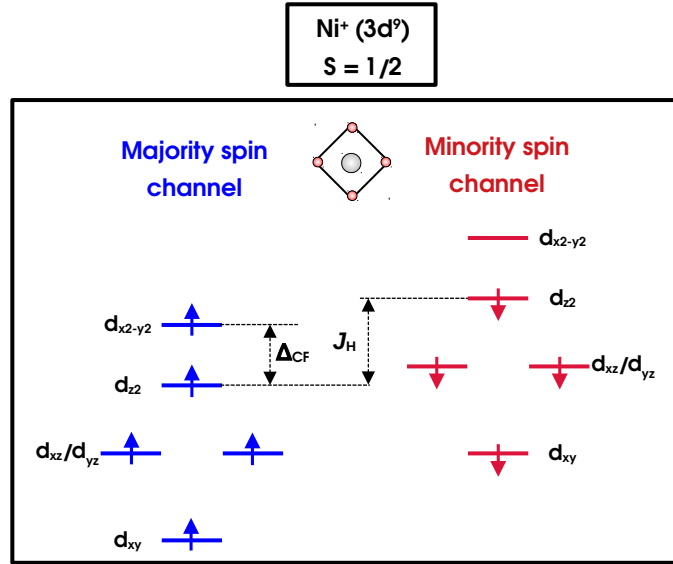


Fig. 4.13 Energy levels of each Ni cation on the RNiO₂ compounds with the different orbitals on the majority (in blue) and minority (in red) spin channels. The crystal field Δ_{CF} between the d_{z^2} and $d_{x^2-y^2}$ orbitals is represented as well as the Hund's coupling J_H .

understand the point (iii) we look at the picture in Figure 4.11 and realize that the Γ centered Ni d_{z^2} bands clearly overlap with the La d_{z^2} bands. We can say the same of the La d_{xy} A centered pocket in Figure 4.11 and the Ni d_{z^2} -like orbital that we depicted in Figure 4.12. Thus it becomes evident that the observed hybridization between the La d and Ni d orbitals of point (iii) originates from an overlap of the Ni d_{z^2} with the La d_{xy} and d_{z^2} . This produces a certain level of covalency or a more delocalized structure since the population of the Ni d_{z^2} orbital would not be completely filled and the population of the La d orbitals would not be completely unoccupied as one could expect from a pure ionic picture. We must note that this overlap would not be possible if a $d_{x^2-y^2}$ orbital would be dominant at the Fermi level. In addition, looking at the crystal field picture of Figure 4.13 the fact that the conduction is given by the minority spin channel while the magnetism is given by the non-conduction majority spin channel is what allows the coexistence of antiferromagnetic order and metallicity. The Ni d_{z^2} orbitals would contribute mainly to the conduction with some finite hybridization with the La d states while the $d_{x^2-y^2}$ would be dominant for the magnetism.

This last point is also suggested in Ref. [86] where the resistivity upturn of PrNiO₂ [67], LaNiO₂[123] and NdNiO₂ [66] is explained with a $S = \frac{1}{2}$ Kondo scattering of the conducting Ni d electrons with the magnetic environment produced by the singly occupied and non conducting Ni $d_{x^2-y^2}$ orbital. Thus, in sight of these results, we can say that the rare-earth nickelates are Hund's metals with a magnetic environment given by the non-conducting Ni $d_{x^2-y^2}$ orbital, that allows hosting metallicity and strong nearest neighbors antiferromagnetic interactions at the same time.

4.3.4 Electronic structure and lattice distortions

Depending on the cation size, several lattice distortions can appear in the material, and lower the symmetry of the crystal. We then investigate the effects of these distortions on the electronic structure by considering YNiO_2 as model compound. We restrict this study to a type-C AFM solution since it is the lowest energy state found in our DFT simulations.

We first compute the band structure of YNiO_2 in the highly symmetric P_4/mmm case (see Figure 4.14.a). The band dispersion is quite similar to LaNiO_2 where there is a small change in

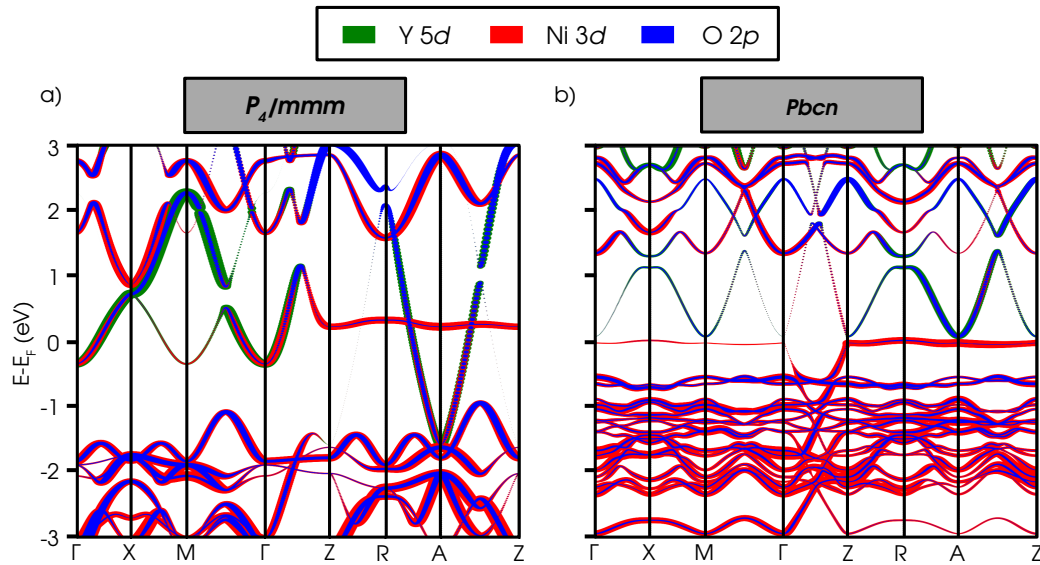


Fig. 4.14 Unfolded band structure for YNiO_2 in the high symmetry phase with P_4/mmm symmetry (a), and in the ground state geometry with $Pbcn$ symmetry (b). High symmetry points correspond to the P_4/mmm symmetry denoted as Γ (0,0,0), X (0,0,0), M ($1/2, 1/2, 0$), Z (0,0, $1/2$), R ($1/2, 0, 1/2$) and A ($1/2, 1/2, 1/2$).

the Fermi level position to upper energies, which produces greater electron pockets at Γ point. Within the low symmetry $Pbcn$ phase the electron pockets at the Γ points have disappeared (see Figure 4.14.b). In addition, we see that the parabolic band centered at the A point is now almost above the Fermi level, and the system is on the verge of becoming an insulator where the only conducting band is the heavy band along the $Z - A - R - Z$ path. These changes in the electronic dispersion signals that the lattice distortions can affect significantly the conducting properties almost bringing the system into an insulating state, which can be rationalized by a reduced overlap between the La d and Ni d states.

This further shows that these nickelates are not purely 2D materials, since the only conduction bands that are able to survive close to the Fermi level are along the $Z - R - A - Z$ path, which implies an out-of-plane conduction. Furthermore, this strongly shows that the structural degrees of freedom should not be overlooked on these compounds since it can greatly affect the electronic structure. The behavior we observe could further explain why only the nickelates with a highly symmetric P_4/mmm structure are prone to produce a superconducting transition

at the right doping content. If this is true, then potentially all nickelates could host SC if the distortions that may appear are suppressed by doping or epitaxial strain.

4.3.5 Effects of H intercalation

Finally, we check the role of H intercalation on the electronic properties of the nickelates in the H-rich LaNiO₂H. This compound presents a Ni cation with a 2+ FOS with a high spin configuration and a H⁻ anion. We compute the projected density of states on Ni 3d and O 2p of LaNiO₂ and compare it with LaNiO₂H in the high symmetry P_4/mmm and in the relaxed LaNiO₂H ground state with I_4/mcm symmetry. Results are depicted in Figure 4.15. We obtain

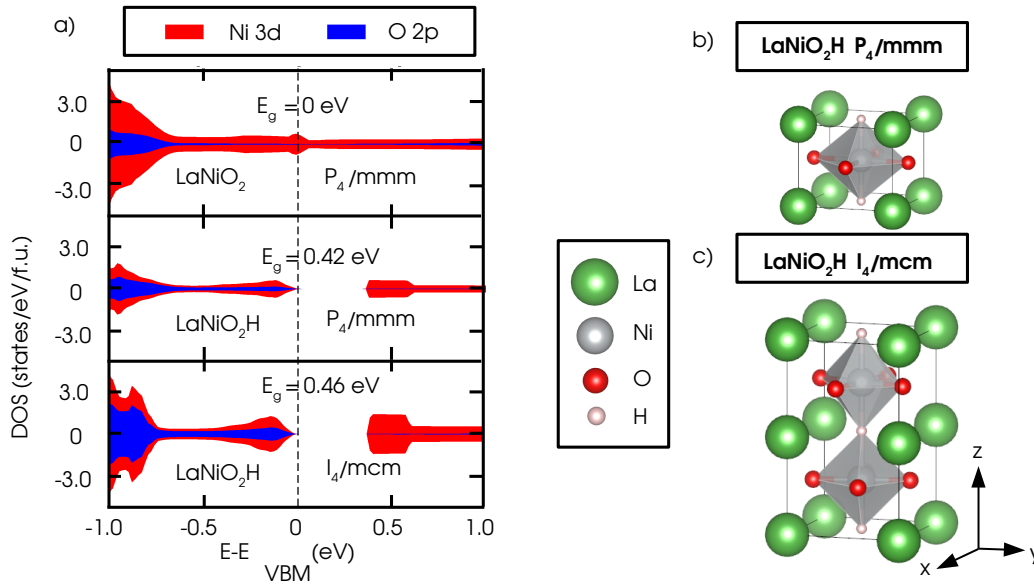


Fig. 4.15 On the left (a) projected density of states of LaNiO₂ (top panel) with ground state P_4/mmm symmetry LaNiO₂H with undistorted P_4/mmm (middle panel) and LaNiO₂H with relaxed structure with rotations and I_4mcm symmetry (bottom panel). Blue area are the O 2p states, red area the Ni 3d states. Positive and negative values of the density of states correspond to the spin-up and spin-down channels. On the right crystal structure of the two geometries of LaNiO₂H considered (b) with P_4/mmm symmetry, and (c) with I_4/mcm symmetry.

that the H rich nickelate LaNiO₂H, is an insulator with a gap of $E_g = 0.42$ eV in the high symmetry P_4/mmm cell (see Figure 4.15.b), and the gap amplitude increases to $E_g = 0.46$ eV in the ground state geometry with I_4/mcm symmetry (see Figure 4.15.c). This behavior is in contrast with the metallic or semi-metallic behavior of LaNiO₂ depicted in Figure 4.15.a. These results in addition to the 3D AFM ground state of LaNiO₂H indicate that (i) the H⁻ traps conducting electrons as we can see by comparing the projected density of states on LaNiO₂ depicted in Figure 4.15.a with the DOS LaNiO₂H depicted in Figure 4.15.b and Figure 4.15.c, (ii) the H intercalation restores the octahedral environment on Ni sites allowing an out-of-plane superexchange interaction that favors antiferromagnetism, and (iii) the system becomes an antiferromagnetic Mott insulator regardless of the geometry. Thus H intercalation does not favor better conducting properties suggesting that it could be actually harmful to the appearance of superconductivity in these compounds.

4.4 Conclusion

We conclude here, that the RNiO_2 compounds present a similar behavior as the RNiO_3 parent phase in terms of lattice distortions and how they correlate with the size of the A-site cation. From the point of view of the magnetic properties, we have shown that these nickelates present a strong nearest neighbor antiferromagnetic coupling between Ni sites in good agreement with the experiments and other theoretical works. In addition, we find a weaker antiferromagnetic coupling between the rare-earth R and the Ni cation when the $4f^n$ states are occupied in the rare-earth. This shows that the main magnetic interactions come from Ni sites and any magnetic-related pairing mechanism is more likely to come from the Ni sites than the rare-earth R. Regarding the electronic properties, we highlight the importance of including the spin degree of freedom and that these compounds are in the Mott regime where the conduction is governed by La d and Ni d electrons in good agreement with the experiments. Furthermore, we have studied the orbital character of the conduction, showing that except in the FM case, the conduction is not given by the Ni $d_{x^2-y^2}$ contrary to what it is assumed. This is a consequence of Hund's coupling J_H being bigger than the crystal field between Ni d_{z^2} and $d_{x^2-y^2}$ orbitals $J_H > \Delta_{\text{CF}}$. Which produces that the conduction is given by doubly occupied Ni d_{z^2} and d_{z^2} -like orbitals on the minority spin channel, with a finite contribution from La d_{xy} and d_{z^2} in a background magnetic environment of singly occupied Ni $d_{x^2-y^2}$ orbitals. Thus these nickelates present themselves as Hund's metals with a Mott character and non-negligible antiferromagnetic interactions. Finally, we have also explored the role of H intercalation in the material in the H-rich limit showing that it produces several lattice distortions, out-of-plane antiferromagnetic interactions, and insulating behavior. Thus suggesting that H intercalation in the material is harmful to the conducting properties of these compounds.

Chapter 5

Superconductivity in doped RNiO_2 nickel oxides

Once the properties of the pristine materials are understood, we can study and rationalize the doping content that is necessary to reach the superconducting phase in these compounds. As we have evidence in chapter 3, one should be careful when dealing with rare-earth compounds since the $4f$ states are not well localized with the SCAN functional. In that regard, we take the case of La-based compounds since La cations do not present these $4f$ states. Additionally, the SCAN functional also underestimates the band gap of transition metal compounds, which is a well-known problem within practiced DFT, and in particular, the behavior of SCAN is worse for compounds with a smaller formal oxidation state (FOS). Thus we benchmark our results with the hybrid HSE06 functional when estimating band gaps.

5.1 Technical parameters of the calculations

The DFT calculations that we present in this chapter have a 650 eV energy cut-off for the plane wave expansion and use the same PAW PBE pseudo potentials as mentioned in the previous chapters for La, Ni, Sr, and O. The magnetic order is PM unless stated otherwise. This choice is guided by the lack of experimentally reported long-range magnetism. In addition, it avoids the inclusion of possible spin-phonon couplings in our simulations that may arise due to an imposed long-range magnetic order. The PM order is modeled with the SQS method for alloys as in chapter 4. We also use this method to model the Sr content x of the disordered solid solution (DSS) of $\text{La}_{1-x}\text{Sr}_x\text{NiO}_2$ type compounds explicitly substituting the La ions by Sr ions. This approach to model the Sr doping content is preferred over the virtual crystal approximation (VCA) since the real potential of the different atoms is considered and *a priori* we do not know whether the doping simply shifts the Fermi level (essentially with VCA) or produces other effects. We use a $3 \times 3 \times 2$ k -mesh to model the 32 f.u. supercell (with 128 ions per supercell) in the case of $\text{La}_{1-x}\text{Sr}_x\text{NiO}_2$ compounds, while we use a $3 \times 3 \times 1$ k -mesh to model the 16 f.u. supercell of La_2NiO_4 (with 112 ions per supercell) and of $\text{La}_3\text{Ni}_2\text{O}_6$ (with

176 ions per supercell). The energy convergence criteria is set to $\Delta E < 10^{-5}$ eV, and forces are optimized on each atom until they are less than $5 \cdot 10^{-2}$ eV/Å.

5.2 Understanding the phase diagram

As we mentioned in chapter 1, the RRP family ($R_{n+1}Ni_nO_{2n+2}$ compounds) hosts the infinite layer (IL) case RNiO₂ since it is the limiting member ($n = \infty$). Thus one may wonder if analyzing the series from the $n = 1$ case instead of the $n = \infty$ can be helpful to understand the phase diagram of these compounds and unveil the origin of the superconductivity. In that regard, we perform electronic structure calculations of La₂NiO₄ ($n = 1$) using the ground state geometry with *Cmce* crystal structure. From our calculations, we find that this compound is an insulator with the conduction band minimum (CBM) mainly dominated by Ni *d* states, while the valence band maximum (VBM) presents some O *p* and Ni *d* states (see Figure 5.1.a). The

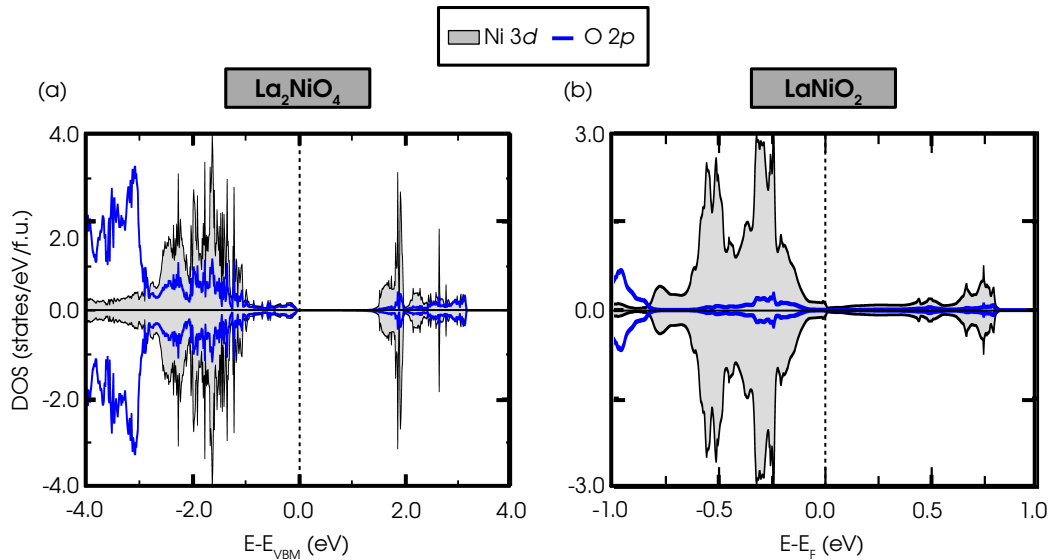


Fig. 5.1 The projected density of states of (a) La₂NiO₄, and (b) LaNiO₂ with a PM magnetic order. In solid grey the Ni *3d* states, and the blue line represents the O *2p* states. Positive values of the density of states correspond to the spin-up channel while negative values correspond to the spin-down channel.

amplitude of the gap is estimated to be $E_g = 1.7$ eV in fair agreement with previous DFT studies with the SCAN functional [162]. The total magnetic moment on Ni sites is $\mu_{Ni} = 1.48\mu_B$, which is reminiscent of a Ni²⁺ cation ($3d^8$) with a high spin configuration $S = 1$ in good agreement with the experiments [236].

The electronic properties of La₂NiO₄ are in contrast with the behavior of LaNiO₂ that shows a clear metallic behavior as we already explored in chapter 4 in more detail (see Figure 5.1.b). The fact that La₂NiO₄ ($n = 1$) is an insulator with a $3d^8$ electron count on Ni sites, suggests that approaching the SC region from this side of the phase diagram requires to electron dope an insulator. This strategy is rather natural for improving the conducting properties of any insulator. Moreover, doping a Mott or CT insulator is a common approach to obtain a

superconductor, such is the case of cuprates, or bismuthates [237–239, 165, 240]. Thus, starting to explore the doping phase diagram from the left side ($n = 1$) as depicted in Figure 1.14 rather than the right side ($n = \infty$) looks much more appealing. From this perspective, we may ask if this approach allows us to identify an intrinsic electronic instability connected to the superconducting mechanism. In that regard, we look for electronic instabilities contained between the R_2NiO_4 ($n = 1$ of the RRP series) compounds, and the SC region in the doping phase diagram.

5.3 Nickelates at half-doping

Following the RRP series, we explore the next member $La_3Ni_2O_6$ ($n = 2$) which would correspond to a half-doped situation where Ni cations present a $3d^{8.5}$ electron count. Nonetheless, we can achieve this electron count by starting from the other side of the phase diagram with the IL phase, with compounds like $La_{0.5}Sr_{0.5}NiO_2$. In that regard, if both approaches are indeed equivalent, we should expect to obtain similar electronic properties from both situations.

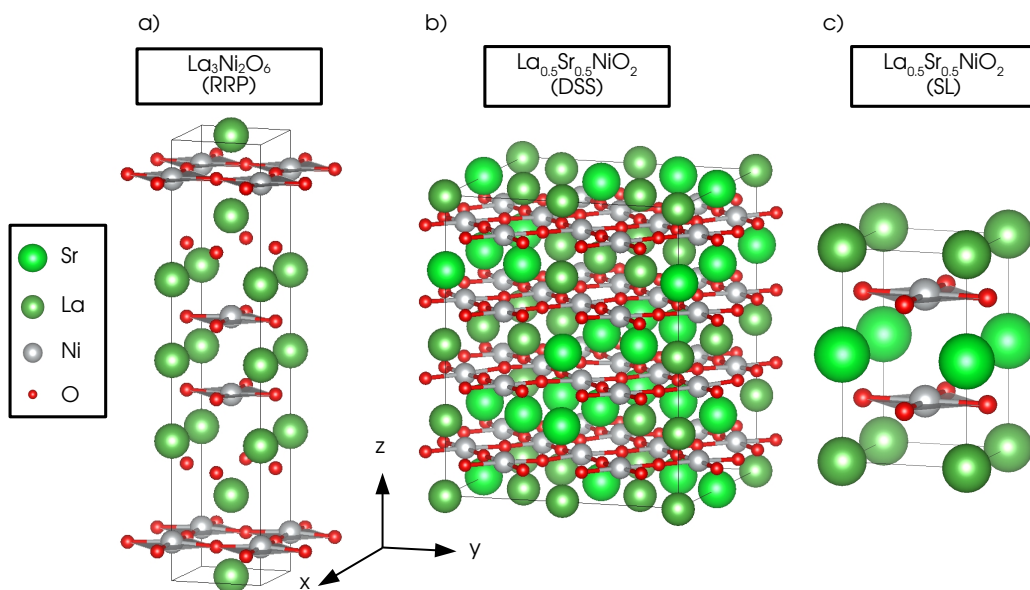


Fig. 5.2 The three different geometries of half doped layered nickelates with $3d^{8.5}$ electron count that are explored. (a) RRP $La_3Ni_2O_6$, (b) DSS $La_{0.5}Sr_{0.5}NiO_2$, and (c) SL $La_{0.5}Sr_{0.5}NiO_2$.

To that aim, we relax the structure of (i) the IL as a super-lattice (SL) with perfect planes of Sr and La stacked along the c axis, (ii) the IL as a completely disordered solid solution (DSS), and (iii) the $n = 2$ RRP compound. The three geometries are depicted in Figure 5.2 and the key quantities extracted from the relaxations are reported in Table 5.1.

After the relaxation, we perform a symmetry mode analysis with respect to the primitive undistorted cell with space group I_4/mmm for the RRP and P_4/mmm in the IL case, from which we obtain that in the three considered cases, that there is a bond disproportionation

Compound	ΔE (meV/f.u.)	$Q_{B_{oc}}$ ($\text{\AA}/\text{NiO}_2$)	$\mu_{\text{Ni}_L}/\mu_{\text{Ni}_S}$ (μ_B)
La ₃ Ni ₂ O ₆ (RRP)	-32	0.09	1.09/0.46
La _{0.5} Sr _{0.5} NiO ₂ (DSS)	-53	0.06	1.03/0.23
La _{0.5} Sr _{0.5} NiO ₂ (SL)	-87	0.07	0.95/0.10

Table 5.1 Extracted key quantities of the relaxed half-doped compounds. Total energy difference ΔE in meV/f.u. of the distorted cell with the B_{oc} mode with respect to the high symmetry phase, I_4/mmm in the RRP and P_4/mmm in the IL. Mode amplitude $Q_{B_{oc}}$ in $\text{\AA}/\text{NiO}_2$ motif, and average magnetic moment on Ni_L and Ni_S sites.

mode (B_{oc}) with sizable amplitudes of $Q_{B_{oc}} = 0.07$, $Q_{B_{oc}} = 0.06$, and $Q_{B_{oc}} = 0.09$ $\text{\AA}/\text{NiO}_2$ motif in the SL, DSS and RRP phases respectively (see Table 5.1). This mode produces a splitting of the Ni sites into cations sitting in compressed (Ni_S) and extended (Ni_L) oxygen complexes forming a layered checkerboard structure (see Figure 5.3).

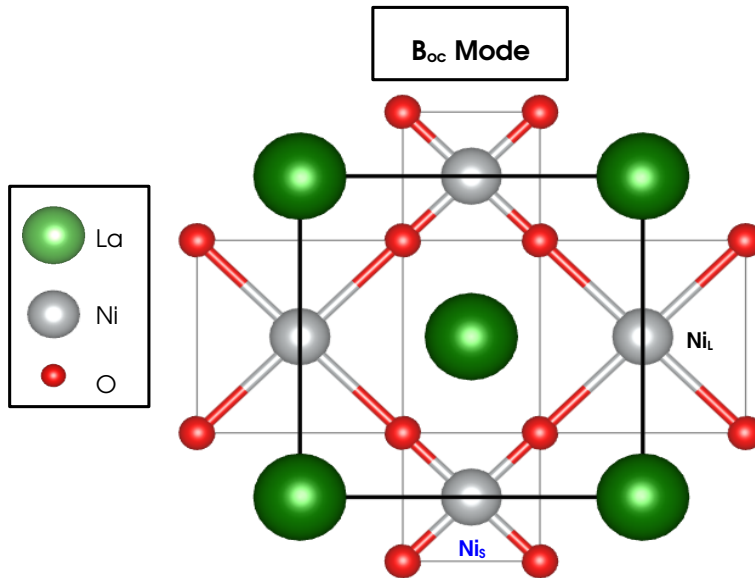


Fig. 5.3 Breathing of oxygen complexes distortion (B_{oc}) producing a double local environment on Ni sites, with Ni_S in the compressed NiO_4 square and Ni_L in the extended NiO_4 square.

The structural relaxations are associated with large energy gains with respect to the undistorted highly symmetric cell in the SL, DSS (with P_4/mmm symmetry), and RRP phase (with I_4/mmm symmetry) of -87 , -53 , and -32 meV/f.u. respectively. By inspecting the magnetic moments on the Ni sites, we can notice the existence of a double local environment since the Ni_L sites bear a magnetic moment of $\mu_{\text{Ni}_L} = 0.99 \pm 0.05 \mu_B$ depending on the nature of the half-doped nickelate (i.e. SL, DSS or RRP), and Ni_S sites have a magnetic moment of $\mu_{\text{Ni}_S} = 0.26 \pm 0.18 \mu_B$. The clear magnetic moment asymmetry suggests that Ni_L cations are in a $\text{Ni}^+(3d^9)$ configuration while Ni_L cations are in a $\text{Ni}^{2+}(3d^8)$ low spin state, producing a charge ordering (CO). The slight deviation from the expected $0 \mu_B$ for Ni_S sites comes from cation and/or spin disorders (inherent to the DSS and PM) yielding a different crystal field Δ_{CF} and exchange splitting Δ_x experienced by each Ni cations.

We further investigate the electronic structure of these compounds, by computing the partial density of states on the IL DSS and projecting on O p , Ni_L d and Ni_S d . Results are shown in Figure 5.4.a. We notice that the effect of the B_{oc} mode is to produce a clear asymmetry of the electronic structure associated with the two different Ni cations (Figure 5.4.c). Nonetheless, we observe that the compound is weakly metallic which is quite unusual for a CO compound. We

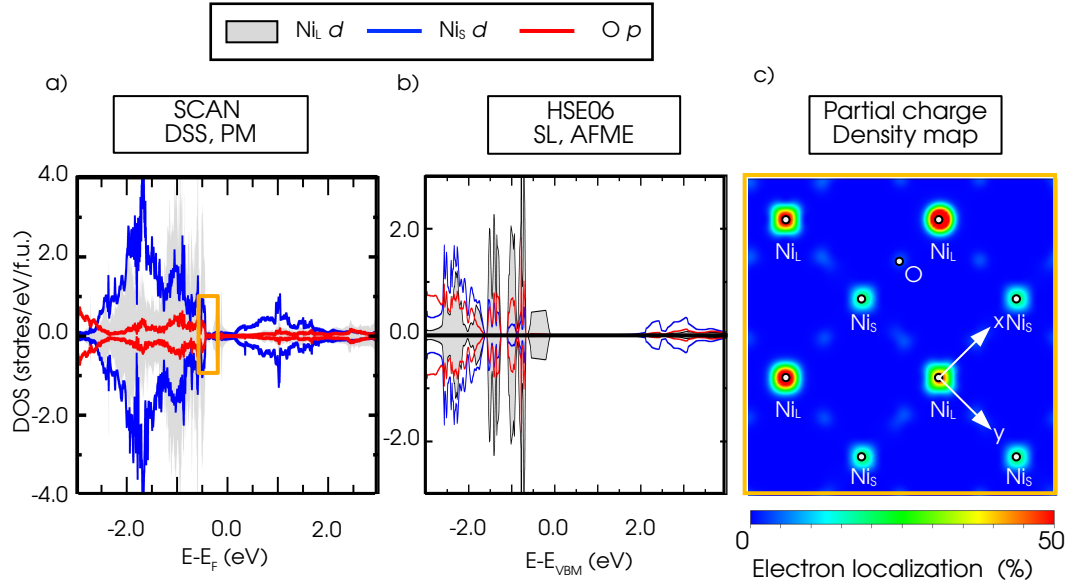


Fig. 5.4 Electronic structure of half-doped nickelates. Projected density of states on O p (in red) Ni d (in blue) and Ni d (in grey) for (a) solid solution (DSS) IL nickelate with PM order using the SCAN functional, and (b) superlattice (SL) IL nickelate with type-E AFM using the HSE06 functional. (c) Partial charge density map of selected bands indicated by the orange square on panel (b).

benchmark these results with the hybrid HSE06 functional on a smaller cell in the SL with a type-E AFM order that is compatible with the charge ordered pattern as discussed in Ref. [26] (see Figure 5.4.b). The latter calculation yields an insulator with a gap amplitude of $E_g = 2$ eV in contrast to SCAN, although preserving the same qualitative picture on the asymmetry of the Ni cations. This behavior from SCAN is nothing but self-interaction errors which become more and more important with smaller formal oxidation states as we discussed in chapter 3. Thus, in the case of the unusual Ni⁺ cation, the SCAN functional yields a slightly delocalized structure producing a metallic system. However, underestimated band gaps are inherent to local or semi-local DFT exchange-correlation functionals which also underestimate as well the gap of uncorrelated semiconductors.

Focusing now on Figure 5.4.b, we notice that the VBM is dominated by Ni_L d states while Ni_S d states are pushed above and below the VBM and dominate the CBM. Furthermore, the O p orbitals do not bring a sizable contribution to the DOS in this energy range and the top of these states are in fact located 1 eV below the CBM. We further investigate the electronic structure by looking at the partial charge density map originating from bands just at the VBM (see Figure 5.4.c). A charge ordering between Ni_L and Ni_S cations (Figure 5.3.b) is identified with Ni_L likely holding more electrons than Ni_L cations. The partial charge density map also

highlights the strong Mott character of these nickelates with negligible spread of the electronic structure on O atoms. The Mott character is in agreement with previous results on undoped materials [84, 241, 87, 93, 226–230].

Regarding the spin configuration on Ni sites, we must note that obtaining a low spin state is quite surprising since La₂NiO₄ presents a Ni²⁺ in a high spin state. We can understand this behavior as an interplay between the local crystal field Δ_{CF} between the d_{z^2} and $d_{x^2-y^2}$ orbitals, and the Hund's coupling J_H on each Ni cation (see Figure 5.5). When all Ni cations in these

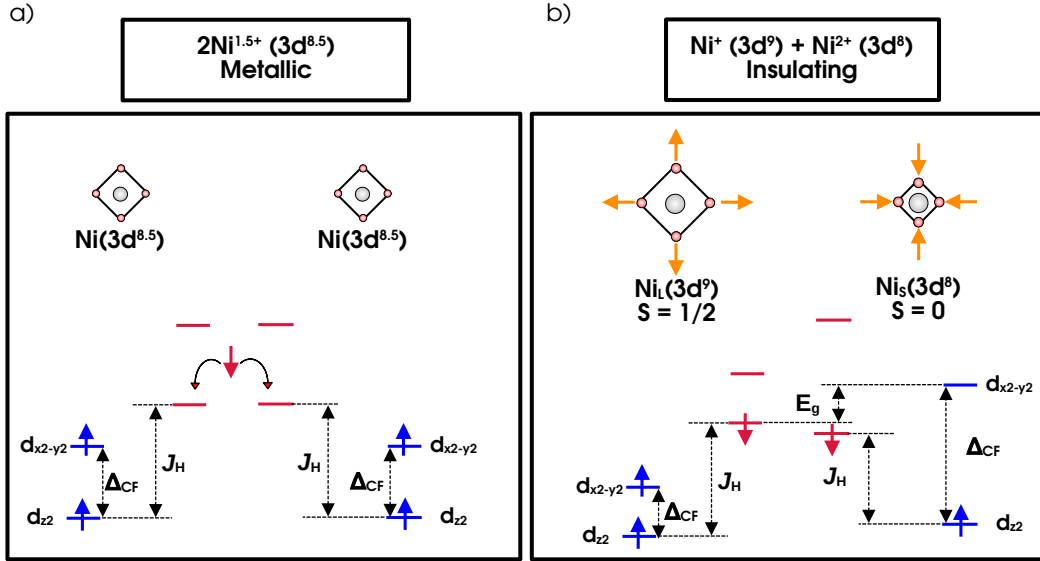


Fig. 5.5 Orbital filling of the energy levels on Ni cations in the square coordinated environment of the RRP or IL phase. Two situations are considered (a) the system presents all Ni cations equivalent and with a Ni^{1.5+}(3d^{8.5}) producing a metallic state, and (b) the system presents two types of Ni cations, with a Ni⁺(3d⁹) configuration as in the case of Ni_L cations, and with a Ni²⁺(3d⁸) configuration as in the case of Ni_S cations, producing an insulating state with gap amplitude E_g .

compounds are equivalent, we have the situation depicted in Figure 5.5.a, where the crystal field in all Ni cations is the same and is smaller than the Hund's coupling $\Delta_{CF} < J_H$. This is the situation that we discussed in chapter 4 for the undoped compounds, and in this case, since the d_{z^2} minority spin channel can be either occupied or unoccupied on different Ni sites, leads to a half-filled band and a metallic system. However, when the B_{oc} disproportionation mode condenses in the material, it produces two types of Ni cations (Ni_L and Ni_S), where the crystal field Δ_{CF} shrinks or enhances, respectively as depicted in Figure 5.5.b. The interesting situation comes from the Ni_S cations since in their case, the crystal field dominates over the Hund's coupling $\Delta_{CF} > J_H$. This produces that the $d_{x^2-y^2}$ orbitals on Ni_S cations are less energetically favored in general than the d_{z^2} in both spin channels, producing all electrons on Ni_S to be paired, a low spin configuration $S = 0$, and a completely unoccupied $d_{x^2-y^2}$ orbital (see Figure 5.5.b). In addition, when the energy levels on Ni_S cations are compared with the Ni_L cations, this double local environment leads to a gap opening between the occupied Ni_L d_{z^2}

orbitals sitting at the VBM, and the unoccupied Ni_S $d_{x^2-y^2}$ orbital at the CBM as it is depicted in Figure 5.5.b, and it can be verified as well from the DOS in Figure 5.4.

5.3.1 Origin of the disproportionation mode

In order to reveal the origin of the disproportionation effects, we examine the potential energy surface (PES) associated with the disproportionation mode B_{oc} in the SL, DSS, and RRP. To that end, we compute the total energy by freezing some amplitude of the B_{oc} mode starting from a high symmetry undistorted P_4/mmm and I_4/mmm cells for the IL and RRP, respectively (see Figure 5.6). In all three forms of half-doped nickelates, we identify a single well

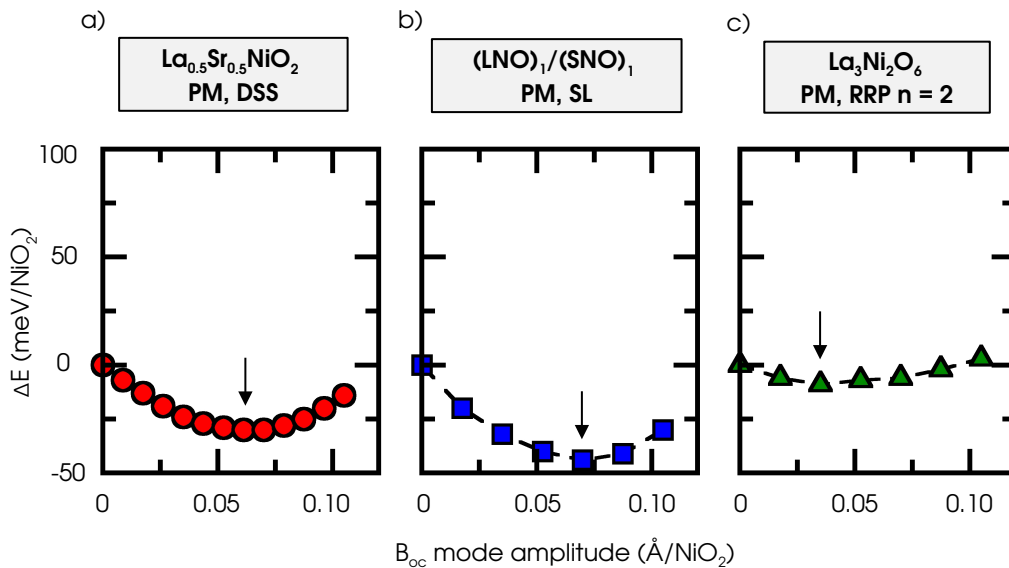


Fig. 5.6 Potential energy surfaces of the B_{oc} mode with a PM magnetic order and several geometries, (a) $\text{La}_{0.5}\text{Sr}_{0.5}\text{NiO}_2$ with PM order, (b) $\text{La}_{0.5}\text{Sr}_{0.5}\text{NiO}_2$ SL with PM order, and (c) $\text{La}_3\text{Ni}_2\text{O}_6$ with PM order. Total energy differences are taken with respect to the high symmetry P_4/mmm and I_4/mmm cells for the IL and RRP, respectively.

potential whose minimum is shifted to a non-zero amplitude of the B_{oc} mode. This indicates the existence of a force associated with an electronic instability acting to remove the electronic degeneracy of the equivalent Ni cations on a $3d^{8.5}$ electronic configuration depicted in Figure 5.5.a [26]. Furthermore, the instability is independent of the form of the structure (i.e. SL vs. RRP) as well as of the order/disorder of A-site cations (i.e. SL vs. DSS). This suggests that the formal occupancy of Ni $3d$ orbitals is the determining factor rather than the form of the nickelate. We conclude here that the $1.5+$ FOS of Ni cations is intrinsically unstable and is willing to disproportionate to more stable $1+$ and $2+$ FOS in the ground state, thereby producing a charge ordering and a bond disproportionation B_{oc} mode.

These results and the existence of a disproportionated insulating state at half doping are confirmed experimentally in Refs. [47, 49, 201] showing the existence of CO and insulating states in $\text{La}_3\text{Ni}_2\text{O}_6$ (RRP $n = 2$), also predicted theoretically in Ref. [242]. Nevertheless, the existence of a half-doped infinite layered phase is yet to be realized experimentally, where other factors

such as thermodynamic stability, miscibility of the precursors of the parent perovskite phase, and the choice of the divalent cation to dope should be carefully studied. However, should such a phase exist, it would be characterized by robust disproportionation effects of Ni^{1.5+} cations.

5.4 Evolution of the charge ordering with the doping

So far, we have seen that the CO instability that produces a bond disproportionation and an insulating state exist at half doping. Thus the question here is what happens when we keep approaching the SC region starting from this CO phase. In that regard, we explore the IL phase with different doping concentrations La_{1-x}Sr_xNiO₂ with a PM order. To that end, we decrease

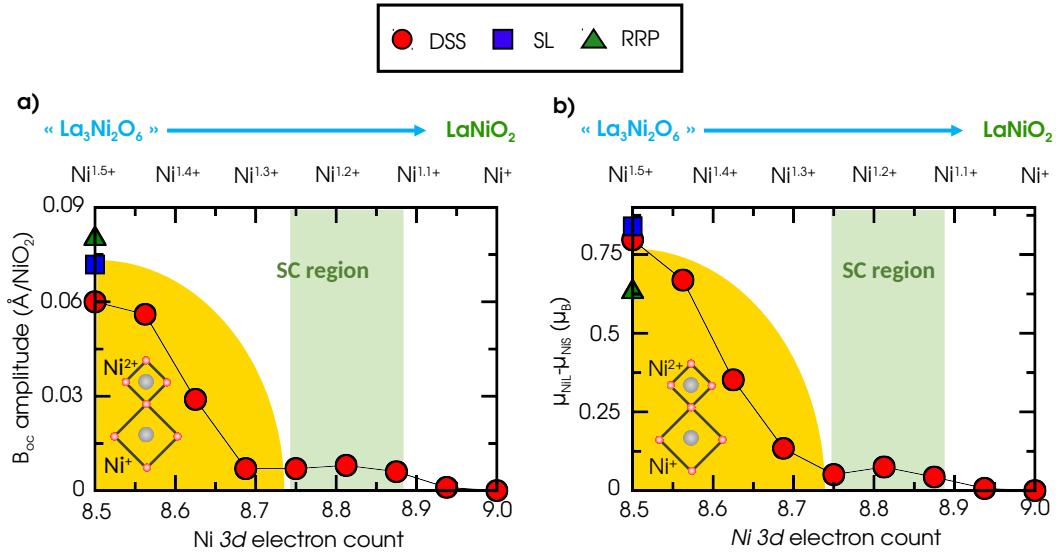


Fig. 5.7 Trends in disproportionation effects with a PM order signaling the charge ordered phase with the 3d electron count for two key quantities (a) the amplitude of the B_{oc} mode in Å/NiO₂ motif, and (b) the absolute value of the difference in the magnetic moment of Ni_L and Ni_S cations. Both quantities are represented for the fully relaxed structures of La_{0.5}Sr_{0.5}NiO₂ solid solution (red dots, DSS), superlattice (blue squares, SL), and La₃Ni₂O₆ (green triangles, RRP).

the Sr concentration starting from $x = 0.5$ until $x = 0$, which translates to an increase of the 3d electron count from a $3d^{8.5}$ (with a Ni^{1.5+} cation) electronic configuration to a $3d^9$ (with a Ni⁺ cation). We report in Figures 5.7.a and 5.7.b the evolution of the B_{oc} mode amplitude and the magnetic moment asymmetry $\Delta\mu = \mu_{\text{Ni}_L} - \mu_{\text{Ni}_S}$ between the two Ni sites as a function of the 3d electron count. We observe that the amplitude of the B_{oc} mode decreases upon increasing the electron count starting from $3d^{8.5}$. The critical point is achieved at a Sr concentration of $x = 0.25$ which corresponds to a $3d^{8.75}$ electron count (see Figure 5.7.a), where the B_{oc} mode is no longer stable. We can extract the same conclusions following the magnetic moments as it is depicted in Figure 5.7.b. We can note that the extinction of the disproportionation mode at $x = 0.25$ is reminiscent of the value at which superconductivity emerges experimentally in these compounds [68].

Concerning the electronic structure, we have already evidence that SCAN would produce a false metal at half-doping. For that reason, we use the hybrid HSE06 and the type-E AFM with

a SL as we did in the half-doped situation but in this case with a doping content of $x = 0.375$. This is achieved with an 8 f.u. supercell which makes the calculations affordable. We present the results in Figure 5.8, and we can appreciate an insulating compound with a sizable B_{oc} mode amplitude $Q_{B_{oc}} = 0.079 \text{ \AA}/\text{f.u.}$ and a clear asymmetry on the Ni magnetic moments of $\Delta\mu = 1 \mu_B$. This suggests that the B_{oc} mode and the CO insulating state will be present for all compounds

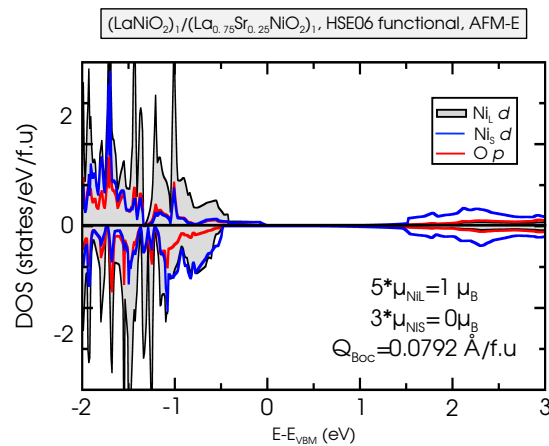


Fig. 5.8 Projected density of states on O p (red line), $Ni_S d$ (blue line) and $Ni_L d$ (solid grey) of $La_{0.625}Sr_{0.375}NiO_2$ in a SL geometry with a type-E AFM. In the inset, the magnetic moment on the 3 Ni_S and 5 Ni_L cations are given as well as the $Q_{B_{oc}}$ mode amplitude.

with $x > 0.3125$ which is when the amplitude of the distortion starts to vanish. From this point, we expect to find a metallic compound. Nonetheless, the exact position might change depending on both rare earth and divalent cations and might be dependent on the strain coming from the substrate since the lattice distortions are affected by pressure effects as we discussed in chapter 4.

Thus we conclude here that increasing the electron count on the Ni site quenches the insulating CO phase producing a metallic region. The existence of a propensity towards a bond and charge ordering has been evidenced on some of the compounds in the RRP series with $n = 3$ [53, 57, 63], as well as some theoretical works on this compound [243, 242] and the IL phase [244].

5.4.1 Evidence of an electronic phase transition

We obtain further evidence on the extinction of the disproportionation mode, by computing the potential energy surface of the B_{oc} mode for different Sr contents x in the DSS. Starting from the half-doped situation $x = 0.5$ depicted in Figure 5.6.a, we obtain a shifted single well for all the doping concentrations until $x = 0.25$ as it is depicted in Figures 5.9.a 5.9.c, noticing that the depth of the well and the minimum are progressively shrunk upon increasing the electron count or decreasing the Sr content x . Further decreasing the content x , we notice that we have a single well potential whose minimum is achieved at zero amplitude (see Figures 5.9.d to 5.9.e), indicating that the electronic instability associated with the B_{oc} mode is suppressed. At this stage, no more CO is expected leaving a metallic region. We explore in more detail this

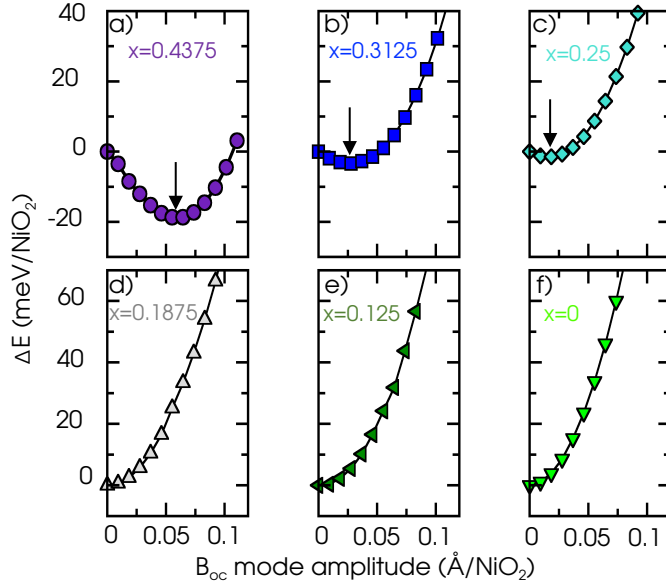


Fig. 5.9 Potential energy surface of the B_{0c} mode for the DSS of $\text{La}_{1-x}\text{Sr}_x\text{NiO}_2$ with a PM order for different values of x (a) $x = 0.4375$, (b) $x = 0.3125$, (c) $x = 0.25$, (d) $x = 0.1875$, (e) $x = 0.125$, and (f) $x = 0$.

transition by computing the frequency of the mode as a function of the Sr doping content x . As we discussed in the previous chapter, we can model the potential energy surface by expanding the energy E in terms of the amplitude of the mode $Q_{B_{0c}}$ as follows

$$E[Q_{B_{0c}}] = E_0 + \alpha Q_{B_{0c}}^2 + \beta Q_{B_{0c}}^4 \quad (5.1)$$

We can easily identify that the harmonic constant is $\alpha = \frac{1}{2}M_O\omega_{B_{0c}}^2 > 0$, with M_O the mass of the oxygen, $\omega_{B_{0c}}$ is the frequency of the B_{0c} mode and $\beta > 0$ is the anharmonic coupling constant. However, under these restrictions $\alpha, \beta > 0$, we are assuming that the minimum is achieved at $Q_{B_{0c}} = 0$, but if the minimum energy is achieved at a non-zero amplitude Q_0 , we can express the energy as

$$E[Q_{B_{0c}} - Q_0] = E_0 + \alpha(Q_{B_{0c}} - Q_0)^2 + \beta(Q_{B_{0c}} - Q_0)^4 \quad (5.2)$$

Expanding the expression we find

$$E[Q_{B_{0c}} - Q_0] = E_0 + \alpha Q_{B_{0c}}^2 + \alpha Q_0^2 - 2\alpha Q_{B_{0c}} Q_0 + \beta Q_{B_{0c}}^4 + \beta Q_0^4 - 4\beta Q_{B_{0c}}^3 Q_0 - 4\beta Q_{B_{0c}} Q_0^3 + 6\beta Q_{B_{0c}}^2 Q_0^2 \quad (5.3)$$

and if we arrange the terms in powers of $Q_{B_{0c}}$

$$E[Q_{B_{0c}} - Q_0] = (E_0 + \alpha Q_0^2 + \beta Q_0^4) - (2\alpha Q_0 + 4\beta Q_0^3)Q_{B_{0c}} + (\alpha + 6\beta Q_0^2)Q_{B_{0c}}^2 - 4\beta Q_0 Q_{B_{0c}}^3 + \beta Q_{B_{0c}}^4 \quad (5.4)$$

With this expression, we can then fit the calculated PES with a 4th degree polynomial in $Q_{B_{0c}}$

$$E[Q_{B_{0c}} - Q_0] = E'_0 + aQ_{B_{0c}} + bQ_{B_{0c}}^2 + cQ_{B_{0c}}^3 + dQ_{B_{0c}}^4 \quad (5.5)$$

and map the coefficients into the previous expression allowing us to obtain the value of β , Q_0 and the harmonic constant α as follows:

$$\begin{aligned}\beta &= d \\ Q_0 &= -\frac{c}{4d} \\ \alpha &= b - \frac{3c^2}{8d}\end{aligned}\quad (5.6)$$

Then it is easy to obtain the frequency as:

$$\omega_{B_{oc}} = \sqrt{\frac{2\alpha}{M_O}} \quad (5.7)$$

which will allow us to obtain the harmonic term of the frequency for any doping concentration x . We report in Figure 5.10 the evolution of $\omega_{B_{oc}}^2$ as a function of x . It is clear that there is

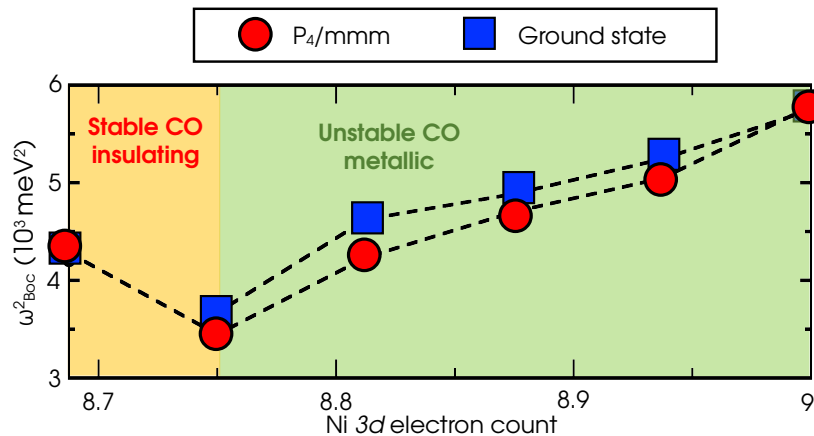


Fig. 5.10 Square of the B_{oc} mode frequency $\omega_{B_{oc}}^2$ as a function of the $3d$ electron count computed in the highly symmetric P_4/mmm cell (red dots) and in the relaxed ground state with $P1$ symmetry (blue squares).

a softening from $x = 0.5$ to $x = 0.25$ and then the mode hardens for $x < 0.25$. This behavior is characteristic of a phase transition where the n -th derivative of the energy with respect to a given order parameter is discontinuous. If we recall that the elastic energy is proportional to the square of the frequency $E \propto \omega_{B_{oc}}^2$, and the doping concentration is proportional to the number of electrons $x \propto N$, it is then easy to see that the discontinuity would be in the chemical potential $\tilde{\mu} = \frac{\partial E}{\partial N}$. Thus it clearly signals an electronic phase transition at $x_c \approx 0.25$, reminiscent of the transition from CO insulator to metal that we observe in the phase diagram.

Focusing now on the metallic region close to the critical point x_c , we can notice that the frequency of the mode is rather soft, and although the mode is not able to localize the electrons, it could still be coupled to the electronic structure opening the possibility of Cooper pair formation. Finally, we also observe a small shift toward higher frequencies, when we compute the frequency of the mode including all the small lattice distortions present in the relaxed ground state. This signals the presence of small couplings between the B_{oc} mode and other

lattice distortions. Thus we conclude here that the SC phase of these layered nickelates is in the vicinity of a CO phase.

5.5 Superconducting model

It is important to note that although in the DFT calculations, the B_{oc} mode does not present a sizable amplitude in the ground state structure, it does not prevent the mode from interacting with the electronic structure. We will then try to build a simplified model taking as an ansatz that the B_{oc} mode is highly coupled to the electronic structure of these nickelates and that this mode would be representative of the types of phonon modes that will contribute to the SC mechanism. We can then use equation (2.92) from chapter 2 for the EPC, and consider the Fermi surface average of only the B_{oc} mode.

$$\lambda_{B_{oc}} = 2N(\varepsilon_F) \sum_{\mathbf{k}} \frac{\hbar^2}{2\omega_{B_{oc}}^2} \left| \sum_j \frac{1}{\sqrt{M_j}} \frac{\Delta\varepsilon_{\mathbf{k}}}{|u_{B_{oc},j}|} \right|^2 \quad (5.8)$$

where $N(\varepsilon_F)$ is the density of states per spin at the Fermi level, M_j is the mass of the moving atoms, $\omega_{B_{oc}}$ is the frequency of the B_{oc} mode and $\Delta\varepsilon_{\mathbf{k}}$ is the change in energy of the Kohn-Sham eigenvalues when the j -th component of the B_{oc} mode distortion is frozen in the compound. Now since the moving atoms are all O atoms, then $M_j = M_O$ and we can write

$$\left| \sum_j \frac{1}{\sqrt{M_j}} \frac{\Delta\varepsilon_{\mathbf{k}}}{|u_{B_{oc},j}|} \right|^2 = \frac{1}{M_O} \left| \sum_j \frac{\Delta\varepsilon_{\mathbf{k}}}{|u_{B_{oc},j}|} \right|^2 = \frac{1}{M_O} \left| \langle \Psi_{n,\mathbf{k}} | \nabla V^{KS} \cdot \epsilon_{B_{oc}} | \Psi_{m,\mathbf{k}'} \rangle \right|^2 \quad (5.9)$$

with $\epsilon_{B_{oc}}$ being polarization vector of the B_{oc} mode. Then we can evaluate $\nabla V^{KS} \cdot \epsilon_{B_{oc}}$ as

$$\nabla V^{KS} \cdot \epsilon_{B_{oc}} = \frac{V^{KS}(\Delta u_{B_{oc}}) - V^{KS}(0)}{|u_{B_{oc}}|} \quad (5.10)$$

Then we combine equations (5.10) and (5.9) obtaining that

$$\left| \sum_j \frac{1}{\sqrt{M_j}} \frac{\Delta\varepsilon_{\mathbf{k}}}{|u_{B_{oc},j}|} \right|^2 = \frac{1}{M_O} \left| \frac{\Delta\tilde{\varepsilon}_{\mathbf{k}}}{|u_{B_{oc}}|} \right|^2 \quad (5.11)$$

with $\Delta\tilde{\varepsilon}_{\mathbf{k}}$ being change in the Kohn-Sham energy eigenvalues when the total B_{oc} distortion is introduced. We then introduce these results back into equation (5.8) and recalling that $|u_{B_{oc}}|$ is directly the amplitude of the mode $Q_{B_{oc}}$ we arrive to the following expression:

$$\lambda_{B_{oc}} = 2N(\varepsilon_F) \sum_{\mathbf{k}} \frac{\hbar^2}{2M_O\omega_{B_{oc}}^2} \left| \frac{\Delta\tilde{\varepsilon}_{\mathbf{k}}}{Q_{B_{oc}}} \right|^2 \quad (5.12)$$

By calculating the electronic band structure for a Sr concentration $x = 0.1875$, which experimentally is superconducting, we realize that the pockets at Γ are no longer relevant, and only the electron pocket centered at the A point is important as it is depicted in Figure 5.11. Thus if

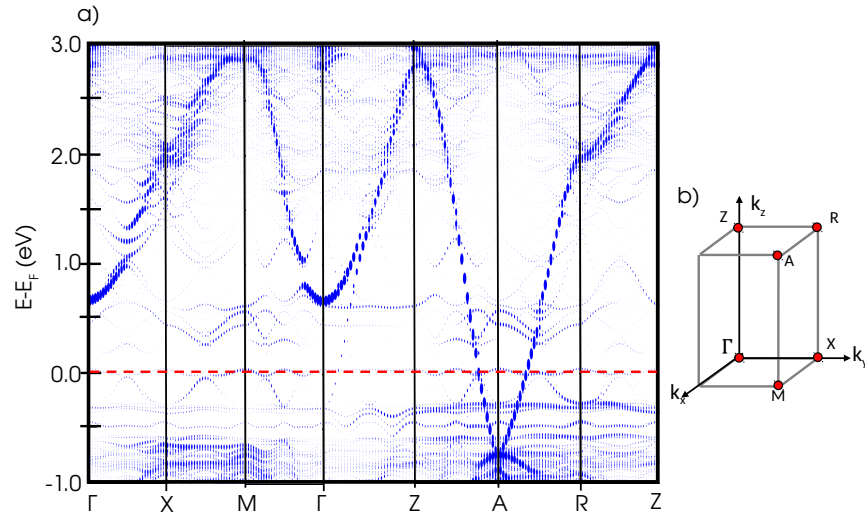


Fig. 5.11 Unfolded band structure for DSS $\text{La}_{0.8125}\text{Sr}_{0.1875}\text{NiO}_2$ with PM magnetic order. (a) The full band structure, (b) a sketch of the Brillouin zone associated to the primitive cell of P_4/mmm symmetry with high symmetry points highlighted. High symmetry points correspond are Γ (0,0,0), X (0,0,0), M (1/2,1/2,0), Z (0,0,1/2), R (1/2,0,1/2) and A (1/2,1/2,1/2).

we consider an average around the Fermi surface, we only consider changes in the Kohn-Sham eigenvalues around the $Z - A - R$ path and close to the Fermi level. In this way, we can then compute the EPC as

$$\lambda_{\text{B}_{\text{oc}}} = 2N(\varepsilon_F) \left\langle \frac{\hbar^2}{2M_O\omega_{\text{B}_{\text{oc}}}^2} \left| \frac{\Delta\varepsilon_{\mathbf{k}}}{Q_{\text{B}_{\text{oc}}}} \right|^2 \right\rangle_{\text{F.S.}} \quad (5.13)$$

We can then calculate the change in the eigenvalues as half of the band splitting ΔE_g once a finite $Q_{\text{B}_{\text{oc}}}$ amplitude is introduced $\Delta\varepsilon_{\mathbf{k}} = \frac{\Delta E_g}{2}$. By introducing this expression back to equation (5.13) we obtain

$$\lambda_{\text{B}_{\text{oc}}} = 2N(\varepsilon_F) \frac{\hbar^2}{2M_O\omega_{\text{B}_{\text{oc}}}^2} \left(\frac{\Delta E_g}{2Q_{\text{B}_{\text{oc}}}} \right)^2 = N(\varepsilon_F) \frac{\hbar^2}{2M_O\omega_{\text{B}_{\text{oc}}}^2} D_{\text{B}_{\text{oc}}}^2 \quad (5.14)$$

where $D_{\text{B}_{\text{oc}}}$ is the reduced electron-phonon matrix element (REPME), which is the response function of the electronic structure to a perturbation induced by a phonon displacement. We then proceed to calculate the EPC for each of the different doping concentrations. Since we have already calculated the frequency of the mode (see Figure 5.9.b) we are only left with the task of obtaining the density of states at the fermi level $N(\varepsilon_F)$ and the REPME $D_{\text{B}_{\text{oc}}}$. For the latter quantity, we introduce an amplitude of $Q_{\text{B}_{\text{oc}}} = 0.1106 \text{ \AA}$, at $x = 0.1875$, producing a band splitting of $\Delta E_g = 0.64 \text{ eV}$ along the $Z - A$ path (see Figure 5.12).

This approach of evaluating the REPME has two main weaknesses that have to be carefully evaluated. The first one is that by evaluating the REPME as $D_{\text{B}_{\text{oc}}} = \frac{\Delta E}{2u_{\text{B}_{\text{oc}},\text{O}}}$, with $u_{\text{B}_{\text{oc}},\text{O}}$ the displacement of a single O atom, we are implicitly assuming that we are within the harmonic regime and the deformation potential is linear with the amplitude $Q_{\text{B}_{\text{oc}}}$. Thus, we have to ensure that the band splitting is linear with the mode amplitude. We compute then the band splitting ΔE_g for different $Q_{\text{B}_{\text{oc}}}$ amplitudes in a SL geometry for $\text{La}_{0.75}\text{Sr}_{0.25}\text{NiO}_2$ with the

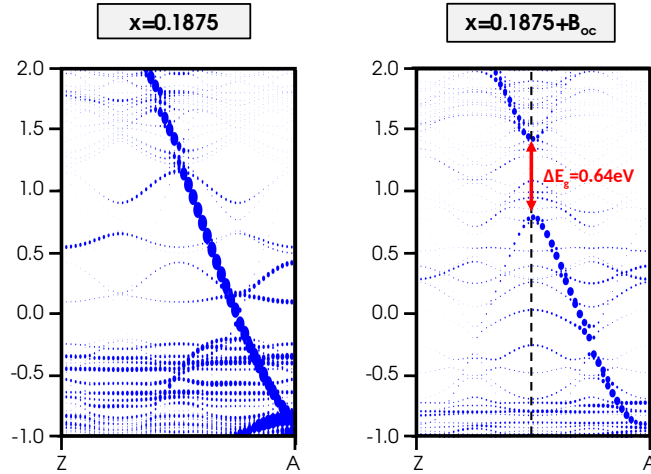


Fig. 5.12 Unfolded band structure of DSS La_{0.825}Sr_{0.187}NiO₂ along the $Z - A$ path with a finite amplitude of the B_{oc} mode (right) and without it (left). High symmetry points correspond to $Z = (0, 0, 1/2)$, and $A = (1/2, 1/2, 1/2)$ of the high symmetry P_4/mmm primitive cell.

SCAN functional and a type-E AFM order. A linear curve is obtained as it is depicted in Figure 5.13, where the slope is $2D_{B_{oc}}$, which is twice the REPME. This ensures that the extracted

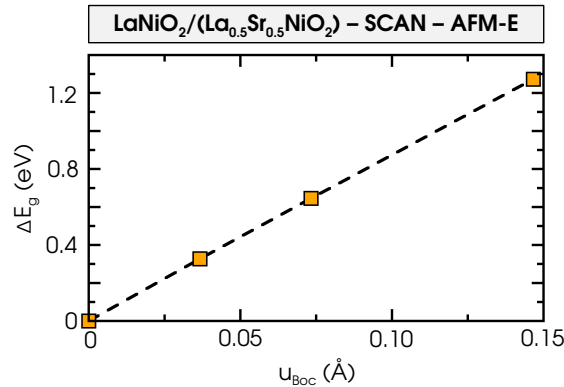


Fig. 5.13 Band splitting ΔE_g as a function of the atomic displacement $u_{B_{oc},O}$. The slope of the linear fit is equivalent to $2D_{B_{oc}}$, which is the REPME.

quantity is independent of the amplitude considered. The second problem is that since we are measuring a band splitting close to the Fermi level, we would suffer from the same inaccuracies as in the case of predicting accurate values for the band gap in the half-doped case. For that reason, we compute the band splitting with the HSE06 functional, on La_{0.75}Sr_{0.25}NiO₂ with a SL geometry and a type-E AFM which produces a band splitting of $\Delta E_g = 0.72$ eV (see Figure 5.14). Then we compute the band splitting with the SCAN functional yielding a value of $\Delta E_g = 0.49$ eV (see Figure 5.14.a). Comparing both gap amplitudes, we obtain an increase of 40% of the band splitting of the HSE06 functional with respect to the SCAN functional. Thus we then compute the REPME for the different Sr doping concentrations with the SCAN functional and then apply this 40% increase correction of the HSE06 functional (see Figure 5.14.b). As we can see, although the SCAN functional does not account quantitatively well for the amplitude of the gap, we can already notice a dome-shaped REPME, reminiscent of the critical temperature

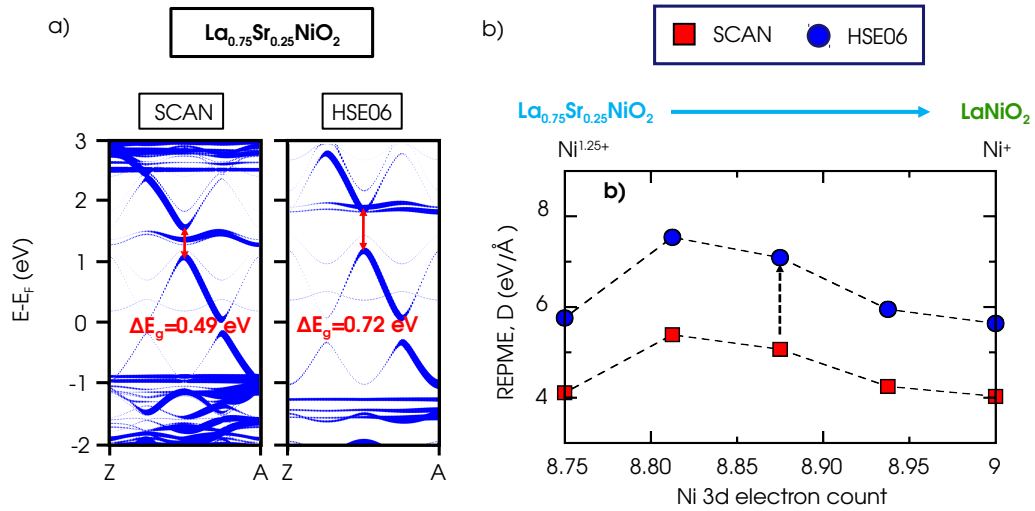


Fig. 5.14 Band splitting computed for $\text{La}_{0.75}\text{Sr}_{0.25}\text{NiO}_2$ with a SL geometry and a type-E AFM with SCAN (left panel) and HSE06 (right panel) functional.

T_c dome observed experimentally.

For evaluating the density of states at the Fermi level, we need a very precise value which implies a very dense k -mesh. This is a big problem since we have a supercell with 128 atoms. Thus in this case we use the Wannier Functions (WF) and the Wannier interpolation which enables us to obtain the total density of states with a $32 \times 32 \times 32$ k -mesh. This yields a highly converged total density of states and we repeat the procedure for the different doping concentrations (see Figure 5.15).

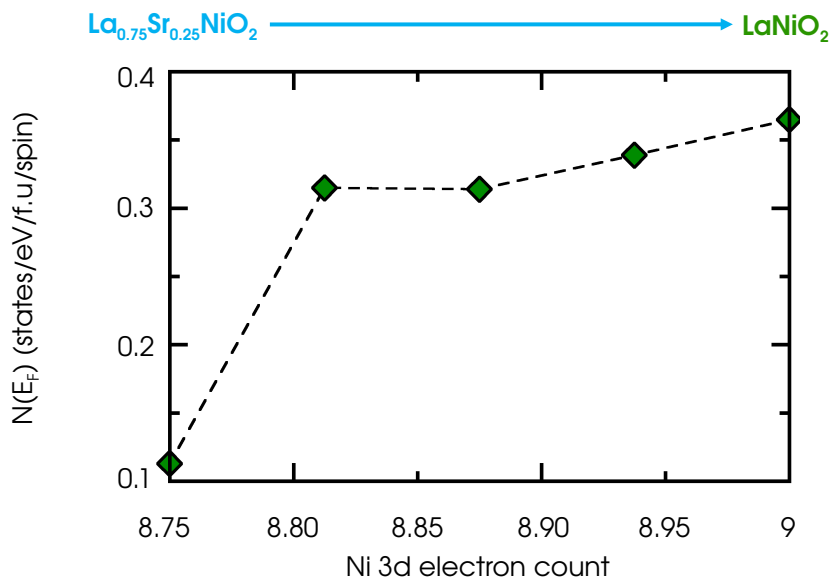


Fig. 5.15 Computed density of states at the Fermi level $N(\varepsilon_F)$ as a function of the electron count in the DSS of $\text{La}_{1-x}\text{Sr}_x\text{NiO}_2$.

One can notice that the density of states is nearly constant until it reaches $x = 0.25$ where it starts to drop signaling the region where the system would become insulating. With these quantities, we can obtain the EPC as a function of the doping content as depicted in Figure 5.16, obtaining a maximum value of $\lambda = 0.51$. This value is in good agreement with the analysis

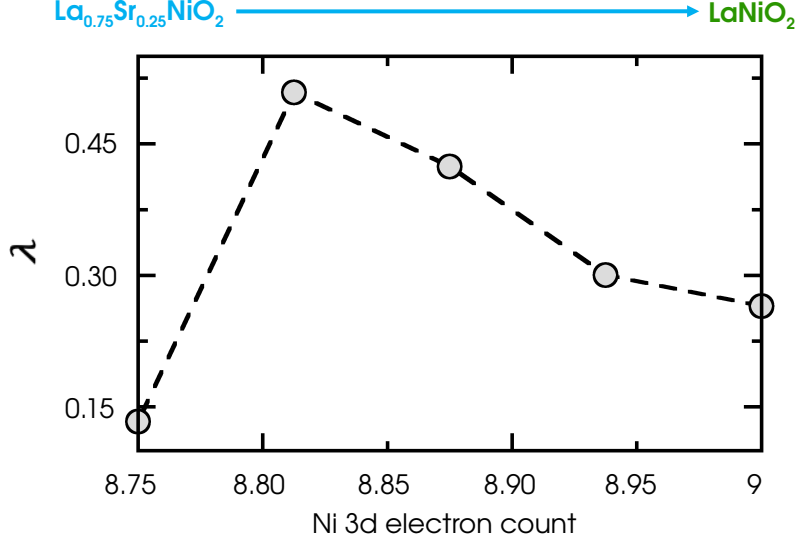


Fig. 5.16 Electron phonon coupling as a function of the 3d electron count.

of the experimental raw data performed by Talantsev, using several superconducting compounds and suggesting a possible electron-phonon SC mechanism with an EPC of $\lambda = 0.58 - 0.60$ [113]. The evolution of the EPC with the different doping concentrations yields a dome-like shape signaling that the dome on T_c found experimentally is intrinsic and not a cause of bad sample quality.

We can finally obtain an estimate of the critical temperature T_c by means of the Mc. Millan-Allens equation that presented in chapter 2 equation (2.93). Nonetheless, the equation presents three parameters λ , ω_c , and μ^* but we only have one λ . In that regard, we first make the approximation that the B_{oc} mode is a representative mode of the interacting phonons with the electronic structure. Now since the B_{oc} mode is a representative mode of the system, we can take it as the characteristic energy scale $\omega_c = \omega_{B_{oc}}$ for the calculation of the T_c . Secondly, we take the same value for the screened Coulomb interaction as $\mu^* = 0.13$ which is the obtained value in Ref. [113] from the analysis of the experimental raw data for a phonon-mediated mechanism. This value is a reasonable approximation since *ab initio* calculations typically show that $\mu^* = 0.1 - 0.15$ [159–161]. Under these approximations, our formula for the critical temperature T_c becomes

$$T_c = \frac{\hbar\omega_{B_{oc}}}{1.2k_B} \exp\left\{-\frac{1.04(1 + \lambda_{B_{oc}})}{\lambda_{B_{oc}} - \mu^*(1 + 0.62\lambda_{B_{oc}})}\right\} \quad (5.15)$$

This enables to calculate the critical temperature as a function of the Ni 3d electron count as depicted in Figure 5.17. Our model yields rather good agreement with the experimental values on Ref. La_{1-x}Sr_xNiO₂ [68], being able to reproduce both SC region and metallic but

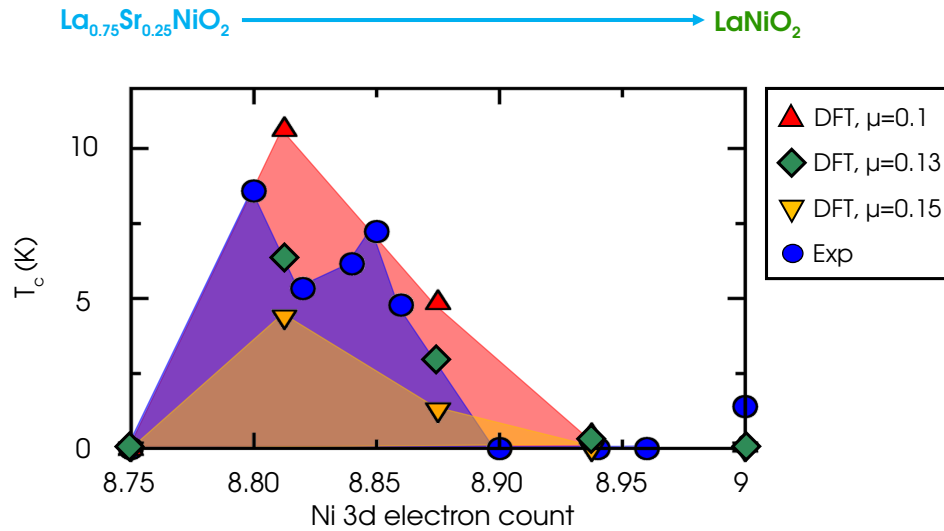


Fig. 5.17 Critical temperature as a function of the 3d electron count on Ni cations for $\text{La}_{1-x}\text{Sr}_x\text{NiO}_2$. Blue dots are the experimental points extracted from Ref. [68], green diamonds and yellow and red triangles are the computed values from DFT using equation (5.15).

not SC region at the end of the phase diagram. However, one may wonder how much the μ^* parameter affects the computed critical temperature. In that regard, we can repeat the calculation for $\mu^* = 0.15$ and $\mu^* = 0.1$ which are the typical upper and lower reasonable values for this parameter. We report the results in Figure 5.17 and we see that the dome shape T_c is still predicted well. Thus the model is able to reproduce qualitatively and quantitatively well, the doping or Ni 3d electron count phase diagram predicting (i) an insulating region with some CO due to an electronic instability, (ii) the SC region for a narrow range of 3d electron count, and (iii) the simply metallic region without the signature of a SC transition. The behavior in the latter region can be ascribed as a consequence of the hardening of the phonon modes that contribute to the SC phase as it is depicted in Figure 5.6.b.

5.6 Discussion

Although explaining qualitatively and quantitatively the experimental phase diagram of these nickelates, our results contradict the analysis performed by Nomura et al. [115] that discarded the possibility of a phonon-mediated scheme. First we must note that the study uses a standard GGA functional to deal with highly localized 3d and 4f states. This is nothing but a good practice since at least a GGA+U approach would be required, to properly describe these highly localized states, that are the main actors in the conduction. Secondly the study uses the NM approximation neglecting completely all the spin-spin correlations, that are expected for transition metal elements with open shells. Other authors have also proposed a phonon-mediated scheme, successfully reproducing the values for the T_c employing the full Eliashberg equations including all phonon modes and using Green's function technique *GW* proposing a multi-gap *s*-wave pairing symmetry scenario [245]. The study, however, uses the NM approximation which

produces the same T_c for all doping contents. This is a crucial point and we will show it in the coming section.

5.6.1 Doping phase diagram and the spin degree of freedom

We divide this section by discussing two main points. First, we discuss how dramatic it is to use the NM approximation in the predictions, and second, we show how the predictions can be affected by long-range magnetic orders.

Role of the spin degree of freedom

We have already evidenced that the NM solution is not suitable for discussing the electronic properties of the undoped IL compounds, since it yields a very different band picture when compared with the random PM solution that we use (see chapter 4). Then we will evidence that it is not suitable for the doped compounds either. To that aim, we relax the whole phase diagram of the IL La_{1-x}Sr_xNiO₂ with the DSS geometry and compare the total energy of the system with respect to the PM phase. We report in Figure 5.18 the energy difference between

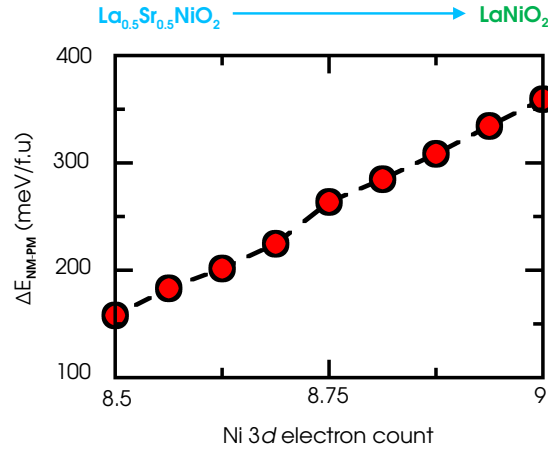


Fig. 5.18 Total energy difference between the non-spin polarized NM solution and the random spin PM solution $\Delta E_{\text{NM-PM}}$ in eV/f.u. as a function of the Ni 3d electron count. Positive values indicate that the PM solution is more stable, while negative values indicate that the NM solution is more stable.

the NM and PM solutions $\Delta E_{\text{NM-PM}}$ as a function of the Ni 3d electron count. We must note that $\Delta E_{\text{NM-PM}} > 0$ implies that the PM is more energetically favorable, while $\Delta E_{\text{NM-PM}} < 0$ implies that the NM is more energetically favorable. As it is evidenced in Figure 5.18, the total energy difference between the two phases is always positive, which means that the PM solution is more stable regardless of the doping content for $0.5 \leq x \leq 0$. In addition, the PM solution is at least 1800 K/f.u. (around 150 meV/f.u.) more stable than the NM phase. This quantity should be compared with the SC T_c not exceeding 23 K in these compounds. Thus important parts of the energy of the system are clearly neglected by not including the spin degree of freedom.

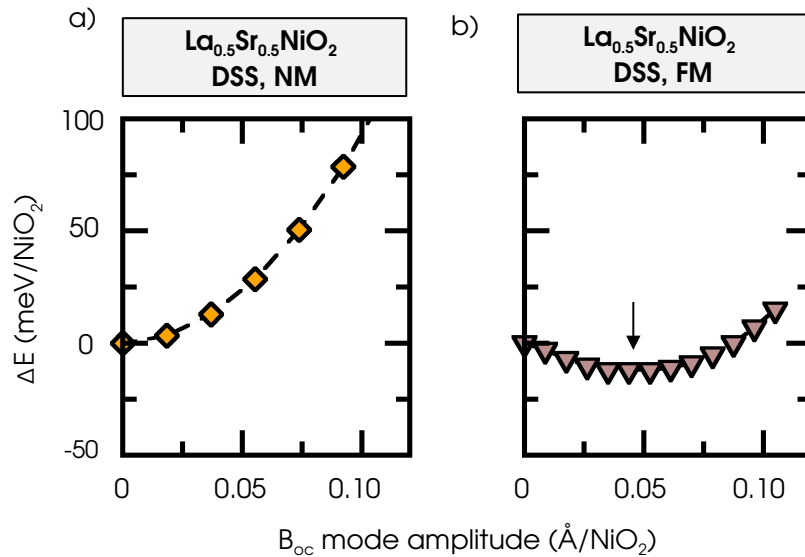


Fig. 5.19 Potential energy surface of the B_{0c} mode in the DSS of $\text{La}_{0.5}\text{Sr}_{0.5}\text{NiO}_2$ with (a) a non-spin polarized solution NM, and (b) a ferromagnetic order FM.

In spite of these important total energy differences, one may still hope that the phonon spectra is still well accounted in the NM solution, and in particular the B_{0c} mode could still be well accounted. In that regard, we compute the PES of the B_{0c} mode with the NM solution and we compare it with a FM solution that is expected to produce less localization. In order to have the highest amplitude of the mode we use the DSS of $\text{La}_{0.5}\text{Sr}_{0.5}\text{NiO}_2$. Unfortunately as it is verified by comparing the curves on Figures 5.19.a and 5.19.b, the NM solution is completely unable to predict the electronic instability and the appearance of the B_{0c} mode at half-doping (see Figure 5.19), since it presents a single well potential with its minimum at zero amplitude. This is at odds with the FM solution that it does present a shifted single well signaling the electronic instability.

Although we have evidenced the lack of success of the NM solution to account for important phonons of the system such as the B_{0c} mode, we could still hope to have a good electronic structure description in the doped materials. We then explore how good the NM approximation is by comparing the electronic structure of the half-doped DSS in the PM case and in the NM solution. Thus we calculate the band structure for both cases reporting them in Figure 5.20. It becomes clear that the NM solution produces a qualitatively different band dispersion to the PM. The band character in both cases is rather similar to the undoped IL phase discussed in chapter 4 (see Figure 4.9). However, the small Γ and A electron pockets have almost disappeared and pushed up, with the Γ centered bands being pushed 1 eV above the Fermi level, and the A centered electron pocket sitting just at the Fermi level in the PM case (see Figure 5.20.a), and with a reduced bandwidth of 0.5 eV in the NM case. However, the biggest difference comes from the highly dispersive band with a Γ centered electron pocket and a M -centered hole pocket of the NM (see Figure 5.20.b). This band as we discussed previously on chapter 4, corresponds to the $d_{x^2-y^2}$ orbital [216–223], which remains dominant at the Fermi level also at this doping

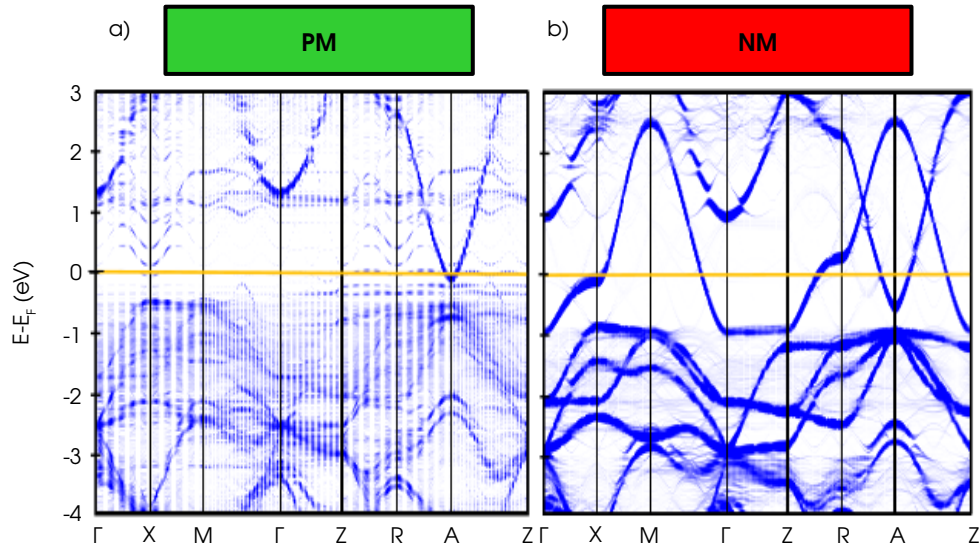


Fig. 5.20 Electronic band structure of La_{0.5}Sr_{0.5}NiO₂ DSS with (a) no magnetism (NM), and (b) with PM order. The band dispersion is unfolded to the primitive P_4/mmm cell. High symmetry points correspond are Γ (0,0,0), X (0,0,0), M (1/2,1/2,0), Z (0,0,1/2), R (1/2,0,1/2) and A (1/2,1/2,1/2).

concentration for the NM solution.

Strictly speaking, both PM and NM solutions produce a metallic compound and we need to use the HSE06 functional to produce an insulating state since the SCAN functional still presents some delocalization errors. Thus one could hope that if the HSE06 functional would be used instead, it would have correctly predicted an insulating compound since the exchange part of the energy would be improved. In that regard, we use the SL to compute the electronic density of states using the NM and HSE06 functional, since the supercell would be much smaller than the DSS. The results are reported in Figure 5.21.

Interestingly the HSE06 functional yields a metallic compound despite of improving the description of the exchange correlation phenomena. The reason is that in the NM approximation, Hund's rule is not satisfied producing a metallic compound with the $d_{x^2-y^2}$ orbital at the Fermi level. This however is completely wrong, since as it can be verified in Figure 5.5.a and 5.5.b, the last occupied orbital is the d_{z^2} on both Ni_L and Ni_S. Thus satisfying the basic Hund's rule for Ni cations is crucial for describing qualitatively well the features of these nickelates since a non-spin polarized (NM) DFT calculation yields (i) a metallic system regardless of how well the exchange-correlation phenomena is described, and (ii) a single well potential for the B_{oc} mode whose minimum is centered at zero amplitude (Figure 5.6.a). In contrast, all additional calculations performed including the spin degree of freedom show the stabilization of the mode (see Figure 5.6 for the PM case and Figure 5.19.b for the FM). This is in agreement with the existence of the breathing mode B_{oc} in the perovskite RNiO₃ phase that requires Hund's rule to be respected [151] (i.e. formation of local spins). Nevertheless, disproportionation effects are

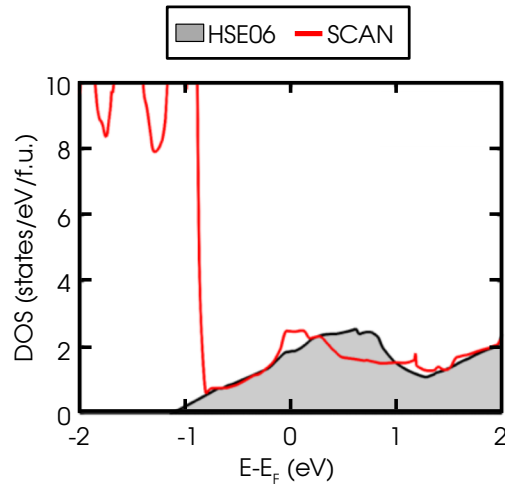


Fig. 5.21 Total density of states of $\text{La}_{0.5}\text{Sr}_{0.5}\text{NiO}_2$ in a SL with the NM solution. The gray area are the results using the SCAN functional, and the red line are the results obtained with the HSE06 functional.

unrelated to correlation effects as is extensively discussed in Refs [151, 165, 13, 246].

With these results, we can state that Ref. [115] fails at discussing the SC properties due to both poor description of the exchange correlation phenomena and the absence of the spin degree of freedom in the calculations. In the case of Ref. [116], the exchange correlation phenomena is very well described but as we saw, neglecting the spin degree of freedom leads to predict a different phonon spectra since it neglects the role of the B_{oc} mode, and in addition, predict a metallic character in the whole doping phase diagram. In fact, in Ref. [116] the T_c is evaluated only for the already known SC region, very likely because the NM approximation predicts a metallic system for all doping concentrations with $0 \leq x \leq 0.5$ (see Figure 5.21). This would possibly lead to predict SC for all doping ranges at odds with the experiments. This further shows the importance of including the spin degree of freedom in the calculations. Thus our model up to date is the only phonon-mediated approach that is able to qualitatively and quantitatively describe the whole phase diagram of these compounds.

Magnetic order independence of the phase diagram

We can further validate our CO dome by repeating the calculations with a type-E AFM and computing both the magnetic moment asymmetry $\Delta\mu$ and the amplitude of the mode $Q_{B_{oc}}$. We obtain exactly the same trend as we can verify in Figure 5.22, suggesting that it is a real physical effect and does not depend on the magnetic order. This highlights that by only including the spin degree of freedom we can already predict the CO insulating region, and at least the simply metallic region for doping contents $x \leq 0.25$ as opposed to the NM solution.

We can then aim at calculating a critical temperature in the SC region using the procedure employed previously. To that aim we take the doping content $x = 0.1875$ which is the doping

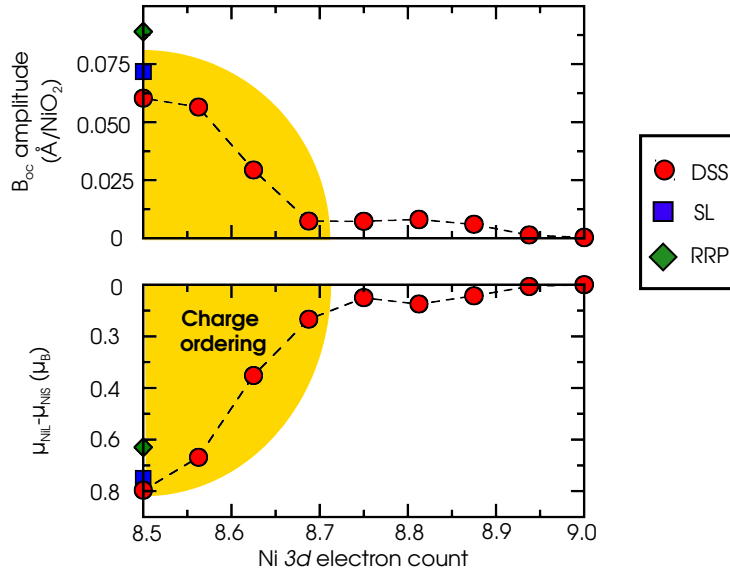


Fig. 5.22 Trends in disproportionation effects with a type-E AFM order signaling the charge ordered phase with the $3d$ electron count for two key quantities (a) the amplitude of the B_{0c} mode in $\text{\AA}/\text{NiO}_2$ motif, and (b) the absolute value of the difference in the magnetic moment of Ni_L and Ni_S cations. Both quantities are represented for $\text{La}_{0.5}\text{Sr}_{0.5}\text{NiO}_2$ solid solution (red dots DSS), superlattice (blue squares SL), and for $\text{La}_3\text{Ni}_2\text{O}_6$ (green triangles RRP).

content that produces the highest calculated critical temperature (see Figure 5.17). We compute the frequency from the PES obtaining $\omega_{B_{0c}} = 62$ meV, which is similar to the obtained for the PM phase. Then we evaluate the density of states at the Fermi level, obtaining $N(\varepsilon_F) = 0.46$ states/eV/f.u./spin, which is similar to the values reported in Figure 5.15. Finally we evaluate the REPME with SCAN obtaining a value of $D_{B_{0c}} = 4.27$ eV/ \AA , which is also close to the value reported in Figure 5.14. Then we apply the 40% enhancement that we reported for the SL using the HSE06 functional, yielding a final value of $D_{B_{0c}} = 6.03$ eV/ \AA . With these three quantities and equation (5.14), we estimate the EPC to be $\lambda = 0.57$. This is rather good when compared to the PM value of $\lambda = 0.51$. Finally we evaluate the critical temperature with equation (5.15), taking $\mu^* = 0.1 - 0.15$ we can estimate the critical temperature to be $T_c = 14 - 7$ K, in fair agreement with the reported values in Figure 5.17 from both PM DFT calculations and experiments.

Thus with this results we confirm that by allowing the spin degree of freedom, the DFT calculations are able to reproduce at least qualitatively well the doping phase diagram since the three regions, (i) CO insulating, (ii) metallic but not SC, and (iii) metallic with a SC transition, can be predicted. However the exact magnetic order does not seem to be so important to predict the low energy physics trends of these materials.

5.6.2 Pairing symmetry

Several authors suggest complex pairing symmetries beyond the simple s -wave case [111, 74, 247–251]. Thus one may question the validity of the Mc. Millan-Allens equation for evaluating the T_c . Nonetheless, we can recall the discussion in chapter 1 about the pairing

symmetry, where we have shown that imposing a given symmetry on the gap function, yields the same type of equation for the T_c as we stated in equation (1.67), where the important point is to obtain the right energy scale ω_c^l and the coupling parameter $\lambda^l = V_0^l N$. As a consequence, we can be confident about the validity of equation (5.15), that albeit does not give us any information about the symmetry. It is true that the most common pairing symmetry within a phonon-mediated mechanism is the s -wave which is also suggested in Refs [112, 113] since it is the easiest explanation and it is not in conflict with several experiments on London penetration depth [74, 111] as well as optical response on the SC state [114]. However, we can point out that a phonon-mediated mechanism does not imply an isotropic pairing symmetry or even an s -wave pairing symmetry. In fact, some studies show that the electron-phonon interactions are anisotropic and in particular the breathing distortion. Thus the proposed model based on optical phonons strongly coupled to the electronic structure is not in conflict with the available experimental data.

5.6.3 Similarities with other superconductors

In what concerns the Cu based superconductors, we do not see a clear equivalence between the superconducting mechanism in these nickelates and in the cuprates. There are some similarities such as an important in-plane exchange constant, as we saw in chapter 4, as well as the layered structure, but the orbitals involved in the conduction, the Mott or CT character, and the doping phase diagram seems rather different when the nickelates are compared with the cuprates. Nonetheless, the existence of a CO phase in the vicinity of the SC phase of these nickelates, makes these compounds rather close to the case of bismuth-like superconductors, where the superconducting phase is also close to a charge-ordered phase [165, 240]. In particular, the very same type of phonon that is responsible for the charge-ordered insulating phase in the bismuthates plays also an important role in the superconducting mechanism, where the phonon associated with the charge order, is still highly coupled to the electronic structure and can produce a sizable electron-phonon coupling (EPC) [165]. In that regard, since both systems seem to be rather similar, we can propose that the superconductivity in these nickelates can be phonon mediated and the main actor will be the B_{oc} mode.

5.7 Conclusion

We conclude here that the layered nickel oxides are better understood starting from the first member of the RRP phase ($n = 1$) instead of the last one corresponding to the IL phase ($n = \infty$). This approach allows us to reveal the existence of a CO instability in the phase diagram that produces a bond and charge ordering on the NiO_4 square complexes and an insulating phase. Then we show that this CO insulating phase can be destabilized by increasing the effective number of d electrons per Ni site which ultimately leads to a metallic regime at the right doping content. We further show that the SC region is just in the vicinity of the stable CO phase where the phonon modes responsible for the CO instability are also responsible for the pairing in the SC phase. We also explain that the SC region within the metallic phase is not present

everywhere and is a consequence of the hardening of the CO modes at higher $3d$ electron count. In addition, we highlight that the model should be general for all the rare earth compounds that present this layered structure and are doped with a divalent cation.

Chapter 6

Strengths and limitations of the superconducting model

As we have seen, the superconducting mechanism of the IL phase compounds can be explained as a consequence of an electron-phonon coupling (EPC) associated with a charge ordering (CO) and a bond disproportionation phonon mode, where the key characteristics of the experiments are well reproduced. Nonetheless, we have assumed that the IL phase belongs to the broader family of compounds of the RRP series, being the limiting member $n = \infty$, and then we have suggested that the properties of these layered materials are universal regardless of the geometry.

However, we have only shown that the universality is true for one member of the series corresponding to a half-doped situation ($n = 2$). Thus one could object that formally we have not demonstrated such equivalence. In that regard, we will explore in this chapter the phase diagram of the La-based RRP compounds ($\text{La}_{n+1}\text{Ni}_n\text{O}_{2n+2}$) from $n = 1$ to $n = 5$ to reveal whether our assumption holds true or not.

Furthermore, we highlighted in the previous chapter that an accurate description of the exchange and correlation (xc) phenomena is needed for computing the reduced electron-phonon matrix element (REPME). Thus instead of using both the SCAN and the HSE06 functionals, we explore the phase diagram of $\text{La}_{n+1}\text{Ni}_n\text{O}_{2n+2}$ compounds using only HSE06. In that regard, we use the CRYSTAL 17 code [252, 253] in which hybrid DFT calculations are well implemented and are computationally less expensive since the code uses a gaussian basis set. Additionally, we explore the limitations of our model and how other degrees of freedom apart from the Ni FOS can change the physics of these nickelates with particular interest in designing SC compounds. To that aim, we collaborated with an experimental team from the CRISMAT laboratory that aimed to synthesize a superconducting nickelate guided solely by the FOS of Ni cations.

6.1 General phase diagram of layered nickel oxides

As we mentioned in the previous chapter, the reduced Ruddlesden-Popper compounds (RRP) are a series of materials that originate mainly from the reduction of a parent perovskite-like

Ruddlesden-Popper (RP) phase. This new family is similar to the RP series although it

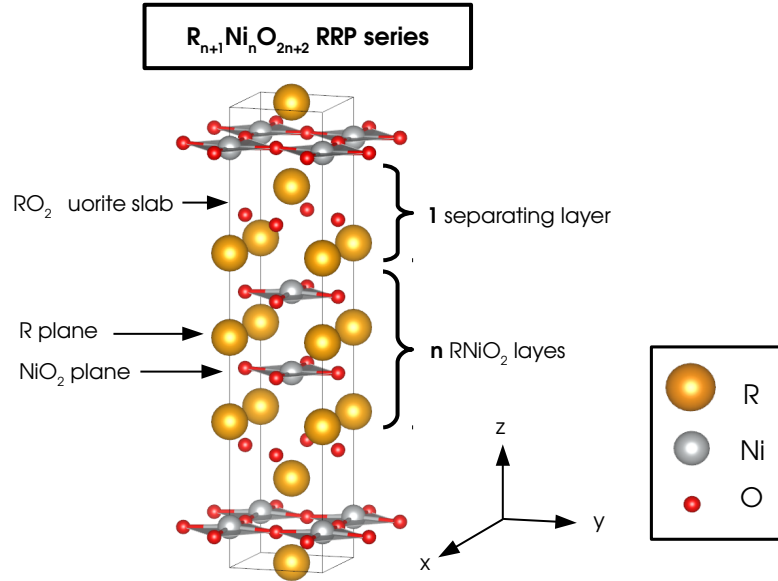


Fig. 6.1 Crystal structure of the reduced Ruddlesden-Popper series (RRP) with chemical formula $R_{n+1}Ni_nO_{2n+2}$.

presents some important differences. The most general chemical formula of the RRP series is $R_{n+1}Ni_nO_{2n+2}$, which is characterized by a positive integer number n . The crystal structure of these compounds is characterized by NiO_2 planes stacked along the c axis with a rare earth cation in between R, and after a period of n layers, a separating RO_2 fluorite layer is found (see Figure 6.1). It is remarkable to notice that the effective Ni formal oxidation state (FOS labeled δ) changes in the series, and it can be computed for each member n with the following relation $\delta = \frac{n+1}{n}$.

In the existing literature, few studies discuss the RRP series, where either they focus on specific cases of the series [38–41, 47–64, 201, 243] or they study the whole series but neglect the spin and/or the structural degrees of freedom, leading to either all compounds to be metallic [254, 255] or insulating if a long-range antiferromagnetic (AFM) order is imposed [256]. This behavior is at odds with the experiments where the $n = 2$ ($\delta = 1.5$) compounds are insulating [47–50], the $n = 3$ ($\delta = 1.33$) case is found to be insulating at low temperatures [52–54, 59–61] but a small pressure effect can turn it to a metal [55, 56] and the $n = 5$ ($\delta = 1.2$) case is found superconducting [73]. This collection of experimental results shows that there has to be a transition between insulating to metallic character with increasing n in the RRP series of compounds. This is rather similar to the IL case and in that regard, we should be able to reproduce well these results from our calculations.

We perform electronic structure calculations with CRYSTAL 17 setting an energy convergence criteria of 10^{-9} Hartree for all the calculations with this code. The structural optimizations include lattice parameters and atomic positions, and they are performed until the root mean square of the gradients and estimated displacements are lower than $3 \cdot 10^{-4}$ Hartree/Bohr. Regarding the basis set, we use Gaussian type orbitals (GTO) with core electrons treated in the

pseudopotentials for La cations [257, 258], and all-electron basis set is used for Ni cations and O ions [259, 260].

6.2 Importance of spin polarization

Before studying in detail the RRP series, we evidence once more the need to include the spin degree of freedom by performing a study of the phase diagram ($n = 1 - 5$), using the non-spin-polarized NM approximation.

Compound	RRP n value	Ni FOS	Space group	$a(\text{\AA})$	$c(\text{\AA})$	$E_g(\text{eV})$
La_2NiO_4	1	2.00+	I_4/mmm	3.70	13.45	1.36
$\text{La}_3\text{Ni}_2\text{O}_6$	2	1.50+	I_4/mmm	3.95	18.93	0
$\text{La}_4\text{Ni}_3\text{O}_8$	3	1.33+	I_4/mmm	3.96	25.36	0
$\text{La}_5\text{Ni}_4\text{O}_{10}$	4	1.25+	I_4/mmm	3.96	31.84	0
$\text{La}_6\text{Ni}_5\text{O}_{12}$	5	1.20+	I_4/mmm	3.96	38.33	0

Table 6.1 Summary of the key quantities of the RRP $\text{La}_{n+1}\text{Ni}_n\text{O}_{2n+2}$ compounds with ($n = 1 - 5$) obtained from the DFT calculations with a NM solution. Including the ground state structure space group, lattice parameters in the conventional cell a and c in \AA , Ni formal oxidation state (FOS), and gap amplitude E_g in eV.

By inspecting the key quantities extracted from the calculations in Table 6.1, we find that (i) all compounds present conducting behavior except the first member ($n = 1$) that is insulating and (ii) all ground states are achieved with a high symmetry I_4/mmm crystal structure as in previous studies [254, 255].

As we mentioned, the $n = 1$ case is identified to be a band insulator with a band gap of 1.36 eV. This is understood by realizing that within the NM approximation, a $3d^8$ low spin ($S = 0$) electronic configuration is enforced (see Figure 6.2). This means that the Hund's coupling is neglected and the crystal field splitting of doubly occupied $3d$ shell for Ni^{2+} cation is the responsible of opening a band gap. (see Figure 6.2.a). However, this is in contrast with experiments that reveal the existence of a magnetic moment of $1.48\mu_B$ per Ni cation in La_2NiO_4 [38, 236], and thus suggesting a high spin configuration as depicted in Figure 6.2.b. The high symmetry cell identified with DFT is also at odds with the experimental structure exhibiting $a^-a^-c^+$ octahedral rotations with $Cmce$ space group [38, 261, 262]. Even though we start from this structure, it relaxes back to a I_4/mmm cell with no distortion. Regarding higher members of the series, the observation of a metallic character for $n = 2$ or $n = 3$ disagrees with the experimental observation of an insulating state at low temperatures [47–50, 52–54, 59–61].

This general failure of the NM approximation is grounded on the fact that Hund's rule is broken and important terms in the energy are not well accounted. We evidence our claims by performing spin-polarized FM calculations in the high symmetry I_4/mmm cell and compute the

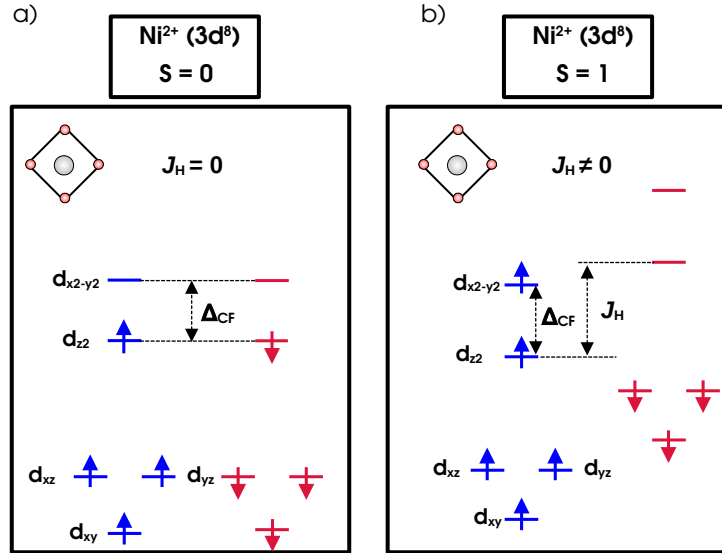


Fig. 6.2 Diagram of the crystal field splitting in on Ni^{2+} cations with a $3d^8$ electronic configuration in the case of La_2NiO_4 for two different situations, (a) when Hund's coupling is neglected and a NM solution is employed in the DFT calculations producing a $S = 0$ spin state, and (b) when Hund's coupling is included and the spin degree of freedom is allowed in the DFT calculations producing a $S = 1$ spin state.

total energy difference between the two types of calculations. This allows us to reveal the sole effect of the spin degree of freedom in the energy of the system without including any lattice distortions that may appear in the global ground state. We report the results in a graph on Figure 6.3. It becomes evident that there is a massive energy gain $\Delta E_{\text{NM-FM}}$ of at least 375 meV/ NiO_2 motif for all $n = 1 - 5$ RRP compounds, signaling that by not including the spin degree of freedom a huge part of the energy of the system is not well accounted for. We can further deduce that the RRP compounds are characterized by a large Hund's coupling, since the $n = 1 - 4$ RRP compounds are now predicted to be insulators once the structure is allowed to relax to lowest symmetry while the $n = 5$ is a metal, we discuss each member in detail in the next section. These results are much more consistent with the experiments highlighting the importance of the spin degree of freedom.

Thus we conclude here that (i) local Ni spin formation in these nickelates is a key factor that should not be overlooked in the DFT simulations and (ii) even though we treat exchange correlation phenomena at the highest level in DFT simulations, the NM solutions remain irrelevant for modeling the electronic properties of oxide superconductors.

6.3 Properties of La based RRP compounds

We now allow the spin polarization at the lowest level by imposing a ferromagnetic (FM) order in the DFT simulations. Although some compounds may exhibit antiferromagnetic (AFM) interactions such as $n = 2$ and $n = 3$ members [51, 62], the choice to restrict the study to a

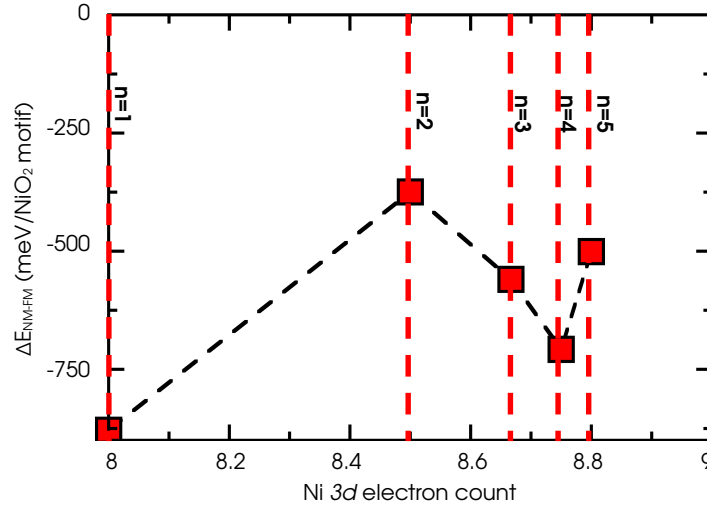


Fig. 6.3 Energy difference $\Delta E_{\text{NM-FM}}$ between a non-spin-polarized (NM) and ferromagnetic (FM) order (in meV/NiO₂ motif) as a function of the formal Ni 3d occupancy in the reduced Ruddlesden-Popper compound. Red dashed lines indicate the position of each member n of the series.

FM order is guided by the fact that we seek to extract the sole effect of doping within the RRP nickelates without the effect of AFM correlations. We present in Table 6.2 the key results from our calculations where in this case we allow the structure to lower the symmetry and accommodate different lattice distortions. We notice that for almost all members of the series,

Compound	La ₂ NiO ₄	La ₃ Ni ₂ O ₆	La ₄ Ni ₃ O ₈	La ₅ Ni ₄ O ₁₀	La ₆ Ni ₅ O ₁₂
S. group	<i>Cmce</i>	<i>Cmmm</i>	<i>Fmmm</i>	<i>Cmcm</i>	<i>I₄/mmm</i>
a(Å)	5.45	5.61	5.63	11.28	4.01
b(Å)	5.58	5.61	16.88	11.28	4.01
c(Å)	12.51	18.88	25.31	31.71	38.07
E _g (eV)	2.80	1.24	1.00	1.49	0
ΔE (meV/f.u.)	-28	-263	-313	-398	0
μ _{Ni_L} /μ _{Ni_S} (μ _B)	1.73/1.73	0.93/0.09	0.93/0.15	0.93/0.17	0.77/0.77
Q _{B_{oc}} /(Å/NiO ₂)	0	0.088	0.074	0.054	0

Table 6.2 Summary of the key quantities of the RRP La_{*n*+1}Ni_{*n*}O_{2*n*+2} compounds with ($n = 1 - 5$) obtained from the DFT calculations with a FM solution. Including the ground state structure space group, lattice parameters in the conventional cell a , b and c in Å, gap amplitude E_g in eV, energy difference with respect to the high symmetry I_4/mmm cell ΔE in meV/f.u., magnetic moment on the two types of Ni sites (Ni_L and Ni_S) that can be expected in μ_B, and amplitude Q_{B_{oc}} of the disproportionation mode in Å/NiO₂ motif.

the symmetry is lower than the I_4/mmm with important energy gains in some cases. This indicates that the lattice distortions play an important role in these compounds and should not be overlooked. This behavior is much expected as we saw in the previous chapter, the $n = 2$ member presents a charge-ordered insulating (COI) phase that is characterized by a bond disproportionation mode B_{oc} and an asymmetry on the Ni magnetic moments. Thus we explore

in detail these types of distortions in the whole series.

The $n = 1$ member exhibits Ni cations with a 2+ FOS and hence a Ni $3d^8$ electronic configuration. The compound is an insulator thanks to the crystal field splitting and Hund's rule that fills completely the occupied orbitals in both majority and minority spin channels as it is depicted in Figure 6.2.b. This is further verified by the projected density of states of Figure 6.4 where we find an insulating state with a gap of $E_g = 2.70$ eV. This value is slightly overestimated

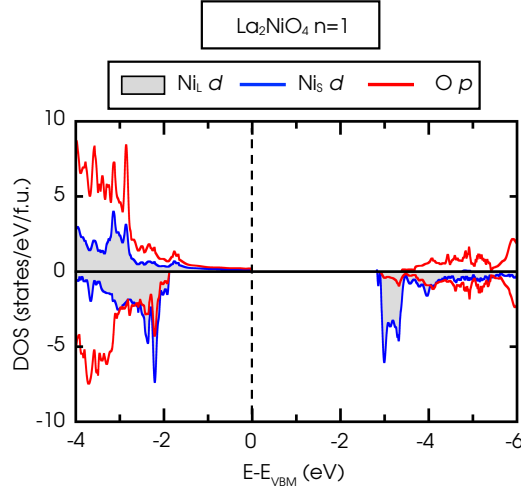


Fig. 6.4 Projected density of states of La_2NiO_4 with a FM order and $Cmce$ crystal symmetry on O p states (red line), Ni_L d states (solid grey) and Ni_S d states (blue line). Positive and negative values of the DOS indicate the majority and minority spin channels.

when compared with experiments measuring 1.5 eV [263]. Nonetheless we must note that (i) the measurements are performed at finite temperature while DFT is a 0K calculation, (ii) the compound is paramagnetic at room temperature while we impose a FM order in the calculation. Thus the exact values for the band gap may differ slightly. The band edges are formed by Ni d states and O p states at the valence band maximum (VBM) and dominantly Ni d states at the conduction band minimum (CBM), indicating that this compound is a charge transfer insulator. The absence of a CO is evident since the magnetic moment on all Ni cations is $1.73\mu_B$ (see Table 6.2) and there is no signature of two types of Ni sites in the density of states (see Figure 6.4). We notice however, that the energy difference between the high symmetry I_4/mmm phase and the low temperature $Cmce$ is rather small $\Delta E = -28$ meV as shown in Table 6.2, and is in contrast with the huge energy gain obtained between the high symmetry NM and the FM depicted in Figure 6.3. This is not surprising since (i) La_2NiO_4 does not present any charge ordering and only at around $T = 750$ K it develops some lattice distortions [38, 261, 262], and (ii) although the compound is characterized by in plane AFM interactions experimentally, we are using a FM solution which favors a more delocalized structure than the AFM orders [26]. Thus the amplitude of the distortions and the overall energy gain is reduced.

Regarding the next member of the series $\text{La}_3\text{Ni}_2\text{O}_6$ ($n = 2$), one could expect a metallic regime due to partly filled Ni d sates ($\text{Ni}^{1.5+}$ with a $3d^{8.5}$ electronic configuration). However, the material is insulating with a band gap of 1.24 eV (see Figure.6.5.a). This is a consequence of the

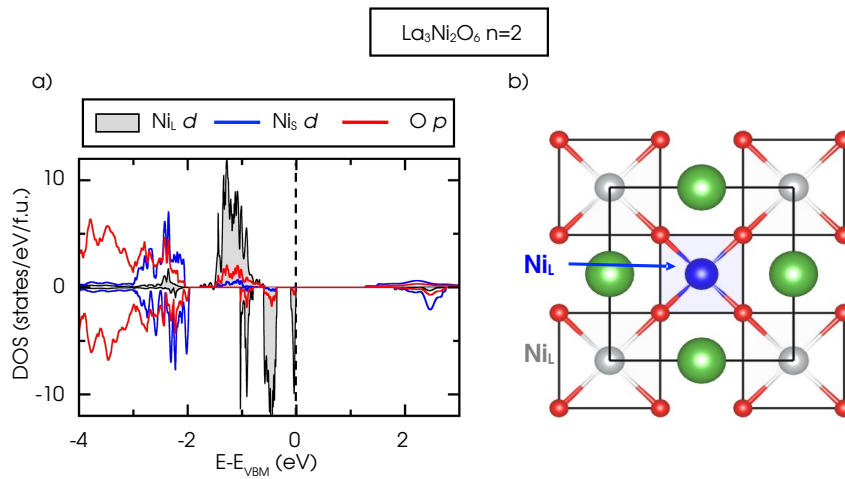


Fig. 6.5 $\text{La}_3\text{Ni}_2\text{O}_6$ (a) projected density of states with a FM order and $Cmmm$ crystal symmetry on O p states (red line), Ni_L d states (solid grey) and Ni_S d states (blue line). Positive and negative values of the DOS indicate the majority and minority spin channels. (b) Crystal structure of the bond disproportionation mode B_{oc} producing two types of Ni cations Ni_L in grey and Ni_S in blue.

appearance of a bond disproportionation mode B_{oc} producing a checkerboard pattern of different Ni cations sitting in compressed (Ni_S) and extended (Ni_L) O_4 complexes (see Figure 6.5.b). It produces a change in the crystal symmetry to $Cmmm$, and an energy gain of $\Delta E = -263$ meV/f.u. with respect to the high symmetry undistorted I_4/mmm cell. Thus unlike in the $n = 1$ case, here both spin and structural degrees of freedom prove to be crucial for describing the low temperature phase of this compound. A consequence of the appearance of this mode is that the electronic structure of Ni cations splits with Ni_L cations possessing a $3d^9$ electronic configuration with a magnetic moment of $\mu_{\text{Ni}_L} = 0.933\mu_B$ while Ni_S cations exhibit a low-spin $3d^8$ configurations with $\mu_{\text{Ni}_S} = 0.091\mu_B$ (see Table 6.2). Therefore, a clear charge ordering with a 1/1 ratio of $\text{Ni}_L^+/\text{Ni}_S^{2+}$ with propagation vector $q = (1/2, 1/2)$, emerges in the material and produces an insulating phase. This is further accompanied by a strong Mott character of the electronic structure with both VBM and CBM dominated by Ni d states as shown on the projected DOS of Figure 6.5.b. These results are consistent with the results obtained in the previous chapter with VASP, other theoretical studies on this compound [243, 242] and with the experiments showing insulating behavior and two types of Ni cations with a 1+ and 2+ FOS [47–51].

We continue exploring the phase diagram with $\text{La}_4\text{Ni}_3\text{O}_8$, where a metallic state is again *a priori* expected for a Ni cation with a 1.33+ FOS ($n = 3$ member). The material is nevertheless found insulating with a gap of $E_g = 1$ eV and a Mott character, where both the CBM and the VBM are dominated by Ni d states (see Table 6.2 and Figure 6.6.a). The structure is characterized by a $Fmmm$ symmetry due to the appearance of an alternative bond disproportionation mode (sketched in Figure 6.6.b), producing stripes of 2 extended and 1 compressed O_4 groups. This is associated with a large energy gain of $\Delta E = -313$ meV/f.u with respect to the high symmetry undistorted cell, signaling again the importance of the structural degrees of freedom. From the projected density of states of Figure 6.6.b, we identify that 2 Ni cations exhibits a $3d^9$

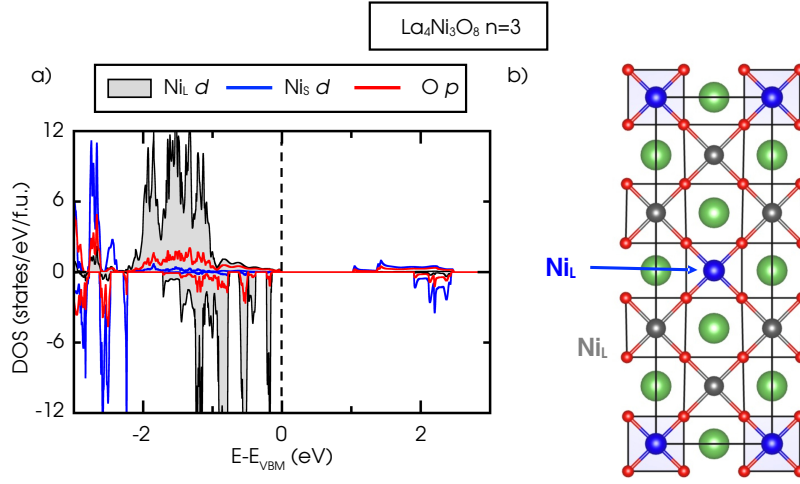


Fig. 6.6 $\text{La}_4\text{Ni}_3\text{O}_8$ (a) projected density of states with a FM order and $Fm\bar{3}m$ crystal symmetry on O p states (red line), Ni_L d states (solid grey) and Ni_S d states (blue line). Positive and negative values of the DOS indicate the majority and minority spin channels. (b) Crystal structure of the bond disproportionation mode B_{oc} producing two types of Ni cations Ni_L in grey and Ni_S in blue.

configuration with a computed magnetic moment $\mu_{\text{Ni}_L} = 0.925\mu_B$ and 1 Ni cation possesses a $3d^8$ low spin configuration with $\mu_{\text{Ni}_S} = 0.152\mu_B$ producing a charge ordering with a 2/1 ratio of $\text{Ni}_L^+/\text{Ni}_S^{2+}$ and a propagation vector of $q = (1/3, 1/3, 0)$. This is consistent with previous theoretical studies identifying a COI state [243], experiments showing a metal-insulator transition at 105K [53–55], and the results that we obtained for the IL case with doping concentrations between $x = 0.375 - 0.3125$ in the previous chapter.

For $\text{La}_5\text{Ni}_4\text{O}_{10}$ ($n = 4$), Ni cations possess a 1.25+ FOS, and the compound is expected to exhibit a metallic character. Similarly, as in the $n = 2$ and $n = 3$ cases, an alternative bond disproportionation producing 3 large and 1 extended O_4 complexes is found in the calculations. This produces a crystal with $Cmcm$ symmetry and an energy gain of $\Delta E = -398$ meV/f.u with respect to the undistorted $I_4/m\bar{3}m$ cell (see Table 6.2 and Figure 6.7.b). We compute the projected density of states (see Figure 6.7) and similarly to the other two previous compounds, we find a 3/1 ratio of $\text{Ni}_L^+/\text{Ni}_S^{2+}$ with a computed magnetic moments $\mu_{\text{Ni}_L} = 0.929\mu_B$ and $\mu_{\text{Ni}_S} = 0.165\mu_B$. This produces a charge ordering with propagation vector $q = (1/2, 0, 0)$ and an insulating state with a band gap of $E_g = 1.49$ eV. In addition, the VBM and the CBM are mainly dominated by Ni d states, more specifically by Ni_L and Ni_S d states respectively. This further shows the strong Mott-insulating character of these compounds. Nonetheless, there is a possibility of a different type of CO with a propagating vector $q = (1/4, 1/4, 0)$ and a $Cmmm$ symmetry (see Figure 6.7.c). However, this type of structure is higher in energy by $\Delta E = 1.89$ eV than the one with $Cmcm$ suggesting that the latter is the preferred geometry. Unfortunately, this compound has not been synthesized yet nor with any other rare-earth cation, thus remaining as an open experimental study.

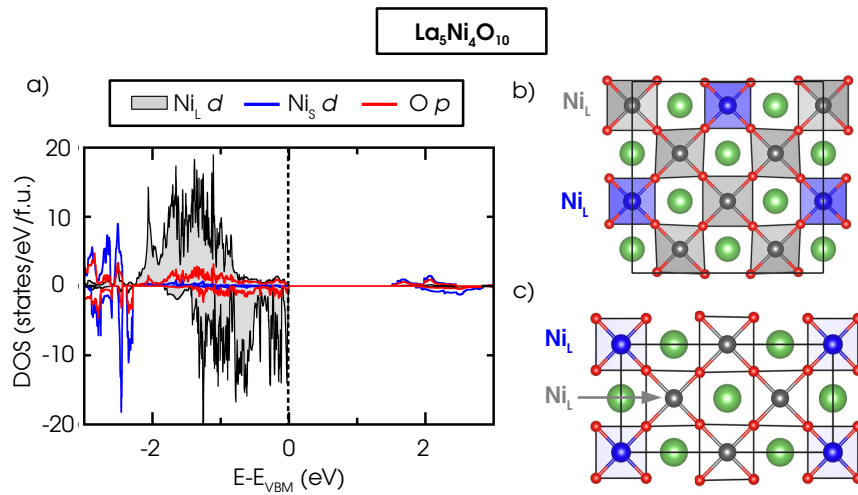


Fig. 6.7 $\text{La}_5\text{Ni}_4\text{O}_{10}$ (a) projected density of states with a FM order and $Fm\bar{m}m$ crystal symmetry on O p (red line), Ni_L d (solid grey) and Ni_S d states (blue line). Positive and negative values of the DOS indicate the majority and minority spin channels. The crystal structure of the bond disproportionation modes B_{oc} producing two types of Ni cations Ni_L in grey and Ni_S in blue is given for (b) the ground state mode with in-plane propagation vector $q = (1/2, 0, 0)$, and (c) the alternative mode with in-plane propagation vector $q = (1/4, 1/4, 0)$

The last compound $\text{La}_6\text{Ni}_5\text{O}_{12}$ ($n = 5$) is found metallic in our DFT simulations and adopts a $I_4/m\bar{m}m$ structure (see Table 6.2 and Figure 6.8). Even though we initially enforce a disproportionation distortion producing a 4/1 ratio of Ni_L⁺/Ni_S²⁺ that would be expected for a CO with a Ni^{1.2+} FOS, it vanishes during the relaxation and all Ni cations are found equivalent with an average magnetic moment of $\mu_{\text{Ni}} = 0.774\mu_B$. Therefore, at large electron doping content, the RRP does not exhibit any type of charge ordering and related distortions and is metallic. This is consistent with experiments on $n = 5$ RRP members [73], and shows that our practiced DFT is able to reproduce the crossover in the phase diagram from insulating to metallic states upon increasing n as we already pointed out in the previous chapter in with the IL phase.

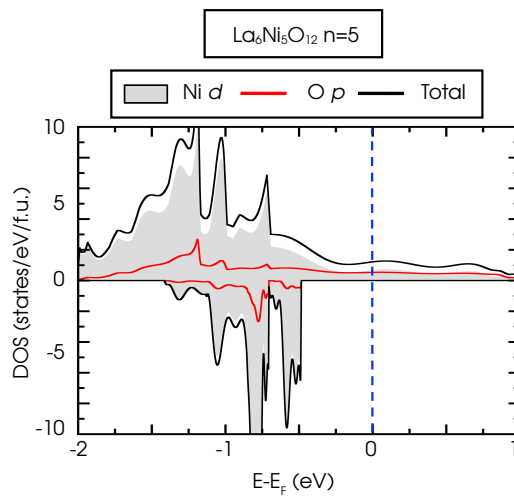


Fig. 6.8 Projected density of states of $\text{La}_6\text{Ni}_5\text{O}_{12}$ with a FM order and $I_4/m\bar{m}m$ crystal symmetry on O p states (red line), Ni d states (solid grey) and total density (black line). Positive and negative values of the DOS indicate the majority and minority spin channels.

6.3.1 Band dispersion of $\text{La}_6\text{Ni}_5\text{O}_{12}$

We can further study the electronic properties of the metallic $n = 5$ member by computing the electronic band structure. Unfortunately, in this case we are not able to unfold it as in previous chapters due to the absence of developed tools to process the output of CRYSTAL17. We report in Figure 6.9 the band dispersion of $\text{La}_6\text{Ni}_5\text{O}_{12}$ with a FM arrangement. It is easy to see that the conduction is given by the majority spin channel that presents 5 bands crossing the Fermi level. This is consistent with the fact that the compound presents 5 Ni cation per formula unit, suggesting that each band corresponds to one of the Ni cations. This observation is consistent with the results obtained in the IL phase with only one Ni cations per formula unit and one band crossing the fermi level. This picture has been suggested as well by Talantsev in Ref. [112] on his experimental data analysis of the IL compounds.

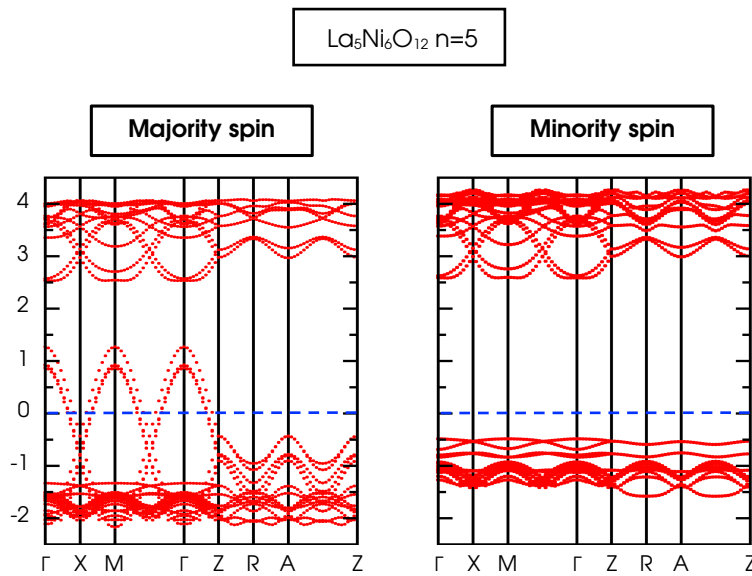


Fig. 6.9 Band structure of $\text{La}_6\text{Ni}_5\text{O}_{12}$ with FM order and I_4/mmm crystal symmetry. Left and right panel present the majority and minority spin channels respectively. The high symmetry points are Γ (0,0,0), X (1/2,0,0), M (1/2,1/2,0), Z (0,0,1/2), R (1/2,0,1/2) and A (1/2,1/2,1/2).

6.4 Origin of the charge orderings on nickelates

As we have seen in previous sections, several compounds in the RRP series present different CO phases. In order to understand the origin of the charge orderings observed in the different nickelate members, we compute the potential energy surface (PES) associated with each type of disproportionation mode. The starting point is the symmetric undistorted I_4/mmm cell with identical O_4 complexes for all Ni cations for each member of RRP $n = 2$ to $n = 4$. Results are reported in Figure 6.10.

The $n = 2$ type of distortion presents a shifted single well potential with its minimum achieved at non-zero values of the mode, producing an energy gain of $\Delta E = -117\text{meV}/\text{NiO}_2$ motif. This signals the presence of an electronic instability associated with the 1.5+ formal

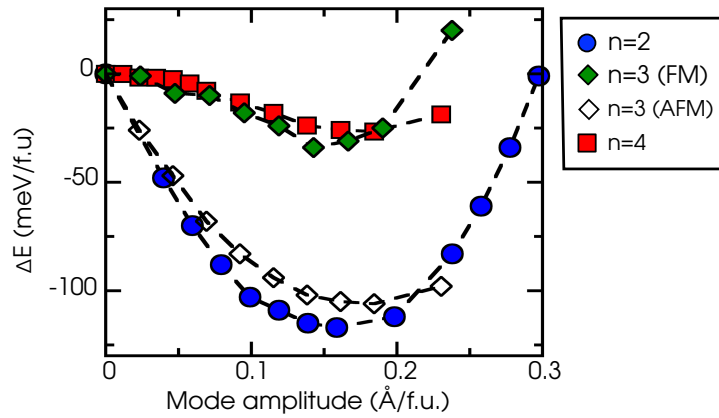


Fig. 6.10 Potential energy surface of the associated bond disproportionation mode present in the $n = 2 - 4$ members of the RRP series.

oxidation state that prefers to transform to more stable 1+ and 2+ in the ground state, even in the absence of lattice distortion. We further support our claim by performing two sets of calculations in the high symmetry cell without any lattice distortion in which (i) we initially force an equal occupancy of all neighboring Ni cations and (ii) a calculation where we initially force neighboring Ni cations to have either a d^8 or d^9 configuration (see Figure 6.11). After the

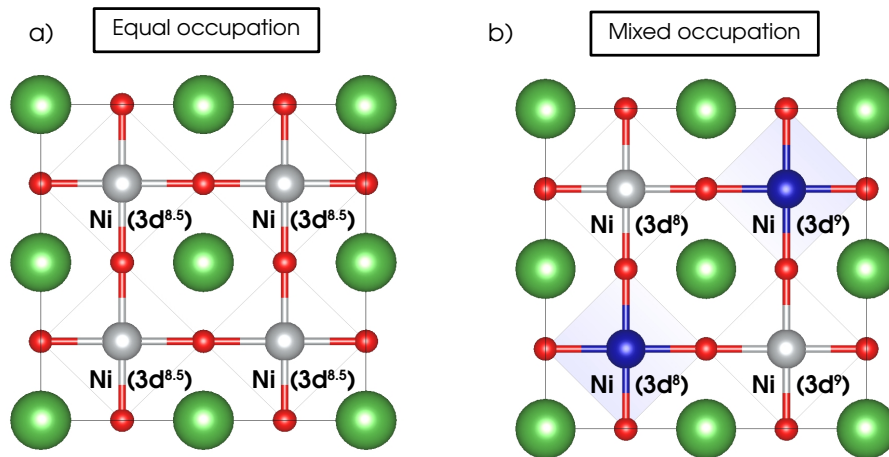


Fig. 6.11 The two situations considered on Ni sites for $\text{La}_3\text{Ni}_2\text{O}_6$ with a FM order and a I_4/mmm crystal symmetry. (a) Equal occupation of electrons in all Ni cations producing a $3d^{8.5}$ electron count, and (b) Mixed occupation of electrons in Ni cations with half of them with a $3d^8$ electron count (in blue) and the other half with a $3d^9$ electron count (in grey) with the same pattern as the B_{oc} mode.

variational self-consistency, we observe that (ii) produces an energy gain of $\Delta E = -35 \text{ meV/NiO}_2$ motif confirming the existence of the electronic instability of Ni with a $3d^{8.5}$ configuration. As a consequence, the material will then develop a lattice distortion to accommodate the charge ordering and produce an insulating state. These results are consistent with those in the previous

chapter with VASP, further showing that the disproportionation mode is highly coupled to the electronic structure.

The potentials for $n = 3$ and $n = 4$ are slightly different with respect to the $n = 2$ mode by showing a double well potential shape as well as smaller energy gains, reaching at most $\Delta E = -34$ meV/NiO₂ motif for the $n = 4$ mode. This, however, does not imply the absence of electronic instability, but rather a screening of it caused by a different band compacity of the Ni d states. This is confirmed by comparing the bandwidth W of occupied Ni d states around the Fermi level in Figures 6.5, 6.6 and 6.7, and realizing that it increases from $W = 1.5$ eV ($n = 2$) to $W = 2.2$ eV for $n = 3$ and $n = 4$. In addition by using a FM order as we mentioned before in the $n = 1$ compound, we would systematically obtain larger bandwidths of Ni d states. In that regard, we can improve the band compacity of Ni d states by imposing an AFM ordering in the $n = 3$ compounds and recomputing the PES of the mode [26]. In this case, we indeed observe a shifted single well potential whose minimum is located at non-zero amplitude and corresponds to a larger energy gain than the FM case ($\Delta E = -102$ meV/NiO₂ motif, Figure 6.10). Thus it becomes clear that the B_{oc}-like modes present in the different members of the series, are strongly coupled to the electronic structure, producing electron localization that leads to a charge-ordered insulating (COI) state. This shows that these types of modes present an important electron-phonon coupling (EPC). In addition, electron doping starting from the $n = 2$ situation alters the electronic instability associated with the unstable FOS of Ni cations, thereby altering the propensity of the material to exhibit COI phases.

The weakening of the electronic instability upon doping can be tracked by quantifying the amplitude of the relevant disproportionation modes in the ground state structures (Figure 6.12). This is obtained by performing a symmetry mode analysis of these structures with respect to

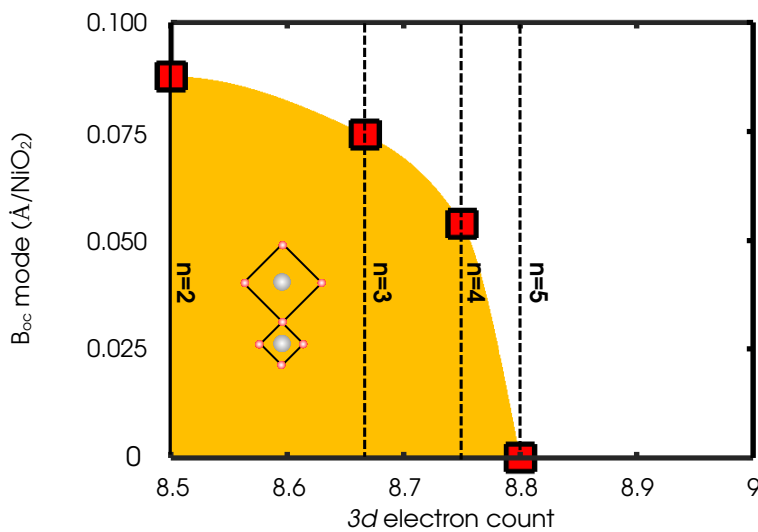


Fig. 6.12 Amplitude in ($\text{\AA}/\text{NiO}_2$ motif) of the different bond disproportionation modes (red squares) B_{oc} present in the RRP compounds as a function of the Ni 3d electron count. Dashed lines indicate the effective electron count of each member of the RRP series from $n = 2$ to $n = 5$.

the high symmetry I_4/mmm undistorted cell. We can observe that upon increasing the number of layers n , from $n = 2$ to $n = 5$, the mode amplitude shrinks until it vanishes at $n = 5$ (Figure 6.12). Therefore, all types of disproportionation effects are quenched by electron doping these nickelates. Hence the metallic region and observed SC RRP compound (i.e. $n = 5$) appear to sit in the vicinity of a CO phase. As we anticipated with the IL and thus validating until this point the analogy between the RRP compounds and the IL phase where the important parameter is the effective $3d$ electron count per Ni site.

6.5 Superconducting properties

Having established a transition between an insulating to a metallic phase as well as the extinction of all types of disproportionation effects and charge orderings, we can wonder if the phonon modes associated with the charge orderings in the insulating phases can still be coupled to the electronic structure in the metallic compounds and mediate Cooper pair formation.

In that regard, we compute the SC properties of the RRP compounds since the $n = 5$ in the Nd case presents a SC transition [73]. Thus, as we did with the IL case, we compute the electron-phonon coupling constant including the relevant modes that we identify in the different members of the series, which can be expressed as

$$\lambda = \frac{2N(\varepsilon_F)}{N_{\mathbf{q}}} \sum_{\mathbf{q},\nu} \frac{\hbar^2}{2\omega_{\mathbf{q},\nu}^2 M_{\text{O}}} D_{\mathbf{q},\nu}^2 \quad (6.1)$$

where $N(E_F)$ is the density of states per spin channel at the Fermi level, $\omega_{\mathbf{q},\nu}$ is the frequency of the ν -th mode at wave vector \mathbf{q} , $D_{\mathbf{q},\nu}$ is the REPME of a given mode (\mathbf{q}, ν) and M_{O} is the oxygen mass. Here, we consider an average coupling over the Fermi surface of the modes (\mathbf{q}, ν)

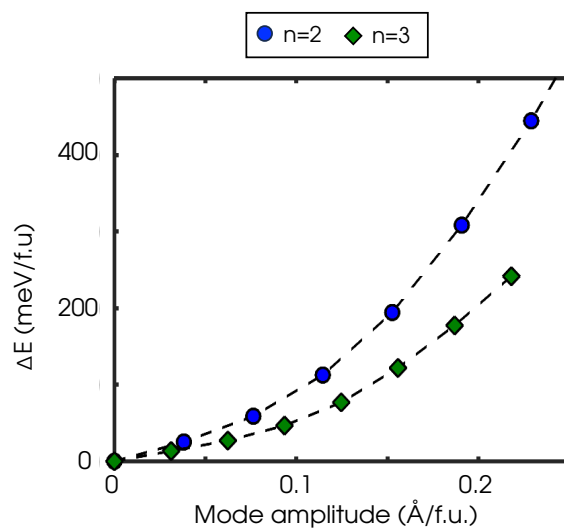


Fig. 6.13 Potential energy surfaces of $\text{La}_6\text{Ni}_5\text{O}_{12}$ associated with the disproportionation modes appearing in $\text{La}_3\text{Ni}_2\text{O}_6$ ($n = 2$ blue circles) and in $\text{La}_4\text{Ni}_3\text{O}_8$ ($n = 3$ green diamonds)

as we did in the IL case, and we consider the disproportionation modes present on the $n = 2$ and

$n = 3$ – we could not include the $n = 4$ type of disproportionation modes in the $n = 5$ RRP for computational cost reasons. In order to evaluate the frequency of each mode, we compute the potential energy surface (PES) associated with the $n = 2$ and $n = 3$ modes within the relaxed $n = 5$ ground state structure. The phonon frequency is obtained by fitting the PES depicted in Figure. 6.13 to the following expression

$$\Delta E(Q_{\mathbf{q},\nu}) = \frac{1}{2}M_0\omega_{\mathbf{q},\nu}^2Q_{\mathbf{q},\nu}^2 + \frac{1}{4}\xi Q_{\mathbf{q},\nu}^4 \quad (6.2)$$

where $Q_{\mathbf{q},\nu}$ is the mode amplitude and ξ is the anharmonic constant. The computed phonon frequencies are $\omega_2 = 64$ meV and $\omega_3 = 48$ meV, for the $n = 2$ and 3 modes, respectively. The $n = 2$ mode is compatible with the frequency computed in the previous chapter for the IL phase to $\omega_2 = 65$ meV.

The REPME is computed by freezing a given phonon amplitude $Q_{\mathbf{q},\nu}$ in the ground state structure, measuring the band splitting ΔE_g appearing in the band structure (see Figure 6.14.a and 6.14.b) and using the expression $D_{\mathbf{q},\nu} = \frac{\Delta E_g}{2Q_{\mathbf{q},\nu}}$ in the harmonic regime, where the deformation potential is independent of the introduced displacement. As we mentioned in

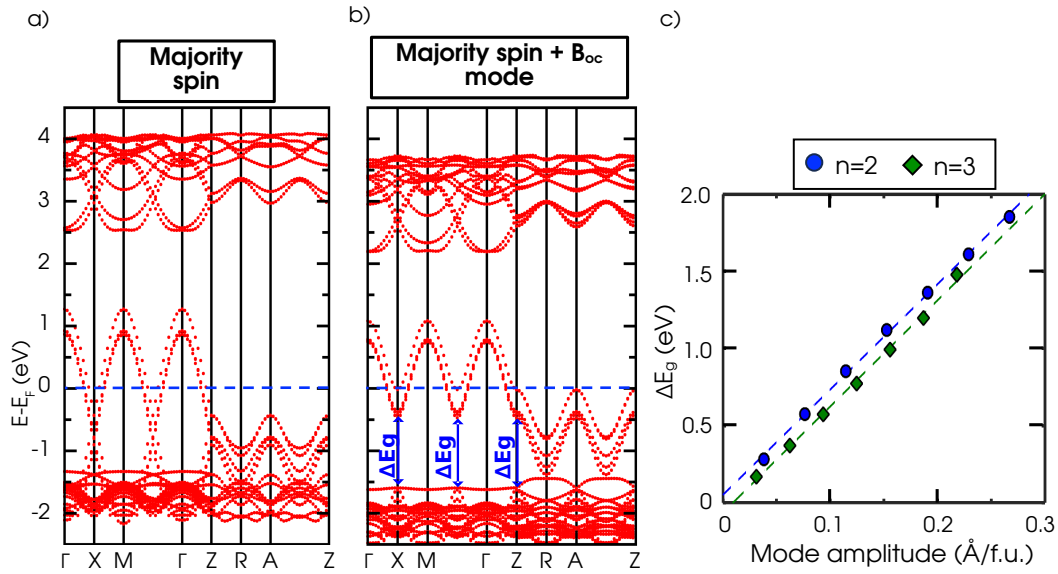


Fig. 6.14 Important quantities for obtaining the deformation potential (REPME). Electronic band structure of $\text{La}_6\text{Ni}_5\text{O}_{12}$ in the majority spin channel (a) with the highly symmetric I_4/mmm ground state and (b) with a finite amplitude of the B_{oc} mode presenting a band splitting ΔE_g . (c) Dependence of the band splitting ΔE_g with the mode amplitude for the $n = 2$ (blue circles) and the $n = 3$ (green diamonds) members of the RRP series

the previous chapter it is necessary to make sure that the electronic response is linear with the amplitude of the disproportionation distortions and we indeed observe a clear linear trend for the ΔE_g versus $Q_{\mathbf{q},\nu}$ curve (see Figure 6.14.c). With a linear fit of these curves, we are able to obtain $D_2 = 3.42$ eV/Å and $D_3 = 3.45$ eV/Å, for the $n = 2$ and $n = 3$ modes respectively.

Finally, we evaluate the density of states at the Fermi level with a coarse k-mesh of $32 \times 32 \times 32$ points and extract $N(E_F) = 0.607$ states/eV/f.u/spin channel (see Figure 6.8). With these values, we evaluate the electron-phonon coupling constant to $\lambda = 0.63$, in fair agreement with the maximum value obtained for the IL phase in the previous chapter ($\lambda = 0.51$) and from experimental data analysis ($\lambda = 0.56 - 0.61$, in Ref [113]) in the doped $R_{1-x}Sr_xNiO_2$ infinite layered case.

We then proceed to evaluate the critical temperature using the Mc. Millan-Allens equation

$$T_c = \frac{\hbar\omega_c}{1.2} \exp\left(-\frac{1.04\lambda}{\lambda - \mu^*(1 + 0.62\lambda)}\right) \quad (6.3)$$

where μ^* is the screened Coulomb interaction and ω_c is the characteristic energy scale of the system. At this point, we will use a similar approximation as in the IL case in chapter 5, where we consider that the B_{oc} -like modes are representative of all the phonons that interact with the electronic structure. Now in this case, since we are considering more than one mode, we evaluate ω_c by calculating the log-average frequency ω_{\log} (this is $\omega_c = \omega_{\log}$) which can be estimated for a finite number of frequencies with

$$\omega_{\log} = \left(\prod_i^n \omega_i\right)^{\frac{1}{n}} \quad (6.4)$$

Within this approximation, and taking typical values of the screening parameter $\mu^* = 0.1 - 0.15$, we estimate the critical temperature T_c between 17 and 9 K, respectively. These values are close to the experimental T_c of $Nd_6Ni_5O_{12}$ ($T_c = 13$ K)[73] and in $La_{0.8}Sr_{0.2}NiO_2$ ($T_c = 9 - 14$ K)[68, 264], where both systems present an effective 1.2+ Ni FOS. With these results, we thus completely validate that the IL phase is indeed a part of the RRP phase, being the limiting member of the series ($n = \infty$), and one of the main parameters governing the different physics of these compounds is the effective $3d$ electron count or FOS on Ni cations.

6.6 Superconductivity and crystal structure

As we have evidence in the previous sections, the determining factor in the superconductivity of these nickelates is the FOS on Ni cations. Thus one could assume that any superconducting nickelate could be obtained as long as the Ni cations present the right $3d$ electron count.

In that regard, an experimental team from the CRISMAT laboratory in Caen aimed to synthesize a nickelate with the optimal $Ni^{1.2+}$ electron count as in the original study on $Nd_{0.8}Sr_{0.2}NiO_2$ in Ref. [66]. Our collaborators then proceeded to synthesize $Nd_{0.8}Sr_{1.2}NiO_4$ on bulk whose crystal structure is the one from the $n = 1$ RRP compound but with I_4/mmm symmetry at this Sr content. The choice of this compound is guided by the 3.2+ FOS on the Ni cation, similar to the parent perovskite compound $Nd_{0.8}Sr_{0.2}NiO_3$ of the SC $Nd_{0.8}Sr_{0.2}NiO_2$ with an IL structure. Then following the procedure in Ref. [66] they perform a topotactic

reduction with CaH_2 on the synthesized $\text{Nd}_{0.8}\text{Sr}_{1.2}\text{NiO}_4$ bulk samples, obtaining a new phase with chemical formula $\text{Nd}_{0.8}\text{Sr}_{1.2}\text{NiO}_3$ and a $\text{Ni}^{1.2+}$ cation.

6.6.1 Structure and physical properties of $\text{Nd}_{0.8}\text{Sr}_{1.2}\text{NiO}_3$

This compound is structurally characterized using both X-ray diffraction (XRD) and Scanning Transmission Electron Microscope (STEM) techniques. From this process, the structure of the material is resolved as one can see in Figure 6.15.b. The obtained compound is an orthorhombic system with $Immm$ symmetry, characterized by the following lattice parameters in the conventional cell $a_{\text{exp}} = 3.97 \text{ \AA}$, $b_{\text{exp}} = 3.74 \text{ \AA}$, and $c_{\text{exp}} = 12.92 \text{ \AA}$. The compound is

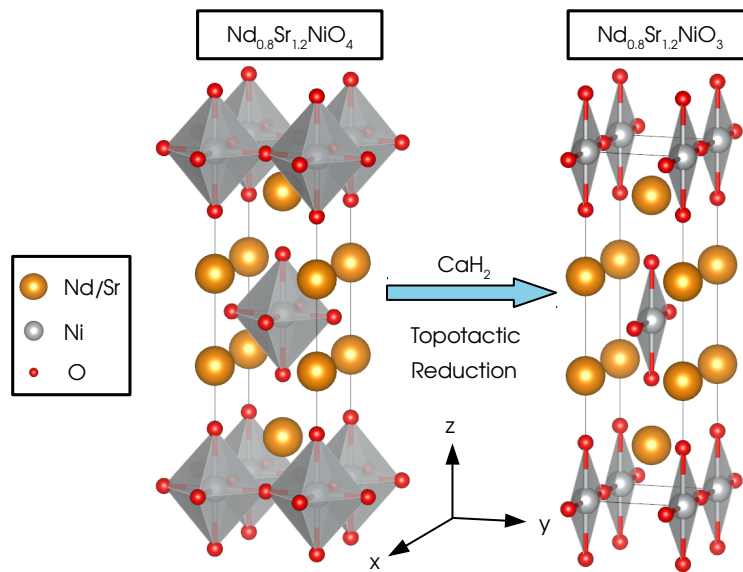


Fig. 6.15 Crystal structure of unreduced parent Ruddlesden Popper phase with I_4/mmm symmetry (left), and reduced phase with $Immm$ symmetry (right)

highly stable experimentally since it can be kept in open-air conditions and the crystalline structure does not degrade.

By comparing the structures of $\text{Nd}_{0.8}\text{Sr}_{1.2}\text{NiO}_4$ and $\text{Nd}_{0.8}\text{Sr}_{1.2}\text{NiO}_3$ depicted in Figure 6.15 on the left and right, respectively, we notice that the topotactic reduction removes the O from the NiO_2 plane instead of the apex of the octahedron, producing a system with NiO_2 square stripes. This feature is quite different from the synthesis of the superconducting $\text{Nd}_{0.8}\text{Sr}_{0.2}\text{NiO}_2$ compound since the latter compound is characterized by a layered structure of perfect NiO_2 planes with Nd planes in between. Nonetheless, the Ni cation on $\text{Nd}_{0.8}\text{Sr}_{1.2}\text{NiO}_3$ presents a $1.2+$ FOS, which makes it rather similar in terms of electron count to the superconducting compound. Thus in spite of the structural differences between $\text{Nd}_{0.8}\text{Sr}_{1.2}\text{NiO}_3$ and $\text{Nd}_{0.8}\text{Sr}_{0.2}\text{NiO}_2$, one may naively hope that there could still be a possibility to have a superconducting compound since we are at the right $\text{Ni}^{1.2+}$ effective valence. These expectations could not be further from reality since the transport measurements performed by our collaborators show a highly insulating compound already at room temperature instead of a superconductor.

In addition to the resistivity measurements, our collaborators perform magnetic hysteresis and magnetic susceptibility measurements on $\text{Nd}_{0.8}\text{Sr}_{1.2}\text{NiO}_3$. The susceptibility is measured with an applied field when cooled (FC) and without the applied field (ZFC). The results of the magnetic measurements are presented in Figure 6.16. From these experiments, it is found that

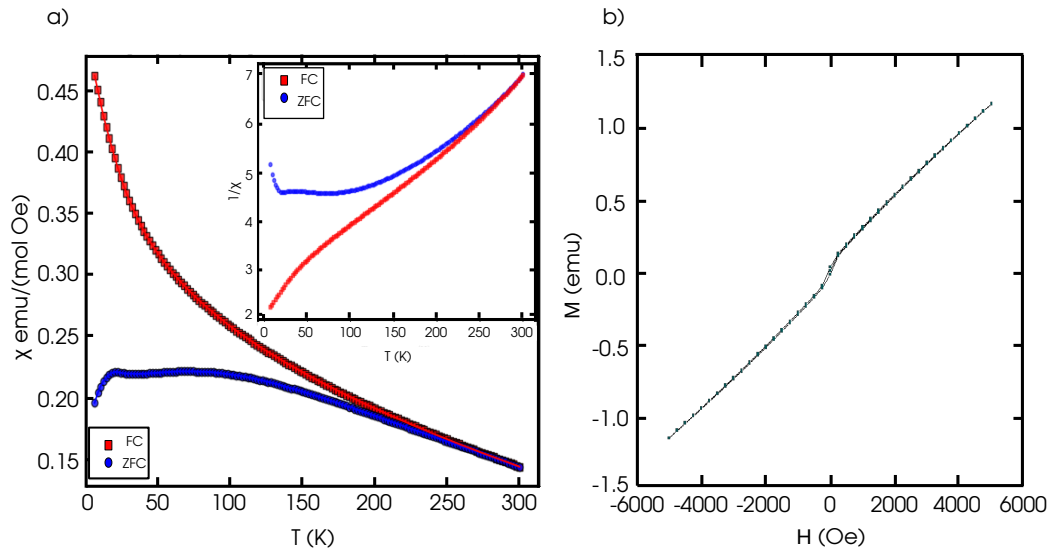


Fig. 6.16 Magnetic measurements of $\text{Nd}_{0.8}\text{Sr}_{1.2}\text{NiO}_3$, (a) the susceptibility χ in (emu/mol·Oe) as a function of temperature T in (K), for field cooled (FC in red) and zero field cooled (ZFC in blue) cases in red and blue, respectively. (b) The hysteresis curve of the induced magnetization M as a function of the applied field H at $T = 5$ K.

(i) $\text{Nd}_{0.8}\text{Sr}_{1.2}\text{NiO}_3$ presents a nontrivial magnetic structure since the FC and ZFC measurements of the susceptibility presented in Figure 6.16.a deviate from each other already at temperatures of 250 K, (ii) from the inverse susceptibility plot (see inset of Figure 6.16.a) the system shows a clear deviation from the Curie-Weiss behavior, which suggest an absence of a paramagnetic phase already at 300 K, and (iii) the induced magnetization M as a function of the applied field H depicted in Figure 6.16.b shows no hysteresis, which suggests an absence of ferromagnetism in the compound. Additionally, ac-susceptibility measurements are performed by our collaborators but show no signature of change in the peak position with the frequency ruling out a possible spin-glass behavior.

Thus from this collection of experimental results, we can state that $\text{Nd}_{0.8}\text{Sr}_{1.2}\text{NiO}_3$ presents a NiO_2 striped structure, it is highly insulating instead of superconducting, and with no PM nor FM phase for the whole temperature range from 0 K to 300 K. This clearly signals that there is a non-negligible degree of freedom that should not be overlooked when designing a superconductor. In that regard, and in order to rationalize these results, we study this compound using DFT.

6.6.2 Electronic structure calculations

We perform electronic structure calculations with the SCAN functional and VASP since we would not require a hybrid functional to describe qualitatively well an insulating compound. In

order to avoid possible self-interaction errors from the $4f$ states but at the same time including all the open-shell electrons, we use La-based compounds instead of Nd.

Before starting to model the synthesized compounds, we prove the stability of the reduction process since one may think that a stable compound with chemical formula $\text{Nd}_{0.8}\text{Sr}_{1.2}\text{NiO}_3$ could still host superconductivity, but with a different crystal structure or the reduction process is not homogeneous enough in bulk. In that regard, we prove the stability of the reduction process by testing different configurations of removing an O from the octahedron in La_2NiO_4 . We consider three possibilities, (i) a pyramidal structure of a half-removed O at the apex of the octahedron depicted in Figure 6.17.a, (ii) a mixed structure with perfect octahedrons and in-plane NiO_2

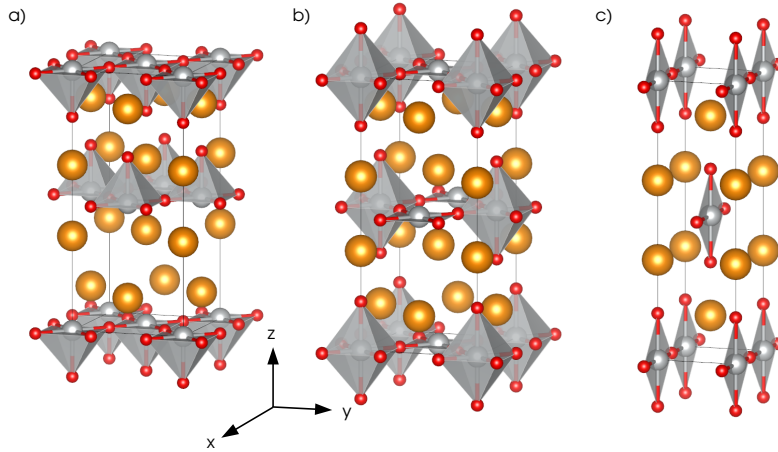


Fig. 6.17 Possible reduced geometries. (a) pyramid, (b) octahedron and NiO_2 square in-plane, and (c) experimental structure

squares depicted in Figure 6.17.b, and (iii) the given phase synthesized by our collaborators depicted in Figure 6.17.c. We relax the structure of these three geometries with a 4 f.u. supercell of La_2NiO_3 . We set the energy cut-off to 650 eV a Γ centered k -mesh of $8 \times 8 \times 4$. The energy convergence criterion is set to 10^{-7} eV and forces are optimized on each atom until they are less than 10^{-3} eV/Å. The core electrons are treated with the same PAW PBE pseudopotentials of previous chapters. The magnetic order is taken to be FM since it is the simplest magnetic order that respects Hund's rule. After the relaxation, we compute the total energy difference between the synthesized phase in Figure 6.17.c, and the other two geometries. Results are reported in Table 6.3.

	Mixed	Pyramidal	Stripes
ΔE (eV/f.u.)	1.52	1.28	0

Table 6.3 Total energy difference between the striped geometry (Stripe) and the geometries considered for La_2NiO_3 . The mixed octahedron and squares (Mixed), and the pyramidal arrangement (Pyramidal).

By comparing the total energy of all three configurations, we find that the synthesized configuration depicted in Figure 6.17.c, with O removed from the NiO_2 plane is much more

stable, with an energy gain of at least $\Delta E = 1.28$ eV/f.u. with respect to the other two considered reduced geometries (see Figure 6.17.a and 6.17.b). Thus it becomes clear to us that indeed the reduction is highly homogeneous since the resolved structure from the XRD and STEM is the most stable reduced compound.

Once we are sure that the reduced geometry is the more stable configuration, we proceed to relax the structure of $\text{La}_{0.8}\text{Sr}_{1.2}\text{NiO}_4$ and $\text{La}_{0.8}\text{Sr}_{1.2}\text{NiO}_3$ and we use a $2 \times 5 \times 1$ supercell with respect to the conventional I_4/mmm and $Immm$ cell of 2 f.u. respectively (this is a 20 f.u. supercell). We model the doping content as in previous chapters directly substituting the atoms with the SQS method. We set the energy cut-off to 650 eV and a $6 \times 4 \times 2$ Γ centered k -mesh. The energy convergence criterion is set to 10^{-5} eV, and the forces are optimized on each atom until they are less than $5 \cdot 10^{-2}$ eV/Å. The core electrons are treated with the PAW PBE pseudopotentials. We use a AFM order analogous to the in-plane AFM order that is found experimentally in La_2NiO_4 [236] since there are important experimental signatures of AFM order in $\text{La}_{0.8}\text{Sr}_{1.2}\text{NiO}_3$. The obtained lattice parameters are reported in Table 6.4 Comparing our SCAN DFT calculations with the experiments from our collaborators and the

Compound	Space Group	a (Å)	b (Å)	c (Å)
exp. $\text{Nd}_{0.8}\text{Sr}_{1.2}\text{NiO}_4$	I_4/mmm	3.80	3.80	12.26
exp. LaSrNiO_4 [265]	I_4/mmm	3.83	3.83	12.56
exp. NdSrNiO_4 [266]	I_4/mmm	3.80	3.80	12.32
exp. $\text{Nd}_{0.8}\text{Sr}_{1.2}\text{NiO}_4$ [266]	I_4/mmm	3.80	3.80	12.26
exp. $\text{Nd}_{0.8}\text{Sr}_{1.4}\text{NiO}_4$ [266]	I_4/mmm	3.81	3.81	12.25
exp. $\text{Nd}_{0.8}\text{Sr}_{1.6}\text{NiO}_4$ [266]	I_4/mmm	3.80	3.80	12.30
DFT $\text{La}_{0.8}\text{Sr}_{1.2}\text{NiO}_4$	I_4/mmm	3.82	3.82	12.31
exp. $\text{Nd}_{0.8}\text{Sr}_{1.2}\text{NiO}_3$	$Immm$	3.97	3.74	12.92
DFT $\text{La}_{0.8}\text{Sr}_{1.2}\text{NiO}_3$	$Immm$	3.98	3.73	12.98

Table 6.4 Summary of the structural parameters that characterize the $\text{R}_{2-x}\text{Sr}_x\text{NiO}_4$ and $\text{R}_{2-x}\text{Sr}_x\text{NiO}_3$ compounds. The first row for each group of compounds is the synthesized materials by our collaborators, and the last row is our DFT calculations. The rest of the rows are the existing literature.

existing literature [265, 266] on $\text{R}_{2-x}\text{Sr}_x\text{NiO}_4$ compounds ($\text{R} = \text{La}, \text{Nd}$ with $x \geq 1$). We observe that we are able to reproduce accurately the experimental structure with less than 1% of error in the lattice parameters. We can obtain the same conclusion by comparing the DFT lattice parameters of $\text{La}_{0.8}\text{Sr}_{1.2}\text{NiO}_3$ with the synthesized $\text{Nd}_{0.8}\text{Sr}_{1.2}\text{NiO}_3$. Thus validating our approach of performing calculations with the La-based compounds instead of Nd.

Once we trust the relaxed structure we proceed to compute the projected DOS of $\text{La}_{0.8}\text{Sr}_{1.2}\text{NiO}_3$ and $\text{La}_{0.8}\text{Sr}_{1.2}\text{NiO}_4$ for comparison purposes (see Figure 6.18). Inspecting the DOS of $\text{La}_{0.8}\text{Sr}_{1.2}\text{NiO}_3$ in Figure 6.18.a, the most obvious and prominent feature one may notice is that it is an insulator with a gap amplitude of $E_g = 1.1$ eV, which compares well with previous theoretical calculations on Sr_2NiO_3 reporting a gap of $E_g = 1.38$ eV [267]. The gap is formed between occupied and unoccupied Ni 3d states at the VBM and CBM, respectively, revealing that $\text{La}_{0.8}\text{Sr}_{1.2}\text{NiO}_3$ is

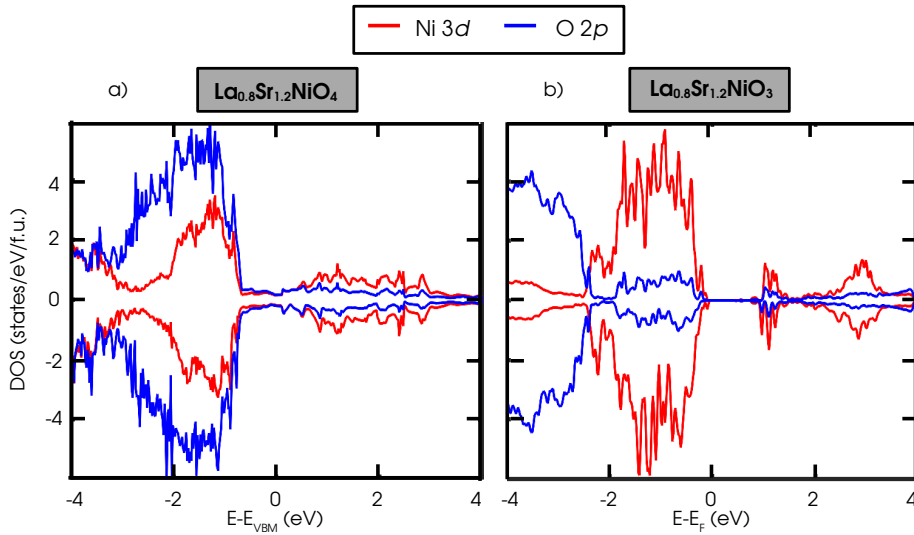


Fig. 6.18 Projected density of states on Ni d (in red) and O p (in blue) for (a) $\text{La}_{0.8}\text{Sr}_{1.2}\text{NiO}_4$ on the left and (b) $\text{La}_{0.8}\text{Sr}_{1.2}\text{NiO}_3$ on the right.

clearly a Mott insulating compound. This behavior is in contrast with the metallic, and CT regime of the parent compound $\text{La}_{0.8}\text{Sr}_{1.2}\text{NiO}_4$ (see Figure 6.18.b). The reason behind this change from CT to Mott is a consequence of removing O^{2-} anions from the material, producing a decrease of the FOS on Ni cations from $\text{Ni}^{3.2+}$ in $\text{La}_{0.8}\text{Sr}_{1.2}\text{NiO}_4$ to $\text{Ni}^{1.2+}$ in $\text{La}_{0.8}\text{Sr}_{1.2}\text{NiO}_3$, which is expected to produce a change from CT to Mott in transition metal compounds [26]. In addition, by comparing the DOS of both systems, we can further understand that removing O atoms from $\text{La}_{0.8}\text{Sr}_{1.2}\text{NiO}_4$, (i) the number of charge carriers at the Fermi level is effectively reduced, (ii) the conducting channels for the electrons are more limited since the O p states are highly hybridized with the Ni d states in $\text{La}_{0.8}\text{Sr}_{1.2}\text{NiO}_4$, acting as bridges between the Ni sites, and (iii) $\text{La}_{0.8}\text{Sr}_{1.2}\text{NiO}_3$ presents only a possible conducting channel through the O atoms that are left in plane. This added to the more ionic structure of a Mott compound, ultimately hinders the conductivity in $\text{La}_{0.8}\text{Sr}_{1.2}\text{NiO}_3$.

6.6.3 Prediction of charge ordering

Inspecting the relaxed structure, we identify a bond disproportionation distortion in one of the NiO_4 squares on each stripe, producing a double local environment of 4 elongated NiO_4 complexes with a Ni_L cation and one compressed NiO_4 complex with a Ni_S cation (see Figure 6.19). If we now compute the magnetic moment on these two types of Ni sites, we find that the average magnetic moment is $\mu_{\text{Ni}_S} = 0.06\mu_B$ on the Ni_S cations, while the average magnetic moment on the Ni_L sites is $\mu_{\text{Ni}_L} = 0.95\mu_B$. This strongly suggests a charge-ordered pattern, reminiscent of the charge order that is present in the layered nickelates like the reduced Ruddlesden-Popper (RRP with $n = 2, 3$ and 4) or the half-doped case of the infinitely layered nickelates presented in chapters 5 and 6. We verify the existence of this CO phase by calculating the partial charge density for all the electrons on the Ni d states band from the 2 eV below the VBM until the VBM, and obtaining that the charge density is absent on the compressed NiO_4 (see Figure 6.19). This is a strong signature of a charge-ordered phase of $\text{Ni}^+(3d^9)$ and $\text{Ni}^{2+}(3d^8)$ low spin $S = 0$

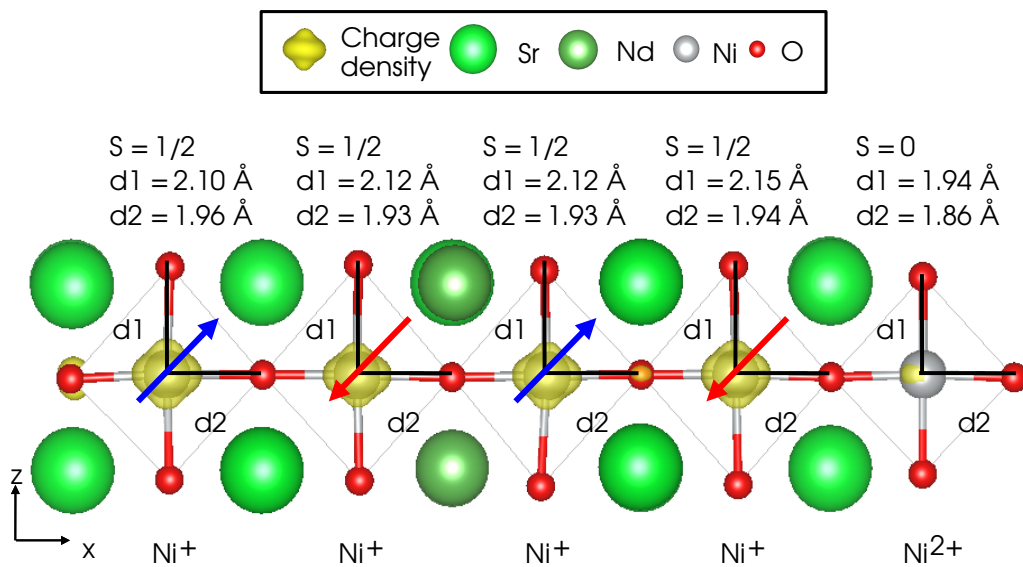


Fig. 6.19 Features of the charge ordering in $\text{La}_{0.8}\text{Sr}_{1.2}\text{NiO}_3$ for one of the NiO_2 stripes with an AFM order. The spins are represented as blue and red arrows for up and down configurations, respectively. The Ni-O bond lengths of the NiO_2 complexes d_1 (along the z-axis) and d_2 (along the x-axis) are given in (Å).

configuration.

We further inspect the direction of the CO and we find the CO pattern depicted in Figure 6.20.a where there are small stripes along the diagonal of the (xy) plane. Nonetheless, we must note that we are limited by the size of our calculation, and it is possible that a CO pattern producing a stripe pattern as depicted in Figure 6.20.b is possible to occur, which is reminiscent of the CO patterns found in the RRP compounds. Thus we find strong evidence that the insulating behavior obtained in this compound is accompanied by charge ordering and is further enhanced by the antiferromagnetic behavior of the interactions, further preventing the conduction and explaining the strong insulating behavior found experimentally.

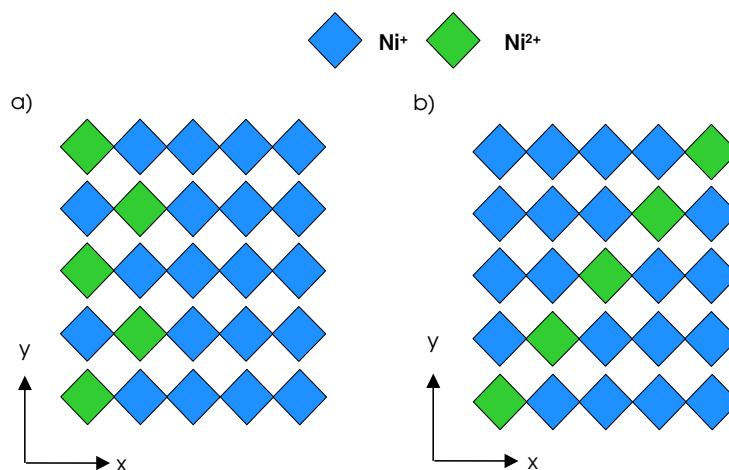


Fig. 6.20 The possible charge ordered patterns of $\text{La}_{0.8}\text{Sr}_{1.2}\text{NiO}_3$ (a) the obtained pattern from the 20 f.u. calculations. (b) the alternative pattern

6.6.4 Understanding the magnetic properties of $\text{Nd}_{0.8}\text{Sr}_{1.2}\text{NiO}_3$

As we saw from the experimental results of our collaborators, $\text{Nd}_{0.8}\text{Sr}_{1.2}\text{NiO}_3$ does not present any signature of PM or FM order already at room temperatures. In that regard, we perform structural relaxations on $\text{La}_{0.8}\text{Sr}_{1.2}\text{NiO}_3$ with a FM order. However, the self-consistent procedure produces the magnetic moments to change the sign and produce an AFM order instead. Thus, we are completely unable to stabilize an FM solution in $\text{La}_{0.8}\text{Sr}_{1.2}\text{NiO}_3$. This is quite surprising but it highlights that $\text{La}_{0.8}\text{Sr}_{1.2}\text{NiO}_3$ has a strong tendency towards the antiferromagnetism. The average magnetic moment on Ni cations is $\langle \mu_{\text{Ni}} \rangle = 0.77 \mu_{\text{B}}$, suggesting a $S = \frac{1}{2}$ state on Ni cations. The fact that we are completely unable to stabilize something different than an AFM solution on $\text{La}_{0.8}\text{Sr}_{1.2}\text{NiO}_3$, added to its stripped crystal structure, and the absence of a spin-glass behavior from the ac-susceptibility on $\text{Nd}_{0.8}\text{Sr}_{1.2}\text{NiO}_3$, suggest that we may have a 1D or quasi-1D AFM system which can be described by the Heisenberg Hamiltonian

$$\mathcal{H}_{\text{Heis}} = J \sum_{\langle i,j \rangle} S_i S_j \quad (6.5)$$

where $J > 0$ is the AFM exchange constant. If we recall the Mermin-Wagner theorem [268], the 1D Heisenberg model, does not have a phase transition, where the ground state is either AFM or FM depending on the exchange constant J . This could actually explain the absence of a clear PM region in the susceptibility, showing that the dimensionality of the system plays a very important role in the magnetic properties of $\text{Nd}_{0.8}\text{Sr}_{1.2}\text{NiO}_3$. Another important feature of the Heisenberg model in 1D is the fact that the Neel state, where all nearest neighbors interactions are antiferromagnetic, is not the ground state of the given Hamiltonian [152]. In fact, a double spinon state is lower in energy than the Neel state, where the lowest energy excitation will present the following dispersion relation

$$E_-(q) = \hbar\omega_-(q) = \frac{\pi}{2}J|\sin(2\pi q)| \quad (6.6)$$

with q the momentum of the excitation, and the upper two spinon excitation energy is given by

$$E_+(q) = \hbar\omega_+(q) = \pi J|\sin(\pi q)| \quad (6.7)$$

Thus, probing the real excitation spectra may show the curves depicted in Figure 6.21. The spectra of the excitations can give a hint of the dimensionality of the magnetic interactions. If the system is closer to a 1-D material, then the dominant contribution will be $E_-(q)$ obtaining a curve close to Figure 6.21.a, while if the material is more of a 2-D material, then there will be a continuum between $E_-(q)$ and $E_+(q)$ as depicted in Figure 6.21. Nonetheless, for this particular Sr content, the charge ordering instability produces a global $S = 0$ state when the 5 Ni sites are considered, with four $S = \frac{1}{2}$ Ni_L cations and one $S = 0$ Ni_S cation. In that regard, we propose to change the Sr content slightly and synthesize single crystals of NdSrNiO_3 , PrSrNiO_3 , or LaSrNiO_3 which would present only a $S = \frac{1}{2}$ Ni^+ cation. Then, resonant inelastic x-ray scattering experiments (RIXS) can be performed to obtain the momentum-resolved excitation spectra of these compounds. If these experiments show any of the curves in Figure 6.21, the

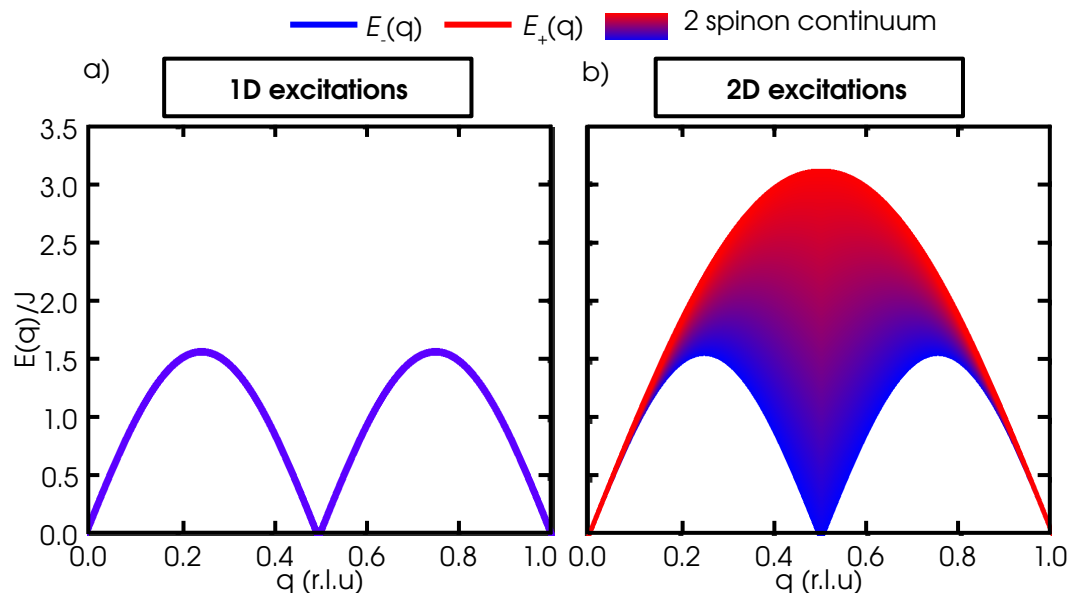


Fig. 6.21 Excitation spectra of a spin chain system in $(E(q)/J)$ units as a function of the momentum q in reciprocal lattice units (r.l.u.). (a) 1D magnetic excitations dominated by the $E_-(q)$ energy curve (in blue), (b) 2D magnetic excitation continuum between $E_-(q)$ (in blue) and $E_+(q)$ (in red) energy curves.

physical properties of RSrNiO_3 compounds would be very similar to the case of Sr_2CuO_3 since (i) it presents the same crystal structure [269], (ii) the $\text{Cu}^{2+}(3d^9)$ configuration is the same as the $\text{Ni}^+(3d^9)$ in RSrNiO_3 compounds with a trivalent cation R^{3+} , (iii) there is no trace of superconductivity since Sr_2CuO_3 is also an insulating compound with a reported gap of $E_g = (1.5 \pm 0.3)$ eV [270], and (iv) Sr_2CuO_3 presents characteristic spinon excitations of a 1-D spin chain [271]. In addition, this could suggest that spin-charge and spin-orbital excitations can be separated in RSrNiO_3 compounds in the same way as they are in Sr_2CuO_3 [272, 273], which are characteristic of 1D or quasi-1D systems. Thus, the $\text{R}_{2-x}\text{Sr}_x\text{NiO}_3$ family of compounds could be full of interesting phenomena in spite of not showing superconductivity at ambient conditions.

6.7 Conclusion

We conclude here that these nickel oxides present a strong propensity to form charge-ordered phases with two different FOS on Ni cations. In addition, it is clear that the structure and the dimensionality of the system play a very important role in determining the physical properties of the synthesized compounds. In particular and strictly speaking, a superconducting transition is not possible in a pure 1D system, and consequently, if the interactions of the system present a strong 1D character, the SC transition would be prevented. Thus, in spite of the universality of the superconducting mechanism that we proposed in chapter 5 and evidenced by studying the $\text{La}_{n+1}\text{Ni}_n\text{O}_{2n+2}$ series of compounds, the crystal structure should not be overlooked since it could lead to obtaining at ambient conditions, insulating phases instead of superconducting ones. Nonetheless, finding a charge-ordered insulating phase could still be a good starting point for finding a superconducting compound. Here, the strategy would be first to bring the 1D

character of the interactions closer to a quasi-1D at least and, at the same time, suppress the charge-order instability by changing the oxidation state with some dopant, different O content or applying pressure in the appropriate manner.

Concerning other superconductors, the SC phase of these compounds seems closer to the bismuth-like superconductors [165, 240] than the cuprates since the SC region appears just in the vicinity of a CO phase and the phonons responsible for the CO in the insulating phase remains strongly coupled to the electronic structure once the insulating phase is quenched producing a SC transition.

Chapter 7

Extension of the model to other systems: Ruthenates

In this chapter, we will try to extend the ideas behind the superconducting model to other systems, showing that the mechanism is more general and can be applied to other compounds in the oxide family.

7.1 Gap openings in perovskite-related compounds

As we have elaborated in the previous chapters, the superconducting mechanism in nickel-based superconductors has its origin in an electronic instability that produces a tendency to form a charge-ordered state. The charge ordering mechanism is in fact responsible for the metal insulator transition (MIT) in many perovskite-like compounds, such as nickelates [24, 274], bismuthates [165, 240, 15], antimonates [275], half doped titanates [276, 277] and half doped vanadates [278] etc. Interestingly enough is the fact that in the case of bismuth and antimony-based superconductors, the charge ordering modes are also responsible for the superconducting state [165, 240, 279] as it is the case of our layered nickelates and several non-oxide materials [280–283].

Nonetheless, the charge and bond order is not the only phonon mode that is able to produce an insulating state in oxides. The other type of phonon is the one associated with the Jahn-Teller effect (JTE) and the Jahn-Teller distortion (JTD) [13, 193]. According to the Jahn-Teller theorem, any degenerate electronic configuration will be subject to develop a structural distortion that lifts the degeneracy [284]. In particular, in the perovskite-like compounds, the Jahn-Teller effect distorts the O_6 octahedral complex by stretching and contracting four of the B-O bonds producing a double local environment on the B site cation and different local crystal fields (see Figure 7.1). This yields electron localization on specific orbitals and one could expect an insulating state, characterized by an orbital ordering (OO) between nearest neighbors B cations. We must however note that the presence of a degenerate electronic configuration is a prerequisite but not a sufficient condition to produce a JTD. If the electronic structure is too hybridized, the JTE would be screened, implying that the JTD phonon would not condensate and no OO

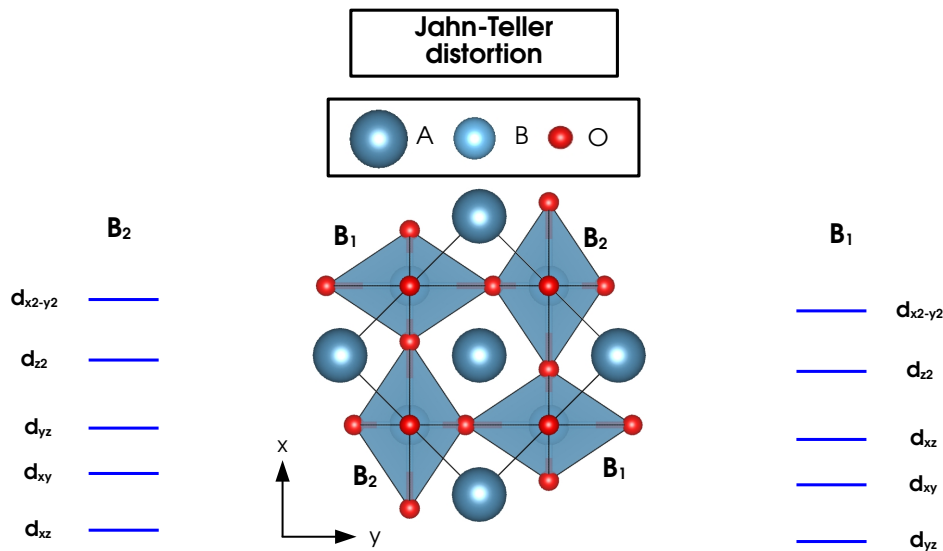


Fig. 7.1 Jahn-Teller distortion in an ABO_3 perovskite where the cation B is a transition metal. The distortion produces two different crystal fields and orderings of the energy levels producing two types of B cations B_1 and B_2 .

would be present in the material. Famous examples of Jahn-Teller active compounds are $KCrF_3$, or RVO_3 with ($R = La-Lu, Y$) [193, 285, 286]. Now in analogy with the charge-ordered case, we can ask if the JTE and JTD producing the OO could in fact drive a SC transition in a metallic compound, and if this is the case, what compounds are in the vicinity of an orbital-ordered phase?

7.2 Ruthenate perovskite-based oxides

Good candidates for a JTE are the A_2RuO_4 compounds with ($A = Sr, Ca$). These compounds are the first member ($n = 1$) of the RP series (see Figure 7.2.a) with Ru^{4+} in a d^4 electronic configuration [287, 288]. In this situation, the octahedral crystal field (CF) lifts the degeneracy of the d orbitals by a magnitude of Δ_{CF} , producing two groups of degenerate partners, $3t_{2g}$ orbitals and $2e_g$ orbitals (see Figure 7.2.b). In addition, since the Hund's coupling J_H is smaller than Δ_{CF} , the system is in a low-spin configuration, $S = 1$ with electronic configuration $(t_{2g\uparrow})^3(t_{2g\downarrow})^1$, which nominally is Jahn-Teller active. Nonetheless, due to the A-to-Ru cation size mismatch, both Ca_2RuO_4 and Sr_2RuO_4 present at low temperatures, a distorted octahedron with the Ru-O bond length c_O along the c axis greater or smaller than the (ab)-plane bond length a_O for the case of Sr_2RuO_4 or Ca_2RuO_4 respectively [287–289]. This local symmetry breaking induced by steric effects produces an additional splitting of magnitude Δ'_{CF} lifting the degeneracy of the t_{2g} levels into a doublet and a singlet, which will have a direct consequence in the compound with respect to the JTE (see Figures 7.2.c and 7.2.d).

In Ca_2RuO_4 , the Δ'_{CF} produces that the lowest orbital in energy is the singlet and as a consequence is completely filled with two electrons (see Figure 7.2.c). This causes the doublet to be half-filled resulting in an insulating state below 357 K [290, 291], with a band gap of

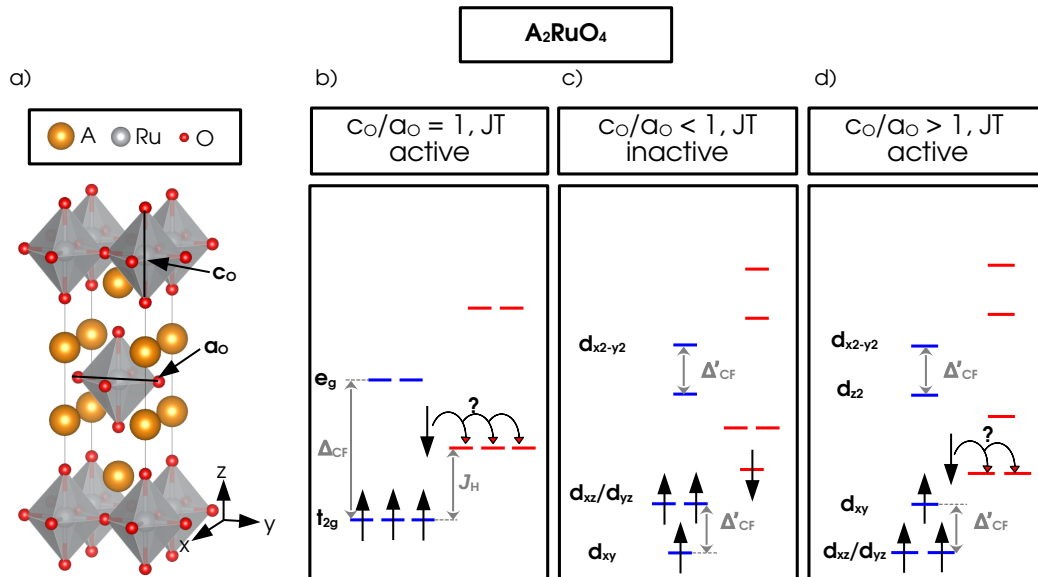


Fig. 7.2 Crystal and electronic structure of A_2RuO_4 compounds, (a) crystallographic conventional cell. Ordering of Ru d states according to the O_6 octahedral deformation for different c_0/a_0 ratios defined in panel (a). Three cases are considered (b) $c_0/a_0 = 1$, (c) $c_0/a_0 < 1$, and (d) $c_0/a_0 > 1$.

at least 0.4 eV [292]. In contrast, the Δ'_{CF} in Sr_2RuO_4 produces the opposite arrangement of the energy levels and produces a degenerate configuration in the minority spin channel with one electron for the doublet formed by the d_{xz} and d_{yz} orbitals (see Figure 7.1.d). With these ingredients, Sr_2RuO_4 is in principle a good candidate for an OO produced by a JTE. However, this compound is found to be metallic at all temperatures, and it presents a transition to the superconducting state with a critical temperature T_c of roughly 1.5 K [293, 294], with no signatures of a JTD to be present. Thus, we can see that Sr_2RuO_4 is likely a candidate for a superconducting compound that could be in the vicinity of an OO phase with an electron-phonon pairing mechanism dominated by the JTD.

7.3 Ground state properties of A_2RuO_4 compounds

We explore the ground state properties of Ca_2RuO_4 and Sr_2RuO_4 performing electronic structure calculations with VASP. The energy cut-off is set to 650 eV for all the calculations and an energy convergence criteria of 10^{-6} eV. The relaxations are performed with a starting unit cell corresponding to the high symmetry undistorted I_4/mmm and $Pbca$ tetragonal unit cells for Sr_2RuO_4 and Ca_2RuO_4 , respectively. The k -mesh is set to $8 \times 8 \times 4$ for a 4f.u. cell and is scaled accordingly to keep a similar k -mesh density for the different unit cells.

7.3.1 Structural relaxation results

We start exploring the bulk of these compounds by performing the structural relaxation of both Sr_2RuO_4 and Ca_2RuO_4 considering several magnetic solutions. This includes the non-spin

polarized solution (NM), and long-range spin orderings such as ferromagnetic (FM), A-type antiferromagnetic (AFMA) which presents in-plane ferromagnetic and out-of-plane antiferromagnetic coupling between consecutive layers along the c axis, C-type AFM (AFMC) with AFM interaction between in-plane nearest neighbors, and random spin arrangement for modeling paramagnetism (PM). The relevant structural parameters as well as the gap amplitude and the Ru magnetic moments are reported in Table.7.1. The first and most evident observation is the fact that the NM solution is metallic in both cases and at least 84 meV/f.u. (corresponding to 1000 K/f.u.) above in energy than any of the spin-polarized solutions. Again, it highlights the fact that the NM approximation is not suitable to describe these ruthenates and including the spin degree of freedom is crucial.

Focusing on the spin-polarized solutions, we find that Ca_2RuO_4 is an insulator regardless of the magnetic arrangement. The lowest magnetic state is the AFMC with a gap of 0.574 eV, in fair agreement with the experimental results showing an AFM transition at 110 K and a band gap greater than 0.4 eV[289, 292]. In contrast, Sr_2RuO_4 is found to be metallic at 0 K and with FM interactions between Ru cations. This is compatible with experimental reports suggesting the presence of short-range FM order [295] and a metallic character [294]. In both compounds, the computed magnetic moments, $\mu_{\text{Ru}} = 1.41 \mu_{\text{B}}/\text{Ru}$ and $\mu_{\text{Ru}} = 1.36 \mu_{\text{B}}/\text{Ru}$ in Ca_2RuO_4 and Sr_2RuO_4 respectively, are compatible with a Ru^{4+} cation in a low spin state ($(t_{2g\uparrow})^3(t_{2g\downarrow})^1$, $S = 1$). We can note however that the total magnetic moment deviates from the naively expected value of $2 \mu_{\text{B}}/\text{Ru}$. This discrepancy originates from the fact that the electronic structure of the Ru- d and O- p states is hybridized, producing a finite spillage of the magnetic moments on surrounding O anions as we will evidence later. The computed values are however in agreement with the experimental value of $1.3 \mu_{\text{B}}$ in Ca_2RuO_4 [289] and those previously computed with LDA+U of $1.38 \mu_{\text{B}}$ in Sr_2RuO_4 [296].

7.3.2 Electronic and structural parameters

We now turn our attention to the two key quantities in these materials, the c_0/a_0 ratio characterizing the octahedral deformation and the amplitude Q_{JT} of the JTD. As inferred in Table.7.1, the correct trend in c_0/a_0 ratio is captured by our DFT simulations regardless of the imposed magnetic order with the exception of the NM solution in Ca_2RuO_4 . The difference with the NM solution comes from imposing two up and down electrons in the octahedral t_{2g} level. This produces an electronic instability on the octahedral t_{2g} degenerate partners and is lifted with an elongation of the octahedron along the z axis splitting the t_{2g} into an unoccupied d_{xy} singlet and a completely occupied d_{xz}/d_{yz} doublet, producing a metallic system at odds with the experiments [290–292]. This again highlights the importance of respecting Hund’s rule by allowing the spin degree of freedom in the calculations.

For the rest of magnetic orders, Ca_2RuO_4 presents a c_0/a_0 ratio lower than one (see Table 7.1) yielding an insulating state for all spin-polarized solutions, with the gap formed between

Mag.	Ca_2RuO_4						Sr_2RuO_4							
	ΔE (meV/f.u.)	$\frac{c_O}{a_O}$	μ_{Ru} (μ_B)	E_g (eV)	Q_{JT} ($\text{\AA}/f.u.$)	$Q_{\phi_z^+}$ ($\text{\AA}/f.u.$)	$Q_{\phi_{xy}^-}$ ($\text{\AA}/f.u.$)	ΔE (meV/f.u.)	$\frac{c_O}{a_O}$	μ_{Ru} (μ_B)	E_g (eV)	Q_{JT} ($\text{\AA}/f.u.$)	$Q_{\phi_z^+}$ ($\text{\AA}/f.u.$)	$Q_{\phi_{xy}^-}$ ($\text{\AA}/f.u.$)
NM	0	1.06	-	0	0	0.52	0.52	0	1.08	-	0	0	0	0
FM	-299	0.98	1.43	0.11	0.02	0.54	0.77	-180	1.06	1.36	0	0	0.35	0
AFMA	-300	0.98	1.43	0.16	0.02	0.56	0.77	-178	1.06	1.36	0	0	0.35	0
AFMC	-302	0.96	1.41	0.57	0.03	0.61	0.74	-84	1.07	1.15	0.12	0.04	0.08	0.10
PM	-299	0.97	1.41	0.50	0.03	0.60	0.75	-142	1.04	1.26	0	0	0.28	0
Exp.	-	0.98	1.30	>0.4	0.01	0.52	0.68	-	1.07	-	0	-	0	0
		[287]	[289]	[292]	[287]	[287]	[287]		[288]		[294]			

Table 7.1 Summary of key quantities of A_2RuO_4 compounds extracted from first-principles calculations: The total energy difference ΔE in meV/f.u. between spin-polarized and non-spin-polarized NM solutions. The average magnetic moment μ_{Ru} exhibited by Ru cations in μ_B . The band gap amplitude E_g in eV. The c_O/a_O ratio quantifying the octahedral deformation, and the mode amplitude of the Jahn-Teller distortion Q_{JT} , in-plane in-phase octahedral rotation $Q_{\phi_z^-}$, and out-of-plane anti-phase octahedral rotations $Q_{\phi_z^+}$ in $\text{\AA}/f.u.$

the occupied d_{xy} singlet in the majority spin channel and the unoccupied d_{xz}/d_{yz} doublet in the minority spin channel (see Table 7.1 and Figure 7.3). In contrast, Sr_2RuO_4 presents a c_O/a_O

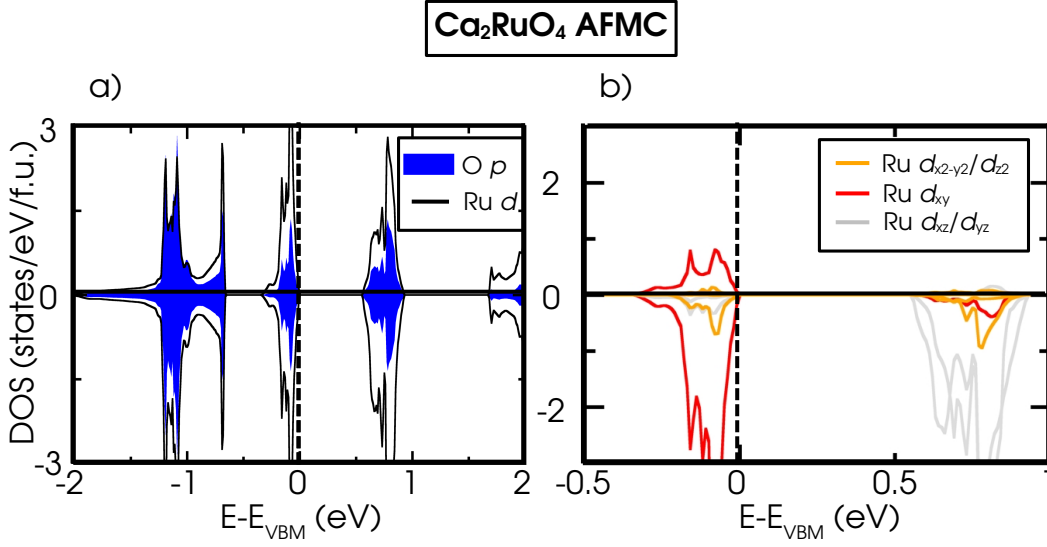


Fig. 7.3 Electronic density of states of Ca_2RuO_4 with a type-C AFM order. Two panels are depicted (a) projected density of states on O p states (solid blue) and Ru d states (black line) are depicted, and (b) the Ru d orbital character is depicted with d_{xy} in red, d_{xz}/d_{yz} in grey and $d_{x^2-y^2}/d_{z^2}$ in orange.

greater than one, producing a metal for all spin orderings except for the AFMC which produces a gap of 0.12 eV (see Table 7.1).

We explore this latter case by means of a symmetry mode analysis of the relaxed structure with respect to the high symmetry undistorted I_4/mmm cell for these ruthenates. We obtain a finite Jahn-Teller distortion $Q_{\text{JT}} = 0.04 \text{ \AA}$, only for the type-C AFM order in Sr_2RuO_4 (see Table 7.1). The same analysis on Ca_2RuO_4 leads to the observation of a finite Q_{JT} regardless of the magnetic order (results presented in Table 7.1). This is quite surprising since Ca_2RuO_4 presents a c_O/a_O ratio lower than one and as a result, it should not be Jahn-Teller active. Along with the appearance of the JTD, the compounds are also prone to exhibit $a^-a^-c^0$ and $a^0a^0c^+$ octahedral rotations, which we denote as ϕ_{xy}^- and ϕ_z^+ , respectively (see Figure 7.4 and Table 7.1). This is a consequence of a Goldschmidt tolerance ratio lower than one which is characterized by two octahedral rotations with amplitude $Q_{\phi_z^+}$ and $Q_{\phi_{xy}^-}$ (see Table 7.1). Then we can perform a free energy expansion in terms of the amplitudes of the distortions modes Q_{JT} , $Q_{\phi_{xy}^-}$, and $Q_{\phi_z^+}$ as we did in previous chapters obtaining

$$\begin{aligned} \mathcal{F}[Q_{\phi_z^+}, Q_{\phi_{xy}^-}, Q_{\text{JT}}] \simeq & \mathcal{F}_0 + \alpha_1 Q_{\phi_z^+}^2 + \beta_1 Q_{\phi_z^+}^4 + \alpha_2 Q_{\phi_{xy}^-}^2 + \beta_2 Q_{\phi_{xy}^-}^4 + \alpha_3 Q_{\text{JT}}^2 + \beta_3 Q_{\text{JT}}^4 + \zeta_1 Q_{\phi_z^+} Q_{\text{JT}} + \\ & \zeta_2 Q_{\phi_z^+}^3 Q_{\text{JT}} + \zeta_3 Q_{\phi_z^+} Q_{\phi_{xy}^-}^2 Q_{\text{JT}} + \lambda_1 Q_{\phi_z^+}^2 Q_{\phi_{xy}^-}^2 + \lambda_2 Q_{\phi_{xy}^-}^2 Q_{\text{JT}}^2 + \delta Q_{\phi_z^+} Q_{\text{JT}}^3 + \dots \end{aligned} \quad (7.1)$$

As one can see, there are several couplings between the octahedral rotations and the JTD which in turn would force the appearance of this mode as it is observed in many other oxide perovskites

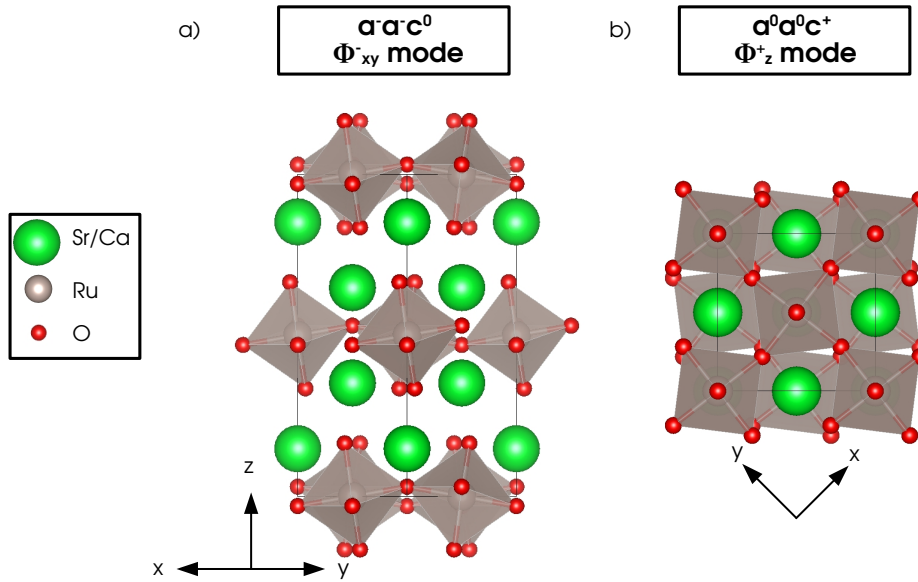


Fig. 7.4 Rotation pattern present in A_2RuO_4 compounds, (a) out of plane anti-phase rotations $a^-a^-c^0$ (ϕ_{xy}^-), and (b) in-plane in-phase rotations $a^0a^0c^+$ (ϕ_z^+).

such as $LaMnO_3$ or $LaTiO_3$ [193, 276]. We can make this more evident by calculating the potential energy surface of the JTD for several fractions of the $a^-a^-c^+$ distortion on Ca_2RuO_4 . The PES depicted in Figure 7.5, it shows that effectively the minimum shifts to a non-zero

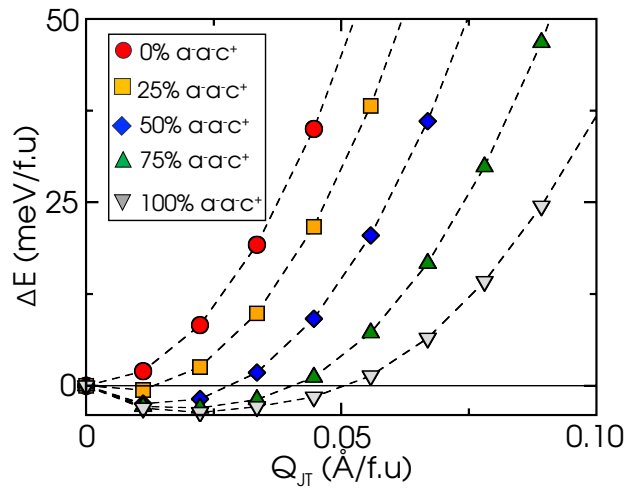


Fig. 7.5 Potential energy surface in Ca_2RuO_4 associated with the Jahn-Teller distortion amplitude Q_{JT} (in $\text{\AA}/\text{f.u.}$) in presence of a percentage of the ground state amplitude of the $a^0a^0c^+$ ($Q_{\phi_z^+}$), $a^-a^-c^0$ ($Q_{\phi_{xy}^-}$) and JTD (Q_{JT}) distortions. A ferromagnetic order is used for the simulations.

value of the Q_{JT} mode once we allow a finite amplitude of the rotation pattern. The free energy associated with the potential energy surface of the Q_{JT} mode, follows the general expression

$$\mathcal{F}[Q_{JT}] = \mathcal{F}'_0 + \zeta_{eff}Q_{JT} + \alpha_{eff}Q_{JT}^2 + \delta_{eff}Q_{JT}^3 + \beta_{eff}Q_{JT}^4 \quad (7.2)$$

where \mathcal{F}'_0 , α_{eff} , β_{eff} , ζ_{eff} and δ_{eff} are functions that depend on $Q_{\phi_z^+}$ and $Q_{\phi_{xy}^-}$ mode amplitudes as follows

$$\begin{aligned}
\mathcal{F}'_0 &= \mathcal{F}_0 + \alpha_1 Q_{\phi_z^+}^2 + \beta_1 Q_{\phi_z^+}^4 + \alpha_2 Q_{\phi_{xy}^-}^2 + \beta_2 Q_{\phi_{xy}^-}^4 \\
\zeta_{eff} &= \zeta_1 Q_{\phi_z^+} + \zeta_2 Q_{\phi_z^+}^3 + \zeta_3 Q_{\phi_z^+} Q_{\phi_{xy}^-}^2 \\
\alpha_{eff} &= \alpha_3 + \lambda_2 Q_{\phi_{xy}^-}^2 \\
\delta_{eff} &= \delta Q_{\phi_z^+} \\
\beta_{eff} &= \beta_3
\end{aligned} \tag{7.3}$$

It is interesting to see that almost all effective coupling constants of the free energy of the JTD, show a dependence on the amplitudes $Q_{\phi_{xy}^-}$, and $Q_{\phi_z^+}$ of the rotation pattern. Thus in general, including a finite amplitude of the $a^-a^-c^+$ rotation pattern, renormalizes the coupling constants in front of the Q_{JT} and yields an energy gain associated with the appearance of a finite amplitude of the JTD. In particular, we notice that the linear term ζ_{eff} becomes important only when there is a non-zero amplitude of $Q_{\phi_z^+}$ or $Q_{\phi_{xy}^-}$, and in the case of $\zeta_{eff} < 0$ it would produce an energy gain. Regarding the PES depicted in Figure 7.5, we see a clear shifted single well potential signaling that $\zeta_{eff} < 0$ is the dominant term responsible for the appearance of the JTD in Ca_2RuO_4 .

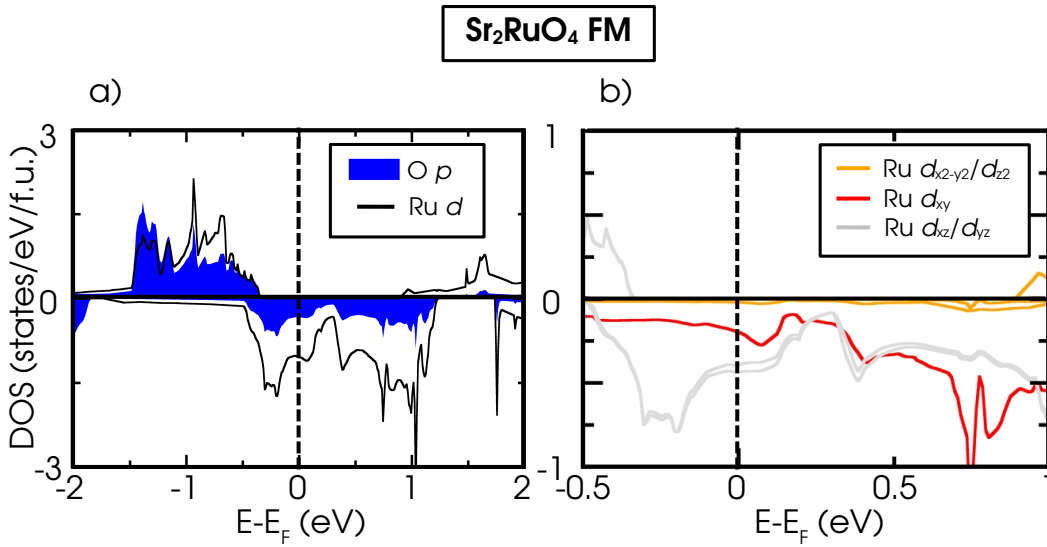


Fig. 7.6 Electronic density of states of Sr_2RuO_4 with a FM order. Two panels are depicted (a) projected density of states on O p states (solid blue) and Ru d states (black line) are depicted, and (b) the Ru d orbital character is depicted with d_{xy} in red, d_{xz}/d_{yz} in grey and $d_{x^2-y^2}/d_{z^2}$ in orange.

Although this mechanism explains the appearance of the JTD in Ca_2RuO_4 , it does not explain why Sr_2RuO_4 only presents a JTD with the AFMC order, although being Jahn-Teller active. In addition, Sr_2RuO_4 presents some finite in-plane rotation ϕ_z^+ which are coupled to the JTD mode, yet there is no signature of a finite stabilization of the mode. We answer this question by exploring the electronic structure of Sr_2RuO_4 calculating the partial density of states projected on O p and Ru d orbitals for the FM case. From Figure 7.6.a, we clearly see that Sr_2RuO_4 is metallic, as we expect from a compound with a c_O/a_O greater than one. The Fermi level is dominated by Ru d states with a non-negligible hybridization

with O p states. By projecting on specific Ru d orbitals, we find that the Fermi level involves mainly the Ru d_{xz}/d_{yz} doublet. This configuration means, that effectively, there is a degeneracy of these orbitals in the minority spin channel and as a result, the compound would be Jahn-Teller active. Interestingly, we can see that the Jahn-Teller distortion is only present in the AFMC order while the other magnetic orders remain metallic without JTD (see Table 7.1).

In order to understand this behavior, we calculate the potential energy surface associated with the JTD for NM, FM, and AFMC solutions, starting from the high symmetry configuration with I_4/mmm space group.

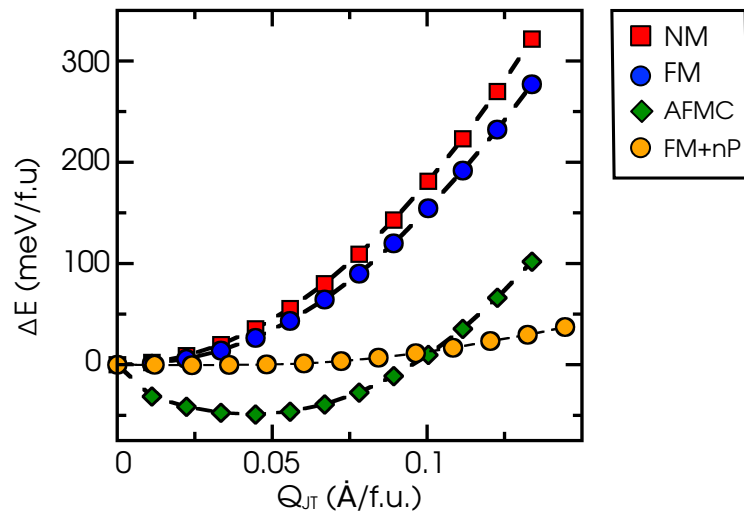


Fig. 7.7 Potential energy surface of the Q_{JT} mode (in $\text{\AA}/\text{f.u.}$) of the JTD for the NM (red filled squares), FM (blue filled circles), AFMC (green filled diamonds) and FM with a negative Pressure (FM-nP, orange filled circles)

From the results depicted in Figure 7.7, we notice that the NM, and FM solutions present a single well potential while the AFMC presents a shifted single well with the minimum located at finite Q_{JT} amplitude. This signals that the system presents an electronic instability caused by the degeneracy of the electronic structure. Thus, if the system was characterized by dominant in-plane AFM interaction, Sr_2RuO_4 would exhibit a JTD that produces an insulating phase. In fact, the insulating AFMC solution presents an OO with the Ru d electrons in the minority spin channel located either at the d_{xz} or d_{yz} orbital alternating on the first nearest neighbors. We can evidence this by calculating the partial charge density of the states at the top of the valence band of the AFMC solution as depicted in Figure 7.8.

The system, however, presents an FM ground state, and as a result, it does not show such type of orbital ordering, in spite of being Jahn-Teller active. By comparing the total density of states of Sr_2RuO_4 with FM and AFMC orders (see Figure 7.9), we notice that the bandwidth is significantly different in both cases. As we can extract from Figure 7.9 the FM solution presents the biggest bandwidth with $W_{t_{2g}}^{FM} = 2.04\text{eV}$, while the AFMC state presents the smallest

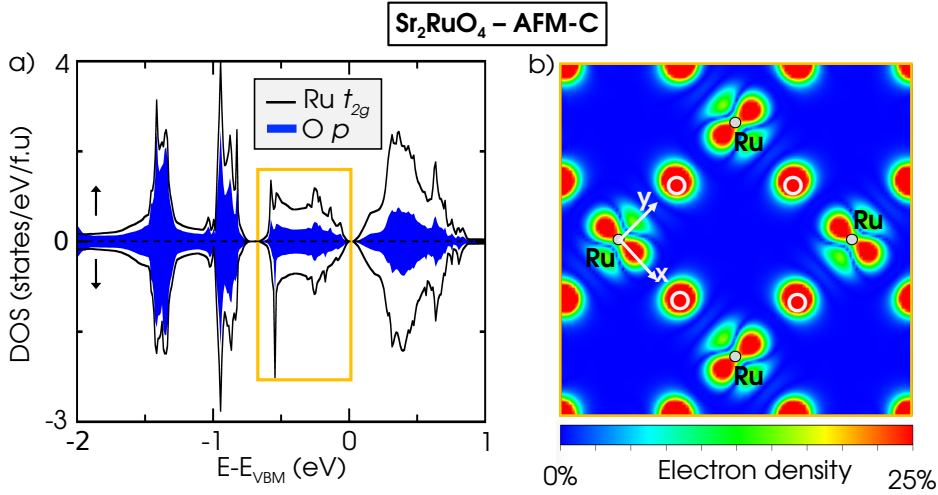


Fig. 7.8 Orbital-ordering exhibited by Sr_2RuO_4 AFMC ground state. a) Density of states (in states/eV/f.u) for spin-up (positive values) and spin-down (negative values) channels projected on Ru t_{2g} (black line) and O p (blue filled area) states. b) Partial charge density map associated with states around the Fermi level indicated by the orange area in panel (a).

bandwidth of the studied cases with $W_{t_{2g}}^{\text{AFMC}} = 1.04\text{eV}$. This could signal that in fact the absence of a JTD for the rest of the magnetic orders is a matter of band compatibilities. We can then try to explore the absence of the Jahn-Teller distortion by calculating the potential energy surface of the FM solution but with an 8% of negative pressure (FM-nP). We do this by increasing the size of the lattice parameters isotropically so that the volume is an 8% larger. From Figure 7.7 we notice that the JTD softens although still developing a single well potential (see Figure 7.7). This is quite interesting because it signals that the JTE is screened by the hybridization since by increasing the distance between the Ru sites, the overlap between Ru d and O p states would be smaller, and the system would finally develop the JTD at some point. We can further see that it is a matter of band compatibilities by calculating the partial density of states of the t_{2g} states in the FM-nP configuration and measuring a bandwidth $W_{t_{2g}}$. The results in Figure 7.9 on the FM-nP show a metallic behavior but with a smaller band with of $W_{t_{2g}}^{\text{FM-nP}} = 1.48\text{eV}$. We can further support this by calculating the potential energy surface of the FM solution by employing a DFT+U scheme with a U potential on Ru d states of $U = 5\text{eV}$. This would enforce a higher orbital localization, improve the band compatibilities, and in turn modify the couplings between different lattice distortions. This is verified from the curve of Figure 7.10 where we clearly find a shifted single well with the minimum obtained at a finite amplitude Q_{JT} of the JTD.

From the structural point of view, we mentioned that the system also presents a finite stabilization of the $a^0a^0c^+$ mode, and so the Free energy expansion for the Q_{JT} in the ground

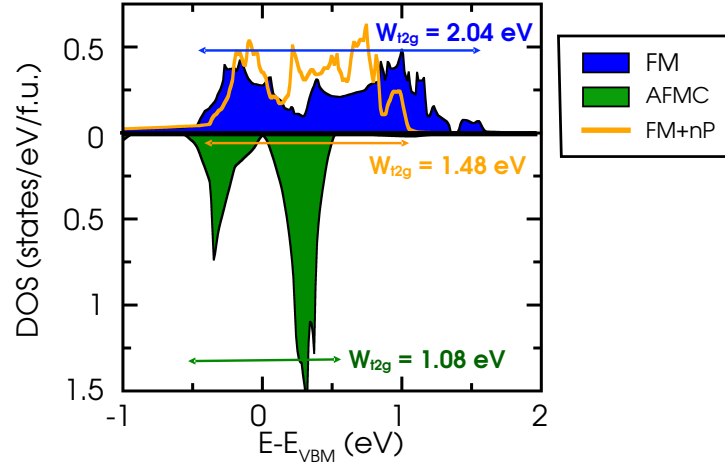


Fig. 7.9 Projected density of states of Sr_2RuO_4 on the t_{2g} orbitals for the FM in solid blue, AFMC in solid green), and FM with negative pressure (FM-nP) with a yellow line. Bandwidths are depicted as insets in the figure.

state would follow the expression in (7.2) but the coupling constants would be

$$\begin{aligned}
 \mathcal{F}'_0 &= \mathcal{F}_0 + \alpha_1 Q_{\phi_z^+}^2 + \beta_1 Q_{\phi_z^+}^4 \\
 \zeta_{eff} &= \zeta_1 Q_{\phi_z^+} + \zeta_2 Q_{\phi_z^+}^3 \\
 \alpha_{eff} &= \alpha_3 \\
 \delta_{eff} &= \delta Q_{\phi_z^+} \\
 \beta_{eff} &= \beta_3
 \end{aligned} \tag{7.4}$$

From this expression, we see that effectively, the JTD is allowed by symmetry and would couple to the in-plane rotations. However, this is not a sufficient condition to stabilize a finite distortion, since the amplitude of the JTD would depend on how strong are the coupling constants δ , ζ_1 , and ζ_2 . These constants would depend on the structure of the material and as a consequence, if they are too small, the JTD and the JTE would be screened as it is the case of Sr_2RuO_4 . From these findings, and recalling that AFM orders produce higher band capacities [26], we can understand the presence or absence of the JTD in Sr_2RuO_4 , since imposing different magnetic orders would change the electronic density which in turn would have a direct effect on the coupling constants of the different distortions. As a result, the AFMC order presents an instability towards the JTE while it is screened with an FM order. Thus with all these results and indicators, we can conclude that Sr_2RuO_4 is intrinsically in the vicinity of a JTE and an OO phase.

7.4 Superconductivity in ruthenate compounds

As we have shown in the previous section, Sr_2RuO_4 is at the vicinity of an OO phase produced by a JTD, so in analogy with the nickelate case and the CO, we build a model where the main interacting phonon is the Jahn-Teller phonon.

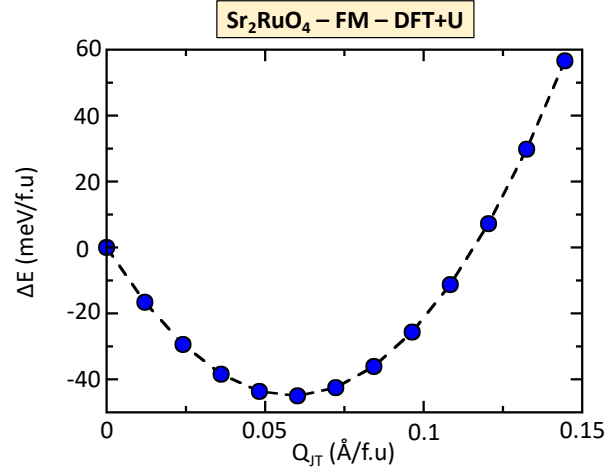


Fig. 7.10 Potential energy surface of JTD in Sr_2RuO_4 with DFT+U associated with the Jahn-Teller distortion amplitude Q_{JT} (in Å/f.u.). A ferromagnetic order is used for the simulations, and a U potential of 5 eV is introduced on Ru d states to prevent delocalization of the electronic structure.

7.4.1 Band structure of Sr_2RuO_4 ground state

In that regard, we calculate the electronic band structure of the ground state FM order (see Figure 7.11.a). We can notice that in the undistorted FM band structure, the majority spin channel presents a gap between the occupied t_{2g} and the unoccupied e_g states, as expected for a half-filled configuration. This automatically means that the conduction will be given by the minority spin channel which presents three main bands crossing the Fermi level. The first one is a parabolic band centered at the Γ point with a bandwidth of 3.52eV and a dominant d_{xy} orbital character. The other two bands come from the degenerate d_{xz} and d_{yz} , also centered at Γ but dispersing only on 1.72eV. In addition, we can note that there are no bands splitting, or gap openings suggesting that the electrons are almost free from any interaction with the lattice.

7.4.2 Evaluating the electron-phonon coupling

As we mentioned in chapters 5 and 6 on the nickelates, our goal is to evaluate the electron-phonon coupling λ , in this case originating from the JTD and given by

$$\lambda_{JT} = N(\varepsilon_F) \sum_k \frac{\hbar^2}{2\omega_{JT}^2} \left| \sum_j \frac{1}{\sqrt{M_j}} \frac{\Delta\varepsilon_k}{|u_{JT,j}|} \right|^2 \quad (7.5)$$

where $u_{JT,j}$ is the displacement of the j -th atom and $\Delta\varepsilon_k$ is the band splitting produced by freezing the JTD in the material. Now since in the JTD mode, there are only O atoms involved. we can express the EPC in a similar way as in the case of the B_{oc} mode in the nickelates,

$$\lambda_{JT} = 2N(\varepsilon_F) \sum_k \frac{\hbar^2}{2M_O\omega_{JT}^2} \left(\frac{\Delta\varepsilon_k}{Q_{JT}} \right)^2 \quad (7.6)$$

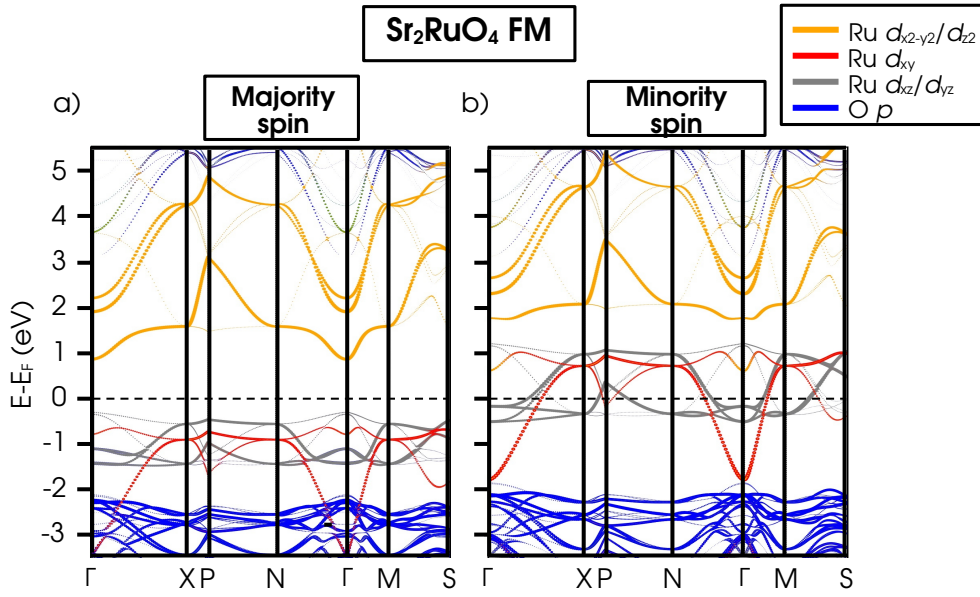


Fig. 7.11 Band structure of Sr_2RuO_4 superconductors with a FM magnetic order, (a) majority spin channel and (b) minority spin channel. The bands are unfolded with respect to the primitive I_4/mmm cell and projected on O p (blue), Ru d_{xy} (red), Ru d_{xz}/d_{yz} (grey), and Ru $d_{x^2-y^2}/d_{z^2}$ (orange). High symmetry points correspond to $\Gamma = (0, 0, 0)$, $X = (0, 0, 1/2)$, $P = (1/4, 1/4, 1/4)$, $N = (0, 1/2, 0)$, $M = (1/2, 1/2, -1/2)$, and $S = (0.2727, 0.7272, -0.2727)$

With this equation, our main task becomes to evaluate $\Delta\varepsilon_k$ from the band structure for different k points, as well as computing the frequency of the JTD mode ω_{JT} . If we introduce a finite Q_{JT} amplitude in the FM ground state structure of Sr_2RuO_4 , we can see that there is a band splitting of the d_{xz}/d_{yz} bands completely isotropic for all k points at the Fermi surface (see Figure 7.12.a). Thus we can recover equation (7.6) for the EPC and average over the Fermi surface as we did with the B_{oc} mode for the nickelates.

$$\lambda_{\text{JT}} = 2N(\varepsilon_F) \left\langle \frac{\hbar^2}{2M_{\text{O}}\omega_{\text{JT}}^2} \left(\frac{\Delta\varepsilon_k}{Q_{\text{JT}}} \right)^2 \right\rangle_{\text{F.S.}} \quad (7.7)$$

Then we substitute the band splitting $\Delta E_g = \frac{\Delta\varepsilon_k}{2}$ into (7.7) and we obtain

$$\lambda_{\text{JT}} = 2N(\varepsilon_F) \frac{\hbar^2}{2M_{\text{O}}\omega_{\text{JT}}^2} \left(\frac{\Delta E_g}{2Q_{\text{JT}}} \right)^2 = N(\varepsilon_F) \frac{\hbar^2}{2M_{\text{O}}\omega_{\text{JT}}^2} D_{\text{JT}}^2 \quad (7.8)$$

where $D_{\text{JT}} = \frac{\Delta E_g}{2u_{\text{JT},\text{O}}}$ is the reduced electron-phonon matrix element (REPME) associated with the JTD mode and $u_{\text{JT},\text{O}}$ is the atomic displacement of one O atom. From our analysis of the electronic band structure and equation (7.8), it becomes evident that the quantity that we must calculate is the REPME. We compute the band splitting ΔE_g for several values of the amplitude Q_{JT} of the JTD mode and, then with a linear fit of ΔE_g as a function of $u_{\text{JT},\text{O}}$ (see Figure 7.12.b), we obtain $D_{\text{JT}} = 7.76\text{eV}/\text{\AA}$.

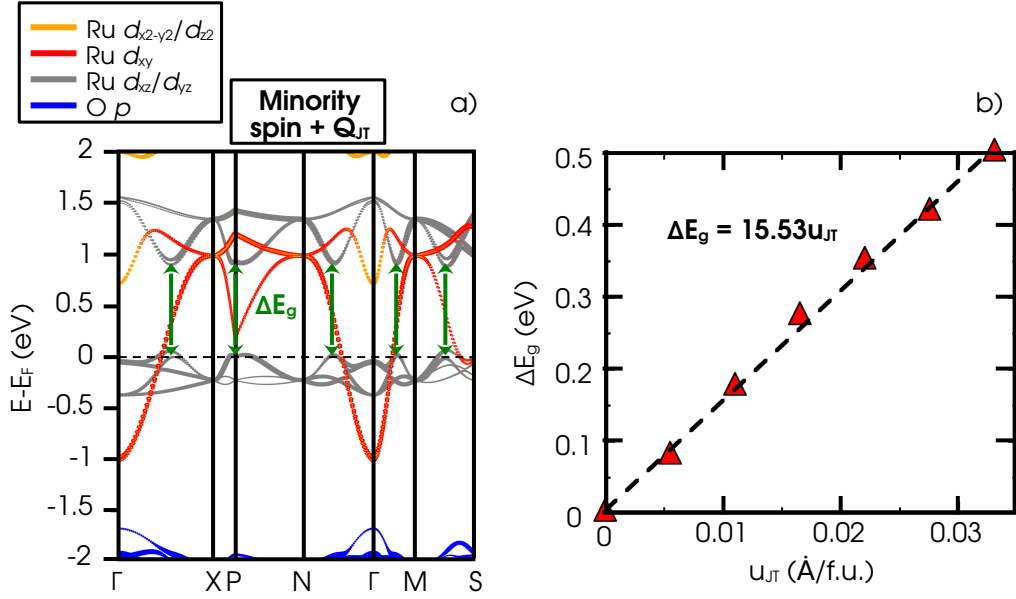


Fig. 7.12 Key features of the interacting potential D_{JT} or REPME. (a) Electronic band structure of FM Sr_2RuO_4 ground state in the minority spin channel with a non-zero amplitude of the JTD producing a band splitting ΔE_g . Projections are made on O p (blue), Ru d_{xy} (red), Ru d_{xz}/d_{yz} (grey), and Ru $d_{x^2-y^2}/d_{z^2}$ (orange). High symmetry points correspond to $\Gamma = (0, 0, 0)$, $X = (0, 0, 1/2)$, $P = (1/4, 1/4, 1/4)$, $N = (0, 1/2, 0)$, $M = (1/2, 1/2, -1/2)$, and $S = (0.2727, 0.7272, -0.2727)$. (b) Band splitting ΔE_g as a function of the introduced amplitude $u_{JT,O}$, with a linear fit as an inset.

The next quantity to compute is the harmonic frequency of the JT ω_{JT} which we evaluate directly from the potential energy surface depicted in Figure 7.7 and by mapping the energy into

$$\Delta E(Q_{JT}) = \frac{1}{2} M \omega_{JT}^2 Q_{JT}^2 + \frac{1}{4} \xi Q_{JT}^4 \quad (7.9)$$

in a similar manner as with the B_{oc} mode in the nickelates, obtaining a frequency of $\omega_{JT} = 81\text{meV}$.

Finally and in this case the most critical quantity to evaluate precisely is the density of states at the Fermi level. As we have noted, before, the experimental T_c is around 1.5 K, and as a result, small inaccuracies in the λ can lead to predict that the material will not present a superconducting transition at any temperature. In order to have accurate results, we have built the Wannier Functions associated with the minority spin channel aiming to extract atomic-like Wannier Functions with d_{xy} , d_{xz} and d_{yz} character centered on Ru cations. This allows us to converge the density of states in a very coarse k-mesh and extract the contributions given by the d_{xz}/d_{yz} orbitals only since these are the two main orbitals affected by the JTD (see Figure 7.13).

With this procedure, we obtain a value of $N(\varepsilon_F) = 0.2908$ states/eV/spin/f.u. for the d_{xz}/d_{yz} with a converged k-mesh of $256 \times 256 \times 64$ points for the Wannier Functions. With these values, we can evaluate the electron-phonon coupling to be $\lambda_{JT} = 0.35$ yielding a calculated T_c that oscillates between 1.65 K and 0.5 K for usual screened Coulomb interaction μ^* of 0.1 and 0.15 respectively and using the Mc. Millans-Allens equation where the characteristic energy scale is

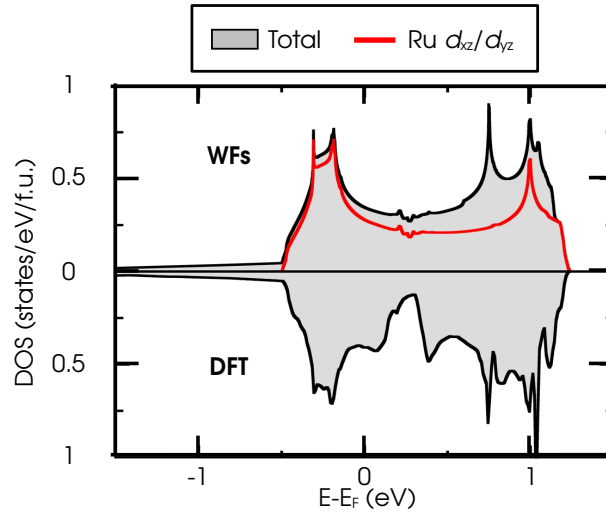


Fig. 7.13 Density of states of the FM ground state of Sr_2RuO_4 in the minority spin channel. Top panel the calculation is made with WFs, while the bottom panel is obtained with DFT. Solid grey is the total density of states, and red line is the projected DOS on Ru d_{xz}/d_{yz} orbitals.

given by the Jahn-Teller frequency in a similar fashion as with the nickelates $\omega_c = \omega_{\text{JT}}$

$$T_c = \frac{\hbar\omega_{\text{JT}}}{1.2} \exp\left\{-\frac{1.04(1 + \lambda_{\text{JT}})}{\lambda_{\text{JT}} - \mu^*(1 + 0.62\lambda_{\text{JT}})}\right\} \quad (7.10)$$

The obtained upper and lower bounds of T_c are reminiscent of the experimental value of 1.5 K, suggesting that Sr_2RuO_4 would be the first identified case of a JT superconductor in oxides.

7.5 Confirmation of the model in Ca_2RuO_4 nanofilm

Although we have been able to obtain a similar critical temperature between theory and experiments, one could, of course, be rather skeptical about the results since the values might be within the accuracy of DFT. Luckily, recent studies have shown superconductivity in Ca_2RuO_4 nanofilm single crystals under pressure with a critical temperature of 64 K coexisting with ferromagnetism [297]. In contrast to the bulk, the nanofilm corresponds to a pressured material with a c_O/a_O greater than one and is expected to exhibit a JTE and JTD as in bulk Sr_2RuO_4 .

Thus in order to validate the model identified in Sr_2RuO_4 , we perform DFT simulations on Ca_2RuO_4 but fixing the lattice parameters to those given in Ref. [297] for the SC nanofilm (namely $a = 5.343 \text{ \AA}$, $b = 5.350 \text{ \AA}$ and $c = 12.778 \text{ \AA}$). We then only relax the atomic positions so that they accommodate to the imposed lattice parameters keeping the same k -mesh and force and energy criteria as in the previous simulations. From this calculation, we obtain a c_O/a_O ratio of 1.05 and a metallic compound with an FM order.

We then perform a symmetry mode analysis in a similar way as we did with the bulk of Ca_2RuO_4 , obtaining a non-zero amplitude for the three lattice distortions $Q_{\text{JT}} = 0.01 \text{ \AA}$,

$Q_{\phi_z^+} = 0.46 \text{ \AA}$, and $Q_{\phi_{xy}^-} = 0.62 \text{ \AA}$. By comparing these values, with those presented in Table 7.1 for the FM ground state of Ca_2RuO_4 , we notice that the amplitudes of the modes are smaller in the strained nanofilm configuration than in the bulk ground state, although retaining some of the JTD amplitude Q_{JT} . This is in fact a consequence of the rotations that are coupled to this mode and allow a finite stabilization of it. However, in spite of presenting a finite JTD, the pressured compound remains metallic, signaling that the JTE is screened and is not able to enforce electron localization. This is a similar situation to Sr_2RuO_4 , where the JTE effect is screened and does not produce an insulating state despite the presence of the ϕ_z^+ rotations.

From the electronic structure point of view, we obtain a rather similar band dispersion as in Sr_2RuO_4 (see Figure 7.14), where the conduction is given by the minority spin channel, with the same orbital character of Γ centered bands dominated by Ru d_{xy} and d_{xz}/d_{yz} states. Nonetheless, we observe that there are some small band splittings of some of the bands, originating from the non-zero amplitude Q_{JT} of the JTD.

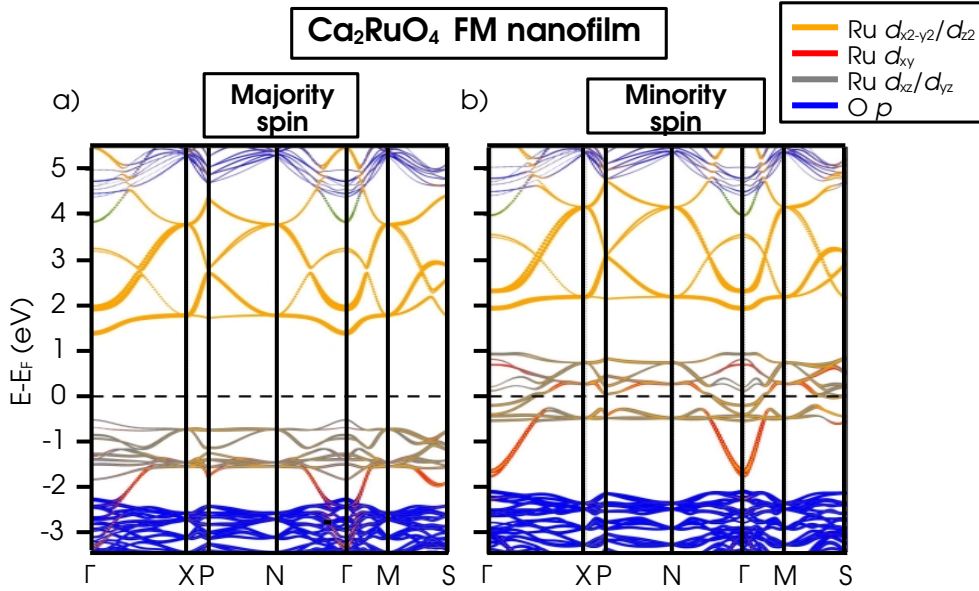


Fig. 7.14 Electronic band structure for FM Ca_2RuO_4 nanofilm under pressure, (a) in the majority spin channel, and (b) in the minority spin channel. Projections are made on O p (blue), Ru d_{xy} (red), Ru d_{xz}/d_{yz} (grey), and Ru $d_{x^2-y^2}/d_{z^2}$ (orange). High symmetry points correspond to $\Gamma = (0, 0, 0)$, $X = (0, 0, 1/2)$, $P = (1/4, 1/4, 1/4)$, $N = (0, 1/2, 0)$, $M = (1/2, 1/2, -1/2)$, and $S = (0.2727, 0.7272, -0.2727)$.

The next step is to evaluate the electron-phonon coupling constant, for which we need to compute the REPME D_{JT} , the frequency of the mode ω_{JT} , and the density of states at the Fermi level $N(\varepsilon_F)$ for the two orbitals involved. We repeat the same procedure as we presented for Sr_2RuO_4 for the three quantities (see Figure 7.15).

We must note one technical difference for evaluating the frequency. When we use equation (7.9) to extract the frequency, it is assumed that the amplitude Q_{JT} of the JTD mode is zero in the ground state. This however is not true in the pressured Ca_2RuO_4 nanofilm. Nonetheless,

the non-zero amplitude of the JTD is not caused by an electronic instability since it is screened, but a coupling with the other lattice distortions. Thus since we seek to obtain the harmonic term, we will compute the potential energy surface in the relaxed ground state structure and fit to the following polynomial expansion

$$E[Q_{JT}] = E_0 + \zeta_{eff}Q_{JT} + \alpha_{eff}Q_{JT}^2 + \delta_{eff}Q_{JT}^3 + \beta_{eff}Q_{JT}^4 \quad (7.11)$$

and then compute the frequency as

$$\omega_{JT} = \sqrt{\frac{2\alpha_{eff}}{M_O}} \quad (7.12)$$

For the REPME we extract it computing the band splitting ΔE_g for a given amplitude Q_{JT} as it is depicted in Figure 7.15.a, and then with several amplitudes use a linear fit (see Figure

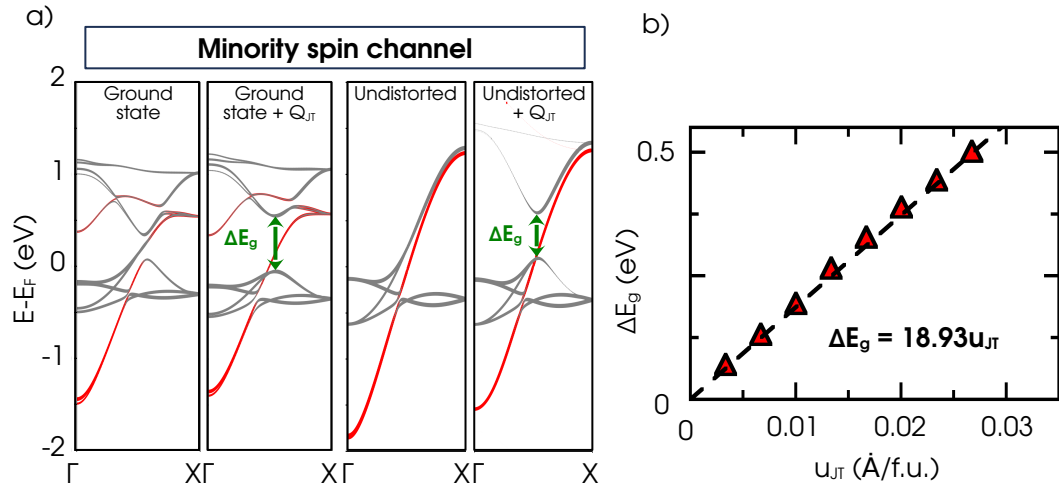


Fig. 7.15 Electronic band structure of the FM minority spin channel of Ca₂RuO₄ nanofilm along the $\Gamma - X$ path with and without a JTD, for the ground state and a completely undistorted structure (a). The band splitting ΔE_g as a function of the amplitude of the mode Q_{JT} , with a linear fit as an inset (b)

7.15.b) that allows us to obtain a value of $D_{JT} = 9.46 \text{ eV/\AA}$. Finally, for the density of states we make use again of the Wannier functions to extract only the contribution of the d_{xz}/d_{yz} orbitals. This allows us to obtain a huge electron-phonon coupling $\lambda_{JT} = 1.68$, yielding a T_c between 73 and 63 K for μ^* of 0.1 and 0.15, respectively in fair agreement with the experimental value of 64 K [297]. Thus our model based on a JTD responsible for the Cooper pair formation in the ruthenates is validated since it is able to account for the superconducting transition of Sr₂RuO₄, and Ca₂RuO₄ nanofilm under pressure.

One may have realized, that although both systems seem to be rather similar in terms of electronic structure, c_O/a_O ratio, and presenting an isotropic coupling with the JTD mode (see Figures 7.14 and 7.15), the electron-phonon coupling in Ca₂RuO₄ is much bigger than in Sr₂RuO₄, and consequently the T_c in the first compound is more than forty times bigger than

in the latter. At odds with Sr_2RuO_4 , Ca_2RuO_4 as a nanofilm material retains its octahedral rotations with amplitudes of $Q_{\phi_z^+} = 0.62 \text{ \AA}/\text{f.u.}$, and $Q_{\phi_{xy}^-} = 0.46 \text{ \AA}/\text{f.u.}$, for the ϕ_z^+ and ϕ_{xy}^- modes, respectively. We can then recall that the free energy expansion on (7.1), presents several couplings between the rotations and the JT mode. As a result, the free energy in the ground state will be given by (7.2). Now since we are extracting the harmonic constant, we would be only interested in the term proportional to Q_{JT}^2 which would be

$$\mathcal{F} \propto (\alpha_3 + \lambda_2 Q_{\phi_{xy}^-}^2) Q_{\text{JT}}^2 \quad (7.13)$$

We can then see that a finite stabilization of the rotation can actually change the effective frequency of the JTD mode. We can have two possibilities, if $\lambda_2 > 0$ the effective frequency would be higher and the JTD mode would be harder. In contrast if $\lambda_2 < 0$ the effective frequency would be smaller and the JTD mode would become softer. We can then calculate the potential energy surface in both cases, (i) in the high symmetry case with only the JTD present and (ii) in the ground state with the octahedral rotations (see Figure 7.16). From these curves and equations (7.11) and (7.12), we are able to obtain the frequencies in both cases. The fits are

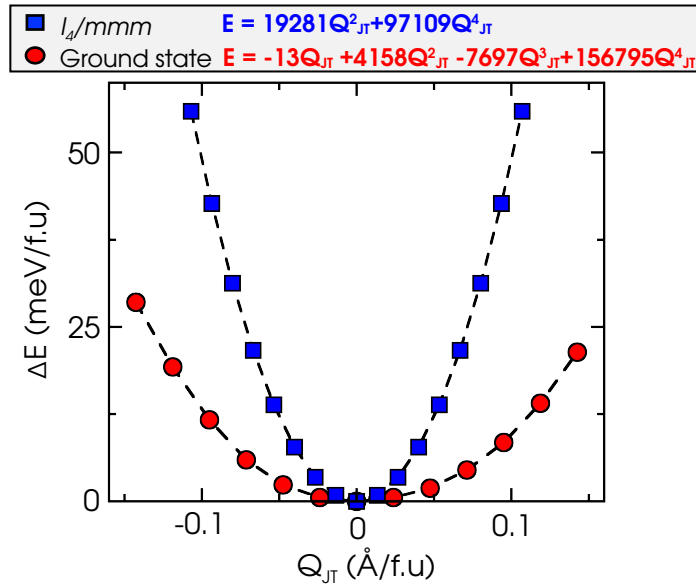


Fig. 7.16 Potential energy surface of Ca_2RuO_4 for the Q_{JT} of the JTD alone (blue squares) and with all the distortions appearing in the relaxed ground state (red circles)

provided as insets in Figure 7.16, yielding a frequency of $\omega_{\text{JT}}^{\text{HS}} = 100 \text{ meV}$ and $\omega_{\text{JT}}^{\text{GS}} = 46 \text{ meV}$ in the high symmetry and the ground state respectively. We can notice that although we are in the ground state, the fit of the curve yields a linear term signaling a minimum at non-zero amplitude. Nonetheless, this is just numerical noise since the minimum would be located at $Q_{\text{JT}} = 0.001 \text{ \AA}$, with a force at the origin of $-13 \text{ meV}/\text{\AA}/\text{f.u.}$, which is within the accuracy of the DFT calculations.

Now recalling the expression for the electron-phonon coupling in (7.6), we can see that it is inversely proportional to the square of the frequency of the JTD mode

$$\lambda_{\text{JT}} \propto \frac{1}{\omega_{\text{JT}}^2} \quad (7.14)$$

Hence it is natural that reducing the frequency by almost half of the value produces an EPC four times bigger. One could also point out that the frequency of the mode is not the only quantity that can change drastically with the pressure, since for instance the density of states $N(\varepsilon_F)$ or the REPME D can be modified. However, this is not the case, since in Ca_2RuO_4 we obtain a REPME of $D = 9.55 \text{ eV/\AA}$ in the high symmetry phase and $D = 8.77 \text{ eV}$ in the low symmetry phase being rather close to the value of 7.76 eV/\AA in Sr_2RuO_4 . We obtain a similar conclusion by analyzing the values of the density of states (see Figure 7.17), Ca_2RuO_4

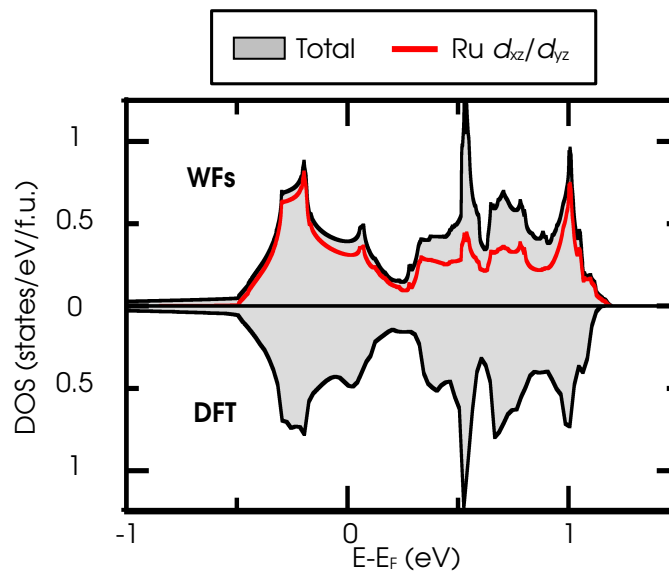


Fig. 7.17 Density of states of the FM ground state of pressured Ca_2RuO_4 nanofilm in the minority spin channel. In the top panel, the calculation is made with WFs, bottom panel with DFT. Solid grey is the total density of states, and the red line is the projected DOS on Ru d_{xz}/d_{yz} orbitals.

presents a density of states at the Fermi level of $N(\varepsilon_F) = 0.31 \text{ states/eV/f.u.}$ for the d_{xz}/d_{yz} orbitals, while in Sr_2RuO_4 we have $0.29 \text{ states/eV/f.u.}$. Thus we can conclude here that the strong softening of the JTD in Ca_2RuO_4 yields an EPC of $\lambda_{\text{JT}} = 1.68$ and ultimately results in a huge increase of the critical temperature T_c with respect to Sr_2RuO_4 .

7.6 Conclusion

From these results, we can already point out that the coupling between lattice distortions such as rotations to the phonons that mediate the SC pairing, can promote the pairing by softening the modes and as a result enhance the critical temperature. As a final remark, we

can conclude here that the ruthenates are the first identified oxide material where the SC is mediated by phonons in the proximity of orbital ordering instability.

Conclusion and perspectives

In this thesis, we have explored in detail the physics of the layered nickelates mainly from the theoretical point of view using DFT, where we have employed a state-of-the-art parameter-free functional SCAN, that we have previously tested intending to establish its limitations and strengths. We reveal that although the meta-GGA SCAN functional is a big improvement over the usual GGA functionals at a reasonable computational cost, it is still unable to deal with highly localized $4f$ states. Being aware of these limitations allows us to understand how reliable are the obtained results and decide easily in which situations a more advanced method is required.

Once we have established the reliability of the methods employed, we begin studying these nickelates by relaxing the structure of several RNiO_2 compounds. This allows us to study the structural, magnetic, and electronic properties that characterized these materials, finding that the crystal structure is prone to present several lattice distortions that correlate with the size of the rare-earth cation R. From the point of view of the magnetism, we reveal that the magnetic interactions are mainly given by Ni cations pointing to an antiferromagnetic ground state. We have also investigated the electronic band structure for several magnetic orders revealing that the RNiO_2 compounds are a rare case of AFM metals with a Mott character, and the band dispersion for the PM phase is not well modeled using non-spin-polarized calculations and a random spin arrangement is closer to the results obtained with higher accuracy methods like DMFT. Additionally, we find that the H can get trapped in the system and produce a Mott-insulating compound.

We then proceed to study the doping phase diagram closely following the existing literature and propose that the IL phase belongs to a broader family of layered nickelate compounds that we denote as RRP, with the general chemical formula $\text{R}_{n+1}\text{Ni}_n\text{O}_{2n+2}$ and characterized by a positive integer number n , and show that the IL phase is the last member of the series ($n = \infty$) which allows us to start the analysis from the first member instead ($n = 1$). This approach proves to be much more revealing since the undoped IL phase presents a weakly metallic character while the RRP $n = 1$ compound is an insulator. We then show that increasing the number n in the series means introducing more electrons into the system, finding that in the half-doped case, the compounds are prone to develop a charge-ordered insulating phase that produces a bond disproportionation distortion on the NiO_4 complexes. This character proves to be universal and depends only on the effective Ni $3d$ electron count, where both the RRP $n = 2$ compound and the doped IL phase show the same behavior. Then further increasing the $3d$ electron count either by doping the IL phase or increasing the number n on the RRP series, destabilizes the

charge-ordered phase until is completely quenched and produces a metallic region. Within this metallic region, the SC phase is hosted and we show that it is just in the vicinity of the CO phase, where the same phonon modes responsible to the charge ordering, play also an important role in the SC phase since they still present a non-negligible electron-phonon coupling. With this model, we are able to reproduce correctly the trends of the superconducting T_c as a function of the doping content on the IL phase and as a function of the number n in the RRP series further showing that the mechanism is universal and mainly depends on the Ni $3d$ electron count.

Nonetheless, we show that the $3d$ electron count is not the only factor to keep in mind, where the dimensionality of the system plays also an important role. In that regard, through a collaboration with an experimental team in CRISMAT lab, we explore the low-energy physics of a newly synthesized compound with chemical formula $\text{Nd}_{0.8}\text{Sr}_{1.2}\text{NiO}_3$ that presents the same $3d$ electron count as the superconducting nickelates but shows insulating behavior. We further reveal that the origin of the insulating character is a charge ordering reminiscent of the charge ordering in the RRP series and that the system shows a strong antiferromagnetic character with a possible two-spinon excitation spectrum.

Finally, we extend the superconducting model to other compounds, recalling that the other existing electronic instability that produces an insulating character in the perovskite-like compounds, is the Jahn-Teller distortion. We then explore the ruthenate case of Sr_2RuO_4 and Ca_2RuO_4 revealing that at normal conditions, the first compound is at the vicinity of an orbital-ordered phase denoted by OO, caused by a screened Jahn-Teller effect and Jahn-Teller distortion. Nonetheless, the phonon mode presents a non-negligible electron-phonon coupling that is sufficient to reproduce the experimental T_c of the SC transition. This is further supported by being able to reproduce the insulating behavior of Ca_2RuO_4 at normal conditions and the SC T_c under pressure. Thus showing that Sr_2RuO_4 is the first SC compound driven by an orbital-ordered instability.

In summary, we explore the SC properties of nickelates and other perovskite-like compounds and develop models based on phonons that are able to reproduce quantitatively the trends on the SC T_c . The mentioned models are based on connecting electronic instabilities that are able to produce an insulating state in transition metal oxides, with the superconducting mechanism, suggesting that both the insulating state and the SC phase are connected and share the same mechanism with different strengths of the coupling parameter. In this way, at strong coupling, we may have Mott and Charge transfer insulators, while at moderate coupling we have SC compounds. Thus future strategies to obtain superconducting compounds should consider charge and orbital ordering instabilities in the phase diagram, and destabilize the insulating phases with for instance doping or applying pressure.

List of figures

1.1	Representation of two functions for the magnetic field \mathbf{B} as a function of the radial coordinate r . The first $f(r) = \frac{e^{-r}}{r}$ (in blue) and the second $g(r) = \frac{1}{r}$ (in red).	3
1.2	Picture of (a) one Cooper pair formed by two electrons, and (b) Feynman diagram of the effective electron-electron interaction.	5
1.3	Typical Fermi surface of the Cu-based superconductors (a) the nesting vector $\mathbf{Q}_{\text{AFM}} = (\pm\frac{\pi}{a}, \pm\frac{\pi}{a})$ connecting two regions of the Fermi surface, and (b) the positive and negative regions of the superconducting gap $\Delta_{\mathbf{k}}$ with a sign + and – respectively and the dashed lines represent the nodal lines of the gap function.	15
1.4	Cubic perovskite crystal structure ABX_3 .	16
1.5	Structure of the Ruddlesden-Popper compounds $\text{A}_{n+1}\text{B}_n\text{O}_{3n+1}$.	16
1.6	Crystal field splitting Δ_{CF} of the d orbital in a O_6 octahedral environment.	18
1.7	Crystal field splitting Δ_{CF} of the d orbital in a O_6 octahedral environment with a strong Hund's coupling J_H splitting the two spin channels completely.	18
1.8	Experimental phase diagram of RNiO_3 compounds as a function of the tolerance factor t and the Ni-O-Ni angle for different rare-earth species. Squares and circles represent the MIT temperature (T_{MIT}) and the Neel temperature (T_{N}). Adapted from Refs. [18–22].	20
1.9	The different tilt patterns found in RNiO_3 compounds, (a) the out-of-plane anti-phase rotations $a^-a^-c^0$, (b) the in-plane in-phase rotations $a^0a^0c^+$, (c) the breathing distortion B_{oc} , and (d) the in-plane anti-phase rotations $a^0a^0a^-$.	21
1.10	Potential energy surface of YNiO_3 associated with the B_{oc} mode in the presence of a finite percentage amplitude of the $a^-a^-c^+$ distortion. Adapted from Ref. [25].	22
1.11	Crystal structure of the reduced Ruddlesden-Popper series (RRP) with chemical formula $\text{R}_{n+1}\text{Ni}_n\text{O}_{2n+2}$, for different members of the series.	23
1.12	Charge ordering patterns of Ni^+ and Ni^{2+} cations for (a) the case of $\text{R}_3\text{Ni}_2\text{O}_6$ ($n = 2$) compounds, and (b) $\text{R}_4\text{Ni}_3\text{O}_8$ ($n = 3$).	24
1.13	Resistivity curves of NdNiO_2 (in red) and $\text{Nd}_{0.8}\text{Sr}_{0.2}\text{NiO}_2$ (in blue). Adapted from [66].	25
1.14	Critical temperature T_c of the different superconducting nickelates as a function of the electron count. Experimental critical temperatures T_c are taken from Ref. [68–74]. Blue and red arrows indicate electron and hole doping the extremes of the phase diagrams respectively.	26

1.15	Comparison of the electronic structure of IL cuprates and nickelates. Adapted from [87].	28
2.1	Sketch of the distribution of the magnetic moments in a PM arrangement. . . .	47
2.2	Picture of the free energy \mathcal{F} for two phases A and B (red and blue line, respectively) with an order parameter η	49
2.3	Electronic band structure of MgB_2 . (a) bare band structure, and (b) band structure with the E_{2g} phonon mode frozen in the compound adapted from [158].	53
3.1	Projected density of states on Ti d (red line), O p (dashed blue line), and Eu $4f$ (orange area) in EuTiO_3 using the meta-GGA SCAN and hybrid HSE06 functionals and involving or not the $4f$ states in the simulations.	58
3.2	Projected density of states on Ti d (red line), O p (dashed blue line), and Gd $4f$ (orange area) in GdTiO_3 using the meta-GGA SCAN and hybrid HSE06 functionals and involving or not the $4f$ states in the simulations.	59
3.3	Projected density of states on Cr and Fe d (red line), O p (dashed blue line), and Pr and Dy $4f$ (orange area) in PrCrO_3 (left panels) and DyFeO_3 (right panels) using the meta-GGA SCAN and hybrid HSE06 functionals and involving or not the $4f$ states in the simulations.	61
3.4	Unfolded band structure to the high-symmetry primitive P_4/mmm cell of PrNiO_2 (top panels) and LaNiO_2 (lower panels) using the meta-GGA SCAN functional (left panels) and hybrid HSE06 (right panels) functionals. Calculations are performed with in plane antiferromagnetic interactions (AFMC) order. Coordinates of the high-symmetry points are $\Gamma(0,0,0)$, $X(\frac{1}{2},0,0)$, $M(\frac{1}{2},\frac{1}{2},0)$, $Z(0,0,\frac{1}{2})$, $A(\frac{1}{2},\frac{1}{2},\frac{1}{2})$, and $R(\frac{1}{2},0,\frac{1}{2})$	62
4.1	Crystal structure of YNiO_2 for a) undistorted P_4/mmm symmetry, b) ground state geometry with $Pbcn$ symmetry, c) out of plane in-phase rotations ϕ_{xy}^+ , d) in-plane anti-phase rotations ϕ_z^- , and e) antipolar motion of the A site cation A_p .	66
4.2	Total energy difference starting from the undistorted P_4/mmm cell in meV/f.u. as a function of the normalized mode amplitude Q in \AA , for the anti-phase rotations ϕ_z^- (red circles), the in-phase rotations ϕ_{xy}^+ (cyan squares) and the antipolar motion A_p (magenta diamonds) in YNiO_2	67
4.3	Potential energy surface of (a) the ϕ_{xy}^+ mode in the presence of a fraction of the ground state amplitude of the ϕ_z^- mode, and (b) A_p mode in presence of a fraction of the ground state amplitude of the ϕ_z^- mode.	68
4.4	Potential energy surface of the ϕ_{xy}^+ mode in the presence of (a) a fraction of the ground state amplitude of the ϕ_z^- mode, and (b) a fraction of the ground state amplitude of both A_p and ϕ_z^- modes.	69
4.5	Potential energy surface for the ground state geometry of the ϕ_z^- on YNiO_2 with the ground state geometry (GS), the in-plane lattice parameters of SrTiO_3 (STO), and the in-plane lattice parameters of (LSAT)	71

- 4.6 Crystal structure of the two relaxed geometries for the H intercalation in RNiO_2H compounds, with (a) H at the apex of Ni cations, and (b) H in the NiO_2 plane. 72
- 4.7 Binding energy (in meV/f.u.) for hydrogen intercalation in different two-dimensional (2D) nickelates. The reference energy is set to pristine materials with a P_4/mmm space group. The RNiO_2H compound is taken to have P_4/mmm symmetry (red circles), I_4/mcm symmetry (green triangles) and global ground state geometry (blue squares), corresponding to I_4/mcm for La, and Pr, $Pbcn$ for GdNiO_2 , and $Pbnm$ for YNiO_2 . Arrows correspond to the binding energy for the hydrogenated ground state with respect to the pristine material ground state structure (blue open squares) P_4/mmm for LaNiO_2 and PrNiO_2 , I_4/mcm for GdNiO_2 and $Pbcn$ for YNiO_2 73
- 4.8 Sketch of the exchange coupling constants considered in a generic RNiO_2 compound. 76
- 4.9 Electronic band structure of (a) DFT in the NM approximation for LaNiO_2 , (b) DFT in the random spin PM magnetic solution for LaNiO_2 , and (c) DFT+DMFT self-consistent PM solution adapted from [215] for NdNiO_2 . For panels (a) and (b) the bands include projections on O $2p$ states (in blue), Ni $3d$ states (in red) and La $5d$ states (in green). For panel (c) the bands present projections on Ni (red) Nd (blue) and O with an interstitial orbital (green). High symmetry points of the first Brillouin Zone are Γ (0,0,0), X (0,0,0), M (1/2,1/2,0), Z (0,0,1/2), R (1/2,0,1/2) and A (1/2,1/2,1/2). 79
- 4.10 Unfolded band structures for LaNiO_2 in the ground state geometry for (a) FM, (b) type-A AFM, (c) type-C AFM, and (d) type-G AFM. Projected spectral weights are presented for La $5d$ (green), O $2p$ (blue) and Ni $3d$ (red) states. High symmetry points correspond to Γ (0,0,0), X (0,0,0), M (1/2,1/2,0), Z (0,0,1/2), R (1/2,0,1/2) and A (1/2,1/2,1/2). 80
- 4.11 Orbital decomposed band structure on selected Ni d (in red) and La d (in green) orbitals for type-C AFM order with the full band structure including O p states in (blue) on the top left panel. High symmetry points correspond to the P_4/mmm symmetry denoted as Γ (0,0,0), X (0,0,0), M (1/2,1/2,0), Z (0,0,1/2), R (1/2,0,1/2) and A (1/2,1/2,1/2). 82
- 4.12 Band structure of the AFMC order on the left panel. Partial charge density on a given energy window (green region on the left panel) centered at the Ni sites as a 3D model isosurface on the right. 83
- 4.13 Energy levels of each Ni cation on the RNiO_2 compounds with the different orbitals on the majority (in blue) and minority (in red) spin channels. The crystal field Δ_{CF} between the d_{z^2} and $d_{x^2-y^2}$ orbitals is represented as well as the Hund's coupling J_H 84
- 4.14 Unfolded band structure for YNiO_2 in the high symmetry phase with P_4/mmm symmetry (a), and in the ground state geometry with $Pbcn$ symmetry (b). High symmetry points correspond to the P_4/mmm symmetry denoted as Γ (0,0,0), X (0,0,0), M (1/2,1/2,0), Z (0,0,1/2), R (1/2,0,1/2) and A (1/2,1/2,1/2). 85

- 4.15 On the left (a) projected density of states of LaNiO_2 (top panel) with ground state P_4/mmm symmetry LaNiO_2H with undistorted P_4/mmm (middle panel) and LaNiO_2H with relaxed structure with rotations and I_4mcm symmetry (bottom panel). Blue area are the O $2p$ states, red area the Ni $3d$ states. Positive and negative values of the density of states correspond to the spin-up and spin-down channels. On the right crystal structure of the two geometries of LaNiO_2H considered (b) with P_4/mmm symmetry, and (c) with I_4/mcm symmetry. 86
- 5.1 The projected density of states of (a) La_2NiO_4 , and (b) LaNiO_2 with a PM magnetic order. In solid grey the Ni $3d$ states, and the blue line represents the O $2p$ states. Positive values of the density of states correspond to the spin-up channel while negative values correspond to the spin-down channel. 90
- 5.2 The three different geometries of half doped layered nickelates with $3d^{8.5}$ electron count that are explored. (a) RRP $\text{La}_3\text{Ni}_2\text{O}_6$, (b) DSS $\text{La}_{0.5}\text{Sr}_{0.5}\text{O}_2$, and (c) SL $\text{La}_{0.5}\text{Sr}_{0.5}\text{O}_2$ 91
- 5.3 Breathing of oxygen complexes distortion (B_{oc}) producing a double local environment on Ni sites, with Ni_S in the compressed NiO_4 square and Ni_L in the extended NiO_4 square. 92
- 5.4 Electronic structure of half-doped nickelates. Projected density of states on O p (in red) Ni d (in blue) and Ni d (in grey) for (a) solid solution (DSS) IL nickelate with PM order using the SCAN functional, and (b) superlattice (SL) IL nickelate with type-E AFM using the HSE06 functional. (c) Partial charge density map of selected bands indicated by the orange square on panel (b). 93
- 5.5 Orbital filling of the energy levels on Ni cations in the square coordinated environment of the RRP or IL phase. Two situations are considered (a) the system presents all Ni cations equivalent and with a $\text{Ni}^{1.5+}(3d^{8.5})$ producing a metallic state, and (b) the system presents two types of Ni cations, with a $\text{Ni}^+(3d^9)$ configuration as in the case of Ni_L cations, and with a $\text{Ni}^{2+}(3d^8)$ configuration as in the case of Ni_S cations, producing an insulating state with gap amplitude E_g . 94
- 5.6 Potential energy surfaces of the B_{oc} mode with a PM magnetic order and several geometries, (a) $\text{La}_{0.5}\text{Sr}_{0.5}\text{NiO}_2$ with PM order, (b) $\text{La}_{0.5}\text{Sr}_{0.5}\text{NiO}_2$ SL with PM order, and (c) $\text{La}_3\text{Ni}_2\text{O}_6$ with PM order. Total energy differences are taken with respect to the high symmetry P_4/mmm and I_4/mmm cells for the IL and RRP, respectively. 95
- 5.7 Trends in disproportionation effects with a PM order signaling the charge ordered phase with the $3d$ electron count for two key quantities (a) the amplitude of the B_{oc} mode in $\text{\AA}/\text{NiO}_2$ motif, and (b) the absolute value of the difference in the magnetic moment of Ni_L and Ni_S cations. Both quantities are represented for the fully relaxed structures of $\text{La}_{0.5}\text{Sr}_{0.5}\text{NiO}_2$ solid solution (red dots, DSS), superlattice (blue squares, SL), and $\text{La}_3\text{Ni}_2\text{O}_6$ (green triangles, RRP). 96

5.8	Projected density of states on O p (red line), Ni _S d (blue line) and Ni _L d (solid grey) of La _{0.625} Sr _{0.375} NiO ₂ in a SL geometry with a type-E AFM. In the inset, the magnetic moment on the 3 Ni _S and 5 Ni _L cations are given as well as the $Q_{B_{oc}}$ mode amplitude.	97
5.9	Potential energy surface of the B _{oc} mode for the DSS of La _{1-x} Sr _x NiO ₂ with a PM order for different values of x (a) $x = 0.4375$, (b) $x = 0.3125$, (c) $x = 0.25$, (d) $x = 0.1875$, (e) $x = 0.125$, and (f) $x = 0$	98
5.10	Square of the B _{oc} mode frequency $\omega_{B_{oc}}^2$ as a function of the $3d$ electron count computed in the highly symmetric P_4/mmm cell (red dots) and in the relaxed ground state with $P1$ symmetry (blue squares).	99
5.11	Unfolded band structure for DSS La _{0.8125} Sr _{0.1875} NiO ₂ with PM magnetic order. (a) The full band structure, (b) a sketch of the Brillouin zone associated to the primitive cell of P_4/mmm symmetry with high symmetry points highlighted. High symmetry points correspond are Γ (0,0,0), X (0,0,0), M (1/2,1/2,0), Z (0,0,1/2), R (1/2,0,1/2) and A (1/2,1/2,1/2).	101
5.12	Unfolded band structure of DSS La _{0.825} Sr _{0.187} NiO ₂ along the $Z - A$ path with a finite amplitude of the B _{oc} mode (right) and without it (left). High symmetry points correspond to $Z = (0, 0, 1/2)$, and $A = (1/2, 1/2, 1/2)$ of the high symmetry P_4/mmm primitive cell.	102
5.13	Band splitting ΔE_g as a function of the atomic displacement $u_{B_{oc},O}$. The slope of the linear fit is equivalent to $2D_{B_{oc}}$, which is the REPME.	102
5.14	Band splitting computed for La _{0.75} Sr _{0.25} NiO ₂ with a SL geometry and a type-E AFM with SCAN (left panel) and HSE06 (right panel) functional.	103
5.15	Computed density of states at the Fermi level $N(\varepsilon_F)$ as a function of the electron count in the DSS of La _{1-x} Sr _x NiO ₂	103
5.16	Electron phonon coupling as a function of the $3d$ electron count.	104
5.17	Critical temperature as a function of the $3d$ electron count on Ni cations for La _{1-x} Sr _x NiO ₂ . Blue dots are the experimental points extracted from Ref. [68], green diamonds and yellow and red triangles are the computed values from DFT using equation (5.15)	105
5.18	Total energy difference between the non-spin polarized NM solution and the random spin PM solution ΔE_{NM-PM} in eV/f.u. as a function of the Ni $3d$ electron count. Positive values indicate that the PM solution is more stable, while negative values indicate that the NM solution is more stable.	106
5.19	Potential energy surface of the B _{oc} mode in the DSS of La _{0.5} Sr _{0.5} NiO ₂ with (a) a non-spin polarized solution NM, and (b) a ferromagnetic order FM.	107
5.20	Electronic band structure of La _{0.5} Sr _{0.5} NiO ₂ DSS with (a) no magnetism (NM), and (b) with PM order. The band dispersion is unfolded to the primitive P_4/mmm cell. High symmetry points correspond are Γ (0,0,0), X (0,0,0), M (1/2,1/2,0), Z (0,0,1/2), R (1/2,0,1/2) and A (1/2,1/2,1/2).	108

5.21	Total density of states of $\text{La}_{0.5}\text{Sr}_{0.5}\text{NiO}_2$ in a SL with the NM solution. The gray area are the results using the SCAN functional, and the red line are the results obtained with the HSE06 functional.	109
5.22	Trends in disproportionation effects with a type-E AFM order signaling the charge ordered phase with the $3d$ electron count for two key quantities (a) the amplitude of the B_{oc} mode in $\text{\AA}/\text{NiO}_2$ motif, and (b) the absolute value of the difference in the magnetic moment of Ni_L and Ni_S cations. Both quantities are represented for $\text{La}_{0.5}\text{Sr}_{0.5}\text{NiO}_2$ solid solution (red dots DSS), superlattice (blue squares SL), and for $\text{La}_3\text{Ni}_2\text{O}_6$ (green triangles RRP).	110
6.1	Crystal structure of the reduced Ruddlesden-Popper series (RRP) with chemical formula $\text{R}_{n+1}\text{Ni}_n\text{O}_{2n+2}$	114
6.2	Diagram of the crystal field splitting in on Ni^{2+} cations with a $3d^8$ electronic configuration in the case of La_2NiO_4 for two different situations, (a) when Hund's coupling is neglected and a NM solution is employed in the DFT calculations producing a $S = 0$ spin state, and (b) when Hund's coupling is included and the spin degree of freedom is allowed in the DFT calculations producing a $S = 1$ spin state.	116
6.3	Energy difference $\Delta E_{\text{NM-FM}}$ between a non-spin-polarized (NM) and ferromagnetic (FM) order (in meV/NiO_2 motif) as a function of the formal Ni $3d$ occupancy in the reduced Ruddlesden-Popper compound. Red dashed lines indicate the position of each member n of the series.	117
6.4	Projected density of states of La_2NiO_4 with a FM order and $Cmce$ crystal symmetry on O p states (red line), Ni_L d states (solid grey) and Ni_S d states (blue line) . Positive and negative values of the DOS indicate the majority and minority spin channels.	118
6.5	$\text{La}_3\text{Ni}_2\text{O}_6$ (a) projected density of states with a FM order and $Cmmm$ crystal symmetry on O p states (red line), Ni_L d states (solid grey) and Ni_S d states (blue line) . Positive and negative values of the DOS indicate the majority and minority spin channels. (b) Crystal structure of the bond disproportionation mode B_{oc} producing two types of Ni cations Ni_L in grey and Ni_S in blue.	119
6.6	$\text{La}_4\text{Ni}_3\text{O}_8$ (a) projected density of states with a FM order and $Fmmm$ crystal symmetry on O p states (red line), Ni_L d states (solid grey) and Ni_S d states (blue line) . Positive and negative values of the DOS indicate the majority and minority spin channels. (b) Crystal structure of the bond disproportionation mode B_{oc} producing two types of Ni cations Ni_L in grey and Ni_S in blue.	120

- 6.7 $\text{La}_5\text{Ni}_4\text{O}_{10}$ (a) projected density of states with a FM order and $Fmmm$ crystal symmetry on O p (red line), Ni_L d (solid grey) and Ni_S d states (blue line). Positive and negative values of the DOS indicate the majority and minority spin channels. The crystal structure of the bond disproportionation modes B_{oc} producing two types of Ni cations Ni_L in grey and Ni_S in blue is given for (b) the ground state mode with in-plane propagation vector $q = (1/2, 0, 0)$, and (c) the alternative mode with in-plane propagation vector $q = (1/4, 1/4, 0)$ 121
- 6.8 Projected density of states of $\text{La}_6\text{Ni}_5\text{O}_{12}$ with a FM order and I_4/mmm crystal symmetry on O p states (red line), Ni d states (solid grey) and total density (black line). Positive and negative values of the DOS indicate the majority and minority spin channels. 121
- 6.9 Band structure of $\text{La}_6\text{Ni}_5\text{O}_{12}$ with FM order and I_4/mmm crystal symmetry. Left and right panel present the majority and minority spin channels respectively. The high symmetry points are Γ (0,0,0), X (1/2,0,0), M (1/2,1/2,0), Z (0,0,1/2), R (1/2,0,1/2) and A (1/2,1/2,1/2). 122
- 6.10 Potential energy surface of the associated bond disproportionation mode present in the $n = 2 - 4$ members of the RRP series. 123
- 6.11 The two situations considered on Ni sites for $\text{La}_3\text{Ni}_2\text{O}_6$ with a FM order and a I_4/mmm crystal symmetry. (a) Equal occupation of electrons in all Ni cations producing a $3d^{8.5}$ electron count, and (b) Mixed occupation of electrons in Ni cations with half of them with a $3d^8$ electron count (in blue) and the other half with a $3d^9$ electron count (in grey) with the same pattern as the B_{oc} mode. . . . 123
- 6.12 Amplitude in ($\text{\AA}/\text{NiO}_2$ motif) of the different bond disproportionation modes (red squares) B_{oc} present in the RRP compounds as a function of the Ni $3d$ electron count. Dashed lines indicate the effective electron count of each member of the RRP series from $n = 2$ to $n = 5$ 124
- 6.13 Potential energy surfaces of $\text{La}_6\text{Ni}_5\text{O}_{12}$ associated with the disproportionation modes appearing in $\text{La}_3\text{Ni}_2\text{O}_6$ ($n = 2$ blue circles) and in $\text{La}_4\text{Ni}_3\text{O}_8$ ($n = 3$ green diamonds) 125
- 6.14 Important quantities for obtaining the deformation potential (REPME). Electronic band structure of $\text{La}_6\text{Ni}_5\text{O}_{12}$ in the majority spin channel (a) with the highly symmetric I_4/mmm ground state and (b) with a finite amplitude of the B_{oc} mode presenting a band splitting ΔE_g . (c) Dependence of the band splitting ΔE_g with the mode amplitude for the $n = 2$ (blue circles) and the $n = 3$ (green diamonds) members of the RRP series 126
- 6.15 Crystal structure of unreduced parent Ruddlesden Popper phase with I_4/mmm symmetry (left), and reduced phase with $Immm$ symmetry (right) 128
- 6.16 Magnetic measurements of $\text{Nd}_{0.8}\text{Sr}_{1.2}\text{NiO}_3$, (a) the susceptibility χ in (emu/mol·Oe) as a function of temperature T in (K), for field cooled (FC in red) and zero field cooled (ZFC in blue) cases in red and blue, respectively. (b) The hysteresis curve of the induced magnetization M as a function of the applied field H at $T = 5$ K. 129

6.17	Possible reduced geometries. (a) pyramid, (b) octahedron and NiO ₂ square in-plane, and (c) experimental structure	130
6.18	Projected density of states on Ni <i>d</i> (in red) and O <i>p</i> (in blue) for (a) La _{0.8} Sr _{1.2} NiO ₄ on the left and (b) La _{0.8} Sr _{1.2} NiO ₃ on the right.	132
6.19	Features of the charge ordering in La _{0.8} Sr _{1.2} NiO ₃ for one of the NiO ₂ stripes with an AFM order. The spins are represented as blue and red arrows for up and down configurations, respectively. The Ni-O bond lengths of the NiO ₂ complexes <i>d</i> ₁ (along the z-axis) and <i>d</i> ₂ (along the x-axis) are given in (Å).	133
6.20	The possible charge ordered patterns of La _{0.8} Sr _{1.2} NiO ₃ (a) the obtained pattern from the 20 f.u. calculations. (b) the alternative pattern	133
6.21	Excitation spectra of a spin chain system in (<i>E</i> (<i>q</i>)/ <i>J</i>) units as a function of the momentum <i>q</i> in reciprocal lattice units (r.l.u). (a) 1D magnetic excitations dominated by the <i>E</i> ₋ (<i>q</i>) energy curve (in blue), (b) 2D magnetic excitation continuum between <i>E</i> ₋ (<i>q</i>) (in blue) and <i>E</i> ₊ (<i>q</i>) (in red) energy curves.	135
7.1	Jahn-teller distortion in an ABO ₃ perovskite where the cation B is a transition metal. The distortion produces two different crystal fields and orderings of the energy levels producing two types of B cations B ₁ and B ₂	138
7.2	Crystal and electronic structure of A ₂ RuO ₄ compounds, (a) crystallographic conventional cell. Ordering of Ru <i>d</i> states according to the O ₆ octahedral deformation for different <i>c</i> _O / <i>a</i> _O ratios defined in panel (a). Three cases are considered (b) <i>c</i> _O / <i>a</i> _O = 1, (c) <i>c</i> _O / <i>a</i> _O < 1, and (d) <i>c</i> _O / <i>a</i> _O > 1.	139
7.3	Electronic density of states of Ca ₂ RuO ₄ with a type-C AFM order. Two panels are depicted (a) projected density of states on O <i>p</i> states (solid blue) and Ru <i>d</i> states (black line) are depicted, and (b) the Ru <i>d</i> orbital character is depicted with <i>d</i> _{<i>xy</i>} in red, <i>d</i> _{<i>xz</i>} / <i>d</i> _{<i>yz</i>} in grey and <i>d</i> _{<i>x²-y²</i>} / <i>d</i> _{<i>z²</i>} in orange.	142
7.4	Rotation pattern present in A ₂ RuO ₄ compounds, (a) out of plane anti-phase rotations <i>a</i> ⁻ <i>a</i> ⁻ <i>c</i> ⁰ (<i>φ</i> _{<i>xy</i>} ⁻), and (b) in-plane in-phase rotations <i>a</i> ⁰ <i>a</i> ⁰ <i>c</i> ⁺ (<i>φ</i> _{<i>z</i>} ⁺).	143
7.5	Potential energy surface in Ca ₂ RuO ₄ associated with the Jahn-Teller distortion amplitude <i>Q</i> _{JT} (in Å/f.u) in presence of a percentage of the ground state amplitude of the <i>a</i> ⁰ <i>a</i> ⁰ <i>c</i> ⁺ (<i>Q</i> _{<i>φ</i>_{<i>z</i>}⁺}), <i>a</i> ⁻ <i>a</i> ⁻ <i>c</i> ⁰ (<i>Q</i> _{<i>φ</i>_{<i>xy</i>}⁻}) and JTD (<i>Q</i> _{JT}) distortions. A ferromagnetic order is used for the simulations.	143
7.6	Electronic density of states of Sr ₂ RuO ₄ with a FM order. Two panels are depicted (a) projected density of states on O <i>p</i> states (solid blue) and Ru <i>d</i> states (black line) are depicted, and (b) the Ru <i>d</i> orbital character is depicted with <i>d</i> _{<i>xy</i>} in red, <i>d</i> _{<i>xz</i>} / <i>d</i> _{<i>yz</i>} in grey and <i>d</i> _{<i>x²-y²</i>} / <i>d</i> _{<i>z²</i>} in orange.	144
7.7	Potential energy surface of the <i>Q</i> _{JT} mode (in Å/f.u) of the JTD for the NM (red filled squares), FM (blue filled circles), AFMC (green filled diamonds) and FM with a negative Pressure (FM-nP, orange filled circles)	145

- 7.8 Orbital-ordering exhibited by Sr_2RuO_4 AFMC ground state. a) Density of states (in states/eV/f.u) for spin-up (positive values) and spin-down (negative values) channels projected on Ru t_{2g} (black line) and O p (blue filled area) states. b) Partial charge density map associated with states around the Fermi level indicated by the orange area in panel (a). 146
- 7.9 Projected density of states of Sr_2RuO_4 on the t_{2g} orbitals for the FM in solid blue, AFMC in solid green), and FM with negative pressure (FM-nP) with a yellow line. Bandwidths are depicted as insets in the figure. 147
- 7.10 Potential energy surface of JTD in Sr_2RuO_4 with DFT+U associated with the Jahn-Teller distortion amplitude Q_{JT} (in Å/f.u). A ferromagnetic order is used for the simulations, and a U potential of 5 eV is introduced on Ru d states to prevent delocalization of the electronic structure. 148
- 7.11 Band structure of Sr_2RuO_4 superconductors with a FM magnetic order, (a) majority spin channel and (b) minority spin channel. The bands are unfolded with respect to the primitive I_4/mmm cell and projected on O p (blue), Ru d_{xy} (red), Ru d_{xz}/d_{yz} (grey), and Ru $d_{x^2-y^2}/d_{z^2}$ (orange). High symmetry points correspond to $\Gamma = (0, 0, 0)$, $X = (0, 0, 1/2)$, $P = (1/4, 1/4, 1/4)$, $N = (0, 1/2, 0)$, $M = (1/2, 1/2, -1/2)$, and $S = (0.2727, 0.7272, -0.2727)$ 149
- 7.12 Key features of the interacting potential D_{JT} or REPME. (a) Electronic band structure of FM Sr_2RuO_4 ground state in the minority spin channel with a non-zero amplitude of the JTD producing a band splitting ΔE_g . Projections are made on O p (blue), Ru d_{xy} (red), Ru d_{xz}/d_{yz} (grey), and Ru $d_{x^2-y^2}/d_{z^2}$ (orange). High symmetry points correspond to $\Gamma = (0, 0, 0)$, $X = (0, 0, 1/2)$, $P = (1/4, 1/4, 1/4)$, $N = (0, 1/2, 0)$, $M = (1/2, 1/2, -1/2)$, and $S = (0.2727, 0.7272, -0.2727)$. (b) Band splitting ΔE_g as a function of the introduced amplitude $u_{\text{JT},O}$, with a linear fit as an inset. 150
- 7.13 Density of states of the FM ground state of Sr_2RuO_4 in the minority spin channel. Top panel the calculation is made with WFs, while the bottom panel is obtained with DFT. Solid grey is the total density of states, and red line is the projected DOS on Ru d_{xz}/d_{yz} orbitals. 151
- 7.14 Electronic band structure for FM Ca_2RuO_4 nanofilm under pressure, (a) in the majority spin channel, and (b) in the minority spin channel. Projections are made on O p (blue), Ru d_{xy} (red), Ru d_{xz}/d_{yz} (grey), and Ru $d_{x^2-y^2}/d_{z^2}$ (orange). High symmetry points correspond to $\Gamma = (0, 0, 0)$, $X = (0, 0, 1/2)$, $P = (1/4, 1/4, 1/4)$, $N = (0, 1/2, 0)$, $M = (1/2, 1/2, -1/2)$, and $S = (0.2727, 0.7272, -0.2727)$ 152
- 7.15 Electronic band structure of the FM minority spin channel of Ca_2RuO_4 nanofilm along the $\Gamma - X$ path with and without a JTD, for the ground state and a completely undistorted structure (a). The band splitting ΔE_g as a function of the amplitude of the mode Q_{JT} , with a linear fit as an inset (b) 153
- 7.16 Potential energy surface of Ca_2RuO_4 for the Q_{JT} of the JTD alone (blue squares) and with all the distortions appearing in the relaxed ground state (red circles) . 154

- 7.17 Density of states of the FM ground state of pressured Ca_2RuO_4 nanofilm in the minority spin channel. In the top panel, the calculation is made with WFs, bottom panel with DFT Solid grey is the total density of states, and the red line is the projected DOS on Ru d_{xz}/d_{yz} orbitals. 155

List of tables

3.1	Summary of the key quantities characterizing the selected compounds that are computed and experimentally obtained from literature, including the different methods used for each compound, magnetic order on the rare earth and transition metal element, Space group of the computed geometry supported by experiments, DFT functional and inclusion or not of $4f$ electrons in the pseudopotential, values of the lattice parameters in Å, band edge orbital character (BEOC) on the conduction band minimum (CVM) and valence band maximum (VBM) depicted as (VBM , CVM), effective magnetic moment on the rare earth cation μ_R in μ_B and amplitude of the band gap E_g in eV. Structural relaxation is only performed with SCAN+ $4f$	57
4.1	Summary of important quantities extracted from first-principles calculations and a symmetry mode analysis on selected infinitely layered nickelates. Ionic radius is taken from Ref. [200] for an eight-coordinated complex.	70
4.2	Calculated total energy difference between the NM and the random PM solution $\Delta E_{\text{NM-PM}}$ in meV/f.u., and average magnetic moment μ_{Ni} on Ni cations extracted from the PM phase in μ_B , for both YNiO ₂ and LaNiO ₂ compounds.	75
4.3	Calculated total energy difference ΔE (meV/f.u) of the different magnetic ground states with respect to the FM order in YNiO ₂ and LaNiO ₂	76
4.4	Summary of the exchange constants obtained for different RNiO ₂ compounds expressed in meV from our calculations and other theoretical works. Experimental values available for different films are also reported. Positive values for the exchange constants $J > 0$ favor antiferromagnetic interactions, while negative values $J < 0$ favor ferromagnetic interactions.	77
5.1	Extracted key quantities of the relaxed half-doped compounds. Total energy difference ΔE in meV/f.u. of the distorted cell with the B _{oc} mode with respect to the high symmetry phase, I_4/mmm in the RRP and P_4/mmm in the IL. Mode amplitude $Q_{\text{B}_{oc}}$ in Å/NiO ₂ motif, and average magnetic moment on Ni _L and Ni _S sites.	92

- 6.1 Summary of the key quantities of the RRP $\text{La}_{n+1}\text{Ni}_n\text{O}_{2n+2}$ compounds with ($n = 1 - 5$) obtained from the DFT calculations with a NM solution. Including the ground state structure space group, lattice parameters in the conventional cell a and c in Å, Ni formal oxidation state (FOS), and gap amplitude E_g in eV. 115
- 6.2 Summary of the key quantities of the RRP $\text{La}_{n+1}\text{Ni}_n\text{O}_{2n+2}$ compounds with ($n = 1 - 5$) obtained from the DFT calculations with a FM solution. Including the ground state structure space group, lattice parameters in the conventional cell a , b and c in Å, gap amplitude E_g in eV, energy difference with respect to the high symmetry I_4/mmm cell ΔE in meV/f.u., magnetic moment on the two types of Ni sites (Ni_L and Ni_S) that can be expected in μ_B , and amplitude Q_{Boc} of the disproportionation mode in Å/ NiO_2 motif. 117
- 6.3 Total energy difference between the striped geometry (Stripe) and the geometries considered for La_2NiO_3 . The mixed octahedron and squares (Mixed), and the pyramidal arrangement (Pyramidal). 130
- 6.4 Summary of the structural parameters that characterize the $\text{R}_{2-x}\text{Sr}_x\text{NiO}_4$ and $\text{R}_{2-x}\text{Sr}_x\text{NiO}_3$ compounds. The first row for each group of compounds is the synthesized materials by our collaborators, and the last row is our DFT calculations. The rest of the rows are the existing literature. 131
- 7.1 Summary of key quantities of A_2RuO_4 compounds extracted from first-principles calculations: The total energy difference ΔE in meV/f.u. between spin-polarized and non-spin-polarized NM solutions. The average magnetic moment μ_{Ru} exhibited by Ru cations in μ_B . The band gap amplitude E_g in eV. The c_O/a_O ratio quantifying the octahedral deformation, and the mode amplitude of the Jahn-Teller distortion Q_{JT} , in-plane in-phase octahedral rotation $Q_{\phi_z^-}$, and out-of-plane anti-phase octahedral rotations $Q_{\phi_z^-}$ in Å/f.u. 141

References

- [1] Andreas Schilling, M Cantoni, JD Guo, and HR Ott. Superconductivity above 130K in the Hg–Ba–Ca–Cu–O system. *Nature*, 363(6424):56–58, 1993.
- [2] Alexander L Fetter and John Dirk Walecka. *Quantum theory of many-particle systems*. Courier Corporation, 2012.
- [3] Lukong Cornelius Fai. *Quantum field theory: feynman path integrals and diagrammatic techniques in condensed matter*. CRC Press, 2019.
- [4] Radi A Jishi. *Feynman diagram techniques in condensed matter physics*. Cambridge University Press, 2013.
- [5] Philip L Taylor and Olle Heinonen. *A quantum approach to condensed matter physics*. Cambridge university press, 2002.
- [6] Michael Tinkham. *Introduction to superconductivity*. Courier Corporation, 2004.
- [7] Kazumi Maki and Hyekyung Won. Why *d*-wave superconductivity? *Journal de Physique I*, 6(12):2317–2326, 1996.
- [8] M Houzet. Applications of symmetries in superconductivity. In *EPJ Web of Conferences*, volume 22, page 00014. EDP Sciences, 2012.
- [9] PHILIP W Anderson and Pierre Morel. Generalized bardeen-cooper-schrieffer states and the proposed low-temperature phase of liquid He₃. *Physical Review*, 123(6):1911, 1961.
- [10] Daniel Sando, A Barthélémy, and M Bibes. BiFeO₃ epitaxial thin films and devices: past, present and future. *Journal of Physics: Condensed Matter*, 26(47):473201, 2014.
- [11] Victor Moritz Goldschmidt. Die gesetze der krystallochemie. *Naturwissenschaften*, 14(21):477–485, 1926.
- [12] Anthony M Glazer. The classification of tilted octahedra in perovskites. *Acta Crystallographica Section B: Structural Crystallography and Crystal Chemistry*, 28(11):3384–3392, 1972.
- [13] Julien Varignon, Manuel Bibes, and Alex Zunger. Origin of band gaps in 3d perovskite oxides. *Nature communications*, 10(1):1–11, 2019.
- [14] PM Woodward, DE Cox, E Moshopoulou, AW Sleight, and S Morimoto. Structural studies of charge disproportionation and magnetic order in CaFeO₃. *Physical Review B*, 62(2):844, 2000.
- [15] S. Tajima, S. Uchida, A. Masaki, H. Takagi, K. Kitazawa, S. Tanaka, and S. Sugai. Electronic states of BaPb_{1-x}Bi_xO₃ in the semiconducting phase investigated by optical measurements. *Phys. Rev. B*, 35:696–703, Jan 1987.
- [16] VI Anisimov, D Bukhvalov, and TM Rice. Electronic structure of possible nickelate analogs to the cuprates. *Physical Review B*, 59(12):7901, 1999.

- [17] Jiří Chaloupka and Giniyat Khaliullin. Orbital order and possible superconductivity in $\text{LaNiO}_3/\text{LaMO}_3$ superlattices. *Physical Review Letters*, 100(1):016404, 2008.
- [18] Sara Catalano, M Gibert, J Fowlie, J Íñiguez, JM Triscone, and Jens Kreisel. Rare-earth nickelates RNiO_3 : thin films and heterostructures. *Reports on Progress in Physics*, 81(4):046501, 2018.
- [19] Jose A Alonso, Maria J Martinez-Lope, Maria T Casais, Miguel AG Aranda, and Maria T Fernandez-Diaz. Metal-insulator transitions, structural and microstructural evolution of RNiO_3 (R= Sm, Eu, Gd, Dy, Ho, Y) perovskites: evidence for room-temperature charge disproportionation in monoclinic HoNiO_3 and YNiO_3 . *Journal of the American Chemical Society*, 121(20):4754–4762, 1999.
- [20] G Catalan. Progress in perovskite nickelate research. *Phase Transitions*, 81(7-8):729–749, 2008.
- [21] JB Torrance, P Lacorre, AI Nazzal, EJ Ansaldo, and Ch Niedermayer. Systematic study of insulator-metal transitions in perovskites NiO_3 (R= Pr, Nd, Sm, Eu) due to closing of charge-transfer gap. *Physical Review B*, 45(14):8209, 1992.
- [22] JA Alonso, MJ Martínez-Lope, MT Casais, JL García-Muñoz, and MT Fernández-Díaz. Room-temperature monoclinic distortion due to charge disproportionation in RNiO_3 perovskites with small rare-earth cations (R= Ho, Y, Er, Tm, Yb, and Lu): A neutron diffraction study. *Physical Review B*, 61(3):1756, 2000.
- [23] I. Vobornik, L. Perfetti, M. Zacchigna, M. Grioni, G. Margaritondo, J. Mesot, M. Medarde, and P. Lacorre. Electronic-structure evolution through the metal-insulator transition in RNiO_3 . *Phys. Rev. B*, 60:R8426–R8429, Sep 1999.
- [24] Julien Varignon, Mathieu N Grisolia, Jorge Íñiguez, Agnès Barthélémy, and Manuel Bibes. Complete phase diagram of rare-earth nickelates from first-principles. *npj Quantum Materials*, 2(1):21, 2017.
- [25] Alain Mercy, Jordan Bieder, Jorge Íñiguez, and Philippe Ghosez. Structurally triggered metal-insulator transition in rare-earth nickelates. *Nature communications*, 8(1):1677, 2017.
- [26] Julien Varignon, Oleksandr I Malyi, and Alex Zunger. Dependence of band gaps in d -electron perovskite oxides on magnetism. *Physical Review B*, 105(16):165111, 2022.
- [27] Zhaoliang Liao, Nicolas Gauquelin, Robert J Green, Knut Müller-Caspary, Ivan Lobato, Lin Li, Sandra Van Aert, Johan Verbeeck, Mark Huijben, Mathieu N Grisolia, et al. Metal-insulator-transition engineering by modulation tilt-control in perovskite nickelates for room temperature optical switching. *Proceedings of the National Academy of Sciences*, 115(38):9515–9520, 2018.
- [28] J. L. García-Muñoz, M. Suaaidi, M. J. Martínez-Lope, and J. A. Alonso. Influence of carrier injection on the metal-insulator transition in electron- and hole-doped $\text{R}_{1-x}\text{A}_x\text{NiO}_3$ perovskites. *Phys. Rev. B*, 52:13563–13569, Nov 1995.
- [29] P.-H. Xiang, S. Asanuma, H. Yamada, I. H. Inoue, H. Akoh, and A. Sawa. Room temperature mott metal-insulator transition and its systematic control in $\text{Sm}_{1-x}\text{Ca}_x\text{NiO}_3$ thin films. *Applied Physics Letters*, 97(3):032114, 07 2010.
- [30] Lucia Iglesias, Manuel Bibes, and Julien Varignon. First-principles study of electron and hole doping effects in perovskite nickelates. *Physical Review B*, 104(3):035123, 2021.

- [31] Grace A Pan, Qi Song, Dan Ferenc Segedin, Myung-Chul Jung, Hesham El-Sherif, Erin E Fleck, Berit H Goodge, Spencer Doyle, Denisse Córdova Carrizales, Pádraic Shafer, et al. Synthesis and electronic properties of $\text{Nd}_{n+1}\text{Ni}_n\text{O}_{3n+1}$ ruddlesden-popper nickelate thin films. *Physical Review Materials*, 6(5):055003, 2022.
- [32] Wenzheng Wei, Kidae Shin, Hawoong Hong, Yeongjae Shin, Arashdeep Singh Thind, Yingjie Yang, Robert F. Klie, Frederick J. Walker, and Charles H. Ahn. Solid state reduction of nickelate thin films. *Phys. Rev. Mater.*, 7:013802, Jan 2023.
- [33] MA Hayward, MA Green, MJ Rosseinsky, and J Sloan. Sodium hydride as a powerful reducing agent for topotactic oxide deintercalation: synthesis and characterization of the nickel (i) oxide LaNiO_2 . *Journal of the American Chemical Society*, 121(38):8843–8854, 1999.
- [34] M Crespin, O Isnard, F Dubois, J Choisnet, and P Odier. LaNiO_2 : Synthesis and structural characterization. *Journal of Solid State Chemistry*, 178(4):1326–1334, 2005.
- [35] D Kaneko, K Yamagishi, A Tsukada, T Manabe, and M Naito. Synthesis of infinite-layer LaNiO_2 films by metal organic decomposition. *Physica C: Superconductivity*, 469(15-20):936–939, 2009.
- [36] Ai Ikeda, Takaaki Manabe, and Michio Naito. Comparison of reduction agents in the synthesis of LaNiO_2 infinite-layer films. *Physica C: Superconductivity and its Applications*, 506:83–86, 2014.
- [37] MA Hayward and MJ Rosseinsky. Synthesis of the infinite layer Ni (I) phase NdNiO_{2+x} by low temperature reduction of NdNiO_3 with sodium hydride. *Solid state sciences*, 5(6):839–850, 2003.
- [38] J Rodriguez-Carvajal, MT Fernandez-Diaz, and JL Martinez. Neutron diffraction study on structural and magnetic properties of La_2NiO_4 . *Journal of Physics: Condensed Matter*, 3(19):3215, 1991.
- [39] Rajesh Dutta, Avishek Maity, Anna Marsicano, J Ross Stewart, Matthias Opel, and Werner Paulus. Revealing the effect of interstitial oxygen on the low-energy crystal electric field excitations of Pr^{3+} in 214-nickelates. *Physical Review B*, 105(19):195147, 2022.
- [40] Yao Shen, G Fabbris, H Miao, Y Cao, D Meyers, DG Mazzone, TA Assefa, XM Chen, K Kisslinger, D Prabhakaran, et al. Charge condensation and lattice coupling drives stripe formation in nickelates. *Physical Review Letters*, 126(17):177601, 2021.
- [41] AM Merritt, AD Christianson, A Banerjee, GD Gu, AS Mishchenko, and Dmitry Reznik. Giant electron–phonon coupling of the breathing plane oxygen phonons in the dynamic stripe phase of $\text{La}_{1.67}\text{Sr}_{0.33}\text{NiO}_4$. *Scientific Reports*, 10(1):11426, 2020.
- [42] Christopher Lane and Jian-Xin Zhu. Landscape of coexisting excitonic states in the insulating single-layer cuprates and nickelates. *Phys. Rev. B*, 101:155135, Apr 2020.
- [43] Christopher Lane, James W. Furness, Ioana Gianina Buda, Yubo Zhang, Robert S. Markiewicz, Bernardo Barbiellini, Jianwei Sun, and Arun Bansil. Antiferromagnetic ground state of La_2CuO_4 : A parameter-free ab initio description. *Phys. Rev. B*, 98:125140, Sep 2018.
- [44] S Uchida, T Ido, H Takagi, T Arima, Y Tokura, and S Tajima. Optical spectra of $\text{La}_{2-x}\text{Sr}_x\text{CuO}_4$: Effect of carrier doping on the electronic structure of the CuO_2 plane. *Physical Review B*, 43(10):7942, 1991.
- [45] JP Falck, A Levy, MA Kastner, and RJ Birgeneau. Charge-transfer spectrum and its temperature dependence in La_2CuO_4 . *Physical review letters*, 69(7):1109, 1992.

- [46] Edoardo Baldini, Michael A Sentef, Swagata Acharya, Thomas Brumme, Evgeniia Shevelova, Fryderyk Lyzwa, Ekaterina Pomjakushina, Christian Bernhard, Mark Van Schilfgaarde, Fabrizio Carbone, et al. Electron–phonon-driven three-dimensional metallicity in an insulating cuprate. *Proceedings of the National Academy of Sciences*, 117(12):6409–6416, 2020.
- [47] Viktor V Poltavets, Konstantin A Lokshin, Sibel Dikmen, Mark Croft, Takeshi Egami, and Martha Greenblatt. $\text{La}_3\text{Ni}_2\text{O}_6$: A new double T' -type nickelate with infinite $\text{Ni}^{1+/2+}\text{O}_2$ layers. *Journal of the American Chemical Society*, 128(28):9050–9051, 2006.
- [48] Syunsuke Sakura, Akitoshi Nakata, Guanghui Hu, Yoshihide Kimishima, Izuru Umehara, and Masatomo Uehara. Pressure effect of low dimensional nickelate and ruthenate. In *Proceedings of the 2nd International Symposium on Science at J-PARC—Unlocking the Mysteries of Life, Matter and the Universe—*, page 034003, 2015.
- [49] Zengjia Liu, Hualei Sun, Mengwu Huo, Xiaoyan Ma, Yi Ji, Enkui Yi, Lisi Li, Hui Liu, Jia Yu, Ziyou Zhang, et al. Evidence for charge and spin order in single crystals of $\text{La}_3\text{Ni}_2\text{O}_7$ and $\text{La}_3\text{Ni}_2\text{O}_6$. *Science China Physics, Mechanics & Astronomy*, 66(1):217411, 2023.
- [50] Yoshiaki Sakurai, Shunsuke Sakura, Guanghui Hu, Shunpeita Suzuki, Izuru Umehara, Yoshihide Kimishima, and Masatomo Uehara. Pressure effects of $\text{Nd}_{3.5}\text{Sm}_{0.5}\text{Ni}_3\text{O}_8$ and $\text{La}_{3-x}\text{Nd}_x\text{Ni}_2\text{O}_6$. In *Proceedings of the 12th Asia Pacific Physics Conference (APPC12)*, page 012086, 2014.
- [51] N. apRoberts Warren, J. Crocker, A. P. Dioguardi, K. R. Shirer, V. V. Poltavets, M. Greenblatt, P. Klavins, and N. J. Curro. NMR evidence for spin fluctuations in the bilayer nickelate $\text{La}_3\text{Ni}_2\text{O}_6$. *Phys. Rev. B*, 88:075124, Aug 2013.
- [52] J.-G. Cheng, J.-S. Zhou, J. B. Goodenough, H. D. Zhou, K. Matsubayashi, Y. Uwatoko, P. P. Kong, C. Q. Jin, W. G. Yang, and G. Y. Shen. Pressure effect on the structural transition and suppression of the high-spin state in the triple-layer T' - $\text{La}_4\text{Ni}_3\text{O}_8$. *Phys. Rev. Lett.*, 108:236403, Jun 2012.
- [53] Junjie Zhang, Yu-Sheng Chen, D Phelan, Hong Zheng, MR Norman, and JF Mitchell. Stacked charge stripes in the quasi-2D trilayer nickelate $\text{La}_4\text{Ni}_3\text{O}_8$. *Proceedings of the National Academy of Sciences*, 113(32):8945–8950, 2016.
- [54] Viktor V Poltavets, Konstantin A Lokshin, Andriy H Nevidomskyy, Mark Croft, Trevor A Tyson, Joke Hadermann, Gustaaf Van Tendeloo, Takeshi Egami, Gabriel Kotliar, Nicholas ApRoberts-Warren, et al. Bulk magnetic order in a two-dimensional $\text{Ni}^{1+}/\text{Ni}^{2+}$ (d^9/d^8) nickelate, isoelectronic with superconducting cuprates. *Physical review letters*, 104(20):206403, 2010.
- [55] Junjie Zhang, AS Botana, JW Freeland, D Phelan, Hong Zheng, V Pardo, MR Norman, and JF Mitchell. Large orbital polarization in a metallic square-planar nickelate. *Nature Physics*, 13(9):864–869, 2017.
- [56] Haoxiang Li, Peipei Hao, Junjie Zhang, Kyle Gordon, A Garrison Linn, Xinglong Chen, Hong Zheng, Xiaoqing Zhou, JF Mitchell, and DS Dessau. Electronic structure and correlations in planar trilayer nickelate $\text{Pr}_4\text{Ni}_3\text{O}_8$. *Science Advances*, 9(2):eade4418, 2023.
- [57] Xinglong Chen, Hong Zheng, Daniel P Phelan, Hao Zheng, Saul H Lapidus, Matthew J Krogstad, Raymond Osborn, Stephan Rosenkranz, and JF Mitchell. Competing charge/spin-stripe and correlated metal phases in trilayer nickelates $(\text{Pr}_{1-x}\text{La}_x)_4\text{Ni}_3\text{O}_8$. *Chemistry of Materials*, 34(10):4560–4567, 2022.
- [58] Junjie Zhang, D. M. Pajerowski, A. S. Botana, Hong Zheng, L. Harriger, J. Rodriguez-Rivera, J. P. C. Ruff, N. J. Schreiber, B. Wang, Yu-Sheng Chen, W. C. Chen, M. R. Norman, S. Rosenkranz, J. F. Mitchell, and D. Phelan. Spin stripe order in a square planar trilayer nickelate. *Phys. Rev. Lett.*, 122:247201, Jun 2019.

- [59] Qing Li, ChengPing He, XiYu Zhu, Jin Si, XinWei Fan, and Hai-Hu Wen. Contrasting physical properties of the trilayer nickelates $\text{Nd}_4\text{Ni}_3\text{O}_{10}$ and $\text{Nd}_4\text{Ni}_3\text{O}_8$. *Science China Physics, Mechanics & Astronomy*, 64(2):227411, 2021.
- [60] Jiahao Hao, Xinwei Fan, Qing Li, Xiaoxiang Zhou, Chengping He, Yaomin Dai, Bing Xu, Xiyu Zhu, and Hai-Hu Wen. Charge-stripe fluctuations in $\text{Nd}_4\text{Ni}_3\text{O}_8$ as evidenced by optical spectroscopy. *Physical Review B*, 103(20):205120, 2021.
- [61] Shangxiong Huangfu, Zurab Guguchia, Tian Shang, Hai Lin, Huanlong Liu, Xiaofu Zhang, Hubertus Luetkens, and Andreas Schilling. Competing spin-glass and spin-fluctuation states in $\text{Nd}_x\text{Pr}_{4-x}\text{Ni}_3\text{O}_8$. *Phys. Rev. B*, 108:014410, Jul 2023.
- [62] JQ Lin, P Villar Arribi, Gilberto Fabbris, AS Botana, Derek Meyers, Hu Miao, Yao Shen, DG Mazzone, Jiatai Feng, SG Chiuzbăian, et al. Strong superexchange in a $d^{9-\delta}$ nickelate revealed by resonant inelastic X-ray scattering. *Physical Review Letters*, 126(8):087001, 2021.
- [63] Y. Shen, J. Sears, G. Fabbris, J. Li, J. Pellicciari, I. Jarrige, Xi He, I. Božović, M. Mitrano, Junjie Zhang, J. F. Mitchell, A. S. Botana, V. Bisogni, M. R. Norman, S. Johnston, and M. P. M. Dean. Role of oxygen states in the low valence nickelate $\text{La}_4\text{Ni}_3\text{O}_8$. *Phys. Rev. X*, 12:011055, Mar 2022.
- [64] Y. Shen, J. Sears, G. Fabbris, J. Li, J. Pellicciari, M. Mitrano, W. He, Junjie Zhang, J. F. Mitchell, V. Bisogni, M. R. Norman, S. Johnston, and M. P. M. Dean. Electronic character of charge order in square-planar low-valence nickelates. *Phys. Rev. X*, 13:011021, Feb 2023.
- [65] VI Anisimov, D Bukhvalov, and TM Rice. Electronic structure of possible nickelate analogs to the cuprates. *Physical Review B*, 59(12):7901, 1999.
- [66] Danfeng Li, Kyuho Lee, Bai Yang Wang, Motoki Osada, Samuel Crossley, Hye Ryoung Lee, Yi Cui, Yasuyuki Hikita, and Harold Y Hwang. Superconductivity in an infinite-layer nickelate. *Nature*, 572(7771):624–627, 2019.
- [67] Motoki Osada, Bai Yang Wang, Berit H. Goodge, Kyuho Lee, Hyeok Yoon, Keita Sakuma, Danfeng Li, Masashi Miura, Lena F. Kourkoutis, and Harold Y. Hwang. A superconducting praseodymium nickelate with infinite layer structure. *Nano Letters*, 20(8):5735–5740, 2020. PMID: 32574061.
- [68] Motoki Osada, Bai Yang Wang, Berit H. Goodge, Shannon P. Harvey, Kyuho Lee, Danfeng Li, Lena F. Kourkoutis, and Harold Y. Hwang. Nickelate superconductivity without rare-earth magnetism: $(\text{La}, \text{Sr})\text{NiO}_2$. *Advanced Materials*, 33(45):2104083, 2021.
- [69] Shengwei Zeng, Chi Sin Tang, Xinmao Yin, Changjian Li, Mengsha Li, Zhen Huang, Junxiong Hu, Wei Liu, Ganesh Ji Omar, Hariom Jani, Zhi Shiuh Lim, Kun Han, Dongyang Wan, Ping Yang, Stephen John Pennycook, Andrew T. S. Wee, and Ariando Ariando. Phase diagram and superconducting dome of infinite-layer $\text{Nd}_{1-x}\text{Sr}_x\text{NiO}_2$ thin films. *Physical Review Letters*, 125:147003, Oct 2020.
- [70] Danfeng Li, Bai Yang Wang, Kyuho Lee, Shannon P. Harvey, Motoki Osada, Berit H. Goodge, Lena F. Kourkoutis, and Harold Y. Hwang. Superconducting dome in $\text{Nd}_{1-x}\text{Sr}_x\text{NiO}_2$ infinite layer films. *Phys. Rev. Lett.*, 125:027001, Jul 2020.
- [71] Motoki Osada, Bai Yang Wang, Kyuho Lee, Danfeng Li, and Harold Y. Hwang. Phase diagram of infinite layer praseodymium nickelate $\text{Pr}_{1-x}\text{Sr}_x\text{NiO}_2$ thin films. *Physical Review Materials*, 4:121801, Dec 2020.
- [72] Shengwei Zeng, Changjian Li, Lin Er Chow, Yu Cao, Zhaoting Zhang, Chi Sin Tang, Xinmao Yin, Zhi Shiuh Lim, Junxiong Hu, Ping Yang, et al. Superconductivity in infinite-layer nickelate $\text{La}_{1-x}\text{Ca}_x\text{NiO}_2$ thin films. *Science advances*, 8(7):eabl9927, 2022.

- [73] Grace A Pan, Dan Ferenc Segedin, Harrison LaBollita, Qi Song, Emilian M Nica, Berit H Goodge, Andrew T Pierce, Spencer Doyle, Steve Novakov, Denisse Córdova Carrizales, et al. Superconductivity in a quintuple-layer square-planar nickelate. *Nature materials*, 21(2):160–164, 2022.
- [74] Kyuho Lee, Bai Yang Wang, Motoki Osada, Berit H Goodge, Tiffany C Wang, Yonghun Lee, Shannon Harvey, Woo Jin Kim, Yijun Yu, Chaitanya Murthy, et al. Linear-in-temperature resistivity for optimally superconducting (Nd, Sr)NiO₂. *Nature*, 619(7969):288–292, 2023.
- [75] Qing Li, Chengping He, Jin Si, Xiyu Zhu, Yue Zhang, and Hai-Hu Wen. Absence of superconductivity in bulk Nd_{1-x}Sr_xNiO₂. *Communications Materials*, 1(1):1–8, 2020.
- [76] Mengwu Huo, Zengjia Liu, Hualei Sun, Lisi Li, Hui Lui, Chaoxin Huang, Feixiang Liang, Bing Shen, and Meng Wang. Synthesis and properties of La_{1-x}Sr_xNiO₃ and La_{1-x}Sr_xNiO₂. *Chinese Physics B*, 31(10):107401, 2022.
- [77] Chao Yang, Roberto A Ortiz, Yi Wang, Wilfried Sigle, Hongguang Wang, Eva Benckiser, Bernhard Keimer, and Peter A van Aken. Thickness-dependent interface polarity in infinite-layer nickelate superlattices. *Nano Letters*, 2023.
- [78] Berit H Goodge, Benjamin Geisler, Kyuho Lee, Motoki Osada, Bai Yang Wang, Danfeng Li, Harold Y Hwang, Rossitza Pentcheva, and Lena F Kourkoutis. Resolving the polar interface of infinite-layer nickelate thin films. *Nature Materials*, 22(4):466–473, 2023.
- [79] X Ren, Q Gao, Y Zhao, H Luo, X Zhou, and Z Zhu. Strain-induced enhancement of T_c in infinite-layer Pr_{0.8}Sr_{0.2}NiO₂ films. *arXiv preprint arXiv:2109.05761*, 2021.
- [80] Xiaorong Zhou, Xiaowei Zhang, Jiabao Yi, Peixin Qin, Zexin Feng, Peiheng Jiang, Zhicheng Zhong, Han Yan, Xiaoning Wang, Hongyu Chen, et al. Antiferromagnetism in Ni-based superconductors. *Advanced Materials*, page 2106117, 2021.
- [81] P. Puphal, B. Wehinger, J. Nuss, K. Küster, U. Starke, G. Garbarino, B. Keimer, M. Isobe, and M. Hepting. Synthesis and physical properties of LaNiO₂ crystals. *Phys. Rev. Mater.*, 7:014804, Jan 2023.
- [82] Yueying Li, Wenjie Sun, Jiangfeng Yang, Xiangbin Cai, Wei Guo, Zhengbin Gu, Ye Zhu, and Yuefeng Nie. Impact of cation stoichiometry on the crystalline structure and superconductivity in nickelates. *Frontiers in Physics*, 9:443, 2021.
- [83] NN Wang, MW Yang, Zhen Yang, KY Chen, Hua Zhang, QH Zhang, ZH Zhu, Yoshiya Uwatoko, L Gu, XL Dong, et al. Pressure-induced monotonic enhancement of T_c to over 30 K in superconducting Pr_{0.82}Sr_{0.18}NiO₂ thin films. *Nature Communications*, 13(1):4367, 2022.
- [84] Mi-Young Choi, Kwan-Woo Lee, and Warren E Pickett. Role of 4*f* states in infinite-layer NdNiO₂. *Physical Review B*, 101(2):020503, 2020.
- [85] Byungkyun Kang, Hyunsoo Kim, Qiang Zhu, and Chul Hong Park. Impact of *f*d kondo cloud on superconductivity of nickelates. *Cell Reports Physical Science*, 4(3), 2023.
- [86] Guang-Ming Zhang, Yi-feng Yang, and Fu-Chun Zhang. Self-doped Mott insulator for parent compounds of nickelate superconductors. *Phys. Rev. B*, 101:020501, Jan 2020.
- [87] Zhuoyu Chen, Motoki Osada, Danfeng Li, Emily M Been, Su-Di Chen, Makoto Hashimoto, Donghui Lu, Sung-Kwan Mo, Kyuho Lee, Bai Yang Wang, et al. Electronic structure of superconducting nickelates probed by resonant photoemission spectroscopy. *Matter*, 5(6):1806–1815, 2022.

- [88] Matthias Hepting, Danfeng Li, CJ Jia, Haiyu Lu, E Paris, Y Tseng, X Feng, M Osada, E Been, Y Hikita, et al. Electronic structure of the parent compound of superconducting infinite-layer nickelates. *Nature materials*, 19(4):381–385, 2020.
- [89] M. Rossi, H. Lu, A. Nag, D. Li, M. Osada, K. Lee, B. Y. Wang, S. Agrestini, M. Garcia-Fernandez, J. J. Kas, Y.-D. Chuang, Z. X. Shen, H. Y. Hwang, B. Moritz, Ke-Jin Zhou, T. P. Devereaux, and W. S. Lee. Orbital and spin character of doped carriers in infinite-layer nickelates. *Phys. Rev. B*, 104:L220505, Dec 2021.
- [90] RA Ortiz, H Menke, F Misják, DT Mantadakis, K Fürsich, E Schierle, G Logvenov, U Kaiser, B Keimer, P Hansmann, et al. Superlattice approach to doping infinite-layer nickelates. *Physical Review B*, 104(16):165137, 2021.
- [91] Haiyu Lu, Matteo Rossi, Abhishek Nag, Motoki Osada, DF Li, K Lee, BY Wang, M Garcia-Fernandez, S Agrestini, ZX Shen, et al. Magnetic excitations in infinite-layer nickelates. *Science*, 373(6551):213–216, 2021.
- [92] Qiang Gao, Shiyu Fan, Qisi Wang, Jiarui Li, Xiaolin Ren, Izabela Biało, Annabella Drewanowski, Pascal Rothenbühler, Jaewon Choi, Yao Wang, et al. Magnetic excitations in strained infinite-layer nickelate PrNiO₂. *arXiv preprint arXiv:2208.05614*, 2022.
- [93] Ruiqi Zhang, Christopher Lane, Bahadur Singh, Johannes Nokelainen, Bernardo Barbiellini, Robert S Markiewicz, Arun Bansil, and Jianwei Sun. Magnetic and f -electron effects in LaNiO₂ and NdNiO₂ nickelates with cuprate-like $3d_{x^2-y^2}$ band. *Communications Physics*, 4(1):118, 2021.
- [94] Yajun Zhang, Xu He, and Philippe Ghosez. Magnetic excitations in infinite-layer LaNiO₂. *Applied Physics Letters*, 122(15), 2023.
- [95] Siheon Rye, Hongkee Yoon, Taek Jung Kim, Min Yong Jeong, and Myung Joon Han. Induced magnetic two-dimensionality by hole doping in the superconducting infinite-layer nickelate Nd_{1-x}Sr_xNiO₂. *Phys. Rev. B*, 101:064513, Feb 2020.
- [96] Hai Lin, Dariusz Jakub Gawryluk, Yannick Maximilian Klein, Shangxiong Huangfu, Ekaterina Pomjakushina, Fabian von Rohr, and Andreas Schilling. Universal spin-glass behaviour in bulk LaNiO₂, PrNiO₂ and NdNiO₂. *New Journal of Physics*, 24(1):013022, 2022.
- [97] Roberto Antonio Ortiz, Pascal Puphal, Marcel Klett, Fabian Hotz, Reinhard K Kremer, Heiko Trepka, Mamoun Hemmida, H-A Krug von Nidda, Masaaki Isobe, Rustem Khasanov, et al. Magnetic correlations in infinite-layer nickelates: An experimental and theoretical multimethod study. *Physical Review Research*, 4(2):023093, 2022.
- [98] G Krieger, L Martinelli, S Zeng, LE Chow, Kurt Kummer, Riccardo Arpaia, M Moretti Sala, Nicholas B Brookes, A Ariando, N Viart, et al. Charge and spin order dichotomy in NdNiO₂ driven by the capping layer. *Physical Review Letters*, 129(2):027002, 2022.
- [99] Yi Cui, Cong Li, Qing Li, Xiyu Zhu, Ze Hu, Yi feng Yang, Jinshan Zhang, Rong Yu, Hai-Hu Wen, and Weiqiang Yu. NMR evidence of antiferromagnetic spin fluctuations in Nd_{0.85}Sr_{0.15}NiO₂. *Chinese Physics Letters*, 38(6):067401, jun 2021.
- [100] Jennifer Fowlie, Marios Hadjimichael, Maria M Martins, Danfeng Li, Motoki Osada, Bai Yang Wang, Kyuho Lee, Yonghun Lee, Zaher Salman, Thomas Prokscha, et al. Intrinsic magnetism in superconducting infinite-layer nickelates. *Nature Physics*, 18(9):1043–1047, 2022.
- [101] D. Zhao, Y. B. Zhou, Y. Fu, L. Wang, X. F. Zhou, H. Cheng, J. Li, D. W. Song, S. J. Li, B. L. Kang, L. X. Zheng, L. P. Nie, Z. M. Wu, M. Shan, F. H. Yu, J. J. Ying, S. M. Wang, J. W. Mei, T. Wu, and X. H. Chen. Intrinsic spin susceptibility and pseudogaplike behavior in infinite-layer LaNiO₂. *Phys. Rev. Lett.*, 126:197001, May 2021.

- [102] SW Zeng, XM Yin, CJ Li, LE Chow, CS Tang, K Han, Z Huang, Y Cao, DY Wan, ZT Zhang, et al. Observation of perfect diamagnetism and interfacial effect on the electronic structures in infinite layer $\text{Nd}_{0.8}\text{Sr}_{0.2}\text{NiO}_2$ superconductors. *Nature communications*, 13(1):1–6, 2022.
- [103] Bai Yang Wang, Danfeng Li, Berit H Goodge, Kyuho Lee, Motoki Osada, Shannon P Harvey, Lena F Kourkoutis, Malcolm R Beasley, and Harold Y Hwang. Isotropic pauli-limited superconductivity in the infinite-layer nickelate $\text{Nd}_{0.775}\text{Sr}_{0.225}\text{NiO}_2$. *Nature Physics*, 17(4):473–477, 2021.
- [104] Xiao-Rong Zhou, Ze-Xin Feng, Pei-Xin Qin, Han Yan, Xiao-Ning Wang, Pan Nie, Hao-Jiang Wu, Xin Zhang, Hong-Yu Chen, Zi-Ang Meng, et al. Negligible oxygen vacancies, low critical current density, electric-field modulation, in-plane anisotropic and high-field transport of a superconducting $\text{Nd}_{0.8}\text{Sr}_{0.2}\text{NiO}_2/\text{SrTiO}_3$ heterostructure. *Rare Metals*, 40(10):2847–2854, 2021.
- [105] Ying Xiang, Qing Li, Yueying Li, Huan Yang, Yuefeng Nie, and Hai-Hu Wen. Physical properties revealed by transport measurements for superconducting $\text{Nd}_{0.8}\text{Sr}_{0.2}\text{NiO}_2$ thin films. *Chinese Physics Letters*, 38(4):047401, 2021.
- [106] Bai Yang Wang, Tiffany C. Wang, Yu-Te Hsu, Motoki Osada, Kyuho Lee, Chunjing Jia, Caitlin Duffy, Danfeng Li, Jennifer Fowlie, Malcolm R. Beasley, Thomas P. Devereaux, Ian R. Fisher, Nigel E. Hussey, and Harold Y. Hwang. Effects of rare-earth magnetism on the superconducting upper critical field in infinite-layer nickelates. *Science Advances*, 9(20):eadf6655, 2023.
- [107] LE Chow, KY Yip, M Pierre, SW Zeng, ZT Zhang, T Heil, J Deuschle, P Nandi, SK Sudheesh, ZS Lim, et al. Pauli-limit violation in lanthanide infinite-layer nickelate superconductors. *arXiv preprint arXiv:2204.12606*, 2022.
- [108] Qiangqiang Gu, Yueying Li, Siyuan Wan, Huazhou Li, Wei Guo, Huan Yang, Qing Li, Xiyu Zhu, Xiaoqing Pan, Yuefeng Nie, et al. Single particle tunneling spectrum of superconducting $\text{Nd}_{1-x}\text{Sr}_x\text{NiO}_2$ thin films. *Nature communications*, 11(1):6027, 2020.
- [109] Rui-Feng Wang, Yan-Ling Xiong, Hang Yan, Xiaopeng Hu, Motoki Osada, Danfeng Li, Harold Y Hwang, Can-Li Song, Xu-Cun Ma, and Qi-Kun Xue. Observation of coulomb blockade and coulomb staircases in superconducting $\text{Pr}_{0.8}\text{Sr}_{0.2}\text{NiO}_2$ films. *Physical Review B*, 107(11):115411, 2023.
- [110] Shannon P Harvey, Bai Yang Wang, Jennifer Fowlie, Motoki Osada, Kyuho Lee, Yonghun Lee, Danfeng Li, and Harold Y Hwang. Evidence for nodal superconductivity in infinite-layer nickelates. *arXiv preprint arXiv:2201.12971*, 2022.
- [111] Lin Er Chow, S Kunniniyil Sudheesh, Proloy Nandi, SW Zeng, ZT Zhang, XM Du, Zhi Shiuh Lim, Elbert EM Chia, and Ariando Ariando. Pairing symmetry in infinite-layer nickelate superconductor. *arXiv preprint arXiv:2201.10038*, 2022.
- [112] EF Talantsev. Classifying superconductivity in an infinite-layer nickelate $\text{Nd}_{0.8}\text{Sr}_{0.2}\text{NiO}_2$. *Results in Physics*, 17:103118, 2020.
- [113] Evgeny F. Talantsev. Quantifying interaction mechanism in infinite layer nickelate superconductors. *Journal of Applied Physics*, 134(11):113904, 09 2023.
- [114] Rebecca Cervasio, Luca Tomarchio, Marine Verseils, Jean-Blaise Brubach, Salvatore Macis, Shengwei Zeng, Ariando Ariando, Pascale Roy, and Stefano Lupi. Optical properties of superconducting $\text{Nd}_{0.8}\text{Sr}_{0.2}\text{NiO}_2$ nickelate. *ACS Applied Electronic Materials*, 5(9):4770–4777, 2023.

- [115] Yusuke Nomura, Motoaki Hirayama, Terumasa Tadano, Yoshihide Yoshimoto, Kazuma Nakamura, and Ryotaro Arita. Formation of a two-dimensional single-component correlated electron system and band engineering in the nickelate superconductor NdNiO₂. *Phys. Rev. B*, 100:205138, Nov 2019.
- [116] Simone Di Cataldo, Paul Worm, Liang Si, and Karsten Held. Absence of electron-phonon-mediated superconductivity in hydrogen-intercalated nickelates. *arXiv preprint arXiv:2304.03599*, 2023.
- [117] Andreas Kreisel, Brian M. Andersen, Astrid T. Rømer, Ilya M. Eremin, and Frank Lechermann. Superconducting instabilities in strongly correlated infinite-layer nickelates. *Phys. Rev. Lett.*, 129:077002, Aug 2022.
- [118] Jun Chang, Jize Zhao, and Yang Ding. Hund-heisenberg model in superconducting infinite-layer nickelates. *The European Physical Journal B*, 93:1–7, 2020.
- [119] Christopher Lane, Ruiqi Zhang, Bernardo Barbiellini, Robert S Markiewicz, Arun Bansil, Jianwei Sun, and Jian-Xin Zhu. Competing incommensurate spin fluctuations and magnetic excitations in infinite-layer nickelate superconductors. *Communications Physics*, 6(1):90, 2023.
- [120] Matteo Rossi, Motoki Osada, Jaewon Choi, Stefano Agrestini, Daniel Jost, Yonghun Lee, Haiyu Lu, Bai Yang Wang, Kyuho Lee, Abhishek Nag, et al. A broken translational symmetry state in an infinite-layer nickelate. *Nature Physics*, 18(8):869–873, 2022.
- [121] Xiaolin Ren, Ronny Sutarto, Qiang Gao, Qisi Wang, Jiarui Li, Yao Wang, Tao Xiang, Jiangping Hu, Fu-Chun Zhang, J Chang, et al. Symmetry of charge order in infinite-layer nickelates. *arXiv preprint arXiv:2303.02865*, 2023.
- [122] Haoran Ji, Yi Liu, Yanan Li, Xiang Ding, Zheyuan Xie, Chengcheng Ji, Shichao Qi, Xiaoyue Gao, Minghui Xu, Peng Gao, et al. Rotational symmetry breaking in superconducting nickelate Nd_{0.8}Sr_{0.2}NiO₂ films. *Nature Communications*, 14(1):7155, 2023.
- [123] Ai Ikeda, Yoshiharu Krockenberger, Hiroshi Irie, Michio Naito, and Hideki Yamamoto. Direct observation of infinite NiO₂ planes in LaNiO₂ films. *Applied Physics Express*, 9(6):061101, 2016.
- [124] Yajun Zhang, Xu He, Jingtong Zhang, Jie Wang, and Philippe Ghosez. Incommensurate magnetic order in hole-doped infinite-layer nickelate superconductors due to competing magnetic interactions. *Advanced Functional Materials*, page 2304187, 2023.
- [125] P. Hohenberg and W. Kohn. Inhomogeneous electron gas. *Phys. Rev.*, 136:B864–B871, Nov 1964.
- [126] W. Kohn and L. J. Sham. Self-consistent equations including exchange and correlation effects. *Phys. Rev.*, 140:A1133–A1138, Nov 1965.
- [127] Seymour H Vosko, Leslie Wilk, and Marwan Nusair. Accurate spin-dependent electron liquid correlation energies for local spin density calculations: a critical analysis. *Canadian Journal of physics*, 58(8):1200–1211, 1980.
- [128] John P Perdew and Yue Wang. Accurate and simple analytic representation of the electron-gas correlation energy. *Physical review B*, 45(23):13244, 1992.
- [129] David C Langreth and MJ Mehl. Beyond the local-density approximation in calculations of ground-state electronic properties. *Physical Review B*, 28(4):1809, 1983.
- [130] Axel D Becke. Density-functional exchange-energy approximation with correct asymptotic behavior. *Physical review A*, 38(6):3098, 1988.

- [131] John P. Perdew, Kieron Burke, and Matthias Ernzerhof. Generalized gradient approximation made simple. *Phys. Rev. Lett.*, 77:3865–3868, Oct 1996.
- [132] John P. Perdew, J. A. Chevary, S. H. Vosko, Koblar A. Jackson, Mark R. Pederson, D. J. Singh, and Carlos Fiolhais. Atoms, molecules, solids, and surfaces: Applications of the generalized gradient approximation for exchange and correlation. *Phys. Rev. B*, 46:6671–6687, Sep 1992.
- [133] A. D. Becke. Density-functional exchange-energy approximation with correct asymptotic behavior. *Phys. Rev. A*, 38:3098–3100, Sep 1988.
- [134] Chengteh Lee, Weitao Yang, and Robert G. Parr. Development of the colle-salvetti correlation-energy formula into a functional of the electron density. *Phys. Rev. B*, 37:785–789, Jan 1988.
- [135] Burkhard Miehlich, Andreas Savin, Hermann Stoll, and Heinzwerner Preuss. Results obtained with the correlation energy density functionals of becke and lee, yang and parr. *Chemical Physics Letters*, 157(3):200–206, 1989.
- [136] Jianmin Tao, John P. Perdew, Viktor N. Staroverov, and Gustavo E. Scuseria. Climbing the density functional ladder: Nonempirical meta-generalized gradient approximation designed for molecules and solids. *Phys. Rev. Lett.*, 91:146401, Sep 2003.
- [137] Jianwei Sun, Adrienn Ruzsinszky, and John P. Perdew. Strongly constrained and appropriately normed semilocal density functional. *Physical Review Letters*, 115:036402, Jul 2015.
- [138] D. I. Bilc, R. Orlando, R. Shaltaf, G.-M. Rignanese, Jorge Íñiguez, and Ph. Ghosez. Hybrid exchange-correlation functional for accurate prediction of the electronic and structural properties of ferroelectric oxides. *Phys. Rev. B*, 77:165107, Apr 2008.
- [139] Philip J Stephens, Frank J Devlin, Cary F Chabalowski, and Michael J Frisch. Ab initio calculation of vibrational absorption and circular dichroism spectra using density functional force fields. *The Journal of physical chemistry*, 98(45):11623–11627, 1994.
- [140] Aliaksandr V Krukau, Oleg A Vydrov, Artur F Izmaylov, and Gustavo E Scuseria. Influence of the exchange screening parameter on the performance of screened hybrid functionals. *The Journal of chemical physics*, 125(22):224106, 2006.
- [141] Vladimir I. Anisimov, Jan Zaanen, and Ole K. Andersen. Band theory and mott insulators: Hubbard u instead of stoner i. *Phys. Rev. B*, 44:943–954, Jul 1991.
- [142] Georg Kresse and Jürgen Hafner. Ab initio molecular dynamics for liquid metals. *Physical review B*, 47(1):558, 1993.
- [143] Georg Kresse and J Hafner. Ab initio molecular dynamics for open-shell transition metals. *Physical Review B*, 48(17):13115, 1993.
- [144] Georg Kresse and Jürgen Furthmüller. Efficiency of ab-initio total energy calculations for metals and semiconductors using a plane-wave basis set. *Computational materials science*, 6(1):15–50, 1996.
- [145] Peter E Blöchl. Projector augmented-wave method. *Physical review B*, 50(24):17953, 1994.
- [146] Nicola Marzari and David Vanderbilt. Maximally localized generalized wannier functions for composite energy bands. *Physical review B*, 56(20):12847, 1997.
- [147] Ivo Souza, Nicola Marzari, and David Vanderbilt. Maximally localized wannier functions for entangled energy bands. *Physical Review B*, 65(3):035109, 2001.

- [148] Giovanni Pizzi, Valerio Vitale, Ryotaro Arita, Stefan Blügel, Frank Freimuth, Guillaume Géranton, Marco Gibertini, Dominik Gresch, Charles Johnson, Takashi Koretsune, Julen Ibañez-Azpiroz, Hyungjun Lee, Jae-Mo Lihm, Daniel Marchand, Antimo Marrazzo, Yuriy Mokrousov, Jamal I Mustafa, Yoshiro Nohara, Yusuke Nomura, Lorenzo Paulatto, Samuel Poncé, Thomas Ponweiser, Junfeng Qiao, Florian Thöle, Stepan S Tsirkin, Małgorzata Wierzbowska, Nicola Marzari, David Vanderbilt, Ivo Souza, Arash A Mostofi, and Jonathan R Yates. Wannier90 as a community code: new features and applications. *Journal of Physics: Condensed Matter*, 32(16):165902, jan 2020.
- [149] AAMACG Van De Walle, M Asta, and G Ceder. The alloy theoretic automated toolkit: A user guide. *Calphad*, 26(4):539–553, 2002.
- [150] Alex Zunger, S.-H. Wei, L. G. Ferreira, and James E. Bernard. Special quasirandom structures. *Physical Review Letters*, 65:353–356, Jul 1990.
- [151] Julien Varignon, Manuel Bibes, and Alex Zunger. Mott gapping in 3d ABO₃ perovskites without Mott-Hubbard interelectronic repulsion energy u . *Physical Review B*, 100:035119, Jul 2019.
- [152] Hans-Jürgen Mikeska and Alexei K Kolezhuk. One-dimensional magnetism. *Quantum magnetism*, pages 1–83, 2004.
- [153] Harold T Stokes and Dorian M Hatch. *Isotropy subgroups of the 230 crystallographic space groups*. World Scientific, 1988.
- [154] Danel Orobengoa, Cesar Capillas, Mois I Aroyo, and J Manuel Perez-Mato. Amplimodes: symmetry-mode analysis on the bilbao crystallographic server. *Journal of Applied Crystallography*, 42(5):820–833, 2009.
- [155] JM Perez-Mato, D Orobengoa, and MI Aroyo. Mode crystallography of distorted structures. *Acta Crystallographica Section A: Foundations of Crystallography*, 66(5):558–590, 2010.
- [156] Dorian M Hatch and Harold T Stokes. Invariants: program for obtaining a list of invariant polynomials of the order-parameter components associated with irreducible representations of a space group. *Journal of applied crystallography*, 36(3):951–952, 2003.
- [157] HT Stokes, DM Hatch, and BJ Campbell. Isotropy, software suite (2007). <http://iso.byu.edu>.
- [158] JM An and WE Pickett. Superconductivity of MgB₂: covalent bonds driven metallic. *Physical Review Letters*, 86(19):4366, 2001.
- [159] H. J. Xiang, Zhenyu Li, Jinlong Yang, J. G. Hou, and Qingshi Zhu. Electron-phonon coupling in a boron-doped diamond superconductor. *Phys. Rev. B*, 70:212504, Dec 2004.
- [160] S. B. Dugdale. First-principles study of electron-phonon superconductivity in YSn₃. *Phys. Rev. B*, 83:012502, Jan 2011.
- [161] Y. Kong, O. V. Dolgov, O. Jepsen, and O. K. Andersen. Electron-phonon interaction in the normal and superconducting states of mgb₂. *Phys. Rev. B*, 64:020501, May 2001.
- [162] James W Furness, Yubo Zhang, Christopher Lane, Ioana Gianina Buda, Bernardo Barbiellini, Robert S Markiewicz, Arun Bansil, and Jianwei Sun. An accurate first-principles treatment of doping-dependent electronic structure of high-temperature cuprate superconductors. *Communications Physics*, 1(1):1–6, 2018.
- [163] Christopher Lane, James W Furness, Ioana Gianina Buda, Yubo Zhang, Robert S Markiewicz, Bernardo Barbiellini, Jianwei Sun, and Arun Bansil. Antiferromagnetic ground state of La₂CuO₄: A parameter-free ab initio description. *Physical Review B*, 98(12):125140, 2018.

- [164] Yoyo Hinuma, Hiroyuki Hayashi, Yu Kumagai, Isao Tanaka, and Fumiyasu Oba. Comparison of approximations in density functional theory calculations: Energetics and structure of binary oxides. *Physical Review B*, 96(9):094102, 2017.
- [165] Julien Varignon. Origin of superconductivity in hole doped SrBiO₃ bismuth oxide perovskite from parameter-free first-principles simulations. *npj Computational Materials*, 9(1):30, 2023.
- [166] Alejandro J Garza and Gustavo E Scuseria. Predicting band gaps with hybrid density functionals. *The journal of physical chemistry letters*, 7(20):4165–4170, 2016.
- [167] Roland Gillen, Stewart J Clark, and John Robertson. Nature of the electronic band gap in lanthanide oxides. *Physical Review B*, 87(12):125116, 2013.
- [168] Juarez LF Da Silva, M Veronica Ganduglia-Pirovano, Joachim Sauer, Veronika Bayer, and Georg Kresse. Hybrid functionals applied to rare-earth oxides: The example of ceria. *Physical Review B*, 75(4):045121, 2007.
- [169] Andreas Savin. Models and corrections: Range separation for electronic interaction—lessons from density functional theory. *The Journal of Chemical Physics*, 153(16):160901, 2020.
- [170] Shoaib Khalid, Abhishek Sharan, and Anderson Janotti. Hybrid functional calculations of electronic structure and carrier densities in rare-earth mononictides. *Physical Review B*, 101(12):125105, 2020.
- [171] TR McGuire, MW Shafer, RJ Joenk, HA Alperin, and SJ Pickart. Magnetic structure of EuTiO₃. *Journal of Applied Physics*, 37(3):981–982, 1966.
- [172] J Köhler, R Dinnebier, and A Bussmann-Holder. Structural instability of EuTiO₃ from X-ray powder diffraction. *Phase Transitions*, 85(11):949–955, 2012.
- [173] JH Lee, X Ke, NJ Podraza, L Fitting Kourkoutis, T Heeg, M Roeckerath, JW Freeland, CJ Fennie, J Schubert, DA Muller, et al. Optical band gap and magnetic properties of unstrained EuTiO₃ films. *Applied physics letters*, 94(21):212509, 2009.
- [174] AC Komarek, H Roth, M Cwik, W-D Stein, J Baier, M Kriener, F Bourée, T Lorenz, and M Braden. Magnetoelastic coupling in RTiO₃ (R= La, Nd, Sm, Gd, Y) investigated with diffraction techniques and thermal expansion measurements. *Physical Review B*, 75(22):224402, 2007.
- [175] D. J. Lovinger, E. Zoghlin, P. Kissin, G. Ahn, K. Ahadi, P. Kim, M. Poore, S. Stemmer, S. J. Moon, S. D. Wilson, and R. D. Averitt. Magnetoelastic coupling to coherent acoustic phonon modes in the ferrimagnetic insulator GdTiO₃. *Phys. Rev. B*, 102:085138, Aug 2020.
- [176] MN Grisolia, FY Bruno, D Sando, HJ Zhao, E Jacquet, XM Chen, L Bellaiche, A Barthélémy, and M Bibes. Structural, magnetic, and electronic properties of GdTiO₃ Mott insulator thin films grown by pulsed laser deposition. *Applied Physics Letters*, 105(17):172402, 2014.
- [177] Lars Bjaalie, Amit Verma, Burak Himmetoglu, Anderson Janotti, Santosh Raghavan, Vladimir Protasenko, EH Steenbergen, Debdeep Jena, Susanne Stemmer, and Chris G Van de Walle. Determination of the Mott-Hubbard gap in GdTiO₃. *Physical Review B*, 92(8):085111, 2015.
- [178] R Mguedla, A Ben Jazia Kharrat, M Saadi, K Khirouni, N Chniba-Boudjada, and W Boujelben. Structural, electrical, dielectric and optical properties of PrCrO₃ orthochromite. *Journal of Alloys and Compounds*, 812:152130, 2020.

- [179] Shuijin Lei, Lei Liu, Chunying Wang, Chuanning Wang, Donghai Guo, Suyuan Zeng, Baochang Cheng, Yanhe Xiao, and Lang Zhou. General synthesis of rare-earth orthochromites with quasi-hollow nanostructures and their magnetic properties. *Journal of Materials Chemistry A*, 1(38):11982–11991, 2013.
- [180] N Shamir, H Shaked, and Shmuel Shtrikman. Magnetic structure of some rare-earth orthochromites. *Physical Review B*, 24(11):6642, 1981.
- [181] R Mguedla, A Ben Jazia Kharrat, O Taktak, H Souissi, S Kammoun, K Khirouni, and W Boujelben. Experimental and theoretical investigations on optical properties of multiferroic PrCrO_3 ortho-chromite compound. *Optical Materials*, 101:109742, 2020.
- [182] Clemens Ritter, Rui Vilarinho, Joaquim Agostinho Moreira, Matus Mihalik, Marian Mihalik, and Stanislav Savvin. The magnetic structure of DyFeO_3 revisited: Fe spin reorientation and Dy incommensurate magnetic order. *Journal of Physics: Condensed Matter*, 34(26):265801, 2022.
- [183] Y Tokunaga, S Iguchi, T-H Arima, and Y Tokura. Magnetic-field-induced ferroelectric state in DyFeO_3 . *Physical review letters*, 101(9):097205, 2008.
- [184] MA Butler, DS Ginley, and M Eibschutz. Photoelectrolysis with YFeO_3 electrodes. *Journal of Applied Physics*, 48(7):3070–3072, 1977.
- [185] SY Smolin, MD Scafetta, GW Guglietta, JB Baxter, and SJ May. Ultrafast transient reflectance of epitaxial semiconducting perovskite thin films. *Applied Physics Letters*, 105(2):022103, 2014.
- [186] Yajun Zhang, Jingtong Zhang, Xu He, Jie Wang, and Philippe Ghosez. Rare-earth control of phase transitions in infinite-layer nickelates. *PNAS nexus*, 2(5):pgad108, 2023.
- [187] Chengliang Xia, Jiakuan Wu, Yue Chen, and Hanghui Chen. Dynamical structural instability and its implications for the physical properties of infinite-layer nickelates. *Physical Review B*, 105:115134, Mar 2022.
- [188] F. Bernardini, A. Bosin, and A. Cano. Geometric effects in the infinite-layer nickelates. *Physical Review Materials*, 6:044807, Apr 2022.
- [189] Jianwei Sun, Richard C Remsing, Yubo Zhang, Zhaoru Sun, Adrienn Ruzsinszky, Haowei Peng, Zenghui Yang, Arpita Paul, Umesh Waghmare, Xifan Wu, et al. Accurate first-principles structures and energies of diversely bonded systems from an efficient density functional. *Nature chemistry*, 8(9):831–836, 2016.
- [190] Yubo Zhang, Daniil A Kitchaev, Julia Yang, Tina Chen, Stephen T Dacek, Rafael A Sarmiento-Pérez, Maguel AL Marques, Haowei Peng, Gerbrand Ceder, John P Perdew, et al. Efficient first-principles prediction of solid stability: Towards chemical accuracy. *npj Computational Materials*, 4(1):1–6, 2018.
- [191] Haowei Peng, Zeng-Hui Yang, John P Perdew, and Jianwei Sun. Versatile van der waals density functional based on a meta-generalized gradient approximation. *Physical Review X*, 6(4):041005, 2016.
- [192] Tomohisa Takamatsu, Masatsune Kato, Takashi Noji, and Yoji Koike. Low-temperature synthesis of the infinite-layer compound LaNiO_2 by soft-chemical techniques. *Japanese Journal of Applied Physics*, 49(9R):093101, 2010.
- [193] Julien Varignon, Manuel Bibes, and Alex Zunger. Origins versus fingerprints of the jahn-teller effect in d -electron ABX_3 perovskites. *Physical Review Research*, 1:033131, Nov 2019.

- [194] H Guo, ZW Li, L Zhao, Z Hu, CF Chang, C-Y Kuo, W Schmidt, A Piovano, TW Pi, O Sobolev, et al. Antiferromagnetic correlations in the metallic strongly correlated transition metal oxide LaNiO_3 . *Nature communications*, 9(1):43, 2018.
- [195] JL García-Muñoz, J Rodríguez-Carvajal, and P Lacorre. Neutron-diffraction study of the magnetic ordering in the insulating regime of the perovskites RNiO_3 ($\text{R} = \text{Pr}$ and Nd). *Physical Review B*, 50(2):978, 1994.
- [196] J-S Zhou, JB Goodenough, and B Dabrowski. Transition from curie-weiss to enhanced pauli paramagnetism in RNiO_3 ($\text{R} = \text{La}, \text{Pr}, \dots \text{Gd}$). *Physical Review B*, 67(2):020404, 2003.
- [197] Alaska Subedi. Possible structural quantum criticality tuned by rare-earth ion substitution in infinite-layer nickelates. *Physical Review Materials*, 7(2):024801, 2023.
- [198] Harold T Stokes and Dorian M Hatch. FINDSYM: program for identifying the space-group symmetry of a crystal. *Journal of Applied Crystallography*, 38(1):237–238, 2005.
- [199] Harold T Stokes, DM Hatch, and BJ Campbell. FINDSYM. *ISOTROPY Software Suite, iso. byu. edu*, 2017.
- [200] RD T Shannon and C Tfc Prewitt. Effective ionic radii in oxides and fluorides. *Acta Crystallographica Section B: Structural Crystallography and Crystal Chemistry*, 25(5):925–946, 1969.
- [201] Konstantin A Lokshin, Daniel Mitchell, Maxim V Lobanov, Viktor Struzhkin, and Takeshi Egami. Synthesis and characterization of pure infinite layer ni^{+} nickelates: LnNiO_2 ($\text{Ln} = \text{La}, \text{Nd}, \text{Pr}$) and $\text{La}_3\text{Ni}_2\text{O}_6$. *ECS Journal of Solid State Science and Technology*, 11(4):044008, 2022.
- [202] Binbin Chen, Nicolas Gauquelin, Robert J Green, Jin Hong Lee, Cinthia Piamonteze, Matjaz Spreitzer, Daen Jannis, Johan Verbeeck, Manuel Bibes, Mark Huijben, et al. Spatially controlled octahedral rotations and metal–insulator transitions in nickelate superlattices. *Nano letters*, 21(3):1295–1302, 2021.
- [203] Sara Passuti, Julien Varignon, Adrian David, and Philippe Boullay. Scanning precession electron tomography (spet) for structural analysis of thin films along their thickness. *Symmetry*, 15(7):1459, 2023.
- [204] Jennifer Fowlie, Bernat Mundet, Constance Toulouse, Alexander Schober, Mael Guennou, Claribel Domínguez, Marta Gibert, Duncan TL Alexander, Jens Kreisel, and Jean-Marc Triscone. Crossover between distinct symmetries in solid solutions of rare earth nickelates. *Apl Materials*, 9(8), 2021.
- [205] Jonathan Hwang, Zhenxing Feng, Nenian Charles, Xiao Renshaw Wang, Dongkyu Lee, Kelsey A Stoerzinger, Sokseiha Muy, Reshma R Rao, Dongwook Lee, Ryan Jacobs, et al. Tuning perovskite oxides by strain: Electronic structure, properties, and functions in (electro) catalysis and ferroelectricity. *Materials Today*, 31:100–118, 2019.
- [206] Jennifer Fowlie, Céline Lichtensteiger, Marta Gibert, Hugo Meley, Philip Willmott, and Jean-Marc Triscone. Thickness-dependent perovskite octahedral distortions at heterointerfaces. *Nano letters*, 19(6):4188–4194, 2019.
- [207] Deepak Kumar, Adrian David, Arnaud Fouchet, Alain Pautrat, Julien Varignon, Chang Uk Jung, Ulrike Lüders, Bernadette Domengès, Olivier Copie, Philippe Ghosez, et al. Magnetism tailored by mechanical strain engineering in PrVO_3 thin films. *Physical Review B*, 99(22):224405, 2019.

- [208] Liang Si, Wen Xiao, Josef Kaufmann, Jan M Tomczak, Yi Lu, Zhicheng Zhong, and Karsten Held. Topotactic hydrogen in nickelate superconductors and akin infinite-layer oxides ABO_2 . *Physical review letters*, 124(16):166402, 2020.
- [209] Oleksandr I. Malyi, Julien Varignon, and Alex Zunger. Bulk $NdNiO_2$ is thermodynamically unstable with respect to decomposition while hydrogenation reduces the instability and transforms it from metal to insulator. *Physical Review B*, 105:014106, Jan 2022.
- [210] Liang Si, Paul Worm, and Karsten Held. Fingerprints of topotactic hydrogen in nickelate superconductors. *Crystals*, 12(5):656, 2022.
- [211] Ya-Hui Zhang and Ashvin Vishwanath. Type-II $t - J$ model in superconducting nickelate $Nd_{1-x}Sr_xNiO_2$. *Phys. Rev. Res.*, 2:023112, May 2020.
- [212] Mi Jiang, Mona Berciu, and George A. Sawatzky. Critical nature of the Ni spin state in doped $NdNiO_2$. *Phys. Rev. Lett.*, 124:207004, May 2020.
- [213] Yuhao Fu and David J. Singh. Applicability of the strongly constrained and appropriately normed density functional to transition-metal magnetism. *Phys. Rev. Lett.*, 121:207201, Nov 2018.
- [214] Qijing Zheng. Vaspbandunfolding. <https://github.com/QijingZheng/VaspBandUnfolding>, 2012.
- [215] Ruoshi Jiang, Zi-Jian Lang, Tom Berlijn, Wei Ku, et al. Variation of carrier density in semimetals via short-range correlation: a case study with nickelate $NdNiO_2$. *Physical Review B*, 108(15):155126, 2023.
- [216] Zhao Liu, Zhi Ren, Wei Zhu, Zhengfei Wang, and Jinlong Yang. Electronic and magnetic structure of infinite-layer $NdNiO_2$: trace of antiferromagnetic metal. *npj Quantum Materials*, 5(1):1–8, 2020.
- [217] Yusuke Nomura, Motoaki Hirayama, Terumasa Tadano, Yoshihide Yoshimoto, Kazuma Nakamura, and Ryotaro Arita. Formation of a two-dimensional single-component correlated electron system and band engineering in the nickelate superconductor $NdNiO_2$. *Physical Review B*, 100(20):205138, 2019.
- [218] Xiangang Wan, Vsevolod Ivanov, Giacomo Resta, Ivan Leonov, and Sergey Y. Savrasov. Exchange interactions and sensitivity of the ni two-hole spin state to hund’s coupling in doped $NdNiO_2$. *Physical Review B*, 103:075123, Feb 2021.
- [219] Peiheng Jiang, Liang Si, Zhaoliang Liao, and Zhicheng Zhong. Electronic structure of rare-earth infinite-layer $RNiO_2$ ($R = La, Nd$). *Physical Review B*, 100(20):201106, 2019.
- [220] Xianxin Wu, Domenico Di Sante, Tilman Schwemmer, Werner Hanke, Harold Y Hwang, Srinivas Raghu, and Ronny Thomale. Robust $d_{x^2-y^2}$ -wave superconductivity of infinite-layer nickelates. *Physical Review B*, 101(6):060504, 2020.
- [221] A. S. Botana and M. R. Norman. Similarities and differences between $LaNiO_2$ and $CaCuO_2$ and implications for superconductivity. *Phys. Rev. X*, 10:011024, Feb 2020.
- [222] K.-W. Lee and W. E. Pickett. Infinite-layer $LaNiO_2$: Ni^{1+} is not Cu^{2+} . *Phys. Rev. B*, 70:165109, Oct 2004.
- [223] Y. Wang, C.-J. Kang, H. Miao, and G. Kotliar. Hund’s metal physics: From $SrNiO_2$ to $LaNiO_2$. *Phys. Rev. B*, 102:161118, Oct 2020.
- [224] Frank Lechermann. Doping-dependent character and possible magnetic ordering of $NdNiO_2$. *Physical Review Materials*, 5(4):044803, 2021.

- [225] Frank Lechermann. Assessing the correlated electronic structure of lanthanum nickelates. *Electronic Structure*, 4(1):015005, 2022.
- [226] Keisuke Higashi, Mathias Winder, Jan Kuneš, and Atsushi Hariki. Core-level X-ray spectroscopy of infinite-layer nickelate: LDA+ DMFT study. *Physical Review X*, 11(4):041009, 2021.
- [227] Y. Wang, C.-J. Kang, H. Miao, and G. Kotliar. Hund’s metal physics: From SrNiO₂ to LaNiO₂. *Phys. Rev. B*, 102:161118, Oct 2020.
- [228] Yuhao Gu, Sichen Zhu, Xiaoxuan Wang, Jiangping Hu, and Hanghui Chen. A substantial hybridization between correlated Ni-*d* orbital and itinerant electrons in infinite-layer nickelates. *Communications Physics*, 3(1):84, 2020.
- [229] Mi-Young Choi, Warren E. Pickett, and Kwan-Woo Lee. Fluctuation-frustrated flat band instabilities in NdNiO₂. *Phys. Rev. Res.*, 2:033445, Sep 2020.
- [230] Jonathan Karp, Alexander Hampel, Manuel Zingl, Antia S. Botana, Hyowon Park, Michael R. Norman, and Andrew J. Millis. Comparative many-body study of Pr₄Ni₃O₈ and NdNiO₂. *Phys. Rev. B*, 102:245130, Dec 2020.
- [231] Antia S Botana, Fabio Bernardini, and Andrés Cano. Nickelate superconductors: an ongoing dialog between theory and experiments. *Journal of Experimental and Theoretical Physics*, 132:618–627, 2021.
- [232] Hu Zhang, Lipeng Jin, Shanmin Wang, Bin Xi, Xingqiang Shi, Fei Ye, and Jia-Wei Mei. Effective hamiltonian for nickelate oxides Nd_{1-x}Sr_xNiO₂. *Phys. Rev. Res.*, 2:013214, Feb 2020.
- [233] Yusuke Nomura and Ryotaro Arita. Superconductivity in infinite-layer nickelates. *Reports on Progress in Physics*, 85(5):052501, 2022.
- [234] Philipp Werner and Shintaro Hoshino. Nickelate superconductors: Multiorbital nature and spin freezing. *Phys. Rev. B*, 101:041104, Jan 2020.
- [235] Valerio Olevano, Fabio Bernardini, Xavier Blase, and Andrés Cano. Ab initio many-body *GW* correlations in the electronic structure of LaNiO₂. *Phys. Rev. B*, 101:161102, Apr 2020.
- [236] K Yamada, T Omata, K Nakajima, S Hosoya, T Sumida, and Y Endoh. Magnetic structure and weak ferromagnetism of La₂NiO_{4+δ}. *Physica C: Superconductivity*, 191(1-2):15–22, 1992.
- [237] Damian Rybicki, Michael Jurkutat, Steven Reichardt, Czesław Kapusta, and Jürgen Haase. Perspective on the phase diagram of cuprate high-temperature superconductors. *Nature communications*, 7(1):11413, 2016.
- [238] Damjan Pelc, MJ Veit, CJ Dorow, Y Ge, N Barišić, and M Greven. Resistivity phase diagram of cuprates revisited. *Physical Review B*, 102(7):075114, 2020.
- [239] Y Krockenberger, J Kurian, A Winkler, A Tsukada, M Naito, and L Alff. Superconductivity phase diagrams for the electron-doped cuprates R_{2-x}Ce_xCuO₄ (R= La, Pr, Nd, Sm, and Eu). *Physical Review B*, 77(6):060505, 2008.
- [240] Z. P. Yin, A. Kutepov, and G. Kotliar. Correlation-enhanced electron-phonon coupling: Applications of *GW* and screened hybrid functional to bismuthates, chloronitrides, and other high-*T_c* superconductors. *Phys. Rev. X*, 3:021011, May 2013.

- [241] Berit H. Goodge, Danfeng Li, Kyuho Lee, Motoki Osada, Bai Yang Wang, George A. Sawatzky, Harold Y. Hwang, and Lena F. Kourkoutis. Doping evolution of the Mott–Hubbard landscape in infinite-layer nickelates. *Proceedings of the National Academy of Sciences*, 118(2), 2021.
- [242] Victor Pardo and Warren E Pickett. Metal-insulator transition in layered nickelates $\text{La}_3\text{Ni}_2\text{O}_{7-\delta}$ ($\delta = 0.0, 0.5, 1$). *Physical Review B*, 83(24):245128, 2011.
- [243] Antia S. Botana, Victor Pardo, Warren E. Pickett, and Michael R. Norman. Charge ordering in $\text{Ni}^{1+}/\text{Ni}^{2+}$ nickelates: $\text{La}_4\text{Ni}_3\text{O}_8$ and $\text{La}_3\text{Ni}_2\text{O}_6$. *Phys. Rev. B*, 94:081105, Aug 2016.
- [244] K. G. Slobodchikov and I. V. Leonov. Spin density wave, charge density wave, and bond disproportionation wave instabilities in hole-doped infinite-layer RNiO_2 . *Phys. Rev. B*, 106:165110, Oct 2022.
- [245] Zhenglu Li and Steven G Louie. Two-gap superconductivity and decisive role of rare-earth d electrons in infinite-layer nickelates. *arXiv preprint arXiv:2210.12819*, 2022.
- [246] G. M. Dalpian, Q. Liu, J. Varignon, M. Bibes, and Alex Zunger. Bond disproportionation, charge self-regulation, and ligand holes in $s - p$ and in d -electron ABX_3 perovskites by density functional theory. *Phys. Rev. B*, 98:075135, Aug 2018.
- [247] Zhan Wang, Guang-Ming Zhang, Yi-feng Yang, and Fu-Chun Zhang. Distinct pairing symmetries of superconductivity in infinite-layer nickelates. *Phys. Rev. B*, 102:220501, Dec 2020.
- [248] Chao Chen, Runyu Ma, XueLei Sui, Ying Liang, Bing Huang, and Tianxing Ma. Antiferromagnetic fluctuations and dominant d_{xy} -wave pairing symmetry in nickelate-based superconductors. *Phys. Rev. B*, 106:195112, Nov 2022.
- [249] Andreas Kreisel, Brian M. Andersen, Astrid T. Rømer, Ilya M. Eremin, and Frank Lechermann. Superconducting instabilities in strongly correlated infinite-layer nickelates. *Phys. Rev. Lett.*, 129:077002, Aug 2022.
- [250] Lun-Hui Hu and Congjun Wu. Two-band model for magnetism and superconductivity in nickelates. *Phys. Rev. Res.*, 1:032046, Dec 2019.
- [251] Chen Lu, Lun-Hui Hu, Yu Wang, Fan Yang, and Congjun Wu. Two-orbital model for possible superconductivity pairing mechanism in nickelates. *Phys. Rev. B*, 105:054516, Feb 2022.
- [252] Roberto Dovesi, Alessandro Erba, Roberto Orlando, Claudio M Zicovich-Wilson, Bartolomeo Civalleri, Lorenzo Maschio, Michel Rérat, Silvia Casassa, Jacopo Baima, Simone Salustro, et al. Quantum-mechanical condensed matter simulations with CRYSTAL. *Wiley Interdisciplinary Reviews: Computational Molecular Science*, 8(4):e1360, 2018.
- [253] R Dovesi, VR Saunders, C Roetti, R Orlando, CM Zicovich-Wilson, F Pascale, B Civalleri, K Doll, NM Harrison, IJ Bush, et al. CRYSTAL17 user’s manual. University of Torino. URL <http://www.crystal.unito.it>, 2017.
- [254] Harrison LaBollita and Antia S Botana. Electronic structure and magnetic properties of higher-order layered nickelates: $\text{La}_{n+1}\text{Ni}_n\text{O}_{2n+2}$ ($n = 4 - 6$). *Physical Review B*, 104(3):035148, 2021.
- [255] Harrison LaBollita, Myung-Chul Jung, and Antia S Botana. Many-body electronic structure of $d^{9-\delta}$ layered nickelates. *Physical Review B*, 106(11):115132, 2022.

- [256] Myung-Chul Jung, Harrison LaBollita, Victor Pardo, and Antia S Botana. Antiferromagnetic insulating state in layered nickelates at half filling. *Scientific reports*, 12(1):17864, 2022.
- [257] Kh E El-Kelany, C Ravoux, JK Desmarais, P Cortona, Y Pan, JS Tse, and A Erba. Spin localization, magnetic ordering, and electronic properties of strongly correlated Ln_2O_3 sesquioxides (Ln= La, Ce, Pr, Nd). *Physical Review B*, 97(24):245118, 2018.
- [258] Jacques Kontak Desmarais, A Erba, and R Dovesi. Generalization of the periodic LCAO approach in the CRYSTAL code to g -type orbitals. *Theoretical Chemistry Accounts*, 137:1–11, 2018.
- [259] MD Towler, NL Allan, Nicholas M Harrison, VR Saunders, WC Mackrodt, and E Apra. Ab initio study of MnO and NiO. *Physical Review B*, 50(8):5041, 1994.
- [260] Anna Maria Ferrari and Cesare Pisani. An ab initio periodic study of NiO supported at the Pd (100) surface. Part 1: the perfect epitaxial monolayer. *The Journal of Physical Chemistry B*, 110(15):7909–7917, 2006.
- [261] M Medarde and J Rodríguez-Carvajal. Oxygen vacancy ordering in $\text{La}_{2-x}\text{Sr}_x\text{NiO}_{4-\delta}$ ($0 \leq \delta \leq 0.5$): the crystal structure and defects investigated by neutron diffraction. *Zeitschrift für Physik B Condensed Matter*, 102:307–315, 1997.
- [262] Akihiko Hayashi, Hiroyasu Tamura, and Yutaka Ueda. Successive structural phase transitions in stoichiometric La_2NiO_4 observed by x-ray diffraction. *Physica C: Superconductivity*, 216(1-2):77–82, 1993.
- [263] R Laouici, S Douafer, H Lahmar, G Rekhila, M Trari, and M Benamira. Elaboration and studies of physical and photo-electrochemical properties of La_2NiO_4 and its use with SnO_2 in photo-evolution of hydrogen under visible light irradiation. *Optik*, 236:166654, 2021.
- [264] Motoki Osada, Kohei Fujiwara, Tsutomu Nojima, and Atsushi Tsukazaki. Improvement of superconducting properties in $\text{La}_{1-x}\text{Sr}_x\text{NiO}_2$ thin films by tuning topochemical reduction temperature. *Phys. Rev. Mater.*, 7:L051801, May 2023.
- [265] A Chouket, W Cheikhrouhou-Koubaa, A Cheikhrouhou, V Optasanu, O Bidault, and M Khitouni. Structural, microstructural and dielectric studies in multiferroic $\text{LaSrNiO}_{4-\delta}$ prepared by mechanical milling method. *Journal of Alloys and Compounds*, 662:467–474, 2016.
- [266] Ekaterina Kravchenko, Dmitry Khalyavin, Kiryl Zakharchuk, Jekabs Grins, Gunnar Svensson, Vladimir Pankov, and Aleksey Yaremchenko. High-temperature characterization of oxygen-deficient K_2NiF_4 -type $\text{Nd}_{2-x}\text{Sr}_x\text{NiO}_{4-\delta}$ ($x = 1.0 - 1.6$) for potential soft/soec applications. *Journal of Materials Chemistry A*, 3(47):23852–23863, 2015.
- [267] Hong Gui, Xin Li, Zhenjie Zhao, and Wenhui Xie. Magnetic and optical properties in the 1D TM–O chain compounds Sr_2TMO_3 (TM= Ni, Co): A first-principle investigation. *Modern Physics Letters B*, 30(08):1650119, 2016.
- [268] N. D. Mermin and H. Wagner. Absence of ferromagnetism or antiferromagnetism in one- or two-dimensional isotropic heisenberg models. *Phys. Rev. Lett.*, 17:1133–1136, Nov 1966.
- [269] Chr L Teske and Hk Müller-Buschbaum. Über erdalkalimetall—oxocuprate. ii. zur kenntnis von Sr_2CuO_3 . *Zeitschrift für anorganische und allgemeine Chemie*, 371(5-6):325–332, 1969.
- [270] K. Maiti, D. D. Sarma, T. Mizokawa, and A. Fujimori. Electronic structure of one-dimensional cuprates. *Phys. Rev. B*, 57:1572–1578, Jan 1998.

- [271] J Schlappa, U Kumar, KJ Zhou, S Singh, M Mourigal, VN Strocov, A Revcolevschi, L Patthey, HM Rønnow, S Johnston, et al. Probing multi-spinon excitations outside of the two-spinon continuum in the antiferromagnetic spin chain cuprate Sr_2CuO_3 . *Nature Communications*, 9(1):5394, 2018.
- [272] J Schlappa, K Wohlfeld, KJ Zhou, M Mourigal, MW Haverkort, VN Strocov, L Hozoi, C Monney, S Nishimoto, S Singh, et al. Spin-orbital separation in the quasi-one-dimensional mott insulator Sr_2CuO_3 . *Nature*, 485(7396):82–85, 2012.
- [273] H Fujisawa, Takayoshi Yokoya, T Takahashi, S Miyasaka, M Kibune, and H Takagi. Spin-charge separation in single-chain compound Sr_2CuO_3 studied by angle-resolved photoemission. *Solid state communications*, 106(8):543–547, 1998.
- [274] M. Medarde, C. Dallera, M. Grioni, B. Delley, F. Vernay, J. Mesot, M. Sikora, J. A. Alonso, and M. J. Martínez-Lope. Charge disproportionation in $r\text{mno}_3$ perovskites ($r =$ rare earth) from high-resolution x-ray absorption spectroscopy. *Phys. Rev. B*, 80:245105, Dec 2009.
- [275] Minu Kim, Graham M McNally, Hun-Ho Kim, Mohamed Oudah, Alexandra S Gibbs, Pascal Manuel, Robert J Green, Ronny Sutarto, Tomohiro Takayama, Alexander Yaresko, et al. Superconductivity in $(\text{Ba},\text{K})\text{SbO}_3$. *Nature Materials*, 21(6):627–633, 2022.
- [276] Julien Varignon, Mathieu N Grisolia, Daniele Preziosi, Philippe Ghosez, and Manuel Bibes. Origin of the orbital and spin ordering in rare-earth titanates. *Physical Review B*, 96(23):235106, 2017.
- [277] NC Bristowe, J Varignon, D Fontaine, E Bousquet, and Ph Ghosez. Ferromagnetism induced by entangled charge and orbital orderings in ferroelectric titanate perovskites. *Nature Communications*, 6:6677, 2015.
- [278] Se Young Park, Anil Kumar, and Karin M. Rabe. Charge-order-induced ferroelectricity in $\text{LaVO}_3/\text{SrVO}_3$ superlattices. *Phys. Rev. Lett.*, 118:087602, Feb 2017.
- [279] Zhihong Yuan, Pengyu Zheng, Yiran Peng, Rui Liu, Xiaobo Ma, Guangwei Wang, Tianye Yu, and Zhiping Yin. Correlation-enhanced electron-phonon coupling and superconductivity in $(\text{Ba},\text{K})\text{SbO}_3$ superconductors. *Phys. Rev. B*, 105:014517, Jan 2022.
- [280] He Zhao, Hong Li, Brenden R Ortiz, Samuel ML Teicher, Takamori Park, Mengxing Ye, Ziqiang Wang, Leon Balents, Stephen D Wilson, and Ilija Zeljkovic. Cascade of correlated electron states in the kagome superconductor CsV_3Sb_5 . *Nature*, 599(7884):216–221, 2021.
- [281] Lijun Li, Xiaoyu Deng, Zhen Wang, Yu Liu, Milinda Abeykoon, Eric Dooryhee, Aleksandra Tomic, Yanan Huang, John B Warren, Emil S Bozin, et al. Superconducting order from disorder in $2\text{H-TaSe}_{2-x}\text{S}_x$. *npj Quantum Materials*, 2(1):11, 2017.
- [282] A. F. Kusmartseva, B. Sipos, H. Berger, L. Forró, and E. Tutiš. Pressure induced superconductivity in pristine 1T-TiSe_2 . *Phys. Rev. Lett.*, 103:236401, Nov 2009.
- [283] Sudipta Koley, Narayan Mohanta, and Arghya Taraphder. Charge density wave and superconductivity in transition metal dichalcogenides. *The European Physical Journal B*, 93:1–8, 2020.
- [284] Hermann Arthur Jahn and Edward Teller. Stability of polyatomic molecules in degenerate electronic states—I—Orbital degeneracy. *Proceedings of the Royal Society of London. Series A-Mathematical and Physical Sciences*, 161(905):220–235, 1937.
- [285] S Miyasaka, Y Okimoto, M Iwama, and Y Tokura. Spin-orbital phase diagram of perovskite-type RVO_3 ($\text{R} =$ rare-earth ion or Y). *Physical Review B*, 68(10):100406, 2003.
- [286] KI Kugel and DI Khomskii. Crystal-structure and magnetic properties of substances with orbital degeneracy. *Zh. Eksp. Teor. Fiz.*, 64:1429–1439, 1973.

- [287] O Friedt, M Braden, G André, P Adelman, S Nakatsuji, and Y Maeno. Structural and magnetic aspects of the metal-insulator transition in $\text{Ca}_{2-x}\text{Sr}_x\text{RuO}_4$. *Physical Review B*, 63(17):174432, 2001.
- [288] JL Martínez, C Prieto, J Rodríguez-Carvajal, A de Andrés, M Vallet-Regí, and JM González-Calbet. Structural and magnetic properties of Sr_2RuO_4 -type oxides. *Journal of magnetism and magnetic materials*, 140:179–180, 1995.
- [289] M. Braden, G. André, S. Nakatsuji, and Y. Maeno. Crystal and magnetic structure of Ca_2RuO_4 : Magnetoelastic coupling and the metal-insulator transition. *Phys. Rev. B*, 58:847–861, Jul 1998.
- [290] C. S. Alexander, G. Cao, V. Dobrosavljević, S. McCall, J. E. Crow, E. Lochner, and R. P. Guertin. Destruction of the Mott insulating ground state of Ca_2RuO_4 by a structural transition. *Phys. Rev. B*, 60:R8422–R8425, Sep 1999.
- [291] Alexandru B Georgescu and Andrew J Millis. Quantifying the role of the lattice in metal–insulator phase transitions. *Communications Physics*, 5(1):135, 2022.
- [292] S. Nakatsuji, V. Dobrosavljević, D. Tanasković, M. Minakata, H. Fukazawa, and Y. Maeno. Mechanism of hopping transport in disordered Mott insulators. *Phys. Rev. Lett.*, 93:146401, Sep 2004.
- [293] Yoshiteru Maeno, T Maurice Rice, and Manfred Sigrist. The intriguing superconductivity of strontium ruthenate. *Physics Today*, 54(1):42–47, 2001.
- [294] Y Maeno, H Hashimoto, K Yoshida, S Nishizaki, T Fujita, JG Bednorz, and F Lichtenberg. Superconductivity in a layered perovskite without copper. *Nature*, 372(6506):532–534, 1994.
- [295] JE Ortmann, JY Liu, J Hu, M Zhu, J Peng, M Matsuda, X Ke, and ZQ Mao. Competition between antiferromagnetism and ferromagnetism in Sr_2RuO_4 probed by Mn and Co doping. *Scientific reports*, 3(1):2950, 2013.
- [296] Hung-Lung Huang and Horng-Tay Jeng. Orbital ordering and magnetism in layered perovskite ruthenate Sr_2RuO_4 . *Scientific Reports*, 10(1):7089, 2020.
- [297] Hiroyoshi Nobukane, Kosei Yanagihara, Yuji Kunisada, Yunito Ogasawara, Kakeru Isono, Kazushige Nomura, Keita Tanahashi, Takahiro Nomura, Tomohiro Akiyama, and Satoshi Tanda. Co-appearance of superconductivity and ferromagnetism in a Ca_2RuO_4 nanofilm crystal. *Scientific reports*, 10(1):3462, 2020.